UNIVERSITA' DEGLI STUDI DI MODENA E REGGIO EMILIA

Dipartimento di Scienze Chimiche e Geologiche

A new approach for the determination of the PGE content in geological and environmental samples

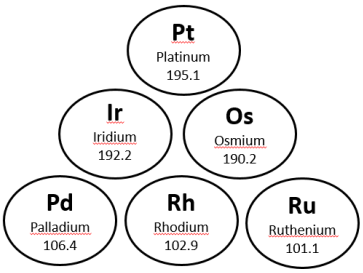

Candidate**:** **Renzo Tassinari**

Tutor: Prof. Maurizio Mazzucchelli

Co-Tutor: Prof.ssa Costanza Bonadiman

PhD Course Coordinator: Prof. Alfonso Pedone

Dottorato di Ricerca in
Models and Methods for Materials and Environmental Sciences
Ciclo XXXIII– A.A. 2019-2020

Abstract

The platinum-group elements (PGEs) are six metallic elements that are grouped together in the periodic table. They consist of rhodium, ruthenium palladium, with progressive atomic numbers from 44 to 46, and platinum iridium, osmium with progressive atomic numbers from 76 to 78. They have similar chemical and physical properties and occur together in nature. The properties of PGEs, such as high melting points, corrosion resistance, and catalytic qualities, make them indispensable for many industrial applications and mining is an economical rewarding activity for many countries (i.e., South Africa, Zimbabwe, Canada, USA, Russia). However, in terms of commercial value and market demand, PGEs are classified as critical raw materials, because the global supply is restricted to limited geographical regions of relatively low geopolitical stability.

PGEs are among the rarest metals on Earth, and their siderophile/chalcophile geochemical affinity determined their differentiation in the Earth's core, during the early stage of the Earth's evolution, leaving a PGE-highly depleted silicate layer (mantle+crust). The upper crust contains about 0.0002-5 parts *per* million (ppm) of platinum.

The determination of PGEs in geological and environmental samples is difficult, due to the low concentration of these elements and their heterogeneous distribution in the rocks (nugget effect). Accurate and simple analytical methods are under theoretical and analytical development to obtain reliable values, measuring bulk rocks without applying pre-concentration procedural methods.

Various natural samples were selected for measurements on a large spectrum of matrices of geological interest. These included 3 meteorites (2 chondrites and a supposed iron meteorite), 9 mantle xenoliths, 13 agricultural and 12 urban soils, 8 pelagic limestones. A large group of certificate Reference materials (CRMs), with similar lithology as the samples used in this study, have been added to the measurement tests, mainly to verify the efficiency of the sample preparation.

The samples were dissolved by applying the dissolution procedure of acid digestion in an open system as it is routine in geological analyses (lithophile trace element analyses; e.g., REE). The measurements were made using the latest generation of the triple-quadrupole TQ-ICP-MS spectrometers, with high capacity in the interference control. This, in combination with the techniques' high sensitivity, allows the direct determination of PGEs in the sample solution, without the need of a pre-concentration step. The prepared solutions were repeatedly analysed over a period of three years (2018-2021), which unfortunately included the shutdown of laboratory activities in Italy and worldwide for the pandemic COVID-19. Therefore, the number of tests is less than the number necessary for the official validation of the proposed analytical protocol.

Notwithstanding this, interesting analytical and scientific results were produced. In matrices containing a high concentration of potential interfering elements, the most accurate PGE values were obtained only with ammonia as a cell reaction gas. However, if the expected abundances are in the range of 10-100 ppb, the use of O_2 as a cell reaction gas, gives plausible and useful results, when elemental interferences have been previously evaluated.

This procedure has proved to be valid in determining Ir even at very low concentrations (< ppb level) in a carbonate matrix, allowing a "minimum Ir enrichment value" to be specified, (i.e., standard value), which can identify a potential meteoritic impact event in similar geological contexts.

Finally, the determination of PGEs in the urban soil of Emilia Romagna region (Italy), allowed to identify a clear link between PGEs in soil and road pollution. The limited analytical tests are promising, but they have to be validated by a large future analytical work, which would take into account many other variables related to the chemical/physical aspects and possibly contribute to the creation of a database of PGE risk in urban zones.

Acknowledgements

These three PhD years have represented for me an unexpected and stimulating opportunity, that, at my age and at this stage of my career, I didn't think it would happen. Unfortunately, the Covid-19 pandemic struck and unprecedented events transformed the last year into something akin to a hurdle race.
I feel very grateful and thankful to my personal supervisor Maurizio Mazzucchelli and to my co-tutor in Ferrara, Costanza Bonadiman for their relentless contributions, feedback and for pushing me to do my best and not to succumb to difficulties. I am very thankful that they gave me the opportunity to deepen my knowledge in various aspects of the geosciences, which helped me to improve the quality of my current and future work.
I would like to extend my sincere thank to all the people who supported me in acquiring those data which integrated my project: Federica Zaccarini (University of Leoben, Austria) for EMPA analyses; Alberto Zanetti (CNR- Pavia, Italy) for LA-ICP-MS analyses; Annalisa Martucci (University of Ferrara, Italy) for powder-XRD analyses. I would like to thank my co-tutor Costanza Bonadiman again, together with Massimo Coltorti at University of Ferrara for providing me with the mantle rocks for this thesis; the same gratitude goes to Roberto Coccioni who sampled the K-T level at Gubbio (Italy) ad hoc for this thesis. A special thank you to the ©Thermo Fisher experts, Matteo Oddone and Matteo Guzzo (Milan, Italy), for their continuous support and advice for the instrument set-up. I am deeply indebted to my colleagues at the Department of Physics and Earth Sciences of the University of Ferrara, Francesco Droghetti, Umberto Tessari and Massimo Verde, for their professional assistance in laboratory activities and their enduring friendship in a difficult period.
A special thank you goes to Emilio Saccani, for his willingness and precious support in the revision work.
Many thanks should also go to my friends Barbara Galassi and Steve Deforie for having supported me since the beginning and in difficult times.
Finally, I would like to thank my family for their patience, that cannot be underestimated, and, in particular, to my wife Elisabetta, my daughter Lisa and my son Raffaele, who have always been there, thoughtfully, motivating me, listening to me, laughing with me and loving me.

1 Introduction

1.1 Motivation of the research

This work is concerned with a specific group of chemical elements -Platinum Group elements (PGEs)- which comprise of platinum (Pt), palladium (Pd), rhodium (Rh), ruthenium (Ru), iridium (Ir) and osmium (Os) with very similar chemical and, to a lesser extent, physical properties (metals). Because of their strong siderophile nature, they occur at very low concentrations in the Silicate Earth (mantle + crust). However, the chemical characteristics of PGEs and other HSEs (Highly Siderophile Elements) such as Au and Re, made these elements economically interesting for industrial applications and scientists from different disciplines continued to work on the development of many concentration and extraction procedures (see chapter 3 for details). The chemical characteristics of PGEs are the basis of pre-concentration methods used in chemical analyses. In particular, because of their siderophile behaviour, fire assay is generally the chosen extraction technique for the analysis of geological samples for mining application.
This experimental thesis investigates the potential for a simplified sample preparation method (without the pre-concentration of the analytes), followed by measurements by the most recent Triple Quadrupole (TQ) plasma mass spectrometry, which significantly improved the control of interferences.
RMs (Reference Materials) and natural samples with different matrices of geological/cosmological and environmental interest were investigated.
It is understandable that such a simplified approach is unlikely to provide high quality results for all the elements and different matrices, when compared with data obtained by well consolidated, more complex and more costly analytical protocols. Instead, the aim is to verify if, with a simplified sample preparation procedure (at least for a subset of studied elements and matrices), the latest generation spectrometers could yield good data for geological/environmental studies.
The benefit of this approach is evident:
a simplified sample preparation protocol would favour the production of a higher amount of data, which, in turn, would contribute to the interpretation modelling in different sectors of geological/environmental disciplines.

1.2 Outline the thesis

This thesis is organised in five chapters.
Chapter 1. Introduction. It includes: the motivation of the research (1.1); the outline of the Tesis (1.2); a brief review of the state of the art in the analytical methods in the PGEs determination and an overview of the economic relevance of the PGEs for modern human activities (updated with the effects of the COV-19 pandemic) (1.3); a description of Earth's main geochemical/cosmochemical PGE reservoirs (1.4) and the impact of anthropogenic activity on the natural background of PGEs in soils (1.5).
Chapter 2. Materials. It introduces the rationale behind the sample selection, and describes the main characteristics of each sample type. It also includes a list of the reference materials.
Chapter 3. Method tests. It introduces the analytical issue in detail and includes analytical procedures (i.e., sample preparation and processing, standards, preliminary tests, instrumental set-up, Electron Microprobe Analysis, Laser Ablation Microprobe ICP-MS analysis), and the passed and/or failed tests are systematically investigated.
Chapter 4. Data description and discussion. The results presented in this chapter enable i) the evaluation of the reliability of bulk rock analytical data experimentally obtained, as compared with in-situ PGE measurements (i.e., sulphides an Fe-Ni alloys in chondrite meteorites) performed with LA-ICP-MS; ii) the evaluation of the efficiency of the analytical procedure applied to detect PGE environmental risk in urban soils; iii) a contribution to one of the most fascinating geological questions: what is the minimum detectable Ir enrichment that a sediment can register due to a meteoritic impact (i.e. K-T/K-Pg boundary).
Chapter 5. Conclusive remarks and future prospects. This is the final and most general chapter, which provides a cumulative summary of the thesis, how it accomplished the goals that defined it, and an outlook on the future laboratory activities that utilize the TQ to measure PGE contents in a geological context without the need for pre-concentrated samples.
Due to the effects of pandemic restrictions and TQ set-up difficulties, most of the results need further validation, before being ready for publication. Notwithstanding this, two manuscripts that include bulk PGE measurements from this thesis are in preparation.

1.3 Overview of the nature of PGEs and their strategic relevance

1.3.1 The Platinum Group Elements

Platinum Group Elements (PGEs), sometimes referred to as platinum-group metals (PGMs), comprise of six elements (Fig. 1.1, Table 1.1): platinum (Pt), palladium (Pd), rhodium (Rh), ruthenium (Ru), iridium (Ir) and osmium (Os).

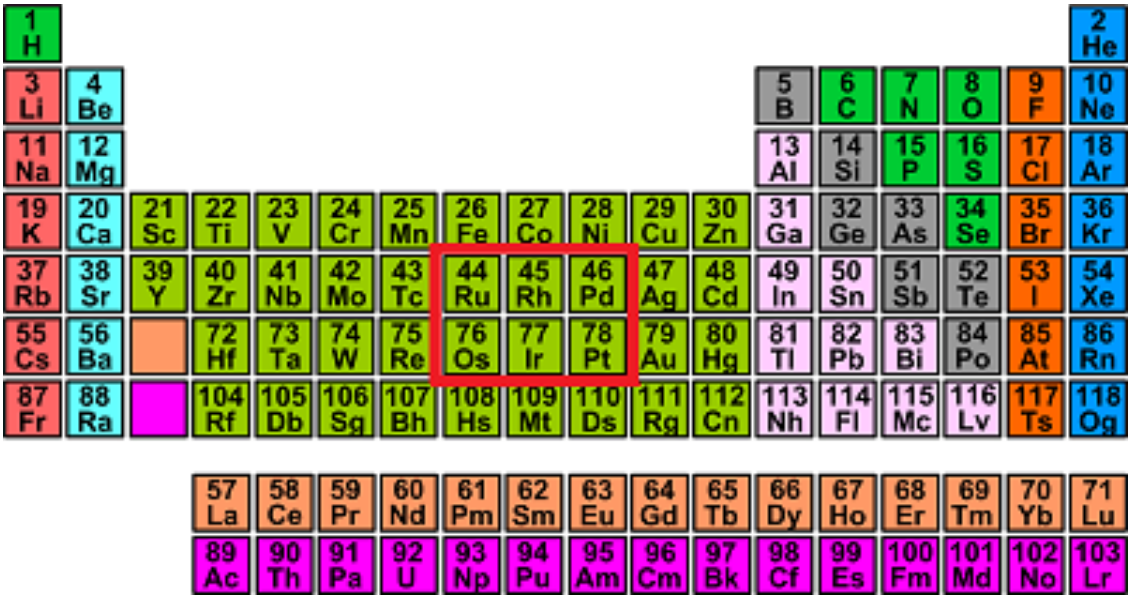

Figure 1.1: Periodic Table of the Elements with highlighted PGEs

	ruthenium	rhodium	palladium	osmium	iridium	platinum
Atomic Number	44	45	46	76	77	78
Standard Atomic Weight	101.07	102.9055	106.42	190.23	192.217	195.084
Density (g/cm^3)	12.37	12.45	12 023	22.59	22.56	21.45
Melting point °K	2607	2237	1828	3306	2739	2041
Vieckers hardness (MPa)	2298	1246	461	4137	1760	549
Thermal Conductivity (W/m K)	120	150	72	88	150	72
Crystal structure	hcp	fcc	fcc	hcp	fcc	fcc
Isotopes and natural abundance	^{96}Ru 5.54% ^{98}Ru 1.87% ^{99}Ru 12.76% ^{100}Ru 12.6% ^{101}Ru 17.06% ^{102}Ru 31.55% ^{104}Ru 18.62%	^{103}Rh 100%	^{102}Pd 1.02% ^{104}Pd 11.14% ^{105}Pd 22.33% ^{106}Pd 27.33% ^{108}Pd 26.46% ^{110}Pd 11.72%	^{184}Os 0.02% ^{186}Os 1.59% ^{187}Os 1.96% ^{188}Os 13.24% ^{189}Os 16.15% ^{190}Os 26.26% ^{192}Os 40.78%	^{191}Ir 37.3% ^{193}Ir 62.7%	^{190}Pt 0.014% ^{192}Pt 0.782% ^{194}Pt 32.97% ^{195}Pt 33.83% ^{196}Pt 25.24% ^{198}Pt 7.163%

Table 1.1: Properties of the PGEs (hcp: hexagonal closed-packed; fcc: face-centred cubic).

1. Introduction

PGEs are scarce natural resources that occur together in nature; they are considered as precious metals, like gold and silver, but they are also widely used for industrial applications such as chemical, electronics and automotive industries catalysts (mainly Pt, Pd and Rh); medical implants (Pt and Rh); anticancer drugs (Pt); fingerprint detection (Os); cleaning liquids (Rh), tipping pens (Ir); compass bearings (Ir); nitric acid production (Rh); jewellery (Pt).
Moreover, their distinct geochemical behaviour is essential in the study of the early solar system evolution and planet formation and differentiation.
Finally, three PGEs are involved in radioisotope decay systems as parent (^{107}Pd–^{107}Ag), daughter (^{187}Re–^{187}Os), or both (^{190}Pt–^{186}Os), which provide chronological data and tracers for geochemical processes (Carlson et al., 2008).
Thanks to advances in analytical chemistry and low-detection multielement analytical facilities, platinum-group elements (PGEs) recently joined the panel of geochemical tracers of the Earth's mantle, thirty years after the rare earth elements (REEs) and other lithophile elements that are concentrated in silicates and oxides. (Lorand et al., 2008).

PGEs are mostly found in rocks of different geological environments, but traces can also be detected in urban air and accumulated on the road surface, in roadside soil and vegetation. Transport of PGEs via stormwater results in contamination of aquatic environments. There is now mounting evidence that a fraction of PGEs in the environment is bioavailable, and potential uptake into the biosphere is raising concern over potential risks for humans and the environment (Rauch and Morrison, 2008).

In most rocks, platinum-group minerals are very small, ranging in size from less than a micron to a few hundred microns in diameter. Their presence, therefore, may be detected by laboratory analysis only, and determining trace and ultratrace PGE concentrations in geological and recycled (environmental) materials is one of the most challenging analytical problems.

The determination of PGEs as well as other highly siderophile elements HSEs (Au and Re) in geological and environmental samples is in fact difficult, due to the low concentration of these elements and their heterogeneous distribution in the rocks (nugget effect). Many methods for their measurement have been developed in the last 20 years (e.g., Becker et al., 2002; Day et al., 2003 and 2017; Ishikawa et al., 2014; Li et al., 2014; Luguet et al., 2007 and 2008; Meisel et al. 2003b; Meisel and Horan, 2016; Pearson et al., 2002). Recently, Chu (2021) has explored the different state-of-the-art sample dissolution and analyte extraction methods carried over the last thirty years by the HSE scientific community. However, the triple quadrupole plasma mass spectrometry (TQ-ICP-MS or QQQ-ICP-MS), has not been taken into account as a measurement means for these elements. Consequently, any attempt to further develop these methods or to find alternative ones specifically focused on the use of this new spectrometry technique, deserves to be investigated.

The determination of precious metals (PGEs plus Au) in most common geological samples is generally described as a two-step process. The first step involves the preparation of a representative sample and the separation / pre-concentration of these metals from the rock/ore matrix. The second step involves the measurement of their concentration in suitable analyte samples prepared by highly sensitive instrumentation. (Balaram et al., 2006).

For a long time, the analysis of PGEs was carried out mostly by neutron activation (Instrumental Neutron Activation Analysis; INAA). This method has been extensively used for Ir because it can be analysed without dissolving the sample and applying radiochemical separation procedures. The other PGEs are less sensitive to INAA therefore samples require a lengthy radiochemical procedure. With the increasing use of ICP-MS (Inductively Coupled Plasma Mass Spectrometry), the INAA lost ground and was progressively abandoned as a suitable technique for PGE analyses.

Nuclear methods (INAA and RNAA Instrumental and Radiochemical Nuclear Activation Analyses) continue to be important in the determination of trace quantities of precious metals in geological materials (Dai et al. 2001), but ICP-MS, as already mentioned, is becoming the most used analytical technique. Moreover, ICP-MS allows the determination of isotopic ratios of the platinum group elements (Re-Os; Pt) (e.g., Becker et al., 2002; Day et al., 2003; Ishikawa et al., 2014; Li et al., 2014; Luguet et al., 2007; Pearson et al., 2002). Finally, the possibility to introduce solid samples by the use of a laser microprobe (LAM-ICP-MS), also allows the punctual determination (in situ) of the elements (e.g., Pearson et al., 2002).

1. Introduction

Despite the ICP-MS's high sensitivity, wide dynamic range and multi-element capability, the determination of PGEs in geological and environmental material is still challenging due to their low content and severe interferences from the matrix. (Desprez et al., 2016). For instance, Whiteley and Murray (2005) highlighted that the accurate determination of Pt, Pd and Rh in environmental samples by ICP-MS is complicated by molecular ion and doubly charged ion interferences (e.g., $CuAr^+$, HfO^+, SrO^+, YO^+, and Pb^{2+}).

The well consolidated methods, which are able to produce high quality data, address the interference problem by separating the analytes from the interfering matrix. The chemical separation procedure is complex. Another approach is based on a correction by mathematical algorithms. The latter was used in several laboratories because it is quicker and simpler, when compared to the chemical separation/pre-concentration processes (e.g., Simitchiev et al., 2008 and references therein).

A further way to address the interference issue is linked to the technological development of analytical instruments (e.g., high-resolution spectrometers HR-ICP-MS or Collisional Reaction Cells), which significantly improved the performance in terms of resolution and interference control by the use of magnetic sectors as mass filter or a device for the control of the main polyatomic interferences.

However, the separation of some of the interferences which affect PGEs requires a mass resolution beyond the capability of the commercially available HR-ICP-MS which has a maximum resolution of 10000. For example, the separation of $^{103}Rh^+$ from $^{87}Sr^{16}O^+$ and $^{105}Pd^+$ from $^{89}Y^{16}O^+$, requires a mass resolution ($M/\Delta M$) of 102900 and 27600 respectively. The use of a Collision Reaction Cell on a single quadrupole ICP-MS is also unable to completely remove such interferences. (Desprez, 2016)

Finally, the latest generation of the triple quadrupole ICP-MS has the capacity to separate interfering elements from the analyte. This, in combination with the very high sensitivity, allows the direct determination of PGEs in the sample solution, without the need of a pre-concentration step (Bokhari et al., 2015; Sugiyama, 2017; Kutscher et al., 2018, 2019).

The interference's control process of the TQ spectrometer is described in detail in Chapter 3. Consolidated methods of sample preparation and analysis of geological and environmental material are briefly described below.

A first relevant obstacle in the development of an analytical method for the determination of PGEs on total rock is the "nugget effect". In terrestrial rocks, PGEs are not generally hosted in the main silicate minerals; instead, they are usually concentrated in trace and rare minerals, like for example sulphides and HSE-alloys, which are scattered in the rock. Not even an accurate grounding process of the sample would guarantee a homogeneous distribution of the elements in the final powder. For commercial mining samples (PGE and other HSE content 0.1-2 µg/g) (Meisel and Horan, 2016), the nugget effect can be controlled by the use of high quantities of material (10-100 g). In fact, the representativeness of a heterogeneous material is directly correlated to the test portion size. The need to process high quantities of the sample, is an important factor that made fusion and subsequent extraction by fire assay the chosen technique in mining applications.
In this technique, the sample powder is mixed with fluxes and melted in a reducing atmosphere in the presence of a proper "collector" (Pb, Ni). A second melting phase (cupellation), this time in an oxidising atmosphere, leads to the concentration of the PGEs by oxidation of the metallic binder. Unfortunately, the use of large quantities of reagents like the metallic binder and of salts of alkaline metals used as fluxes (sodium carbonate and hydroxide, and lithium meta and tetraborate) needed to process these quantities of powder, cause high blank levels and, consequently, high LODs (Limits of Detection) of the technique.

For these reasons, acid digestion (often at high pressure) is generally preferred for samples having lower levels of PGEs and other HSEs than mining samples, as well as most of the rocks and soils with PGE and other HSE contents in the order of ppb or ppt.

For this type of preparation, however, smaller sample quantities can be processed: generally, 0.5-3 g (Meisel and Horan, 2016) are used in geochemical laboratories. Smaller sample quantities would inevitably affect the measurement's repeatability and reproducibility. When a high variance in replicate analyses is observed and it is not imputable to other analytical factors (linked to the preparation protocol: incomplete dissolution and/or contamination, or due to the measurement: spectrum interference and/or instrumental drift), it is clear that the problem lies in an insufficient sample quantity. For each analyte/matrix combination, it should always be assessed if PGEs are homogeneously distributed at the scale of the amount

of dissolved sampled. Knowing the distribution of the analytes in minerals and in metallic alloys can simplify the interpretation of the variance obtained from replicate analyses. As an example, 1 and 3 grams of powder of a fertile peridotite could show a strong variability in the measured Os, but, at the same time, give reasonably constant results for Re (Meisel and Horan, 2016). This can be explained by the fact that Os is only hosted in alloys or in PGE-rich trace minerals, while traces of Re can be also hosted in more widespread silicate or sulphides. The opposite situation (constant Os concentrations and scattered values of Re) has been observed in komatiites (Meisel et al., 2001a; 2001b), due to the heterogeneous distribution of molybdenite (MoS_2), which is richer in Re compared to Os. Pt concentrations were measured and compared in different laboratories on two reference materials: UBN (serpentinised lherzolite) and MUH-1 (harzburgite) (Meisel and Horan, 2016). The results showed the nugget effect on the same analyte in two different matrices. Pt values in UBN do not show a large variation, while in MUH-1 they are very variable, with a tendency to higher concentrations. Harzburgites (residual peridotite) are generally poor in sulphides and Pt is hosted in rare alloy grains or trace sulphides like laurite (Ru, Ir, Os) S_2 (Meisel and Horan, 2016). Laurite is particularly resistant to acid attack (Chu, 2021) and its complete dissolution in aqua regia (AR) may not occur. The large variability of the MUH-1 results, therefore, is not only due to the difficulty of recovering PGEs, but also to the heterogeneity of the sub-samples' values from different laboratories (Fig. 1.2) (Meisel and Horan, 2016).

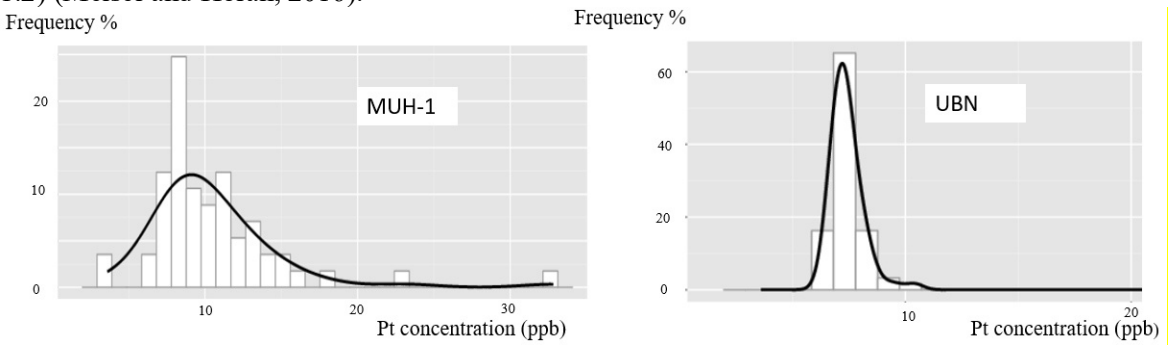

Figure 1.2: *Inter-laboratory comparison of harzburgite MUH-1 and lherzolite UB-N. Scheme and data from Meisel and Horan, 2016.*

In the last three decades, several review papers on the latest developments in the determination of PGEs and Au (precious metals) or PGEs and Re and Au (HSEs) have been published. For example, in 1999 Barefoot and Van Loon selected the main papers published between 1990 and 1998 on this topic. Their work included significant research contributions in the field of sample preparation and of pre-concentration of the precious metals prior to their determinations. In these papers, several instrumental methods were also reviewed.

Ishikawa et al., (2014) focussed on acid attack digestion techniques characterised by protocols which did not include de-silicification. They then compared the results with protocols that included a step of de-silicification by HF either before or after the HNO_3 and HCl acid attack.

In particular, Ishikawa et al., (2014) highlighted the advantages of the acid attack compared to the classic NiS FA (Ni sulphides fire assay) in the determination of PGEs plus Au and Re at low concentrations. The authors insisted on the two main limitations of these procedures: limited amount of processable powder and incomplete digestion (of both silicate minerals and more resistant phases like spinels or problematic alloys). Using reference material of basaltic, ultramafic and sedimentary compositions, they tested several digestion procedures and used different equipment (microwave, Carius tube, high pressure asher), conditions (temperature, duration, sample size) and acid mixtures. The authors tried to asses if an HF dissolution step was needed in order to extract all the PGEs from the silicate portion of the rock. The best results were obtained with Carius tubes at 240°C for 72 hours, followed by a de-silicification step with HF.

Some acid digestion protocols use aqua regia (ratio 3:1 of HCl and HNO_3) for HSE extraction: the strong oxidation power of this mixture is highly effective on elements with a high redox potential. Many other studies used the "inverse" (or "reverse") aqua regia (a mixture in ratio 1:3 of HCl and HNO_3) or 5:2 or 5:3 HCl and HNO_3 mixtures (Meisel and Horan, 2016).

In his paper on the advances in analytical methods of Re-Os and PGEs in geological materials, Chu (2021) provides an overview on the most commonly used sample preparation procedures for mass spectrometry analysis.

The author states that the first stage of the Re-Os and PGE sample digestion is the dissolution of samples with low procedural blanks. The currently followed procedures are: NiS fire assay, low temperature acid attack, alkali fusion or acid dissolution combined with alkali fusion, Carius tube acid digestion and finally the HPA (High Pressure Asher) acid digestion.

NiS Fire Assay - The main advantage (the possibility to process high quantity of material) and disadvantage (high procedural blanks, which in turn increase the LODs) of this procedure have already been addressed.

Low-temperature acid attack - Acid attack dissolution procedures at low temperature use HF + HCl + ethanol or HF + HBr in a PFA beaker for the sample digestion (Walker, 1988; Birck et al., 1997; Reisberg and Meisel, 2002).
The main advantage of this method is the possibility to obtain extremely clear procedural blanks (e.g., Os blank 0.05 pg) (Birck et al., 1997; Gannoun et al., 2007), but the complete dissolution of Os-bearing refractory phases, particularly for peridotites, often cannot be achieved (e.g., Qi et al., 2011). Gannoun et al., (2007) demonstrated that for rocks like MORB (Middle Oceanic Ridge Basalts) this method achieved comparable results to those obtained at high pressure (Carius tube acid digestion). Unfortunately, this is not true for other rocks nor for all types of basalt (Ishikawa et al 2014). The addition of a strong oxidating agent like HNO_3 to the acid mixture facilitates the process but prevents the Os determination (Qi et al., 2011).

Alkali fusion, or acid dissolution combined with alkali fusion techniques – Refractory minerals such as spinel, chromite and PGE alloys can be successfully dissolved for Re-Os-PGE analysis by using the $NaOH/Na_2O_2$ fusion method (Morgan and Walker, 1989; Sun et al., 2001; Reisberg and Meisel, 2002; Meisel et al., 2003a). This method is particularly useful for meteorites (e.g., Morgan and Walker, 1989; Becker and Walker, 2003; Yokoyama et al., 2007; Yokoyama et al., 2010). Unfortunately, the reagent blanks are usually quite high, and the spike-sample equilibration sometimes cannot be completely achieved (Qi and Zhou, 2008).
Qi et al., (2004) proposed a method for lowering the blank level by combining an acid attack with a Na_2O_2 fusion.

Carius tube acid digestion –The Carius tube method has been developed and used since the 40s, but only in 1995 Shirey and Walker applied the technique to the Re-Os isotopic analysis. An oxidising solution (generally reverse aqua regia) allows the dissolution of samples at high temperatures without the loss of OsO_4. Qi et al., (2010) developed a variation of the digestion procedure when sulfides like pyrite or bitumen samples must be analysed, by adding H_2O_2. The advantage of the Carius tube method is that for Re-Os and PGEs measurements, low procedural blanks can be obtained.
Becker et al., (2006) reported a modified method (cf. Gordon et al., 1944) by putting the sealed Carius tube into a pressure steel jacket containing dry ice. The CO_2 pressure that builds up inside the steel pressure vessel upon heating balances the internal pressure in the Carius tube, such that the digestion temperature could be as high as 345°C. For some mantle xenoliths, samples digested at 345°C give higher Os mass fractions and lower $^{187}Os/^{188}Os$ ratios compared to digestions at 220–230 °C (Chu, 2021). Other researchers (e.g., Meisel et al., 2003a; Qi and Zhou, 2008; Ishikawa et al., 2014; Li et al., 2015; Day et al., 2016b) used HF de-silicification and aqua regia in a Carius tube for silicate materials. Qi and Zhou (2008) reported an issue with ultramafic reference material OKUM: 4 to 14% of PGEs present in the silicate phases cannot be extracted by the use of aqua regia not even at a temperature of 300 °C.

HPA (High Pressure Asher) acid digestion – This procedure provides controlled conditions of high temperature and high pressure, which consent a fast and more complete digestion of silicate samples by the use of a high pressure asher (HPA, Anton Paar, Graz) and reusable quartz glass vessels. The method was implemented for Re-Os and PGE analyses by the Meisel's group, Montanuniversität Leoben, Austria (Meisel et al., 2001a; Meisel et al., 2003a; Meisel et al., 2003b; Meisel and Moser, 2004a; Meisel and Moser, 2004b).

According to Meisel and Horan (2016), up to 5 g of powder can be digested by using reverse aqua regia in the HPA containers at 300-320°C. The elements Pt and Pd show a lower PGE blank than with the Carius tube (Meisel et al., 2001a; Meisel et al., 2003b). Unfortunately, the initial economical investment for the equipment and the routine maintenance are rather costly (Meisel and Horan, 2016). Some authors (e.g., Dale et al., 2012; Ishikawa et al., 2014) reported that HF de-silicification was needed for some silicate samples.

After the sample digestion, several different techniques have been adopted in laboratories for the pre-concentration of PGEs, like dry chlorination (Perry et al, 1992), solvent extraction (Togashi and Terashima, 1997; Pearson and Woodland 2000) and Tellurium co-precipitation (Whiteley and Murray, 2005). The latter is also often combined with the nickel sulphide fire array. (Gros et al., 2002; Morcelli et al., 2004; Balaram et al., 2006).
The most applied purification procedures for PGEs, however, are chromatographic, which use ion exchange resin columns. They can be divided into two main categories: columns with anion exchange resins and columns with cation exchange resins (Meisel and Horan, 2016 and reference therein).
Through the use of anion exchange resins (e.g., AG1-X8) and a high molarity acid, the PGEs are separated into groups like Re+Ru and Pt+Ir. They are particularly appropriate for high-resolution ICP-MS analyses. A hydrogen peroxide treatment before the chromatographic separation (e.g., Dale et al., 2012) can reduce the chromium oxides interference on Ru. The limit of the anion exchange resin procedure is the low efficacy in recovering Pd (Meisel and Horan, 2016).
In the cation exchange resin method (Whiteley and Murray, 2005), instead, PGEs are scarcely retained by the resin (e.g., Dowex AG50W-X8) and they easily elute with the use of a weak acid, while the matrix components, like major and most of the trace elements, are blocked inside the resin.
For the separation of Os, the most applied pre-concentration procedure is by solvent extraction, which uses CCl_4 (methane tetrachloride) o $CHCl_3$ (chloroform) for an initial extraction from aqua regia, and HBr (hydrobromic acid) for the back extraction (Cohen and Waters, 1996).
In this method, Os oxidises into OsO_4 and is removed from aqua regia through a liquid-liquid extraction into the solvent. This is repeated three times (each step allows an extraction of about 60-70%) and each time the immiscible solvent portion containing Os is removed. HBr is then added to the organic solvent and shaken into an emulsion to extract Os. In this phase Os is reduced and concentrated in the HBr. Once the organic solvent is removed, the HBr and Os solution is dried. Alternatively, OsO_4 can be directly distilled from the solution after acid digestion (Meisel and Horan, 2016).
For a more complete and detailed reading of the chemical separation/pre-concentration techniques for PGEs and Re, please refer to Chu, 2021. As already mentioned in paragraph 1.1., this work is instead aimed at verifying if the use of TQ-ICP-MS allows the determination of these elements in geological/environmental samples (at least for certain analyte/matrix combinations) avoiding the laborious and time-consuming chemical separation/pre-concentration steps.

1.3.2 PGE strategic relevance

PGEs can be classified as noble metals. Among the various definitions of this term, here it is used to mean "a metal whose potential is positive relative to the hydrogen electrode", since it emphasises the resistance of PGEs to oxidation. This is important for understanding their geochemistry. The high values of the PGE reduction potential reflect the instability of oxides and the stability of metals. The reduction potential of the Ru oxide is at least three times higher than that of FeO and the Pt oxide is the least stable under terrestrial conditions (O'Neill et al., 1995). This reveals the strong tendency of PGEs to partition into metal phases. Assuming equilibrium between metal and silicate, the ratio of the concentration of a PGE in liquid or solid metal to that in a silicate melt at given T, P and fO_2 is known as the geochemical parameter "partition coefficient" ($D_{PGE}^{met/sil}$). By definition, elements with partition coefficient above ~ 10^4 are named highly siderophile elements (HSEs) and they include the PGEs, Re and Au. Moreover, within the range of oxygen and sulphur fugacity, prevalent in the crust and upper mantle, the PGEs also exhibit a chalcophile behaviour (Naldrett and Duke, 1980).
PGEs present a high partition coefficient between sulphide melts and silicate magmas, they are therefore easly concentrated in magmatic ore deposits, which form during the cooling and crystallization of magma. If mafic to ultramafic magmas become saturated in sulphur, and this is strictly related to the Fe contents in silicate magmas (Kiseeva and Wood, 2015), an immiscible sulphide liquid will separate from the silicate

magma and form globules that naturally concentrate metals like nickel, and, as minor/trace contents, the PGEs.

Only a few large ore deposits occur on Earth; among these, South Africa is the main supply of PGEs and its relatively low geopolitical stability results in the **PGEs** to be considered as **critical metals** (Mudd et al., 2018). Critical metals are generally defined as metals in global demand for their use in current technologies, without feasible substitutes, and whose global supply is restricted to limited geographical regions.
The PGEs have been in persistent demand over the past 15 years and this led to an increase in exploration, particularly in North America and other regions of higher geopolitical stability. Exploration and mining companies have found approximately $1.04*10^5$ metric tons of PGEs (with minor gold) in mineral deposits around the world that could be developed. In the United States, the Stillwater Complex, a mafic-to-ultramafic igneous intrusion in Montana, has a deposit that has produced roughly 305 metric tons of platinum and palladium since 1986. Drilling estimates indicate that another 2200 metric tons are present. Rough geological estimates suggest another 1000 to 6200 metric tons of PGEs could be present at depth. In the future, PGEs may be produced from deposits found near the base of the Duluth Complex, another group of igneous intrusions in Minnesota.
Of all the PGEs, **platinum and palladium** are of major commercial significance, with **rhodium** the next most important.

Given the greater commercial importance and use of platinum, palladium and rhodium, there is generally much more information available on these elements than for the other three PGEs. **Osmium** for example, is a little-used, toxic metal, for which there is virtually no quantitative data. The European Union (EU) takes into account the strategic importance of the "critical metals" and monitors and evaluates the available resources in respect to the market demand. For some of these metals, such as PGEs, it is not feasible to carry out a quantitative criticality assessment using the methodology employed in the 2013-2016 studies on the European Union's list of Critical Raw Materials. In 2017, the European Commission introduced a change in methodology for calculating the indicators for the criticality assessment (summarised in Schrijvers et al. 2020) of Os (and all PGEs).

1.3.3 Indicators for the criticality assessment
The criticality matrix was introduced containing axes for supply risk (i.e., probability) of a supply disruption and impact of supply restriction, also referred to as "vulnerability to a supply disruption" (Fig. 1.3)
Four intermingled perspectives were presented, in which environmental and social aspects could affect raw material criticality:
- **Perspective 1**: environmental/social impacts as a source of supply risk (e.g., European Commission (EC) 2010): environmental impacts cause high or low probability of supply disruption of a material due to potential regulations.
- **Perspective 2**: vulnerability of the environment/social values to material use (Graedel et al., 2012): the use of a material has a high or low impact on the environment.
- **Perspective 3**: environmental/social risk (Frenzel et al., 2017): the disrupted availability of a material has a high or low impact on the environment or on social values.
- **Perspective 4**: reputational risk (Schrijvers et al., 2020): the use of a material with a high environmental or social impact affects the reputation of the company.

Several methods apply **perspective 1** and include or mention environmental or health indicators as factors of supply risk. These methods consider that the supply of a material might be impeded or disrupted, or that the price could increase, due to the implementation of regulations (Goddin, 2019). An example of such regulations is the European REACH (Registration, Evaluation, Authorisation and Restriction of Chemicals), which restricts the use of hazardous substances.
Other methods use ecotoxicity measures as an indicator to predict the probability of future regulations. An example regarding social factors is the regulation on the use of "conflict minerals" (Cassiterite (Sn); Columbite (Nb and Ta); Wolframite (W); Gold (Au)) from the Democratic Republic of the Congo (DRC) and adjoining regions.

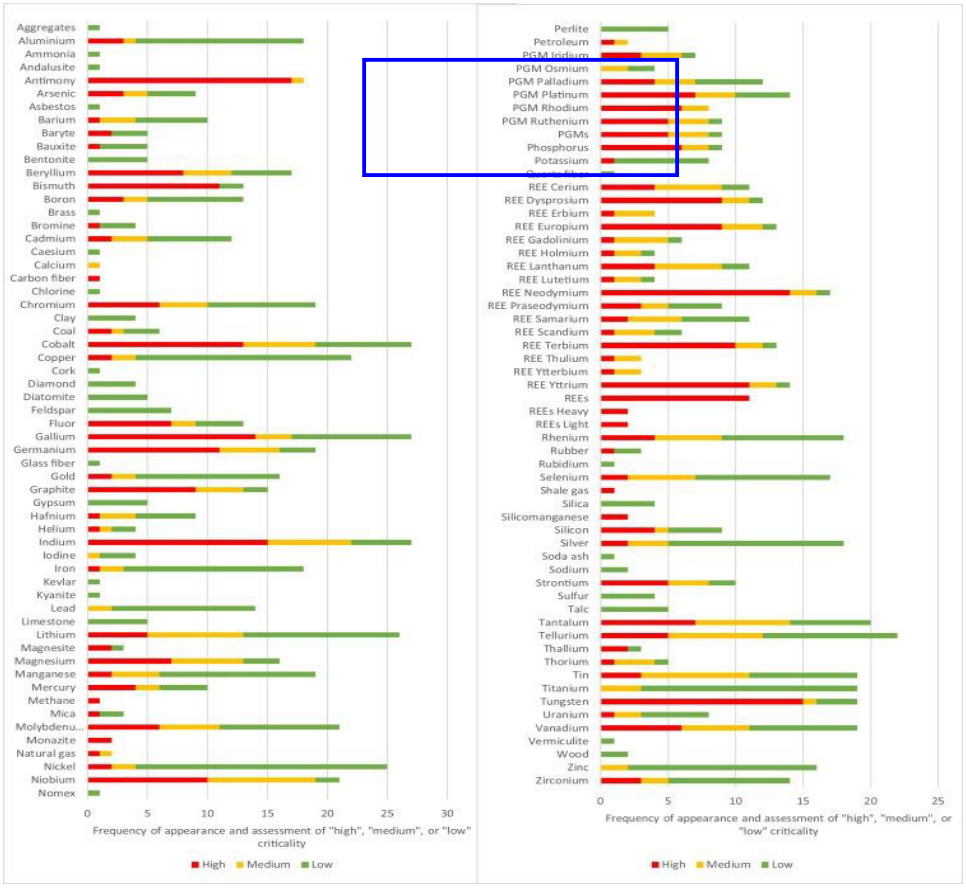

Figure 1.3: Frequency of appearance in criticality assessments and criticality determination (high, medium, or low) of materials. Various methods are included (see text). The critical assessment for PGEs as a group and for individual PGEs is evidenced (from Schrijvers et al., 2020).

The axis "environmental implications" applies **perspective 2**. This parameter considers that high environmental impacts or important social issues lead to low societal acceptance, which subsequently affects the use of a material hence, applying perspective 1. The 2010 European Commission report assessed the method "environmental risk" via a separate dimension that represented "the risk that measures might be taken by countries with the intention of protecting the environment and by doing so endangering the supply of raw materials to the European Union" (European Commission Report 2010). Note that this explanation of "environmental risk" does not follow the interpretation of **Perspective 3**, but instead represents **Perspective 1**. In the EC 2014 assessment, this indicator was evaluated to be an inaccurate predictor of supply disruptions, and was therefore excluded (European Commission Report 2014). However, environmental performance is still covered by indicators of "regulatory quality" (by stringency of environmental regulations) and "government effectiveness" (e.g., drinking water and sanitation, maintenance and waste disposal, and efficient use of resources).

Frenzel et al., (2017) discussed how a criticality assessment can calculate – instead of economic risks – social or environmental risks (**Perspective 3**). Such an assessment could calculate the product of the probability of a supply disruption and the vulnerability of a societal (e.g., human health) or environmental (e.g., climate change) factor. Within this perspective, the system that is at risk could be defined as, for example, "the environment", "the planet", or "social values". Within **perspective 3**, it could also be interesting to consider the potential negative effects of the conflict minerals' legislation on the social circumstances in supplying regions. Such negative effects could take place when companies stop sourcing their materials from conflict regions and the local communities lose their primary source of income.

A perspective that could be relevant for environmental and social factors is the "reputational risk" **(perspective 4):** if the use of a product is associated with high environmental or social impacts, this could affect the reputation of a downstream company. A bad reputation could result in a negative demand shock. This perspective, however, is not implemented in most of the reviewed criticality assessments, except for a few companies (e.g., EBP/Empa, ESSENZ, and SCARCE) who consider that a low societal acceptance can impede the possibility for a company or country to use a certain material.

1.3.4 PGE deposits and updated economic evaluation

PGEs deposits can be found in different geological environments, depending on their genetic origin.
The main hosts of PGEs are plutonic and volcanic mafic to ultramafic igneous rocks of Archaean–Proterozoic–Mesozoic age. PGE deposits tend to predominate in Late Archaean to Paleoproterozoic intrusions (Naldrett, 2010). Examples of these deposits are: Sudbury (Canada); Bushveld (South Africa); Stillwater, Montana (USA), Great Dyke (Zimbabwe) Duluth, Coldwell (USA), Stella (South Africa) and Fedorova–Pana (Russia).
PGEs can also be found in sedimentary and hydrothermal deposits. The sedimentary deposits are either black shale containing marine sedimentary exhalative sulphidic ore, or placer deposits derived from mafic–ultramafic magmatic sources (Deposits of Russia; Nicholson Bay, Saskatchewan (Canada)); the hydrothermal deposits are represented by a vein-like or replacement mode, accumulated by metals transported from the parent body (Sukhoi Log, Russia; Nicholson Bay, (Canada)).
PGEs also occur in contact mineralization deposits and in the mineral cooperite in igneous rocks (Cassard et al., 2015). Enrichment of PGEs has also been described in lateritic environments (Yilgarn Craton in Western Australia; Hoatson, 1998).
The main production and resources of PGEs, however, are mainly linked to two geological features: a layered mafic-to-ultramafic intrusion (Bushveld Complex in South Africa, The Great Dyke in Zimbabwe) and a sill-like intrusion associated with flood basalts (Noril'sk-Talnakh area, Russia).
Due to the geographic location of PGE reserves (Fig. 1.4), the related mining activities are concentrated in very few countries.

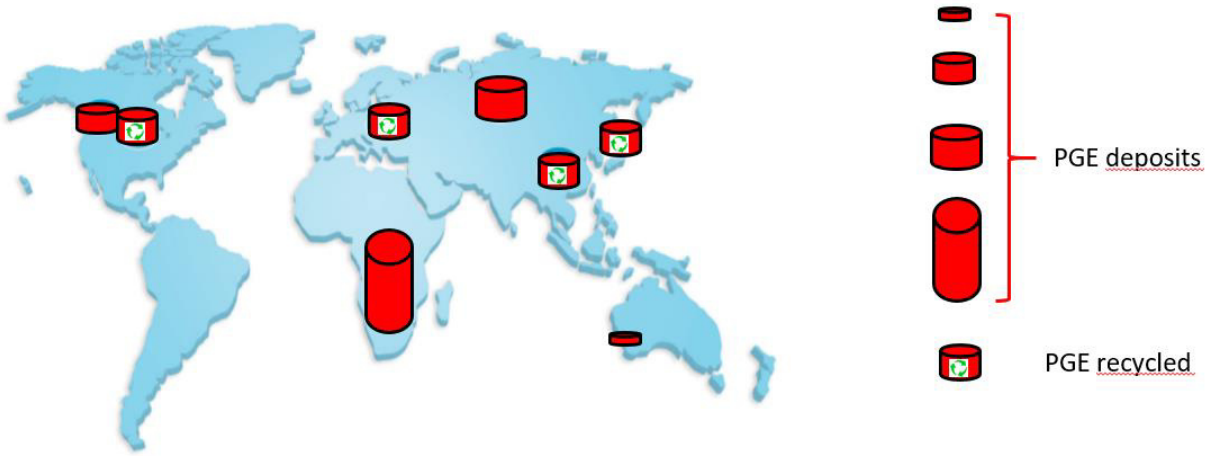

Figure 1.4: Map of the world PGE *main production sites and resources (data from Latunussa et al., 2020).*

In South Africa, the Bushveld Complex contains the world's largest primary PGE resources, based on the Merensky and Upper Group 2 (UG2) reefs within the intrusive complex. In addition, PGEs can also be recovered from the Bushveld's chromitite reefs but this is typically more expensive. In Canada and Russia, PGEs are recovered from Ni-dominant deposits, such as the Sudbury Basin in central Ontario or the Taimyr Peninsula in northern Siberia.
Critical raw material deposits can be classified, according to the metric tons of contained commodity, into: super large deposits class A: >1000 metric tons of contained commodity, large deposits class B: >100 metric tons of contained commodity and medium deposits class C: >10 metric tons of contained commodity.
In Europe, the super large deposits are not present; only two large deposits can be found in Greece (Bertrand et al., 2016).
The introduction of stricter emission standards for motor vehicles is expected to contribute to the demand for platinum, palladium and rhodium, which are used in the fabrication of autocatalysts. An increase in the adoption of fuel cells technology is also expected to be supportive for platinum demand.
PGE prices are high (Table 1.2) and typically volatile because of their limited availability in nature, and the low flexibility for accommodating rapid changes in demand. On the basis of the **JRC Technical Report - EC,** (Torres de Matos et al., 2020), t**he global demand for PGEs for all applications is about 635 tonnes per year (average over the period 2016-2018).**

PGMS

	PRICE
IRIDIUM USD/OZ	6400.00
IRIDIUM GBP/OZ	4577.66
IRIDIUM EUR/OZ	5260.10
RHODIUM USD/OZ	28800.00
RHODIUM GBP/OZ	20599.49
RHODIUM EUR/OZ	23670.43
RUTHENIUM USD/OZ	450.00
RUTHENIUM GBP/OZ	321.87
RUTHENIUM EUR/OZ	369.85

PLATINUM PRICES

	BID	ASK	+/-	%	HIGH	LOW	
PLATINUM USD/OZ	1252.90	1260.55	0.94	0.08	1268.96	1238.05	20:59 LDN
PLATINUM GBP/OZ	894.19	903.59	-6.76	-0.75	908.93	888.95	20:59 LDN
PLATINUM EUR/OZ	1028.97	1036.82	-8.68	-0.84	1045.56	1022.73	20:59 LDN

Table 1.2: Iridium, rhodium, ruthenium, and platinum prices in a selection of currencies (May, 7 2021) (from Precious Metals Management - Johnson Mattey Pic.).

PGEs are of great importance in many modern technologies and products. The catalytic properties of PGEs are the basis of their most important applications in emission control systems in vehicles and in industrial process catalysts for bulk-chemical manufacture and petroleum refining. Other applications include electronics, glass manufacturing, jewellery, dental and medical special alloys (Table 1.3). There are no effective substitutes that provide the same performance as the PGEs. In many applications, a PGE can substitute for another one. Platinum and palladium can be interchanged to a certain extent in autocatalysts, depending on the prices and demand/supply for each; however, they cannot be considered fully substitutable.

	Ir	Os	Pd	Pt	Rh	Ru
Use	alloying agent; electronic, chemical, automotive industries		alloying agent; catalytic converters	Jewellery; alloying agent autocatalysts; chemical sector; drugs anticancer	alloying agent; autocatalysts; glass production, chemical sector	alloying agent; electronics and chemical industries
Supply	mine production and secondary recovery	by-product of refining nickel and some platinum-group metals	mine production and secondary recovery	mine production and secondary recovery	mine production and secondary recovery	mine production and secondary recovery
Source countries	South Africa; Zimbabwe; Canada; Russia	Russia; South Africa; USA; Canada	Russia; South Africa	South Africa; Zimbabwe; Russia	South Africa; Russia	South Africa; Zimbabwe; Russia
Price market	May 2021: US$ 6300 per troy ounce		First trimester 2021: US$ 1550 per troy ounce	March 2021: US$ 1263 per troy ounce	May 2021: US$ 24,000 per troy ounce	May 2021: US$ 450 per troy ounce
Recycling	process catalysts		spent autocatalysts and old jewellery	spent autocatalysts and old jewellery	spent automotive catalysts	process catalysts

Tab. 1.3: Summary of relevant attributes of PGEs.

PGEs (Platinum in particular) have therefore become a strategic commodity for many countries, e.g., USA, China and the Euro-zone countries (Koek et al., 2010; Mudd, 2012).

The global known PGE resources are estimated to be in excess of $1*10^5$ tonnes. South Africa hosts by far the world's most abundant resources (68%), while Russia and Zimbabwe also hold significant proportions of 17% and 9%, respectively. Reserves of PGEs are estimated at 17,000 tonnes, with a similarly high geographical concentration and distribution as resources. The **94% of the world PGE reserves are located in South Africa, Russia, and Zimbabwe**, (Mudd, et al, 2018). The Class B large deposits in the Bushveld Complex (South Africa) and the Class A super large deposits of Norilsk (Russia) account for more than 90% of the annual global production (Fig. 1.4).
PGEs are scarce natural resources produced in low volumes. Global primary production of PGEs in 2017 amounted to 447 tonnes (182 tonnes platinum; 208 tonnes palladium; 23 tonnes rhodium, 34 tonnes iridium and ruthenium). (Source: Latunussa et al., 2020). The largest primary supplier of PGEs worldwide is South Africa, followed by Russia. Supply from South Africa is dominated by platinum and supply from Russia by palladium. South Africa is also the main supplier of the 'minor' PGEs: rhodium, ruthenium, and iridium. The PGEs primary production is highly concentrated, as South Africa and Russia together produce around 82% of the world total, with the remainder coming predominantly from Zimbabwe and North America (Canada and United States). Less than 2 tonnes are produced annually in the EU, mainly in Finland as a by-product of nickel and copper mining. Production in other countries is limited to the mining of smaller deposits including placers, refining of Pt from Ni-rich secondary lateritic deposits and recycling of Pt from industrial wastes (Mungall and Naldrett, 2008; Mudd, 2010).
Due to the different physical-chemical properties of the six elements, each one finds specific uses and different commercial importance.

1.3.5 Iridium

Iridium (Ir) is, after osmium, the second most dense element of the periodic table, with a density of 22.55 g/c m^3 (Table 1.4). It is also the most corrosion-resistant metal known. It is extremely hard and brittle (6.5 hardness on the Mohs scale), over four times harder than platinum, therefore challenging to work, unless it is heated to very high temperatures (Ir melting point: 2716 K), but it has exceptional electrical conductivity (almost two times higher than platinum and palladium) and excellent biological compatibility. Iridium is chiefly used in the form of platinum alloys as it improves considerably the platinum's hardness. (Brenan, 2008a; Reith et al., 2014). For its good resistance to corrosion, it is widely used in the electronic, chemical, and automotive industries. In the latter, Ir is present as an impurity or is found in alloys together with platinum, palladium, and rhodium in automobile catalytic converters. These devices are continuously subjected to physical and chemical stress that leads to the Ir release in airborne particulate matter and a consequent increase in metal levels in the general environment (Iavicoli and Leso, 2015). Applications of iridium in low-carbon technologies are identified in platinum catalysts for fuel cells (polymer electrolyte membrane), as well as in energy-efficient lighting (Iavicoli and Leso, 2015).
Iridium, as ruthenium, is of lower commercial importance compared to platinum, palladium, and rhodium. Global supply (Fig. 1.5) is highly concentrated in terms of both mine production and secondary recovery. The top importer worldwide of the "minor PGEs" (iridium, ruthenium, and osmium) in unwrought and powder form is Japan, and in semi-manufactured forms the United States and China. The leading exporting countries, for unwrought metal and powder are South Africa and Germany, and for semi-manufactured forms the UK and South Africa.
The market for iridium is small and illiquid and subject to high price volatility. In 2018, the price of iridium reached a level of US$1,480 per troy ounce (Source: Precious Metals Management - Johnson Mattey PIc). An explosion in the price has taken place during the COVID-19 pandemic and currently (May 7, 2021 quotation) the price is US$6400 per troy ounce (Source: Precious Metals Management - Johnson Mattey PIc).
The world demand for iridium averaged 6.4 tonnes annually in the years 2012-2016. The import reliance for iridium from primary sources is 100%. The EU is an important global supplier of refined iridium metal originating from secondary materials collected domestically or imported (Source: EU's list of Critical Raw Material, 2020).
The annual mine production of iridium worldwide is estimated at about 6 tonnes. South Africa dominates the world mine production with a share of over 90% where iridium originates from platinum group-metal mining operations as a co-product. Small quantities are also produced in mines in Zimbabwe, Canada and Russia. No primary production occurs in the EU (Source: EU's list of Critical Raw Material, 2020). The end-of-life recycling input rate of iridium is approximated at 14%. Iridium is mostly recovered from process catalysts.

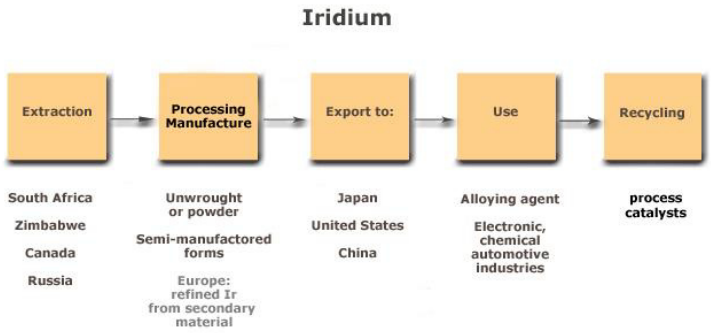

Figure 1.5: Iridium's process flow chart.

1.3.6 Osmium

Osmium (Os) is the rarest of the stable elements: its average abundance in the Earth's crust is about 1 gram per 200 tonnes. Osmium's density (22.587 g cm^{-3}; Table 1.4) just slightly exceeds that of iridium, differing by only 0.1% (Arblaster, 1995). Despite its rarity, osmium is currently far less expensive than the other elements of the platinum group and gold, partly because it has few commercial uses (Source: EU's list of Critical Raw Material, 2020). Today, osmium is obtained commercially as a by-product of refining nickel and some of the more common platinum-group metals. The worldwide annual production of osmium (Fig. 1.6) - approximately 500 kilograms, about 5,000 times less than its gold counterpart - could be easily accommodated in the back seat of an automobile (Source: EU's list of Critical Raw Material, 2020).

Osmium metal is bluish-grey in colour, hard and brittle, with high compressional capacity, so much so that it rivals diamond as the least compressible of all known natural substances (Girolami, 2012).

Osmium can be mixed with other platinum-group elements to form alloys that, owing to their hardness, find specialty uses as electrical contacts, wear-resistant machine parts, and tips for high-priced ink pens.

It can exist in eleven different oxidation states, from –2 to +8; a versatility matched only by another element of the platinum group, ruthenium and a few other transition metals. Furthermore, the high +8 oxidation state reached by osmium — along with iron, ruthenium and xenon — is the highest seen for any chemical element standard conditions. The most useful osmium compound is the tetroxide OsO_4, a colourless solid used as a stain in microscopy and in fingerprint detection. Finally, osmium tetroxide is a key component in a remarkable catalyst mixture that adds two hydroxyl (alcohol) groups to carbon–carbon double bonds. For the discovery/study of this reaction, Karl Barry Sharpless was awarded the Nobel Prize in Chemistry in 2001 (Sharpless, 2002).

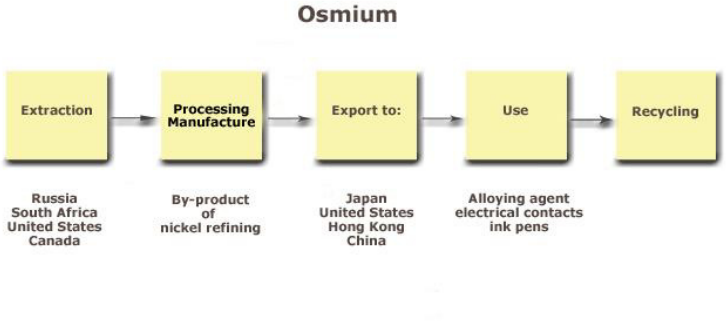

Figure 1.6: Osmium's process flow chart.

1.3.7 Palladium

Palladium (Pd) is a shiny silver-grey metal and the least dense of the PGEs with a density of 12.02 g/cm^3) about the same as silver, and it has the lowest melting point of the PGEs (T = 1827 K; Table 1.4), although

it is still high compared with common metals. Palladium is slightly harder than platinum (4.75 hardness on the Mohs scale) but ductile and smoothly worked when annealed. It has significant temperature stability and resistance to oxidation and corrosion, even though lower than platinum and the rest of the PGEs. Like all PGEs, palladium has unique catalytic properties, and, additionally, metallic palladium is capable of absorbing up to 900 times its volume of hydrogen. Palladium is often used as an alloy, including other PGEs as alloying elements (Brenan, 2008).
Palladium and platinum, are the most commercially important of the PGEs. The market supply from primary sources is highly concentrated in Russia and South Africa (Fig. 1.7), which have a combined share of nearly 80% of the world mine output. Russia is the leading world exporter of palladium in unwrought and powder form, followed by the UK, South Africa and the US. The palladium market is in deficit since 2011, which is reflected in higher prices (Source: EU's list of Critical Raw Material, 2020).
Averaged over the period 2012-2016, the annual palladium demand in Europe amounted to 59 tonnes. The EU consumption of palladium metal in unwrought or powder form is estimated to have been at 46.5 tonnes per year in the same period, mostly sourced through import. Import of semi-manufactured forms of palladium also contribute to the EU demand, as well as production from secondary sources.
By far the leading application of palladium is in catalytic converters for petrol-powered vehicles. The growth of the electric vehicle market could reduce the demand for palladium over time, though hybrid technology is still reliant on these Pd catalysts to control emissions.
The price of palladium has fluctuated considerably in recent years. Palladium's price climbed to a record level of US$ 2550 per troy ounce in February 2020, widening the price gap with platinum considerably (Source: Precious Metal Management - Johnson Mattey PIc, 2020). The global COVID-19 pandemic stabilised the first trimester 2021 prize at US$ 1550 per troy ounce, maintaining it higher than platinum's.
World reserves of palladium are estimated to be 7,200 tonnes in Pd content. About 44% of these reserves are located in South Africa and 41% in Russia. EU mine production makes a small contribution to European palladium supply with an annual output of less than one tonne, of which about 97% is produced in Finland and the remainder in Poland. The secondary supply of platinum is based on the recycling of spent autocatalysts and old jewellery (Source: EU's list of Critical Raw Material, 2020).

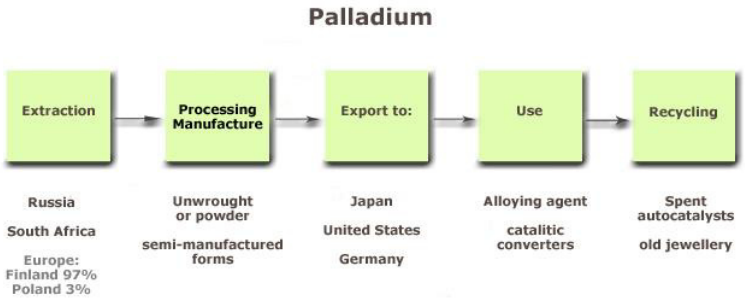

Figure 1.7: Palladium's process flow chart.

1.3.8 Platinum

Platinum (Pt) has a density of 21.45 g/cm^3, and, together with iridium and osmium, is the densest known metal, being about 10% denser than gold and nearly twice as dense as silver or lead (Table 1.4). Platinum has exceptional catalytic properties and is relatively soft (4.3 hardness in Mohs scale) and ductile, making it malleable enough to be worked into intricate shapes or stretched into fine wires. As it is extremely resistant to chemical corrosion and oxidation and has a high melting point (2043 K; Table 1.4), platinum maintains its performance in even the most demanding operating conditions at high temperatures. Moreover, due to its lustrous silver-white colour, platinum is well suited for making jewellery. Platinum is mostly used as an alloy. Its working characteristics, hardness and wear properties are optimised by alloying it with other PGEs such as iridium and ruthenium.
Platinum and palladium are the most significant PGEs of commercial importance. The market supply of platinum from primary sources is highly concentrated in South Africa. South Africa and the United Kingdom hold the largest shares in the world market for exports of platinum in unwrought/powder form, accounting for 25% and 21%, respectively of total exports by value in 2017. Germany is the largest importer globally for platinum in unwrought/powder form. In the longer term, it has been suggested that global

demand may require significant increases in platinum production because of platinum's use in emerging technologies, e.g., fuel cell electric vehicles. (Source: EU's list of Critical Raw Material, 2020).
Since mid-2011 platinum's price is following a declining trend. In October 2017 platinum's price became lower than palladium's price for the first time since 2001. The global COVID-19 pandemic impacted the platinum market's supply and demand dynamics, with supply being affected significantly. While demand for this metal fell approximately 7% in 2020, supply declined about 20%. Platinum has risen more than 90% since its low on March 20, 2020, through to March 26, 2021 (US$ 1263 per troy ounce; Source: Bloomberg).
The average European demand for platinum in the period 2012-2016 was about 64 tonnes *per* year, and the average world demand was approximately 178 tonnes *per* year. EU mine production makes a small contribution to the European platinum supply. South Africa (42%) and the UK (25%) are the main source countries for EU imports of platinum in either unwrought or powder form (Source: EU's list of Critical Raw Material, 2020).
Its use in autocatalysts dominates the demand. In 2018, consumption of platinum in autocatalysts accounted for 39% of global demand and 75% of European demand, reflecting the dominance of diesel vehicles in Europe in comparison with the rest of the world. Besides autocatalysts, other important applications of platinum include the use in jewellery, and as a catalyst in chemical manufacture such as nitric acid production.
South Africa is the dominant producer with a share of over 70% of the world mine production. Russia and Zimbabwe are other important producers with a share of 13% and 7%, respectively (Fig. 1.8). EU mine production makes a small contribution to European platinum supply with an annual output of about one tonne, of which about 95% is produced in Finland and the remainder in Poland. (Source: EU's list of Critical Raw Material, 2020). The secondary supply of platinum is based on the recycling of spent autocatalysts and old jewellery.
Platinum is a material of significance for fuel cells, a key technology for the transition to a low-carbon economy. Fuel cell electric vehicles are expected to play an important role in the achievement of a low-carbon road transport system, especially for heavy vehicles in long-distance transport. Fuel cell technology using platinum catalysts is also applicable for stationary applications to generate heat and power.

Figure 1.8: Platinum's process flow chart.

1.3.9 Rhodium

Rhodium (Rh) is a silvery-white metal with excellent reflective properties. With a density of 12.41 g/cm^3, it is lighter than platinum, iridium and osmium but has a higher melting point (2233 K) than platinum and palladium (Table 1.4). Its hardness (5.5 on the Mohs scale) makes it an excellent alloying element to harden platinum and palladium. In fact, rhodium is predominantly used as an alloy with other PGEs. Rhodium is extremely corrosion resistant and does not tarnish in the air at room temperature. It has exceptional catalytic activity, similar to platinum and palladium, and outstanding electrical conductivity, the highest among PGEs.
Rhodium is the third most commercially important PGE, after platinum and palladium. South Africa is the major source, accounting for almost 60% of the world's rhodium supply (Fig. 1.9). Russia is the second largest producer, although its sales are, as with the other PGEs, volatile and subject to political intervention. There is no production of rhodium from primary sources in the EU. Rhodium is used predominantly in autocatalysts, which account for over 80% of the global demand. Rhodium is also essential in the manufacture of glass and specific process catalysts for the chemicals sector (e.g., nitric acid production).

Cobalt is a potential substitute in process catalysts for aldehydes production, ruthenium in catalysts for acetic acid production, and gold or iridium in glass manufacturing equipment
Since October 2016, the rhodium price has been rising steadily, and in September 2019 peaked to a multi-year high of US$ 5,000 troy ounce. The significant gains in the rhodium price in 2019 coincide with projected increased demand for autocatalysts due to tighter emissions legislation and more stringent testing. The global COVID-19 pandemic impacted the rhodium market's supply and demand increasing the prices dramatically (US$ 24,000 troy ounce- May 2021-; Source: Bloomberg). In the mid- to long-term, the transition to electric mobility may lead to reduced demand for rhodium (Source: EU's list of Critical Raw Material, 2020). Nonetheless, rhodium is almost entirely recycled from spent automotive catalysts, which contributes to a substantial proportion of the total metal supply, a relatively higher share than for platinum and palladium. The global average end-of-life functional recycling rate ranges from 50% to 60%. In 2018, recycling accounted for 31% of rhodium global supply (Source: EU's list of Critical Raw Material, 2020).

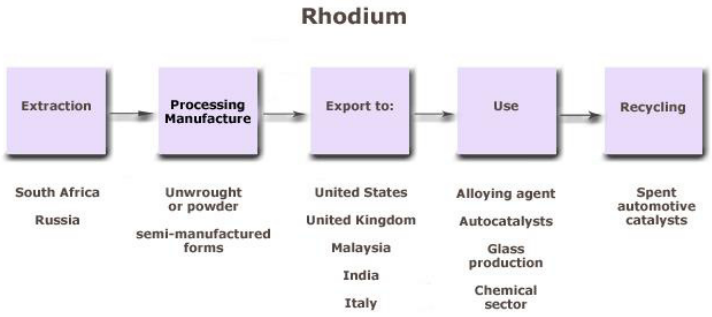

Figure 1.9: Rhodium's process flow chart.

1.3.10 Ruthenium

Ruthenium (Ru) is the fourth PGE in order of commercial significance, after platinum, palladium and rhodium; however, its demand is comparable with that of rhodium in terms of quantity. Ruthenium is a shiny silver-grey metal, considerably lighter than platinum, osmium and iridium with a density of 12.45 g/cm^3, very high melting point of 2583 K, and exceptionally hard (hardness of 6.5 on the Mohs scale), over five times harder than platinum, as well as brittle, even after annealing at temperatures as high as 1773 K (Table 1.4). This implies that the use as a pure compound is constrained because it is extremely difficult to work; instead, ruthenium is generally used as an alloying agent to improve wear resistance in electrical contacts and to impart hardness to platinum and palladium. Also, on account of its exceptional corrosion resistance and very good electrical and catalytic properties, ruthenium finds essential applications in the electronics and chemical industries.
Ruthenium, as iridium, is of lower commercial importance compared to platinum, palladium, and rhodium. Global supply is highly concentrated in terms of both mine production and secondary recovery. The top importers worldwide of the "minor PGEs" (iridium, ruthenium, and osmium) are: Japan, in unwrought and powder form and the US and China in semi-manufactured forms.
South Africa hosts the majority of PGE resources with identified ruthenium occurrences. Ruthenium also occurs in PGE deposits in Zimbabwe and Russia (Fig. 1.10). Data on resources and reserves for ruthenium are not available in the public domain (Source: EU's list of Critical Raw Material, 2020).
The market for ruthenium is small and illiquid and subject to high price volatility. In 2018, the price of ruthenium climbed to a ten-year high of US$ 270 per troy ounce. In the two years of the COVID-19 pandemic the prices have almost doubled (May 2021: US$ 450 per troy ounce; Source: Precious Metal Management - Johnson Mattey Pic).
There is no production of ruthenium in the EU from primary sources. The end-of-life recycling input rate of ruthenium is estimated at 11%. Ruthenium is mostly recovered from process catalysts.

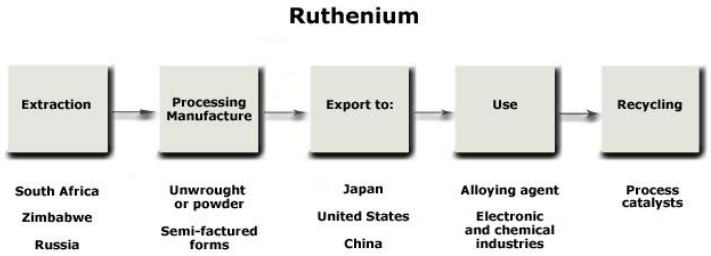

Figure 1.10: Ruthenium's process flow chart.

1.4 PGEs in cosmochemistry

It is widely accepted that PGEs, like any other elements with an atomic number greater than that of iron (A > 26), were formed by a supernova explosion (e.g., McBride and Gilmor, 2005).

Element	**Pd**	**Pt**	**Rh**	**Ru**	**Ir**	**Os**
Density g/cm^3	12.02	21.45	12.41	12.45	22.55	22.59
Hardness (Mohs scale)	4.75	4.30	5.50	6.50	6.50	7.00
Melting Temperature (KELVIN)	1827	2043	2233	2583	2716	3306
Condensation Temperature (KELVIN)	1324	1408	1392	1551	1603	1812

Table 1.4: Main physical characteristics of PGEs, sorted by increasing Condensation Temperature.

PGEs are very important for their distinctive geochemical behaviour that helps to reconstruct some evolutionary aspects of the Earth related to the Solar nebula dissipation and the origin of the planetary bodies (Yokoyama and Walker, 2016).
The elements' classification (i.e., volatile *versus* refractory) is defined in terms of the half-mass condensation temperature of an element during the cooling of a nebular accretion disk and the precipitation into common mineral phases, assuming equilibrium between gas and solid (Grossman, 1972; Palme et al., 2014). According to the cosmochemical classification of elements (Palme et al., 2014), the six elements of the platinum group are highly refractory, (the highest of the periodic table) with condensation temperature (T_c) at P =10^{-4} atm in the range of 1325 K (Pd) to 1810 K (Os) (Brearley and Jones, 1998). Except for palladium, PGEs condensed at temperatures above that of the FeNi alloy and within the range of the formation of calcium-aluminum inclusions (CAIs). At pressure ~ 10-^{4} atm, the metallic iron condenses as the FeNi alloy, at about the same temperature of fosterite (T_c=1444 K, Grossman, 1972; T_c= 1473 K, Wood et al. 2019).
At pressures above 10^{-4} atm, (in the order of ~10^{-3} atm) Fe metal condenses before forsterite, and at lower pressures (~ 10^{-5} atm), this is reversed (Grossman and Larimer, 1974; Brearley and Jones, 1998; Lodders, 2003). Variations in the concentrations of iron and other siderophile elements in meteorites are produced by the incorporation of variable fractions of metals.
The geochemical Earth standard model (e.g., McDonough, 2014) is primarily guided by the metal/silicate partitioning. The metal-silicate segregation is, therefore, a fundamental process in the evolution of differentiated planetary bodies, leading to the formation of metal cores and silicate mantles (and crusts).
These processes occurred quite early in the Solar System's history (e.g., Righter and Drake, 1996; Rushmer et al., 2000; Kleine et al., 2002; Righter, 2003), when impacts dominated the formation of planetary bodies and protoplanets. The Earth grew by the accretion of a few tens of protoplanets (bodies up to thousands of kilometres in diameter) within 10^7 to 10^8 years after the formation of the solar system (Palme et al., 2014).

Due to their high (~10^4) metal–silicate partition coefficients ($D^{met/sil}$) it has been proposed that PGEs delivered to the proto-Earth in the late accretionary stage, predominantly concentrated into the metallic core during the core–mantle separation event, more than 4.5 billion years ago (e.g., Kimura et al., 1974). On the other hand, Earth's compositional models show that the abundance of PGEs in the primitive mantle is at concentration levels well above those expected for their known metal/silicate partition coefficients (McDonough, 2017; Brenan et al., 2008b; 2016; Day et al., 2016). To account for this observation, it was proposed that a relatively small augmentation (~1 wt%) of material enriched in HSEs (in particular PGEs) was supplied late to the Earth's mantle after the core formation was complete, by a meteorite bombardment during 4.5 - 3.8 Ga or a late heavy bombardment at 4.0 - 3.8 Ga, including accretion of asteroids and comets. This process is known as the "late veneer hypothesis", which ended with the Moon formation. This late extraterrestrial influx of PGEs thoroughly mixed within the silicate Earth, but failed to segregate into the core. (Chou, 1978; Rubie et al., 2016; Frank et al., 2016 and references therein Jacobson et al., 2014). The Moon preserves the physical evidence of a "late heavy bombardment" (4.0–3.8 Ga) that produced large impact basins (lunar maria) (Koeberl 2006).
This exogenous explanation for the Earth mantle's HSE signature is, however, not unanimously accepted, and debates with alternative scenarios are on-going (Willbold et al., 2011; Touboul et al., 2012; Puchtel et al., 2014; Touboul et al., 2014; Willbold et al., 2015; Righter et al., 2015; Pilchin and Eppelbaum, 2017).
According to the late veneer hypothesis, for example, the concentration of PGEs in the Earth's metal core must be high and maximal; however, in some iron meteorites, which are interpreted as an analogy of Earth' core matter, the concentration of PGEs is quite low: the content of Ir in some iron meteorites, for instance, is as low as 10 ppb (Weisberg et al., 1996; Papike, 1998; Pilchin and Eppelbaum, 2017 and reference therein). Generally, the iron group of meteorites has an Ir content in the range of 10-100 ppb (source: Tagle and Hecht, 2006). These values are much lower than the mean concentration of Ir in any group of chondrites (Weisberg et al., 1996; Papike, 1998); the mean concentration of Ir in most primitive carbonaceous chondrites ranges from 472 ppb for the CI chondrites to 758 ppb for the CV chondrite groups (source: Tagle and Hecht, 2006). These chondrite contents are difficult to be explained by the late veneer hypothesis (e.g. Righter et al., 2015).

1.4.1. Meteorites (chondrites)

The planetary compositional standard modelling is based on the composition of chondrites, undifferentiated meteorites, which represent the most primitive rocks in the solar system. Chondritic meteorites, which make up the bulk of the meteoritic material (~95% of the falls), also fell to the Earth during historical times and shaped our view of the building blocks of the planets (Engel and McDonough, 2016).
Undifferentiated meteorites are pieces of planetesimals that have never been heated to melting temperatures. Their chemical and isotopic composition should be representative of the bulk parent planetesimal. Undifferentiated meteorites reflect to some degree the composition of the solar nebula from which they formed. CI (metamorphic grade 1) carbonaceous chondrites have the most primitive composition of the various chondrites and closely match the spectroscopically derived composition of the solar photosphere for all elements except H, C, N, O, and the noble gases (Palme et al., 2014). Variability in the composition of undifferentiated meteorites reflects inhomogeneity in the solar nebula or disequilibrium during the formation of solids from gas or both.
Instead, differentiated meteorites come from planetesimals that were molten and differentiated into core, mantle, and crust. A meteorite from such a body will not be representative of the bulk planetesimal or planet, but it allows a direct probe of the processes occurring in the main geochemical reservoirs that built up the Earth and rock bodies of the solar system. Variability in the composition of differentiated meteorites reflects inhomogeneity in the solar nebula or disequilibrium during the formation of solids from gas or both. It is worth noting that the element abundance curve for the solar photosphere, for at least the dozen most abundant elements, is the same as that for other stars in the galaxy and nearby galaxies. Thus, the geochemical principles and partitioning mechanism of elements are applicable for exoplanet building too (Lodders et al., 2009).

1.4.2. Earth's mantle

As outlined earlier, PGEs are important tracers to address fundamental questions such as the core-mantle equilibrium and the Earth's late accretion history. The Earth's upper mantle is characterised by an overabundance of PGEs relative to the concentrations that would be expected if the core had formed in metal-silicate equilibrium at high temperature at near-surface pressure conditions (Jagoutz et al., 1979). Another possibility is that the core could have formed as a result of a HT-HP mechanism by wich a dense

metallic phase may be transported to the deep interior: percolation, diking, diapirism, and direct delivery via impact (i.e., Wood et al., 2010; Rubie et al., 2011). Investigations of mantle rocks since the 1970s, revealed a nearly chondritic relative PGE abundance (Chou 1978; Jagoutz et al., 1979; McDonough and Sun 1995; Fischer-Gödde et al., 2011), but in recent decades (Becker et al., 2006; Lorand et al., 2009, Lorand et al., 2013), refinements of PGE analyses on various mantle rocks yielded a signature of the Primitive Upper Mantle (PUM) characterised by slightly supra-chondritic Ru/Ir and Pd/Ir ratios (2.03 ± 0.12 and 2.06 ± 0.31, respectively; Alard et al., 2000).
Due to the strong siderophile and chalcophile affinity of PGEs, base metal sulphides control the PGEs' budget of the Earth's mantle and this can identify the main processes that shaped the chemical evolution of the Earth's mantle: melting, or melt-rock percolation–reaction (Griffin et al., 2004; Wang et al., 2009; Marchesi et al., 2010; Aulbach et al., 2009; Melchiorre et al., 2010).
At equilibrium, the concentration of all PGEs is at least 10000 times higher in sulphide melts than in coexisting silicate melt, therefore sulphides are extremely potent agents for the collection and segregation of PGEs (e.g., Bockrath et al., 2004; Brenan and McDonough, 2009).
Mantle rocks (peridotite massifs and xenoliths) contain two types of sulphide populations which may be either residual from partial melting or the crystallization products of sulphide melts that segregated from cooling silicate melts. Residual sulphides are commonly found as inclusions within primary silicates (e.g., olivine and pyroxenes; generally referred to as "enclosed"). Those crystallised from migrating melts are commonly deposited interstitially in these silicates ("interstitial"; Alard et al., 2002; Griffin et al., 2004).
In terms of the global behaviour of PGEs during partial melting, Os is the most compatible element of the group, followed by Ir, Ru, Rh, Pt and Pd (the most incompatible). This behaviour is evidenced in the included type sulphides that show IPGE (Ir, Os, Ru) depleted patterns similar to the melt-depleted mantle residuum (i.e., harzburgite), whereas the interstitial-type shows PPGE (Pd, Pt, Rh) enriched patterns resembling the fractionated PGE patterns of the basalt (Mungall and Brenan, 2014).
To represent the PGE behaviour in mantle processes, as for the lithophile trace elements (i.e., REE group), the CI-chondrite normalised pattern is used by convention. The order of elements (Os, Ir, Ru, Rh, Pt, Pd), reflects the decreasing temperature of condensation of these elements and follows their increasing incompatibility trend during the partial melting of the Earth's mantle (Fig. 1.11).

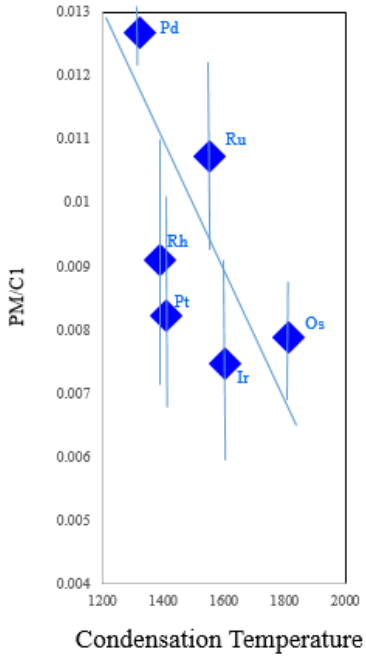

Figure 1.11: PGE condensation temperatures vs. concentration ratios Primitive Mantle/Chondrite CI; PM and CI data from Palme and O'Neill, 2014.

These PGE characteristics of mantle sulphides have been interpreted to be representative of a multi-stage partial melting process of the mantle, melt migration, and melt-rock interactions. The behaviour of sulphides during mantle melting is strongly dependent on: the pressure and temperature at which the melting occurs, the prevalent oxygen fugacity, which determines sulphur solubility in the melt, the FeO content in the melt and the melt's volume (i.e., the degree of melting) that is produced, although the exact relationship of these factors remains poorly understood and the debate on the influence of these factors is

still open (Mavrogenes and O'Neill, 1999; O'Neill and Mavrogenes, 2002; Arndt et al., 2005; Wittig et al., 2010; Fortin et al., 2015; Smythe et al., 2017). In particular, the observed ubiquitous PPGE (Pd, Pt, Rh) depletion in all type of mantle rocks models a melt depletion that must exceed 20% (Pearson et al., 2004; Luguet et al 2007; Luguet and Reisberg, 2016; Becker and Dale, 2016). In addition, large-scale melting (20-30%) is required to remove the high-density sulphide portion from the increasingly refractory, and therefore buoyant, silicate fraction of peridotites (Wittig et al., 2010).

Entering in this fascinating debate is out of the scope of this thesis, however it is worth noting that**, in order to propose, discuss and evaluate any Earth's geochemical modelling for the distribution of PGEs it is imperative to perform precise and accurate measurements of concentrations in bulk of natural crucial samples: meteorites (chondrites and iron meteorites) and Earth's mantle rocks.**

1.5 PGEs in urban soils

As already mentioned, PGEs are primarily concentrated in the Earth's core and secondarily in the mantle, while they are present in extremely low concentrations in the crust. Their abundance in the upper continental crust varies from 0.02 ng/g^{-1} (ppb) for Ir to 0.5 ng/g^{-1} (ppb) for Pt and Pd. In the Earth's crust, PGEs constitute less than the 0.01% of the total budget of the whole planet (Rauch and Morrison, 2008).
Consequently, their presence on the surface is extremely rare. For this reason, until the end of the last century, the environmental impact of PGEs due to anthropic activities and the related health risk have frequently been considered negligible.
Reith et al., (2014) propose an exhaustive model of the Pt cycle on Earth: the route from the mantle to the crust through magmatic differentiation processes and its circulation on the surface due to leaching action, anthropic effect and biochemical cycles (Fig. 1.12).
From the 70s, demand, production and use of these elements have been increasing, due to the introduction of automobile exhaust catalysts and the use of PGEs in catalytic industrial processes. Consequently, there has been an increase in dispersion and concentration of PGEs in the environment, as reported in several papers in recent decades (Palacios et al., 2000; Cinti et al., 2002; Moldovan et al., 2002; Moldovan et al., 2003; Lesniewska et al., 2004; Ravindra et al., 2004; Rauch et al., 2005; Hooda et al., 2007; Sutherland et al., 2007; Cicchella et al., 2008; Dubbiella-Jackowska et al., 2009; Lyubomirova and Djingova, 2015; Hwang et al., 2016; Folens et al., 2017; Folens et al., 2018). It is therefore very important to monitor the pollution level of PGEs, to understand their bioavailability and their role in the food chain, in order to evaluate environmental and human health risks.
Pollution caused by automobile exhaust catalysts is now acknowledged as the main source of Pt, Rh and Pd dispersion in the environment.
These three elements are used in automobile exhaust catalysts for their capability to reduce emissions of harmful nitrogen oxides (NO_x) and carbon monoxide CO. In particular, Pt and Pd are excellent in the oxidation of CO and other unburned hydrocarbons, while Rh plays a crucial role in NO_x reduction (Hwang et al. 2016).
The total amount of PGEs in exhaust catalysts varies between 0.1 and 0.3 % (w/w) and on the type of engine (petrol or diesel) (Hwang et al. 2016).
Besides Pt, Pd and Rh, also Os, Ir and Ru can be present in the exhaust catalysts, but only as impurities and their concentration in the environment is therefore much lower, often not distinguishable from the natural background.
Exhaust catalysts can be considered as small chemical reactors embedded into the exhaust system of combustion engines. Their function is to compensate the imperfect combustion of the air and hydrocarbons mixture which, in ideal conditions, would only produce steam and carbon dioxide. Instead, the incomplete combustion leads to the formation and emission of highly toxic substances: carbon monoxide (CO), nitrogen oxides (NO_x) and other unburned hydrocarbons (Fig. 1.13).
Carbon monoxide is formed by the partial oxidation of the carbon atoms that form the hydrocarbon molecules; nitrogen oxides instead, are the result of the combination of the nitrogen and oxygen present in the air; this combination can occur due to the high temperature reached in the engine cylinders.

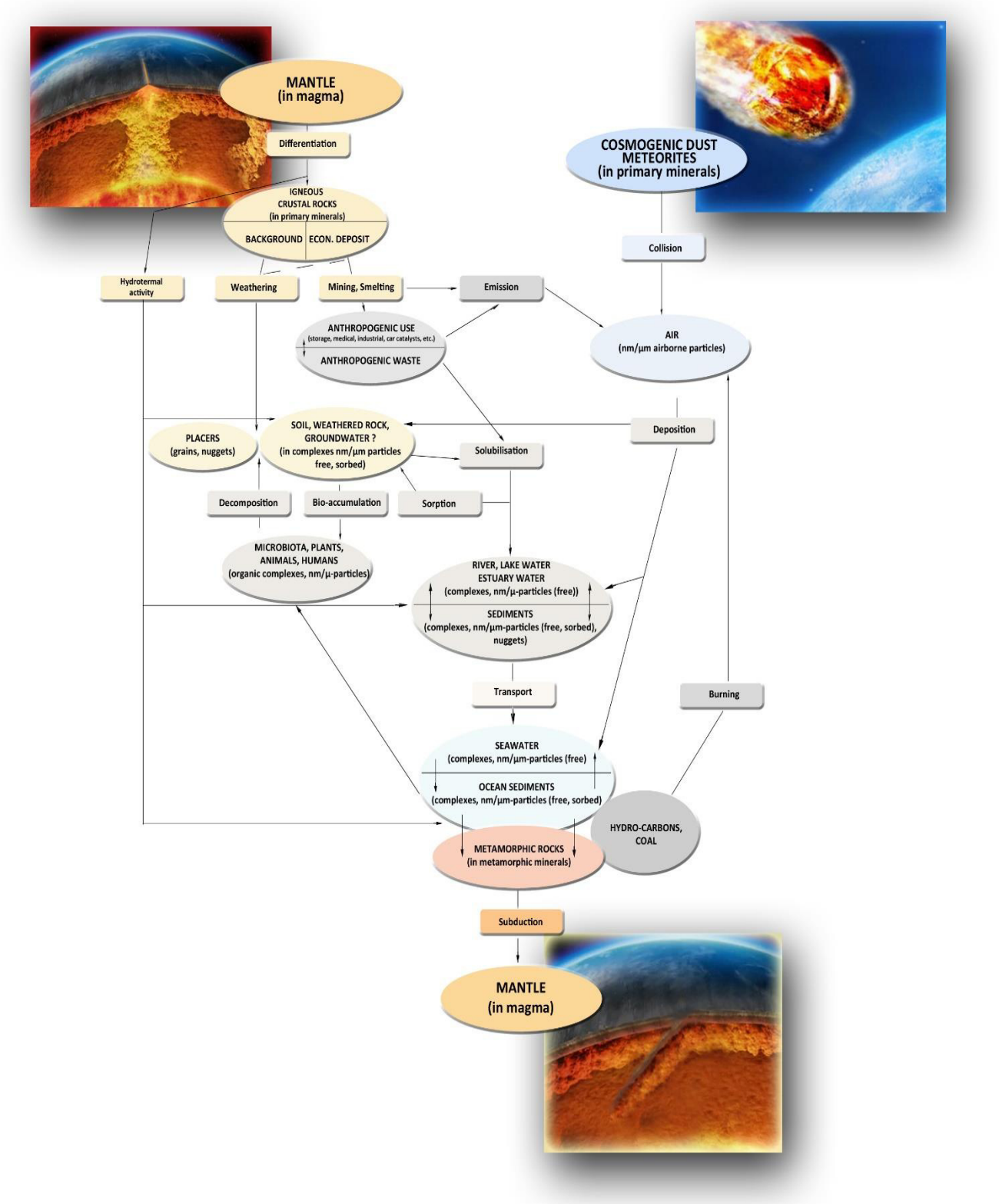

Figure 1.12: Model of the Pt cycle on Earth (modified from Reith et al. 2014).

The most recent "three-way" exhaust catalysts (so called because they can control the three above-mentioned pollutants), use a ceramic block (normally cordierite: $Mg_2Al_4Si_5O_{18}$) characterised by a honeycomb structure with a large surface: the walls of the abundant cavities are covered by a thin layer of metallic catalyst, which is formed by alumina with scattered PGEs in metallic form. The exhaust gases enter a first catalyst section (called a reduction chamber), where the catalyst is mainly rhodium: the unburned hydrocarbons and the steam partially react to form hydrogen and carbon oxide. The hydrogen then reacts with the nitrogen oxides to produce nitrogen and steam. In the second chamber (called oxidation chamber) the presence of the catalysing platinum and palladium allows the oxidation reaction of carbon oxide and of other unburned hydrocarbons.

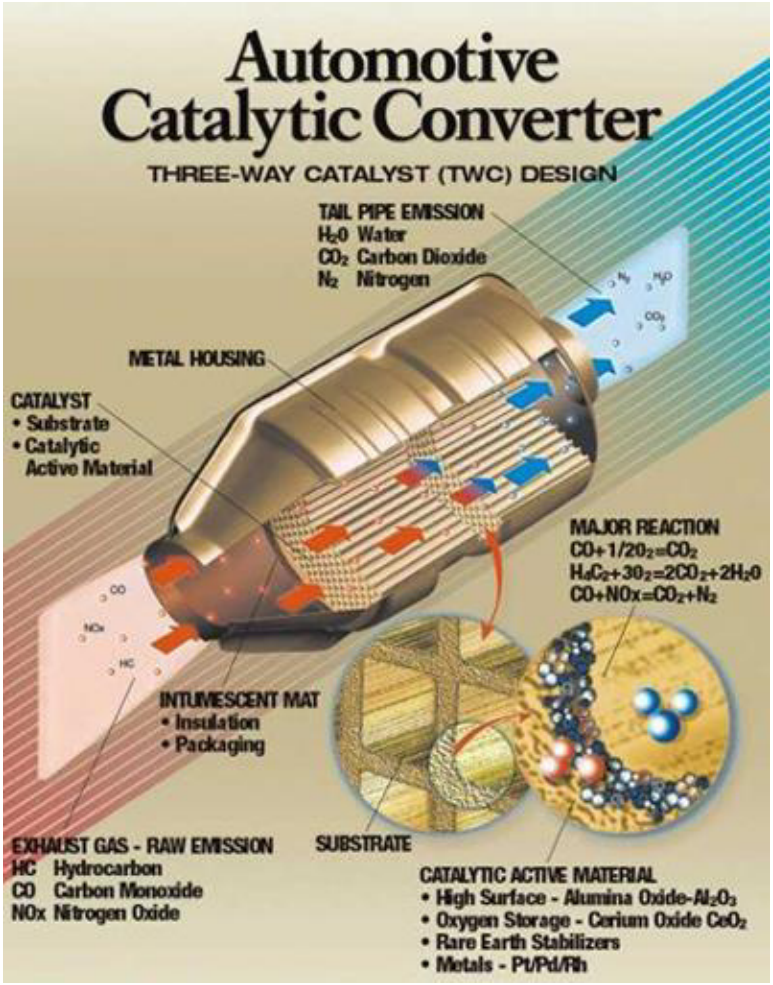

Figure 1.13: schematic drawing of automotive catalytic converter (from: https://product.statnano.com/product/7867/ptrh-only-three-way-catalysts).

Mechanical friction and chemical reactions on the catalyst's surface are responsible for the release of PGEs through the emission gasses. (Moldovan et al., 2002 and 2003). The PGE particles' dimension in the catalysing layer of new exhaust catalysts, generally does not exceed 10 nm, but sintering processes and aging can lead to aggregation and formation of larger particles. Exhaust catalysts tested on rolling roads up to 60000 km showed particles with diameters between 50 and 400 nm (Palacios et al., 2000). Exhaust gasses can therefore release into the environment both small and large particles containing PGEs from the alumina coat (washcoat). Folens et al., (2018) showed that only between 11 and 36% of the total emitted particles, have dimensions smaller than 3.14 µm.

The PGE dispersion rate per vehicle, expressed as ng/km, was estimated by the analysis of exhaustgasses (Palacios et al., 2000, Moldovan et al., 2002) either directly in lab tests on rolling roads and in standard driving conditions (UDC Urban Driving Cycles; EUDC Extra Urban Driving Cycles) or indirectly by modelling the concentrations detected in the road environment. These tests show that the dispersion rate strongly varies with the vehicle mileage: it is nearly an order of magnitude below for older vehicles (30000 km) compared to new vehicles (Palacios et al., 2000).
Direct measurements of emission gasses provide estimates of PGE emission rate in the ng/km levels as being 10-100 times higher for diesel engines as compared to petrol ones (Moldovan et al., 2002).
Indirect estimates of the emission rate (or factor), obtained by modelling the concentrations detected in environmental samples and by traffic data, show higher values, just below the µg/km levels (Rauch and Morrison, 2008).
Helmers (1997) provided two valid reasons to justify the underestimation of the emission rate measured by laboratory tests: first, the bench measurements are generally carried out in ideal conditions with respect to engine's performance. Aging, unsuitable maintenance and several on/off cycles can result in Pt emissions even 1000 times above average.
Second, the emission rate is also affected by the vehicle's speed, driving style and, most of all, traffic conditions. A recent study (Lyubomirova and Dijingova, 2015) on the accumulation and distribution of Pt and Pd in the area surrounding the Bulgarian road network, highlighted that the highest concentrations (up to 800 ppb of Pd) are detected in the environment (road dust, soil and vegetation) near road sections characterised by critical traffic conditions (frequent slowdowns, queues and repeated "stop and go").
In samples collected near motorway segments, Lyubomirova and Djingova (2015) found the lowest concentrations in the proximity of high-speed sections; they observed an increase in the values in areas with forced slowdowns like bends or tunnels. Hoda et al., (2007) reached the same conclusion (traffic conditions are more influential than total traffic volume and vehicle's speed) on samples (soil and grass) collected near English roads (four locations around Oxfordshire and one in outer west London).
To summarise, the variables linked to real road conditions such as slope changes, slowdown and acceleration due to the alternation of bends and straight sections, together with traffic conditions, strongly affect the PGE emission rate in the environment and they cannot be reproduced in laboratory rolling road tests.
Assuming 500 million as the number of catalysed vehicles and an annual average mileage of 15000 km, Rauch et al., (2005) estimated 0.8-6 tons of Pt globally released in the environment.
Traces of PGEs can be detected in urban air and accumulate on the road surface, in roadside soil and vegetation. Transport of PGEs via stormwater results in the contamination of aquatic environments. There is now mounting evidence that a fraction of PEs in the environment is bioavailable, and the potential uptake into the biosphere is raising concern over potential risks for humans and the environment (Rauch and Morrison, 2008).
The determination of PGEs in geological and environmental samples is difficult, due to the low concentration of these elements and their heterogeneous distribution in the rocks (nugget effect). Accurate and simple analytical methods are under theoretical and analytical development.

2 Materials

Various natural samples were selected for measurement procedures on a large spectrum of matrices of geological interest. They include:
three meteorites;
nine mantle xenoliths;
thirteen agricultural and 12 urban soils;
eight pelagic limestones of the stratigraphic sequence that marks the Cretaceous–Tertiary (K-T) boundary.
It is worth noticing that the sample selection was made to emphasise the scientific purpose of the analytical data and not to provide a geochemical modelling to disclose important issues about sample genesis.

2.1 Chondrites and iron meteorites

The meteorites selected for this study are two "finds", discovered in the desert region of Draa Valley (central Morocco): two **ordinary chondrites** (named 6A and 1B) and a (supposed) **iron meteorite** (named 5E). They are currently the subject of other studies.
The ordinary chondrites (OC)s are the most abundant of the three chondrite classes (Fig. 2.1) which constitute 90% of all chondrites (Meteoritical Bulletin Database – updated to March, 2021). The OCs consist of olivine and pyroxene chondrules surrounded by a matrix of silicates (olivine, pyroxene, and plagioclase), FeS (troilite), Fe-Ni metal, and in some cases glass. The OCs are divided into three groups: H, L, and LL (Fig. 2.1), based on their Fe-Ni metal abundance and total Fe content: H - high metal and high total Fe; L - low metal and low total Fe; LL - low metal relative to total Fe and low total Fe. In terms of modal abundance, the average abundance of metal in equilibrated H, L, and LL chondrites is 18.2 wt.%, 8.4 wt.%, and 3.5 wt.%, respectively (Dunn et al., 2010).

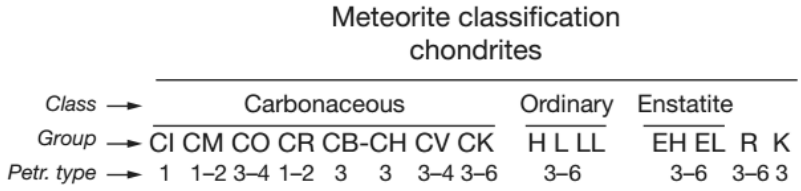

Figure 2.1: Classification of chondrite groups divided into class, group, and petrologic (petr.) type (from Krot et al., 2014).

The major metal phases in ordinary chondrites are predominantly comprised of two major Fe-Ni alloys known as kamacite (low Ni metal phase) and taenite (high Ni metal phase). These two Fe-Ni alloys have different crystal structures where kamacite is body-centred cubic and taenite is face-centred cubic (Wood, 1967). In general, kamacite is most abundant in H chondrites and decreases systematically throughout the ordinary chondrites (H > L > LL), whereas taenite abundances follow an opposite trend: H < L < LL (Afiattalab and Wasson, 1980; Smith et al., 1993; Brearley and Jones, 1998).
Generally speaking, in terms of siderophile elements, specifically Os to Fe, the class of Ordinary Chondrites show a large variability, with H group showing the greatest abundances (Krot et al., 2014).
All groups of ordinary chondrites, except the EH group, are, on average, depleted with respect to the CI chondrite in the chalcophile elements, with the lowest contents from Au to Zn (Fig. 2.2).

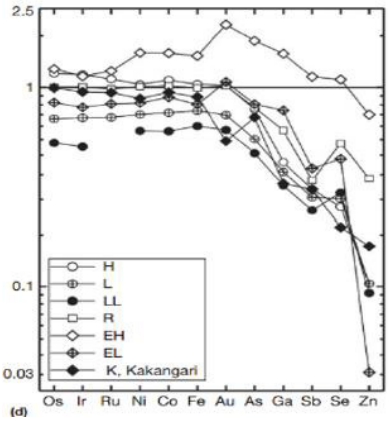

Figure 2.2: Siderophile and chalcophile elements' bulk composition for the different ordinary chondrite groups normalised to Mg and C1 chondrites. Volatility of elements increases from left to right (from Krot et al., 2014).

Iron meteorites are divided into "magmatic" irons and "non-magmatic" or "silicate bearing" irons (Goldstein et al., 2009). Each class includes various groups.
The magmatic irons (groups IIAB, IID, IIIAB, IVA and IVB) (Fig. 2.3) show a trace element (Ga, Ge, Ir) distribution in agreement with the fractional crystallization of the liquid core of asteroid parent bodies for each group (Scott, 1972).
The "non-magmatic" irons (groups IAB, IIICD and IIE) (Fig. 2.3) have a more widespread composition resulting from a complex history. They are rich in silicate inclusions, with some of them having a composition similar to those of chondrites (Bunch et al., 1970) and containing a higher abundance of volatile elements than the other groups (i.e., Ir, Fig. 2.3; Goldstein et al., 2009).
Lastly, there is a large number of "ungrouped" iron meteorites (i.e., 40% of the irons of the Antarctic collection), whose trace element content does not match any reference plot (Weisberg et al., 2006). Since the 1950s, various authors (Goldberg et al., 1951; Wasson and Kimberlin, 1967; Wasson, 1999; Wasson and Kallemeyn, 2002; Wasson and Choi, 2003; Wasson et al., 2007) have extensively determined the abundance of PGEs and other trace elements in the bulk iron meteorites to improve the determination and characterisation of the iron meteorite groups. Schematic trace element plots are shown in Figure 2.3.

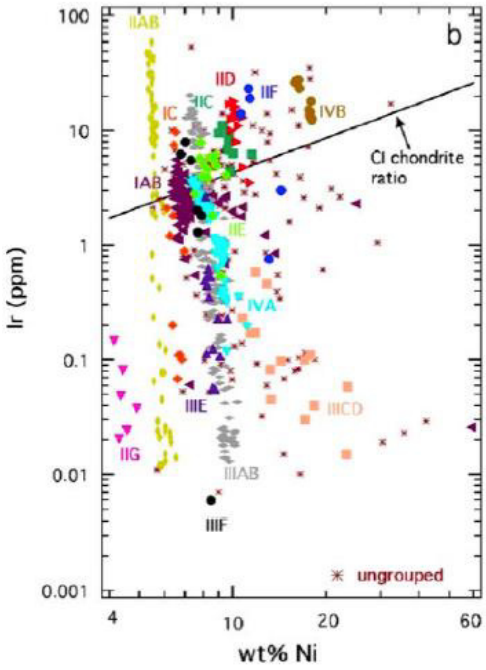

Fig 2.3: Ir vs. Ni Log plot used for the classification of iron meteorites from Goldstein et al., al 2009.

2. Materials

6A meteorite: this rock is formed from a silicate portion (80% in vol), composed of chondrules, individual grains of olivine, pyroxene, rare plagioclase and a very fine grain-matrix, and a metallic portion (20% in vol).
On the basis of Fe-Ni metal abundance and total Fe content (Table 2.1), as well as olivine and pyroxene compositions (Fa: 17.35-18.57; mg# enstatite: 0.83-0.84) in chondrules, this meteorite is classified as an Ordinary Chondrite / group H and 3 as petrological type (Krot et al., 2014).
The chondrule/matrix ratio is approximately 30:70 with the majority of chondrules being type-I (average Fa =17). The DTG (Differential ThermoGravimetric) profile reveals the presence of goethite, which suggests a moderate (W2) weathering grade (Grossman and Breadley, 2005).

Sample	6A H-type	1B H-type
Si (wt%)	14.67	14.80
Ti	0.05	0.05
Al	1.70	1.40
Fe	25.40	25.71
Mn	0.24	0.22
Mg	12.88	13.58
Ca	3.37	1.80
Na	0.81	0.47
K	0.08	0.07
P	0.20	0.16
Ni	1.07	1.28
S*	0.75	1.39
O*	38.8	39.1
Total	100.02	100.04
Cr (ppm)	2985	2921

Table 2.1: XRF Major element contents of meteorites selected for PGE analytical evaluation (values estimated by mass balance calculation).*

1B meteorite: this chondrite is formed from a silicate portion (80% vol), composed of chondrules, individual grains of olivine, pyroxene, rare plagioclase and fine grain-matrix; the metallic portion is scarce (15-18% vol) and it is composed of an Fe-Ni alloy (8% vol.) and Fe-Ni-sulphides (5% vol.). XRD analyses show the same mineralogical composition of 6A, with (forsteritic) olivine, Ca-poor pyroxene and (albitic) plagioclase as the most abundant silicates. On the basis of Fe/Ni-Fe/Mg elemental ratios, the 1B meteorite is classified as H-type chondrite (Fig.2.4), whereas the preliminary

petrographic observation so far obtained, indicates 3 to 6 as petrological type (Krot et. al., 2014; Huss et al., 1993).

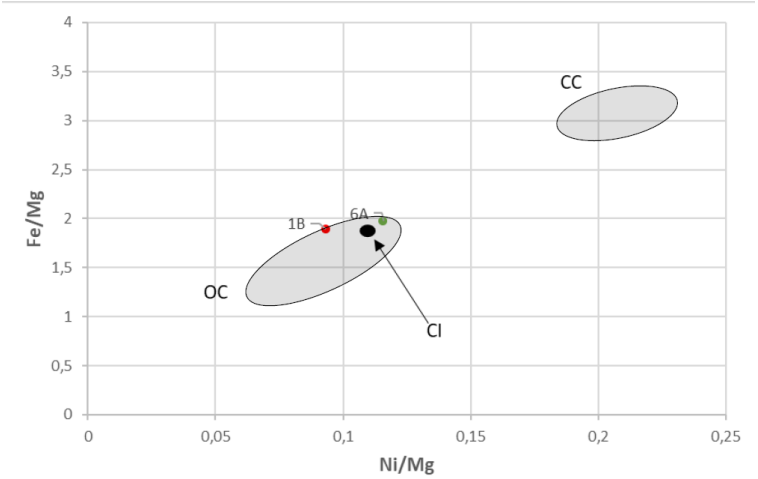

Figure 2.4: Fe/Mg vs Mg/Ni in 6A (green point) and 1B (red point) meteorites. On the basis of the siderophile/lithophile ratio, both meteorites are in the field of ordinary chondrite (OC). Fields of OC and CC (carbonaceous chondrite) are from Johnson et al., 2016.

5E supposed iron meteorite: it is a very dense and non-porous specimen and has a metallic silver/brownish coloured interior. It has the macroscopic features of iron meteorites, but no evidence of iron metal crystallization textures (i.e., a Widmanstätten pattern). Instead, it presents a melting texture resembling iron bleb precipitates (Fig. 2.5).
In terms of mineral composition, this rock contains silicate glasses, pure iron oxides and iron-silicate minerals, which formed in an oxidising environment. Electron microprobe analyses do not reveal measurable nickel contents in any of the phases, thus the PGE content is expected below the detection limits, even when measured with the most sensitive tools.
The peculiar texture and mineral assemblage and composition make the ascription of the rock to an iron-meteorite, quite doubtful. It could represent a product of a metallurgical process, maybe of archaeological interest, but dedicated investigations are obviously required.
For the scope of this thesis, this sample was selected to test the detection limits in such an unusual matrix.

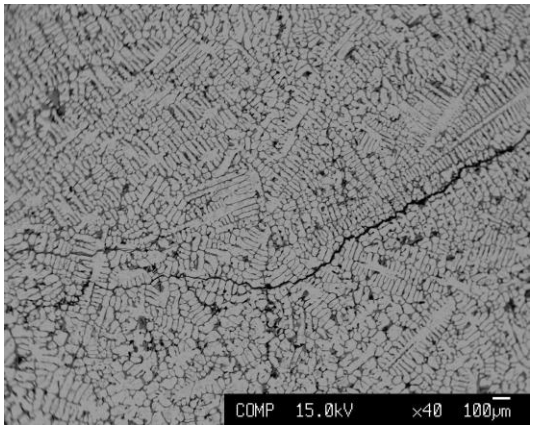

Figure 2.5: BSE image of "metallic sample" (meteorite?)

2.2 Mantle xenoliths

A representative suite of mantle xenoliths covering the peridotite range of compositions was chosen, with the aim of finding a large variety of PGE abundances. As mantle rocks, xenoliths were preferred over other mantle rocks, because they are generally less serpentinised than i.e. massif peridotites and their rapid ascent from the mantle to the surface can better preserve the mineralogical and chemical signatures of their mantle source (Pearson et al., 2003). It is expected that the PGE content in xenoliths is an original feature of the mantle domain they belong to, and not a mobilizing effect due to a large-scale tectonic emplacement within the crust as in peridotite massifs (Griffin et al., 2004; Luguet and Reisberg, 2016).
All 9 samples were supplied by researchers of the University of Ferrara (Italy) and 6 were fully characterised in terms of lithophile major and trace elements. A new xenolith of the well-studied Gran Comore xenolith population, was prepared for this study, because of the shortage of material due to previous analyses of the other samples (Coltorti et al., 1999). Finally, for two mantle xenoliths from the well-known San Carlos (Arizona), only preliminary whole rock and explorative mineral major element analyses have so far been provided.
A short description of the studied samples is reported below, whereas the main chemical features and mineral percentages are given in Table 1.

CN2. This xenolith sampled at Rinibar (Orkney Islands) represents a window on the Scottish lithosphere as it was in late Palaeozoic. The fine-grained protogranular mineral assemblage is composed of anhydrous ferromagnesian silicates (olivine + clinopyroxene + orthopyroxene) and spinels and shows evident secondary hydration, commonly concentrated along fractures (Table 2.2). The sample is classified according to the IUGS scheme (Le Maitre et al., 2002) as spinel-bearing lherzolite. Geochemical and isotopic features evidenced that this sample represents a lithospheric mantle section that was metasomatised by carbonatite metasomatism (Bonadiman et al., 2008) at 550 $\pm$ 50 Ma. Interstitial sulphides are mainly observed in secondary veinlets.

LE5 and LE7. The two samples were collected in Cenozoic basanites from Mount Leura, one of the richest xenolith sites of the Newer Volcanic Province (4.5 Ma - 5000 B.P.), in western Victoria State, southeast Australia. Both xenoliths are sub-rounded in shape, ~7 cm in diameter, apparently free of host magma infiltrations, and exhibit a relatively coarse grain size; because they contain a spinel peridotite assemblage (olivine + clinopyroxene + orthopyroxene + spinel) with less than 5% clinopyroxene (Table 2.2) and according to the IUGS scheme (Le Maitre et al., 2002), they are classified as spinel-bearing harzburgites. LE7 bears observable amounts of phlogopite: (1.9 %) whereas LE5 contains both phlogopite (1.2%) and amphibole (1.4%).
The combination of Cr# (molar Cr / (Cr + Al)) in spinel and the forsterite content of olivine points to a high-degree mantle melting (22- 25%), in agreement with the inference from the bulk rock.
Phlogopite and amphibole of Mount Leura's samples are supposed to have formed simultaneously during the same metasomatic event and achieved equilibrium with the primary anhydrous minerals (Bonadiman et al., 2021). The presence of rare residual (mainly included in clinopyroxene) and interstitial (in veinlets) sulphide made these samples suitable for this study.

TL1 and TL45. These two mantle xenoliths sampled in Tallante (Spain), represent fragments of lithospheric mantle beneath the Betic Cordillera. They are protogranular anhydrous spinel peridotites, at various degrees of fertility.
TL1 is the most refractory sample (spinel-bearing harzbugite, Tab. 2.2), but isotopic signatures (Sr-Nd an Hf systematics) record an enriched mantle comparable to lithospheric domains of the most fertile samples. This has been interpreted as an effect of metasomatic processes induced by OIB (Oceanic Island Basalts)-type metasomatic melts (Beccaluva et al., 2004; Bianchini et al., 2011).

Sample	CN2[a] Lherzolite	LE7[b] Harzburgite	LE5[b] Harzburgite	TL1[c] Harburgite	TL45[c] Lherzolite	GC11/2 [d] Lherzolite	GC11/6 Wehrlite	SC-A4 Harzburgite	SC-A5 Lherzolite
SiO_2 (wt%)	41.77	44.22	44.82	45.55	45.66	44.75	41.14	44.39	44.60
TiO_2	0.06	0.02	0.06	0.06	0.13	0.03	0.166	0.01	0.06
Al_2O_3	1.77	0.21	0.69	1.35	3.85	1.18	1.38	0.64	1.80
FeO_{tot}	8.28	8.39	9.78	7.83	7.78	8.23	12.89	8.06	8.12
MnO	0.11	0.11	0.14	0.11	0.12	0.14	0.268	0.14	0.14
MgO	35.23	45.94	42.91	44.81	39.91	43.8	40.7	44.75	41.16
CaO	2.94	0.48	0.91	1.32	3.23	1.58	3.51	1.04	2.50
Na_2O	0.00	0	0.08	0	0.29	0.19	0.07	0.00	0.09
K_2O	0.05	0.01	0.06	0.03	0.01	0.04	0.008	0.00	0.01
P_2O_5	0.01	0	0.02	0	0	0.03	0.068	0.00	0.00
LOI	9.29	0.63	0.53	0.34	0.02	0.65	0.01	0.11	0.64
	99.50	100.01	100.00	101.40	101.00	100.62	100.21	99.14	99.12
mg#	88.35	91.56	89.68	91.07	90.14	90.46	75.9	90.82	90.04
Cr (ppm)	2579	2051	2900	2796	2890	2696	2498	3060	3437
Ni	1969	2529	2191	2314	2021	2268	2227	2441	2159
Olivine	55	73	69	73	58	75	85	76	69
Orthopyroxene	30	21	24	21	24	18	8	20	18
Clinopyroxene	14	3.7	4	5	11	6	7	4	12
Spinel	1	1	1	1	2	0.2	0.4	1.0	1.1
Phlogopite		1.9	1.2						
Amphibole			1.4						
Plagioclase					5				
Glass						0.1			

mg# =Mg/(Mg+Fe) mol*100

Table 2.2: *XRF Major element contents and modal composition of mantle xenoliths selected for PGE analytical evaluation; (a) Bonadiman et al., 2008; b) Bonadiman et al., 2021; c) Beccaluva et al., 2004; d) Coltorti et al., 1999).*

TL45 is a clinopyroxene-rich lherzolite (Tabl. 2.2) with evidence of in-situ spinel/plagioclase re-equilibration.
However, the interstitial plagioclase widespread throughout the peridotite matrix and in various areas texturally far from spinel crystals, exceed the "normal" modal abundance expected for these accessory phases (1–2%; Pearson et al., 2003). This has to be interpreted as the result of melt impregnation and refertilization. Further evidence of refertilization processes is provided by Hf–Nd isotopic composition that approach DM (Depleted Mantle component) (Beccaluva et al., 2004; Bianchini et al., 2011).
The geochemical and textural extreme variability of TL1 and TL 45 is counter-balanced by the ubiquitous presence of base-metal sulphides forming composite aggregates hosted in pyroxenes of metasomatic origin, therefore interpreted as "insterstitial-type". This feature makes this sample relevant for this analytical study.

GC11/2 and GC11/6. These are peridotite xenoliths from La Grille volcano (Grande Comore Island of the Comores Archipelago, in the northern part of the Mozambique Channel). They represent a fragment of an oceanic mantle domain and are of notable importance as they provide one of the few oceanic occurrences that bear evidence of carbonate-rich metasomatism (Coltorti et al., 1999).
GC11/2 is a clinopyroxene-poor lherzolite. (Table 2.2). It has a porphyroclastic texture with extensive rock/melt reaction textures (Coltorti et al., 1999). On the basis of textural and mineral chemistry features, only olivine and orthopyroxene show relicts of primary crystals, whereas all the clinopyroxenes of these samples are secondary, recrystallised crystals formed by a peridotite/metasomatic melt interaction.
GC11/6 was added to this study because only the GC11/2 xenolith of the fully characterised samples presented in Coltorti et al., 1999 had enough material to be powdered for PGE analyses.
On the basis of a preliminary petrographic observation and the bulk major element composition, GC11/6 is a wherlite with only olivine and rare orthopyroxene as primary phases, whereas clinopyroxene (12%, Table 2.2) occurs only in the recrystallised domains and glassy patches (texture described in Coltorti et al., 1999). In both samples the very few sulphides occur exclusively within the large glassy patches. PGE content measurements in these samples are intriguing from an analytical point of view and they also provide important information about the carbonatite metasomatism in the lithospheric mantle domain.

SC A4 and SC A5. These rocks are from the worldwide known xenolith location of Peridot Mesa in the San Carlos Indian Reservation, Arizona (Bromfield and Schride, 1956), where abundant ultramafic xenoliths were brought up to the surface by a late Tertiary to Quaternary basalt flow.
The samples were cut and powdered for bulk major element analyses and PGE analytical study. As mentioned above, they are at the initial stage of investigation.
These samples are well equilibrated peridotites and, on the basis of bulk major-element chemistry (Tab. 2.2) and a preliminary textural observation, they are a protogranular anhydrous-spinel bearing lherzolite (SC A5) and spinel bearing harburgite (SC A4). Following the original petrographic description of the San Carlos xenoliths of Frey and Prinz, (1978), they belong to group I or to the Cr-diopside-xenolith type of Wilshire and Shervais, 1975.
Frey and Prinz (1978) initially classified the San Carlos xenolith population in:
Group I - xenoliths that are not genetically related to the host basalt but rather represent a mantle residue after extraction of various degrees of partial melt;
Group II - xenoliths, which in terms of bulk composition and textural analyses seem to be chemically related to the host lava and represent cumulate rocks produced by fractional crystallization of a variable evolved magma chemically related to the host magma (Frey and Green, 1974; Frey and Prinz, 1978).
Since these pioneering works, the petrogenesis of San Carlos mantle xenoliths has been the subject of many studies (Zindler and Jagoutz 1980, 1988 Galer and O'Nion 1989), but despite so much attention, the processes that form the mantle domain beneath Arizona (USA) are still unknown.
In addition, since 1980 the forsterite-rich olivine of a San Carlos group I xenoliths (i.e., San Carlos Fo90.1 USNM 111312/444; Jarosewich et al., 1980) is used worldwide as standard for Mg and Si in many geoscience electron microprobe labs.

2.3 Soils

2.3.1 Agricultural soils

For the first analytical tests on the soil matrix, 13 **agricultural soil samples**, previously studied and characterised both chemically and mineralogically, from the villages of Vigarano Mainarda and Vigarano Pieve near Ferrara (Italy) were used. They are alluvial deposits characterised, like almost all the soils of the Po Plain, by a limited profile development: the lack of soil maturity is due to the young depositional age (Holocene), fluvial reworking and agricultural activities (Bianchini et al. 2012). (Fig. 2.6).

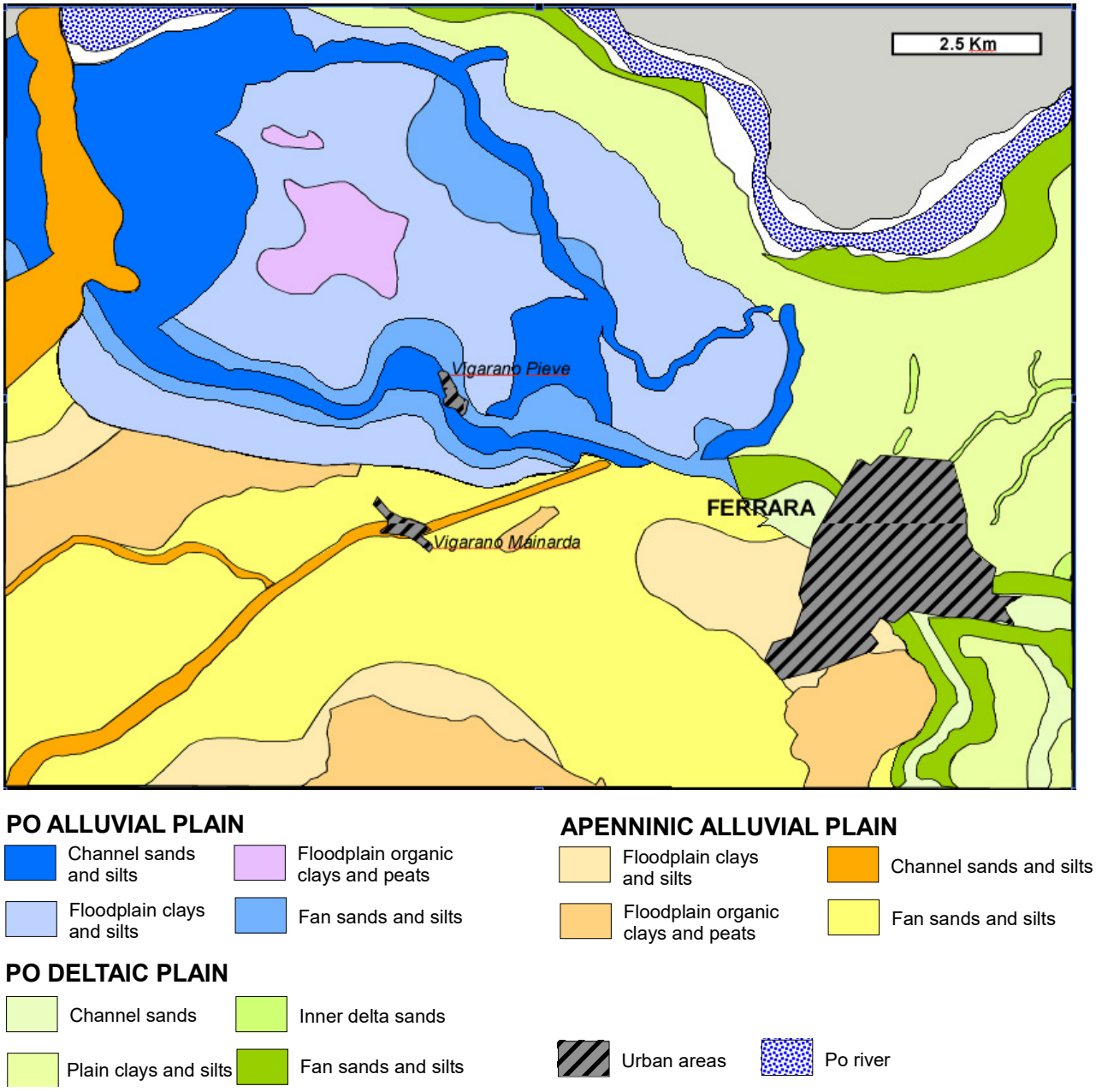

Figure 2.6: Extract from the geological map of Ferrara (Geological, Seismic and Soil Service of Emilia Romagna region).

The sampling was carried out with an Edelman auger (Eijkelkamp) during the spring of 2008. Some samples are representative of the plough horizon (just beneath the roots zone, at a depth of 30–40 cm), whereas the others are representative of the underlying undisturbed layer (100–120 cm deep). These alluvial sediments consist of sand, silt, and clay (Fig. 2.7) and derive from both the Po and Reno rivers (Fig. 2.8).

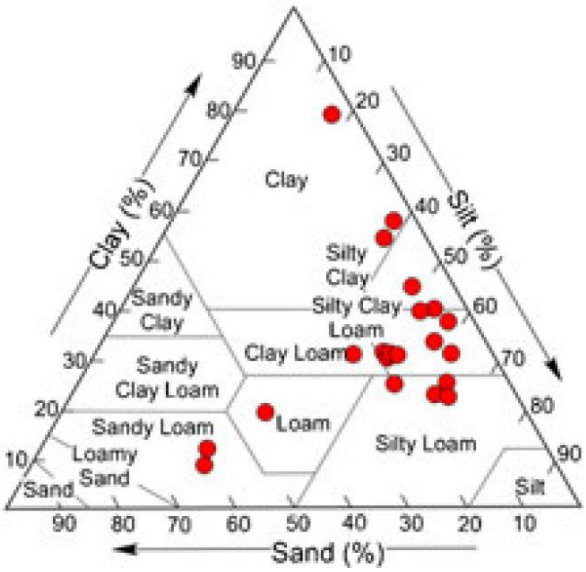

Figure 2.7: Grain-size characteristics of the Vigarano soils (from Bianchini et al., 2012).

XRD (X-Ray Diffraction) analyses and petrographic observations indicated that the Vigarano soils of both Po and Reno provenance contain quartz, feldspars, calcite, and micas, which are prevalent in the coarse sand, as well as phyllosilicates, such as illite, kaolinite, chlorite, serpentine, and smectite, which show a tendency to prevail in the finer fraction. (Bianchini et al., 2012). Heavy metals are mainly partitioned in the fine fraction, probably in association with clay minerals. In their paper, Bianchini et al., (2012) were able to perfectly discriminate between the Po and Reno provenance using Cr and Ni versus MgO and Al2O3 diagrams (Fig. 2.8). They demonstrated that the high concentration of Cr and Ni is a natural (geogenic) feature of local alluvial sediments.

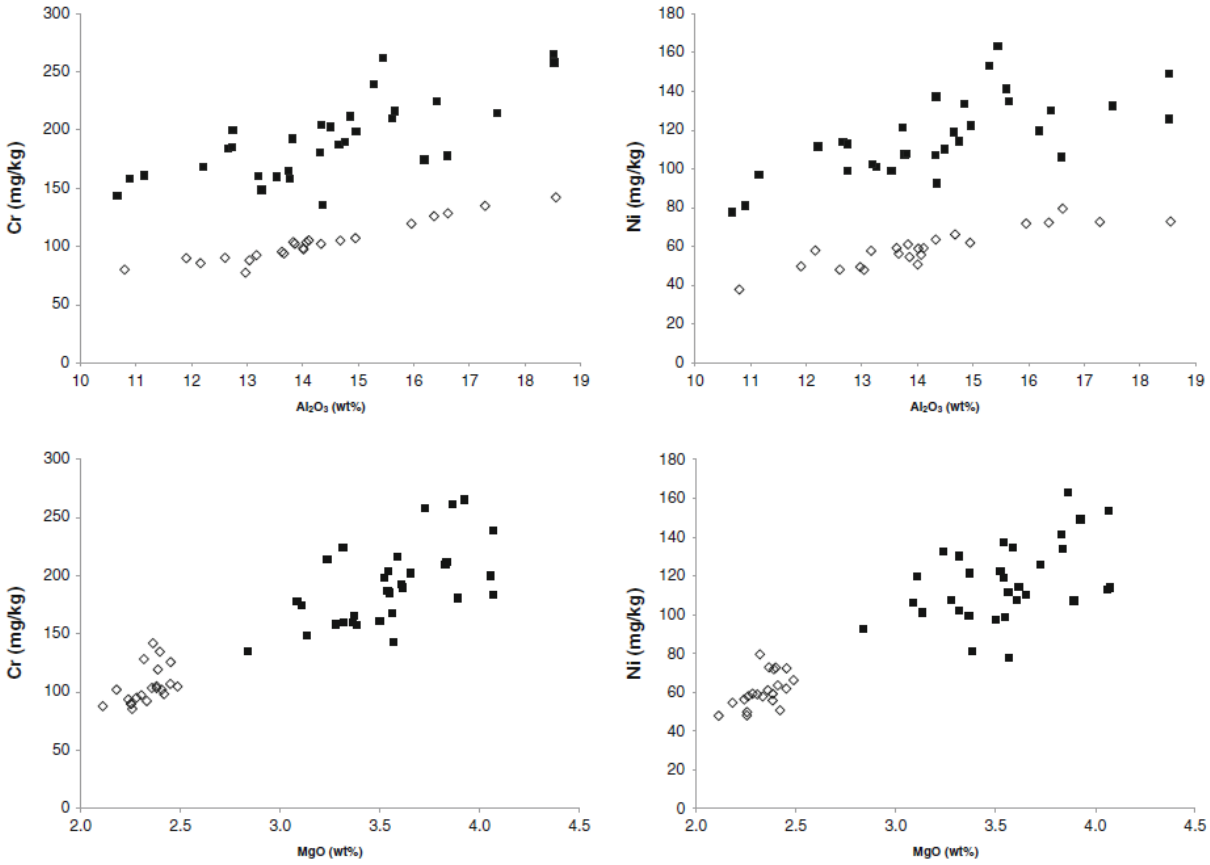

Figure 2.8: Bimodal distribution of Cr and Ni (ppm) versus MgO and Al_2O_3 wt% (weight percent) in the entire population of samples 100-120 cm deep. Filled squares and open diamonds are undisturbed Po and Reno provenance, respectively (From Bianchini et al., 2012).

2.3.2 Urban soils

Urban soils, potentially contaminated by road traffic, were collected in 2018 in Ferrara. For this environmental sampling, a stretch of the Bacchelli Road was chosen (Figure 2.9). This street is characterised by high intensity city traffic and it is surrounded on both sides by green areas: the Sottomura Park to the south and the Giorgio Bassani Park to the north.

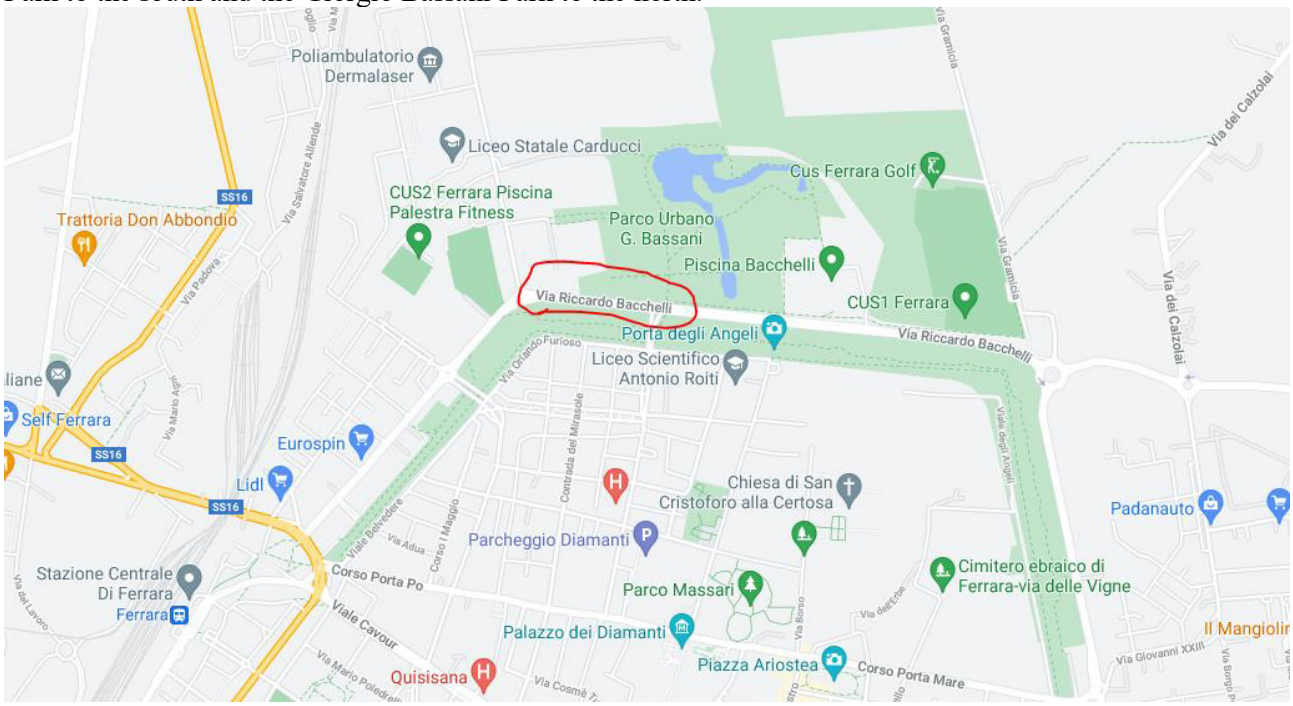

Figure 2.9: Map of Ferrara city with Bacchelli road marked by the red line.

Unlike the previously treated soils of Vigarano, these samples were collected only from the most superficial layers: for each of the five sampling stations, two samples were collected at different depths: between 0 and 5 cm and between 5 and 10 cm. Before the digestion procedure, samples were cleaned by removing the largest lithic and vegetable fragments.

2.4 Pelagic limestones

Eight samples that straddle the well known boundary clay of the Scaglia Rossa Formation from the Contessa section (Gubbio, Italy; Montanari and Coccioni, 2019), were collected *ad hoc* for this thesis (Fig. 2.10) because of the very high Ir content (9 ppb) characteristic of the layer.
An anomalous high concentration of iridium was found in the thin clay layer in the pelagic limestone section of the Bottaccione Gorge, near Gubbio, as well as in other sections around the Umbria-Marche Apennines of central Italy and in various other localities all around the globe (e.g., Alvarez et al., 1980; Coderis et al., 2021). This anomaly formally defines the end of the Mesozoic Era according to the Geological Time Scale (Gradstein et al., 2012) and it is universally known as the K-T (or K-Pg) level.
The K-Pg boundary (~66.05 million years ago) corresponds to one of the five largest mass extinctions of our planet that abruptly and irreversibly reshaped the Earth's biosphere (e.g., Alvarez et al., 1980; Schulte et al., 2010).

The boundary clay contains a concentration of iridium that is anomalously enriched up to four orders of magnitude relative to the continental crust (< 0.02 ppb; Chen et al., 2016). In various localities, an anomalous enrichment is also recorded for the other elements of the PGE group and other moderate (e.g., Co and Ni) and HSE elements (e.g., Re, and Au). It is now widely accepted that the recorded Ir (and other siderophile elements) anomalies reflect the global dispersal of meteoritic matter following the hypervelocity impact of an asteroid approximately 12 km in diameter (Collins et al., 2020) which was responsible for the following large mass extinction. Taking into account the geochemical PGE abundances, most probably the object was an undifferentiated body (carbonaceous?) chondritic in composition and the impact site was identified in the Chicxulub impact structure on the Yucatán Peninsula of Mexico (Shulte et al., 2010).

These kinds of samples are therefore very important for this work, for testing the low limits of the proposed analytical procedures.

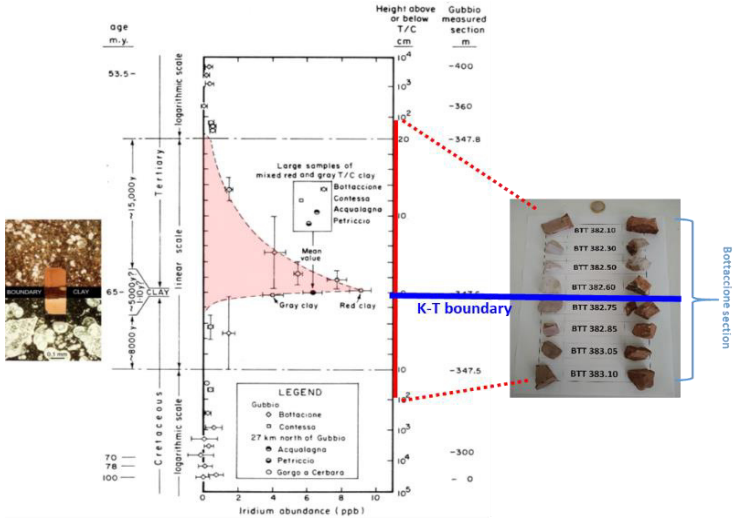

Figure 2.10: The iridium profile across the K/Pg boundary (original scheme from Montanari and Coccioni, 2019); on the right side, the eight samples (two chips per sample) provided for this study.

2.5 Reference Materials for PGE analysis

Certified Reference Materials CRMs make a significant contribution in the development of an analytical method and in the quality control of routine analyses. They can also be used as calibration standards and should be so homogeneous that the contribution of the sample heterogeneity could be negligible, when compared to the measurement uncertainty. The only way to guarantee the RM homogeneity, is to define a minimum sample size quantity, which should be specified in the analysis certificate.
Several well characterised CRMs with certified values and small uncertainties are available and are utilised for the PGEs' determination for analyses of "commercial samples". Three examples are WMG1 (mineralised gabbro, NRCan), SARM-7 (Merensky Reef platinum ore, SA Bureau of Standards) and AMIS 0416 (a platinum ore of African Mineral Standards).
Totally different is the situation for materials with "non-commercial" content of PGEs. There are no suitable RMs available for every geological/environmental matrix. Here, a brief mention of the most commonly used RMs.
For mafic rocks, the most analysed are TDB-1 (basalt) and WGB-1 (gabbro). They are certified for Pd, Pt and Au contents. These reference materials were characterised for quality control methods and they are among the most studied within non mineralised silicate materials with a low PGE content (GEOREM, Jochum et al., 2005). Another basalt, the BIR-1 (a coarse-grained olivine tholeiite from USGS), provided homogeneity for sample sizes below 2 g (Ishikawa et al., 2014). Three further USGS basalts: BHVO-1, BHVO-2 e BCR-2, provided PGE concentration data (Jochum et al., 2005), but systematic comparative studies of the results from different analytical techniques are not yet available (Table 2.3).
For the ultramafic matrix (Table 2.4), komatiite OKUM from Abitibi (Canada) (Wang and Becker, 2014) is characterised for PGEs and the rerefence values are in Guo et al., 2019.
Lherzolites are particularly useful RMs for PGEs, because these rocks may be rich in sulphides, which are easily digested by the peridotite acid attack. GP13 (a fertile lherzolite from the Beni Bousera massif, Morocco) and the above mentioned UBN (a serpentinised lherzolite) have been characterised for the HSE content and the $^{187}Os/^{188}Os$ composition. Suitable RMs for the harzburgitic matrix are not yet available. Only MUH-1 (from the Preg Quarry, Kraubath, Austria) is under the characterisation process, but the preliminary data show challenges due to the incomplete extraction of PGEs during acid digestion and to the powder's homogeneity (nugget effect) (Fig. 1.2).
Several PGE characterisation data were published for JP1 (a peridotite provided by GSJ) (Jochum et al., 2005). The results, however, are still rather dispersed and one study in particular (Meisel and Moser, 2004a) underlined issues related to the powder homogeneity (nugget effect).
RMs for sedimentary matrices (soils and sediments) were not originally developed for the determination of PGEs, but new data can now be found in literature: the GXR1-6 series of soil and deposits from USGS, the

JSd1-3 series of fluvial deposits from GSJ and the MAG-1, a fine-grained grey-brown clayey mud with a low carbonate content, from the Wilkinson Basin of the Gulf of Maine. The available data, however, are still limited and too dispersed to be applied to studies of method quality control (Jochum et al., 2005). Other RMs, like SCo-1 (a shale from USA), SDO-1 (a black shale) and JCh1 (a chert from GSJ) have been sometimes used as inter-laboratory method validation and quality control (Tables 2.5 and 2.6).
All the above mentioned RMs were originally planned and developed for method validation and quality control in routine analyses for the determination of major elements and several trace elements, but not of PGEs. Successively they were also characterised, more or less accurately, for these elements. A different matter concerns BCR 723 (Zischka et al., 2002): the increased interest in PGEs linked to road environmental pollution, led to the development of an *ad hoc* standard (road dust), for the quality control in the determination of Pt, Pd and Rh in environmental samples. This test material was collected from the ceiling of the Tanzenberg Tunnel (Styria/Austria), located 50 km north of the city of Graz (Austria). The sampling was carried out in the ventilation shaft of the tunnel, where the material was collected with small brooms and a vacuum cleaner from the walls of the shaft.

MAFIC ROCKS	**BCR-1 and BCR-2***	**BHVO-1 and BHVO-2**	**BIR-1**	**TDB-1**	**WGB-1**	**WPR-1**
Origin	USA, Oregon	USA, Hawaii	Iceland, Reykjavik	Canada, Tremblay Lake	Canada, Wellgreen Complex	Canada, Wellgreen Complex
Rock type	basalt	basalt	dolerite	diabase	gabbro	mineralised peridotite
Lithophile element contents	certified	certified	certified	characterised	characterised	REE certified
source	USGS	USGS	USGS	CanmetMINING	CanmetMINING	CanmetMINING
comment	** Contaminated with Henderon Molybdenite					

Table 2.3: Most common PGEs mafic rocks reference materials used for method validation and quality control (modified from Meisel and Horan, 2016).

ULTRAMAFIC ROCKS	**GP13**	**UB-N**	**HARZ-01**	**MUH-1**	**JP-1**	**GAS**	**OKUM**
Origin	Morocco, Beni Bousera	France, Voges	Albania, Devolli	Austria, Kraubath	Japan, Horomon	Mongolia	Canada, Abitibi
Rock type	lherzolite	serpentinite	harzburgite	harzburgite	peridotite	dunite	komatiite
Lithophile element contents		characterised	Proficiency testing results available	ISO certified	certified	ISO certified	ISO certified
source	out of stock	SARM-CRPG/CRNS	IAGeo	IAGeo	JGS	IAGeo	IAGeo
comment	out of stock		contaminated with lead glass				

Table 2.4: Most common PGEs' ultramafic rocks reference materials used for method validation and quality control (modified from Meisel and Horan, 2016).

SEDIMENTARY ROCKS	Sco-1	SDO-1	JCh-1	JSd-1	JSd-2	JSd-3
Origin	USA, Wyoming	USA, Kentucky	Japan, Ashikaga-shi	Japan, Ibaraki Prefecture	Japan, Ibaraki Prefecture	Japan, Ibaraki Prefecture
Rock type	Shale	black shale	chert	stream sediment	stream sediment	stream sediment
Lithophile element contents	well characterised	well characterised	well characterised	well characterised	well characterised	well characterised
source	USGS	USGS	JGS	JGS	JGS	JGS
comment	out of stock	out of stock				

Table 2.5: Most common PGEs' sedimentary rocks reference materials used for method validation and quality control (modified from Meisel and Horan, 2016).

GXR series	GXR-1	GXR-2	GXR-3	GXR-4	GXR-5	GXR-6
Origin	USA, Utah	USA, Utah	Usa, Nevada	USA, Utah	USA, Maine	USA, North Caroline
Rock type	Jasperoid	Soil	Fe-Mn-W rich Hot Springs Deposit	Porphyry Copper Mill-Heads	Soil (B zone)	Soil (B zone)
Lithophile element contents	characterised	characterised	characterised	characterised	characterised	characterised
source	USGS	USGS	USGS	USGS	USGS	USGS
comment	significant variation between bottles	significant variation between bottles	significant variation between bottles	significant variation between bottles	significant variation between bottles	significant variation between bottles

Table 2.6: GXR series' reference materials (for which there are some published values of PGEs) (Jochum et al., 2005).

3. Method tests

3.1 Introduction to the analytical issue

Re and PGE mass fractions are usually measured by ICP-MS with ID (Isotopic Dilution) method. This technique is not applicable to mono-isotopic elements like Rh and Au. Some labs use NTIMS (Negative-Thermal Ionisation Mass Spectrometry) for the determination of Re (e.g., Markey et al., 2007; Liu and Selby, 2018), this method, however, is mostly used fo the Os isotopic measurement.
Different types of ICP-MS techniques have been used in the past twenty years.
The single collector analysis with magnetic sector field (ICP-SFMS, e.g., Element XR) (e.g., Fischer-Gödde et al., 2011; Wang and Becker, 2014) and the quadrupole (ICP-QMS) mass spectrometer (e.g., Pearson and Woodland, 2000; Meisel et al., 2003a; Qi et al., 2004; Li et al., 2014; Day et al., 2016b) allow the determination of all PGEs and Re in a single aliquot. They also monitor the interfering elements in-run.
The multi collector MC-ICP-MS (e.g., Day et al., 2003; Chu et al., 2015a) is characterised by a high signal/noise ratio, which makes possible the determination of extremely low amounts of Re and PGEs (e.g., Day et al., 2003). With this technique though, it is problematic to control all interfering elements in-run (Chu, 2021).

None of these instruments, however, is able to completely control polyatomic ions and doubly charged ions, which affect the determination of these elements.
Tables 3.1 and 3.2 report the main spectral interferences (isotopes of other metallic ions, polyatomic ions like hydrides, argides, chlorides, oxides and hydroxides and ions with double charge) that could affect the HSE isotopes.

mass	Elements			Interference						
	Ru	Rh	Pd	M^{++}	Atomic	MH	MO	MOH	MAr	MCl
96	5.54				Zr Nb Mo		SeO	BrOH		
97										
98	1.87				Mo	MoH	SeO		NiAr	CuCl
99	12.76					MoH				ZnCl
100	12.6				Mo		SrO		NiAr	CuCl
101	17.06					MoH	RbO		NiAr	ZnCl
102	31.55		1.02				SrO		NiAr	CuCl ZnCl
103		100		Pb++			SrO RbO		CuAr	ZnCl
104	18.62		11.14				SrO		ZnAr	ZnCl
105			22.33				YO	SrOH	CuAr	ZnCl
106			27.33				ZrO	YOH	ZnAr	
107							ZrO		ZnAr	
108			26.46				ZrO MoO		ZnAr	
109							NbO			
110			11.72				ZrO MnO			

Table 3.1: Potential isobaric interferences on Ru Rh and Pd. Highlighted in yellow, the isotopes generally used in the measurements.

mass	Elements					Interference				
	Re	Os	Ir	Pt	Au	Atomic	MH	MO	MOH	MAr
184		0.02				W				NdAr
185	37.4									NdAr
186		1.59				W		YbO		NdAr
187	62.6	1.96				Re	WH	YbO		SmAr
188		13.24						YbO		SmAr NdAr
189		16.15						YbO		SmAr
190		26.26		0.014				YbO		SmAr NdAr
191			37.3					LuO		EuAr
192		40.78		0.782				YbO LuO HfO		SmAr
193			62.7					HfO		EuAr
194				32.97				HfO		SmAr GdAr
195				33.83				HfO		GdAr
196				25.24		Hg		HfO		GdAr
197					100			TaO	HfOH	GdAr
198				7.163		Hg		WO	TaOH	GdAr

Table 3.2: Potential isobaric interferences on Re, Os, Ir, Pt, and Au. Highlighted in yellow, the isotopes generally used in the measurements.

The new generation of triple quadrupole spectrometers is now able to eliminate the interference on PGE isotopes and allows their direct determination without complex extraction/pre-concentration procedures (Sugiyama and Shikamori, 2015; Sugyama, 2016; Desprez, 2016; Kutscher et al., 2018 and 2019).
The first quadrupole filters untargeted ions, including the "parents" ions. As an example, in the determination of ^{75}As, using oxygen as the reaction gas (Fig. 3.1), the quadrupole removes both the ^{59}Co ion (which, by bonding with ^{16}O, could interfere with the 75 mass of As) and the ^{91}Zr ion, which would otherwise affect the polyatomic ion AsO^+.

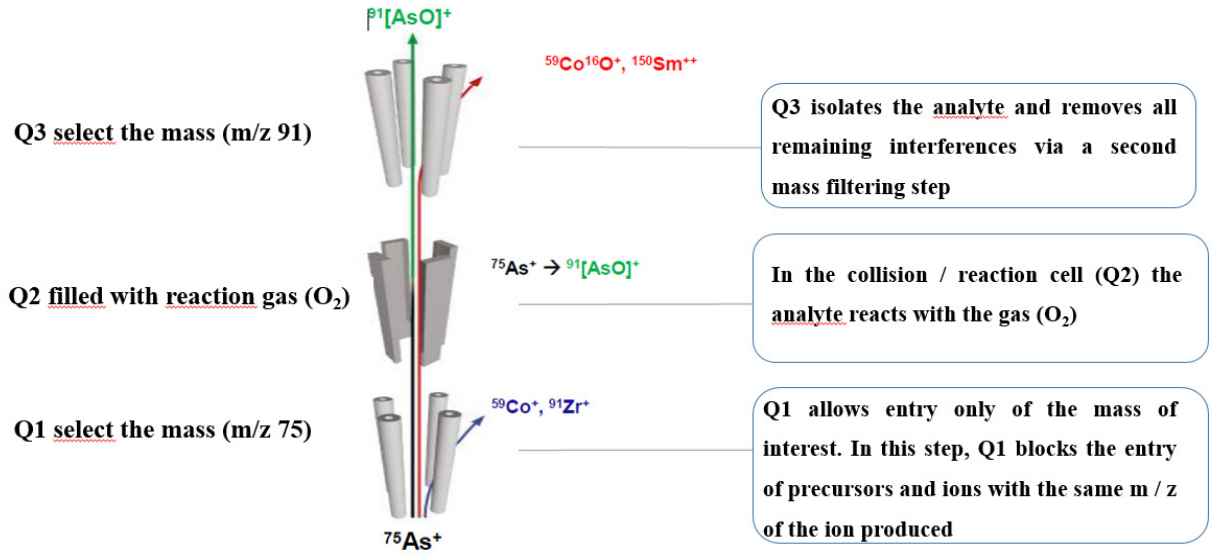

Figure 3.1: Scheme of the triple quadrupole setting for the determination of As (modified from Kutscher et al., 2018).

The second quadrupole is the reaction cell where an appropriate gas (O_2 in this example, but it could also be H_2 or NH_3) selectively reacts with the analyte or with an interfering species.
The setting of the third quadrupole allows two operative modes: on mass, when it is set to the same mass of the first quadrupole, or shift mass, when it is set to filter the product of the reaction between the analyte and the reaction cell's gas. In the above-mentioned example of the determination of As by O_2, the acquisition occurs in shift mass mode: in the second quadrupole, O_2 only reacts with the ion ^{75}As and forms a $^{91}[AsO]^+$ ion; the third quadrupole, which is set to mass 91, then removes the ions with mass above or below 91.
Pt, for example, can be analysed using two different reactive gases, O_2 and NH_3 (ammonia). Using O_2, the operating mode is on mass, whereas using NH_3 it is shift mass. In Fig. 3.2 the reaction pathways in the collision-reaction cell (Q2) are reported.
-on mass mode: because no reaction occurs between Pt and O_2, Pt will pass unimpeded through the cell. In contrast, the interference, HfO, having initially the same mass-to-charge ratio, is converted into HfO_2 and hence eliminated in the analysing quadrupole (Q3). At the same time, the first quadrupole (Q1) filters out all the other ions with lower and higher mass with respect to Pt, which could potentially react in a similar way, and hence create other interferences on the target ion mass.
-shift mass mode (with NH_3): Pt undergoes different reactions forming Pt-NH_3 clusters, with the most abundant product ion being $Pt(NH_3)_2$; this leads to a mass shift of 34 amu. Again, the HfO interferences will not react in the same way and will be removed by the analysing quadrupole.

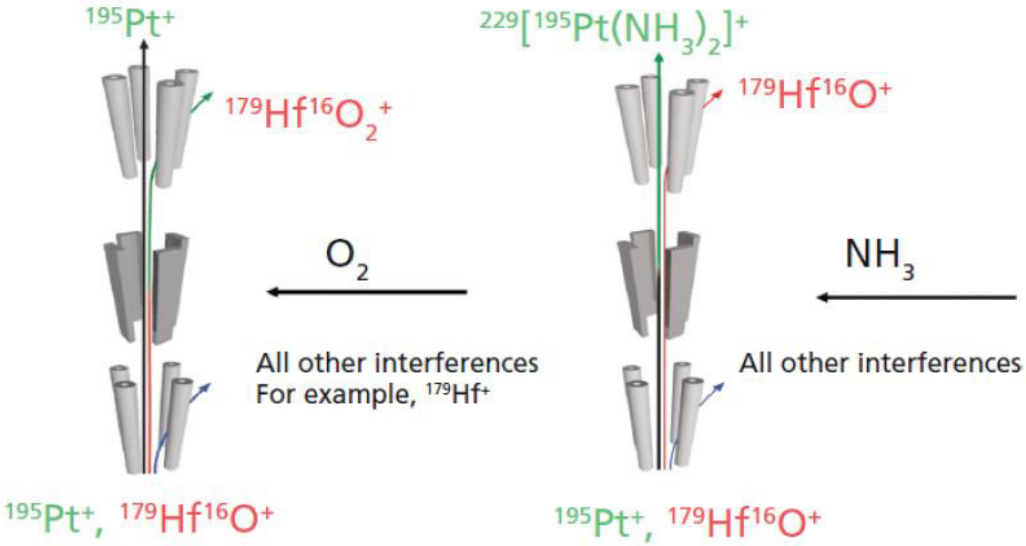

Figure 3.2: Schematic illustration of the analysis of platinum using triple-quadrupole ICP-MS operated with oxygen (O_2) and ammonia (NH_3) as reaction gases (scheme from Kutscher et al., 2018).

3.2 Preliminary test

3.2.1 Test on CRMs and meteorites

In order to verify the possibility to directly determine PGEs plus Au and Re without a pre-concentration process, in low concentration samples, a TQ-ICP-MS spectrometry (Desprez et al., 2016) preliminary test was carried out. The samples were dissolved and the solutions were sent to the two companies who produce triple-quadrupole ICP-MS spectrometers (Agilent© and Thermo Fisher Scientific©).
In 2012 Agilent released the Agilent 8800, the world's first triple quadrupole ICP-MS (TQ-ICP) with MS/MS capability. This ground-breaking instrument opened up new analytical possibilities for analysts in hundreds of laboratories around the world. The instrument used for the test, the new second generation

3. Method tests

8900 TQ-ICP, offers a range of configurations that cover applications from routine analysis to advanced research and high-performance materials analysis.
The other laboratory used the iCAP-TQ-ICP-MS spectrometer (launched at WPC in February 2017), which represents the latest triple-quadrupole ICP-MS generation of Thermo Fisher Scientific. The IUPAC universally recognised definition of TRIPLE QUADRUPOLE "*a multiple mass filter system, which only operates with RF/DC couple, able to stabilise the trajectory of one and only one mass (therefore destabilising the bigger and smaller masses with respect to the target mass). In this technology the trajectory of the selectable ions is only parallel with respect to the spatial arrangement of the multipolar bars of the systems Q1 Q2 Q3*", well applies to these spectrometers.
For this first test, three RMs were selected: two soil samples (GXR5 and GXR6) and one peridotite sample (JP1). The online GeoRem (Jochum et al. 2005) database for the peridotite JP1 provides values for all platinum metals, gold and rhenium. For the soils GXR5 and GXR6, only the reference values of iridium, platinum, palladium and gold are available and generally they are not certified. Table 3.3 reports the reference values available for these RMs.

		GXR5	**GXR6**	**JP1**
		Soil	**Soil**	**Peridotite**
Au	**ppb**	**9-16**	**95**	**0.23-0.35**
Ir	**ppb**	**0.051**	**0.032**	**2**
Os	**ppb**			**7.9**
Pd	**ppb**	**0.4**	**2.2**	**1.3**
Pt	**ppb**	**50**	**150**	**4.9**
Re	**ppb**			**0.015**
Rh	**ppb**			**0.875-1.09**
Ru	**ppb**			**6.5**

Table 3.3: Reference values (in ng/g) available for RMs used in the preliminary test (data from GEOREM Databse, Jochum et al. 2005).

In addition to the already mentioned RMs, two recently acquired meteorite samples were also dissolved and analysed. They are stony meteorites, which were found in the desert region of Draa Valley (central Morocco).
The solutions were prepared by HF and AR acid dissolution on hot plate in an open system. The solutions were then filtered and, without pre-concentration, were divided into three parts: two were sent to the supply companies' laboratories and one was kept for further tests.
The preparation followed these steps:

1) In a teflon beaker, approximately one gram of powder was accurately weighted. 12 ml of HF 40% and 4 ml of HNO_3 65% were added. The beaker was then covered with parafilm and, after 15 minutes in ultrasonic bath, was left to digest for 24 hours at room temperature.
2) The parafilm was removed and the sample was evaporated on a hot plate at 130 °C until incipient dryness (about 4 hours).
3) 12 ml of AR (9 ml of HCL 37% + 3 ml of HNO_3 65%) were added to the residue and it was again evaporated on a hot plate at 130° until incipient dryness (about 2 hours).
4) 8 ml of AR were added to the residue and it was again evaporated on a hot plate (about 1.5 hours)
5) Finally, 4 ml of AR were added and the beaker was then covered with parafilm and put in an ultrasonic bath for 15 minutes.
6) The final solution was filtered with a syringe with a 0.45um cellulose acetate filter in a 100 ml flask, then deionised water Milli-Q (18.02 MHom.cm) was added until the liquid totalled 100ml. The elements were therefore diluted about 100 times (dilution factor = 100 ml / ca 1g) compared to the original concentration in the solid.

3. Method tests

The acids used were Merck "Suprapur®". Together with the samples, a "procedural blank" was also prepared and analysed using the same material and reagents (and in the same quantity) utilised for the samples' dissolution (see Table 3.4 for data of the procedural blank composition, subtracted from the sample readings).
The samples were provided to each laboratory together with a table in which the order of magnitude of the concentrations for each matrix was reported. The laboratories had the freedom to choose the sample's acquisition method.

Procedural blank composition				
Isotope	Lab 1		Lab 2	
	Average (ppt)	%RSD	Average (ppt)	%RSD
^{101}Ru	1.07	27.0	0.35	20.0
^{103}Rh	2.09	9.6	0.32	25.0
^{105}Pd	73.7	3.5	45.0	25.0
^{185}Re	0.81	29.4	<0.05	
^{189}Os	2.47	17.6	0.40	80.0
^{193}Ir	0.72	3.9	10.00	20.0
^{195}Pt	1.13	7.3	<0.1	
^{197}Au	24.3	5.6	0.5	10.0

Table 3.4: Procedural blank composition. (Subtracted from the sample readings). Lab 1: average and %RSD are related to two acquisitions each consisting of three runs; Lab 2: average and %RSD are related to the same solution acquired twice with different gasses (NH_3 and O_2) in the cell.

Lab 1 chose to analyse both samples and blank using two different dilution procedures: 200 and 1000. Each element was then determined in several ways, using different reaction/collision gases and, in some cases, different isotopes. Table 3.5 reports the isotopes and gases used for each element in Lab 1.

Ru	101 -> 101 Ru [H2]	101 -> 101 Ru [He]	101 -> 101 Ru [NH3]	101 -> 101 Ru [O2]
Rh	103 -> 103 Rh [H2]	103 -> 103 Rh [He]	103 -> 103 Rh [NH3]	103 -> 103 Rh [O2]
Pd	105 -> 105 Pd [H2]	105 -> 105 Pd [He]	105 -> 105 Pd [NH3]	105 -> 105 Pd [O2]
Re	185 -> 185 Re [H2]	185 -> 185 Re [He]	185 -> 185 Re [NH3]	185 -> 185 Re [O2]
Os	188 -> 188 Os [H2]	188 -> 188 Os [He]	188 -> 188 Os [NH3]	188 -> 188 Os [O2]
	189 -> 189 Os [H2]	189 -> 189 Os [He]	189 -> 189 Os [NH3]	189 -> 189 Os [O2]
Ir	191 -> 191 Ir [H2]	191 -> 191 Ir [He]	191 -> 191 Ir [NH3]	191 -> 191 Ir [O2]
	193 -> 193 Ir [H2]	193 -> 193 Ir [He]	193 -> 193 Ir [NH3]	193 -> 193 Ir [O2]
Pt	194 -> 194 Pt [H2]	194 -> 194 Pt [He]	194 -> 194 Pt [NH3]	194 -> 194 Pt [O2]
	195 -> 195 Pt [H2]	195 -> 195 Pt [He]	195 -> 195 Pt [NH3]	195 -> 195 Pt [O2]
Au	197 -> 197 Au [H2]	197 -> 197 Au [He]	197 -> 197 Au [NH3]	197 -> 197 Au [O2]

Table 3.5: Isotopes and reaction/collisional gases used in Lab 1 for the preliminary test.

Lab 2 only used O_2 as a reaction gas and determined the whole element set in both modes (Single and Triple quadrupole) to highlight the advantage of the triple quadrupole. The instrumental settings in the two acquisition modes (SQ-KED, Single Quadrupole with Kinetic Energy Discrimination e TQ-O_2 Triple Quadrupole with O_2 as a reaction gas) are reported in Table 3.6.

Parameter	Value
Nebulizer	Glass Expansion MicroMist 400 µL·min^{-1} Quartz Concentric Nebulizer
Spraychamber	Quartz Cyclonic spraychamber, cooled to 2.7°C
Injector	2.5 mm i.d., Quartz
Interface	High-Matrix insert (3.5 mm), Ni Cones
Pump Speed	30 rpm
RF Power	1550 W
Nebulizer Gas Flow	1.09 L·min^{-1}
Analysis Mode	SQ-KED
Gas Flow	100% He @ 4.675 mL·min^{-1}
QCell Bias	-21 V
Q3 Bias	-18 V
Scan Settings	0.1 sec per analyte, 10 sweeps per reading For ^{60}Ni and ^{63}Cu, Q3 resolution set to high

Parameter	Value
Nebulizer	Glass Expansion MicroMist 400 µL·min^{-1} Quartz Concentric Nebulizer
Spraychamber	Quartz Cyclonic spraychamber, cooled to 2.7°C
Injector	2.5 mm i.d., Quartz
Interface	High-Matrix insert (3.5 mm), Ni Cones
Pump Speed	30 rpm
RF Power	1550 W
Nebulizer Gas Flow	1.09 L·min^{-1}
Analysis Mode	TQ-O_2
Gas Flow	100% O_2 @ 0.295 mL·min^{-1}
Scan Settings	0.1 sec per analyte, 10 sweeps per reading For ^{60}Ni and ^{63}Cu, Q3 resolution set to high

Table 3.6: Instrument configuration used in Lab 2: above: the parameter for Single Quad using He and Kinetic Energy Discrimination (SQ-KED), below: the parameter for Triple Quad using O_2 as reaction gas.

Lab 2 also applied a (1/10) dilution before data acquisition (Fig. 3.3), to limit signal suppression on the internal standard (In) in samples with high TDS (Total Dissolved Solids).

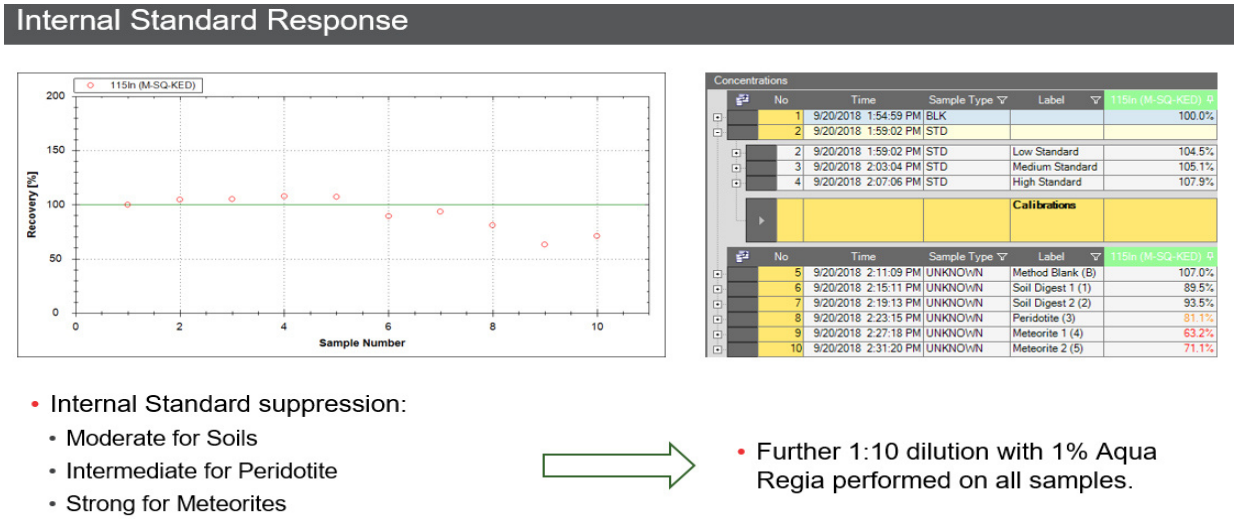

Figure 3.3: On the left: chart of the Internal Standard Response; on the right: numerical report of the recovery % on the Internal Standard signal.

On the whole, the data (reported in Table 3.7) were not easy to interpret:

3. Method tests

Lab 1: comparing the results of the two different dilutions, it looks like that the matrix effect is generally negligible. The only exception is for Pd. Regarding the meteorites, the results are comparable, but at lower concentrations as in the soils and peridotite, dilution and, consequently, the matrix, significantly influence the results.
The evaluation of the optimal method for the single element acquisition is more complex. For example, regarding Ru (101 isotope used) and Rh, different reaction/collision gases do not seem to change significantly the results: all tested gases provide coherent results, although the underestimation of the only available reference values (peridotite JP1), seems to show a limited recovery (about 40%) of the platinum metals in the solid. Even more complex is the recovery of Os, which is surely lost in large amounts in the sample preparation process.
Pt was acquired by both 194 and 195 isotopes. The results strongly depend on the chosen reaction/collision gas. Considering the values obtained with hydrogen and the mixture hydrogen/helium, the recovery for the three standards is comparable (about 40%) with the one for Ru and Rh.
Au and Ir, analysed in the same laboratory and independently of the acquisition method, gave results much higher than expected. At this stage, it was not yet clear if this was due to an incomplete removal of interfering species or if insufficient washing time between different solutions would have affected the memory effect of the calibration solutions. Further tests were necessary to clarify and possibly resolve the problem.

Lab 1	Sample **6A**	Sample **1B**	Std **JP1**		Std **GXR5**		Std **GXR6**	
	measured	measured	measured	Bib	measured	Bib	measured	Bib
^{101}Ru	906	823	2.39	6.5	0.5		0.7	
^{103}Rh	195	162	0.42	*0.97*	0.96		2.4	
^{105}Pd	1320	565	<LOD	1.3	11.9	0.4	4.18	2.2
^{185}Re	33.4	33.0	0.09	0.015	0.62		0.27	
^{189}Os	505	441	0.56	7.9	0.7		0.35	
^{193}Ir	628	602	0.08	2	0.95	*0.051*	1.28	*0.032*
^{195}Pt	784	842	3.24	4.9	16.3	50	24.1	150
^{197}Au	107	94	6.4	0.23 - 0.35	23.8	16	81.3	95

Lab 2	Sample **6A**	Sample **1B**	Std **JP1**		Std **GXR5**		Std **GXR6**	
	measured	measured	measured	Bib	measured	Bib	measured	Bib
^{101}Ru	790	821	1.9	6.5	0.17		0.46	
^{103}Rh	159	165	0.21	*0.97*	0.82		0.16	
^{105}Pd	453	497	1.76	1.3	49	0.4	61.5	2.2
^{185}Re	29.0	33.2	0.06	0.015	1.96		1.76	
^{189}Os	468	466	<LOD	7.9	1.8		<LOD	
^{193}Ir	604	655	0.61	2	6.44	*0.051*	7.46	*0.032*
^{195}Pt	781	923	8.04	4.9	21.6	50	20.4	150
^{197}Au	101	105	0.62	0.23 - 0.35	9.29	16	54.5	95

Table 3.7: Results (in ppb) of the solutions sent to the two companies who produce triple-quadrupole ICP-MS for preliminary test. In column "Bib" the reference compiled values (the "measured values" in italics; data from GEOREM, Jochum, et al. 2005).

Lab 2: the same solutions were analiysed using two methods: single quadrupole with helium as reaction/collision gas and triple quadrupole with oxygen as reaction gas.
The obtained data confirmed problems with the quantification of Pd, although for the peridotite standard the results, both with single and triple quadrupole, are in reasonable agreement with the reference value. Os, being under the detection limit for two of the three standards, confirmed the possible loss during solution preparation. Comparing the few available standard reference values and taking into account the

first laboratory's data, the difficulty to obtain accurate and precise data at very low concentrations, like the peridotite and soils samples, was confirmed.
The meteorite samples mainly provided fairly positive results. At their concentrations (one or two order of magnitude higher than the peridotite), the results from the two different laboratories are comparable and the distribution of the PGEs, except Pd, is compatible for a chondritic composition for both samples.
Lab 2's overestimation in the Pd determination, as clearly showed by the positive anomaly in the chondrite normalised diagram (fig. 3.4), was easily attributed to the incomplete removal of spectral interferences. As it was demonstrated by Desprez, 2016 and Kutscher et al., 2019, only by using ammonia as a cell reaction gas, interferences can be fully controlled. A complete study revealed that Ru^+, Rh^+, Pd^+ had similar low reaction rates with NH_3, while the major interferent ions, i.e., all oxide ions interfering SrO^+, RbO^+, YO^+, showed high reaction rates with NH_3 Sugiyama and Shikamori, 2015.

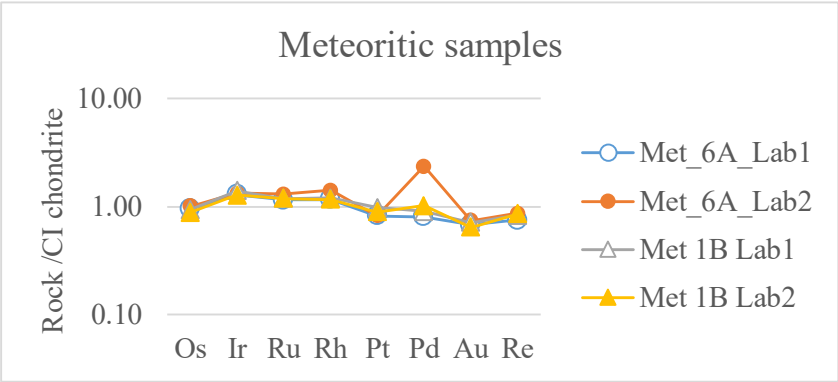

Figure 3.4: Chondrite normalised patterns of the meteoritic samples used in the preliminary test. Normalizing HSE values are from Palme et al., 2014.

3.2.2 First test on ultramafic and soil samples

In the light of the first encouraging results of the preliminary tests, the dissolution procedure by acid digestion was applied to two new sets of samples; the obtained solutions were analysed at the Thermo demo laboratory in Rodano (Milan, Northern Italy) by an iCAPTQ spectrometer using oxygen (ammonia was not available) as a cell reaction gas. Nine peridotite samples (one prepared twice) plus the standard JP1, (Ando 1984) and 13 soil samples (one prepared in duplicate) plus the standard GXR6, (Gladney et al. 1984) were used. The newly prepared standards, were two of the three standards previously dissolved. Recovery tests were also carried out on the two standards, adding to an aliquot of each a multielement spike of PGEs, plus Au and Re. Regarding the ultramafic samples, representative rocks from different tectonic environments were selected (Table 3.8).

Label	Provenience	Lithology	Tectonic Environments	Bibliographic reference
CN2	Rinibar (Scotland)	Sp-Lherzolite	Sub-continental Intraplate mantle	Bonadiman et al. 2008
GC/11/2	Grande Comore (Comoro Islands)	Sp-Lherzolite	Sub-oceanic intraplate mantle	Coltorti et al. 1999
GC/11/6	Grande Comore (Comoro Islands)	Sp-Lherzolite	Sub-oceanic intraplate mantle	this thesis
A4	San Carlos (USA)	Harzburgite	Sub-continental intraplate mantle	this thesis
A5	San Carlos (USA)	Sp-Lherzolite	Sub-continental intraplate mantle	this thesis
LE5	Mount Leura (Australia)	Amph/Ph bearing Harzburgite	Sub-continental intraplate mantle	Bonadiman et al. 2021
LE7	Mount Leura (Australia)	Ph bearing Harzburgite	Sub-continental intraplate mantle	Bonadiman et al. 2021
TL1	Tallante (Spain)	Sp- Harzburgite	Subduction-related mantle	Beccaluva et al. 2004 Bianchini et al. 2011
TL45	Tallante (Spain)	Sp-Lherzolite	Subduction-related mantle	Beccaluva et al. 2004 Bianchini et al. 2011

Table 3.8: Ultramafic samples used in the test.

3. Method tests

The soil samples were selected from alluvial deposits from the Po and Reno rivers (Bianchini et al., 2012) in Vigarano Pieve and Vigarano Mainarda, Ferrara, Italy (Fig. 3.6).

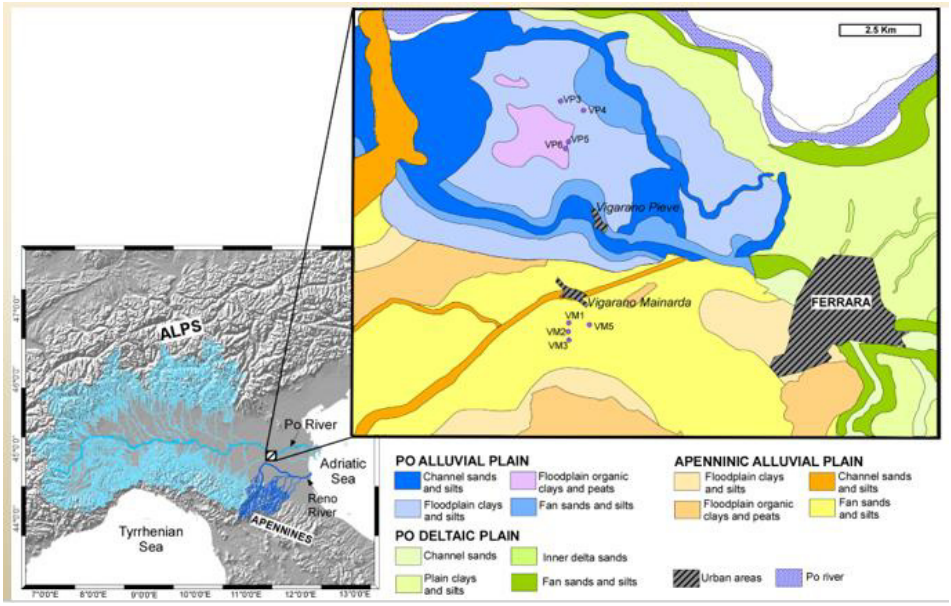

Figure 3.5: Provenience of soil samples analysed at the Thermo demo laboratory at Rodano in 2019. From Bianchini et al., 2012.

Among the 13 studied samples, 6 show affinity with sediments of the River Po and 7 with sediments of the River Reno (Tab. 3.9).

Affinity	**Ps**		**Rs**	
sample depth (cm)	**100-120**	**30-40**	**100-120**	**30-40**
av. n. a.	**31**	**21**	**23**	**24**
Co (mg/kg)	**18**	**18**	**15**	**15**
Cr	**191**	**210**	**104**	**105**
Ni	**117**	**115**	**60**	**58**
V	**104**	**99**	**95**	**92**
Zn	**69**	**74**	**69**	**73**
Cu	**43**	**53**	**50**	**55**
Sc	**14**	**14**	**13**	**12**

Table 3.9: Difference between sediments of the Po and Reno rivers. Abbreviations: av. n.a. = averaged, number of analyses; Ps = River Po sediment affinity; Rs = River Reno sediment affinity. From Bianchini et al. 2012.

Six samples were collected from a shallow depth (between 30 and 40 cm) and 7 from a deeper level (between 100 and 120 cm).
For both types of samples, the intention was to obtain "relatively different" specimens within the same matrix, with the aim of providing clearly defined and detectable PGE contents.

3. Method tests

The preparation procedure followed for the peridotitic samples, differs from the previous year by the use of centrifugation - instead of filtration - for the separation of the solution from the residue after acid digestion:

1) One gram of powder was accurately weighed and placed into a teflon beaker. 12 ml of HF 40% and 4 ml of HNO_3 65% were added. The beaker was then covered with parafilm and, after 15 minutes in an ultrasonic bath, was left to digest overnight at room temperature.
2) The parafilm was removed and the sample was evaporated on a hot plate at 180 °C until incipient dryness (about 3 hours).
3) Three ml of HF 40% and 3 ml of HNO_3 65% were added and it was again evaporated on a hot plate at 180 °C until incipient dryness (about 1.5 hours).
4) Twelve ml of Aqua Regia (9 ml of HCl 37% + 3 ml of HNO_3 65%) were added to the residue. The beaker was then covered with parafilm and, after 15 minutes in an ultrasonic bath, was left to digest overnight at room temperature.
5) The parafilm was removed and the sample was evaporated on a hot plate at 160 °C until incipient dryness (about 2 hours).
6) Eight ml of AR (6 ml of HCl 37% + 2 ml of HNO_3 65%) were added to the residue and it was again evaporated on a hot plate (about 1.5 hours).
7) Finally, 4 ml of AR (3 ml of HCl 37% + 1 ml of HNO_3 65%) were added and the beaker was then covered with parafilm and put in an ultrasonic bath for 15 minutes. 10 ml of deionised water Milli-Q (18.02 MHom.cm) were added and the solution was poured into a 15 ml test tube for a first centrifuge cycle (5 minutes at ca. 2000 rpm).
8) The supernatant was poured into a 100 ml flask. Deionised water was added to the solid residue in the test tube, which was agitated and centrifuged again (5 minutes at ca. 2000 rpm) to thoroughly "wash" the precipitate. The supernatant was added to the sample solution, then deionised water was added until the liquid totalled 100ml. The elements were therefore diluted 100 times (dilution factor = 100 ml / ca 1g) compared to the original concentration in the solid.

The soil samples' preparation was carried out in a similar way, but the 1gram sample was pre-treated with 4 ml of H_2O_2 to decompose the organic matter.

This was followed by different cycles of acid digestion and evaporation. After two days, the samples were centrifuged (by two extracting cycles of the supernatant and an accurate wash of the precipitate):

1) Nine ml of HF + 3 ml of HNO_3 followed by evaporation.
2) Ten ml of AR (7.5 HCl + 2.5 HNO_3) followed by evaporation.
3) Eight ml of AR (6 HCl + 2 HNO_3) followed by evaporation.
4) Four ml of AR (3 HCl + 1 HNO_3) centrifugation (two cycles) and brought to final volume in a 100 ml flask.

   For this matrix, the final dilution ratio is also ca. 1:100.

To carry out the recovery tests, another gram of the same sample powder was used. Before the acid dissolution procedure, 0.1 ml of a PGE multielement solution was added to the beaker on the weighing scales. This "spike" solution, diluted 1000 times (0.1 ml in 100 ml), was then analysed as an unknown sample.

For three soil and three ultramafic rock samples, the solid residue after centrifugation was taken to dryness at 105° C overnight and then diffractometric analyses were carried out to identify the residual phases.

As already mentioned, this second set of solution was analysed at the Thermo demo laboratory at Rodano, using an iCAP-TQ spectrometer, with oxygen as a reaction gas. Unfortunately, ammonia, which is highly recommended by several authors for this kind of analyses, was not available. (The complete data set is in Appendix VI, tables VI.1 and VI.2)

In this second analytical campaign, the concentration of another group of metal elements such as Cu, Sn, Sb, Te and Ni was measured, because of the similar geochemical behaviour (chalcophile and/or siderophile) with PGEs.

3.2.3 Results

The soil's recovery test gave good results, for Ru, Rh, Ir and Pt (between 90 and 105%). In contrast, the recovery test failed for Re (136%) and Pd (66%). Results on the peridotites were worse, but yet encouraging: between 84 and 108% for Ru, Rh, Ir and Re. In contrast, the recovery test failed for Pt (70%) and Pd (61%) (Table 3.10).

Unfortunately, the comparison with literature data is not that encouraging. However, it has to be taken into account that the GXR6 reference values are only available for some PGEs and in literature a range of values

is reported for JP1 (with concentrations at least two orders of magnitude lower). In addition to this, for the GXR series the comment *significant variation between bottles* is reported in the "GEOREM" database (Jochum et al., 2005).

Peridotite	Element	Soil
92%	Ru	101%
89%	Rh	96%
84%	Ir	98%
70%	Pt	91%
108%	Re	136%
61%	Pd	66%

*Table 3.10: Results obtained in the recovery test (recovery = (ppt in spiked sample - ppt in sample) * 100 / ppt spike.*

When compared to the values of elements with similar geochemical behaviour to PGEs, such as the chalcophile and siderophile elements Cu, Sn, Sb, Te and Ni, the results were rather good and often optimal. This could indicate the effectiveness of the acid digestion procedure (Table 3.11).

	GXR6	
ppm (mg/Kg)	Reference value	Analysed
Cu	66	70.8
Sn	1.7	1.3
Sb	3.6	3.77
Ni	27	27.9

Table 3.11: Comparison between reference and measured concentration of some siderophile and /or chalcophile elements in GXR6 reference material. (Reference Value from GEOREM Database, Jochum et al., 2005).

Element	repeatability
Cu	100%
Ni	105%
Ru	92%
Rh	110%
Pd	89%
Re	107%
Ir	101%
Pt	94%
Au	111%

The repeatability was tested by preparing and analysing two aliquots of the same sample separately. The peridotitic matrix showed very good results: between 85% and 115% for almost all elements (Table 3.12). The soil matrix instead, gave very bad results. This is in contrast to the recovery tests, which were good for both matrices. A possible explanation could be an error in the dissolution procedure or poor homogeneity of the sample's powder (nugget effect).

*Table 3.12: Repeatability on the peridotitic sample: (ppt first dissolution / ppt second dissolution) * 100.*

The residual samples for diffractometric analyses were selected based on the volume of the residual material available after centrifugation. Besides the two standards (additional data could facilitate the results' interpretation), four other samples (two peridotites, GC/11/2 and CN2, and two soils VMP1 and VP5P) were chosen.
The diffractometric analyses showed that the composition of the peridotitic residue is similar for all samples. In particular, the diffractograms of GC112 and JP1 are superimposable (Fig. 3.6).
The identified phases (sellaite, zircon, tripuhyite and, only for sample CN2, nitromagnesite) are normally not considered PGE host minerals and this confirms the effectiveness of the digestion procedure.

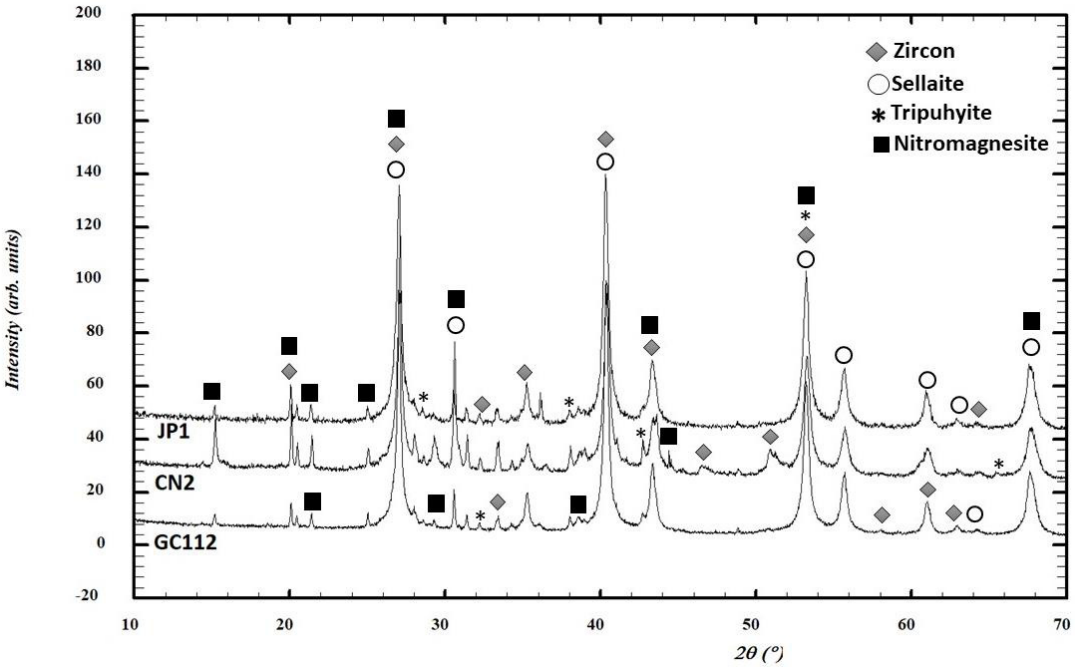

Figure 3.6: Diffractogram analyses of XRPD patterns collected for the three peridotite residues (GC112, CN2 and JP1 samples) showing the reference peaks of pure components (Zircon, Sellaite, Tripuhyite and Nitromagnesite). Each pure pattern has been scaled (from identical maximum intensities) and shifted along the Y axis for a better comparison.

The results of the soil residues are more complex. Their diffractograms differ significantly, most likely due to a higher heterogeneity of the material.
In the VP5P residue, only two mineral phases were identified: a hydrate aluminium fluoride (rosenbergite) and a barium and aluminium phosphate (gorceixite), which are not PGE acceptors.
Three phases were identified in the VMP1 residue: a calcium and aluminium fluoride (jakobssonite), a sulphate (osarizawaite) and a sulphide (pentlandite). The first two are not considered PGE acceptors, but the consistent presence (about 10%) of the pentlandite, which instead can host most PGEs, could undermine the possibility to have completely collected the PGEs in the extracted solution.
The residue diffractogram of the soil standard GXR6 (Fig. 3.7), identified a predominant phase (corundum) and three other phases present in traces (below 1%, according to the Rietveld method for quantitative estimates): a chromium oxide (eskolaite), rosenbergite again, and an iron, chromium and copper sulphide (daubréelite).
The latter is a potential PGE acceptor and its presence causes concern, but the high concentration of copper in the extracted solution, very close to the compiled value (70 ppm vs 66 ppm), seems to suggest that its contribution in retaining PGEs is limited.

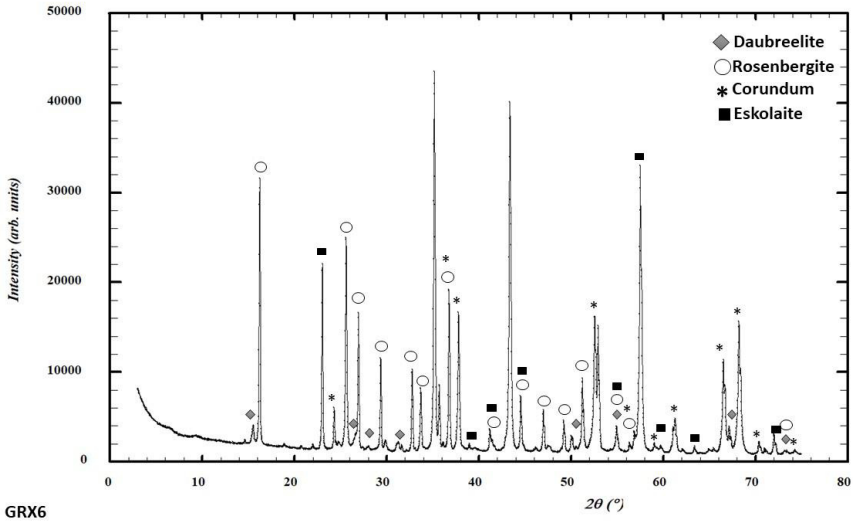

Figure 3.7: XRPD pattern collected for the GRX6 sample, showing the reference peaks of pure components (Daubreelite, Rosenbergite, Corundum and Eskolaite).

Unfortunately, the analyses of these two sample sets did not provide a clear direct link between PGE concentrations and environment of origin:
- the ultramafic samples show a PGE content slightly higher in lherzolites than harzburgites, but no significant differences in the PGE content were observed between samples GC/11/2, GC/11/6 (both from the sub-oceanic intraplate mantle), TL1, TL45 (both from the subduction-related mantle) and the others (from the sub-continental intraplate mantle).
- The sedimentary deposits did not show any difference between samples from the River Reno and the River Po basins (Bianchini et al., 2012).
The comparison with XRF data of Cu and Ni (Fig. 3.8), whose geochemical behaviour (chalcophile and siderophile) is similar to the one of PGEs, seems to confirm that the sample preparation procedure is suitable for an efficient extraction of chalcophile/siderophile elements ($R^2 > 9$ and regression line gradient of about 0.9 for Cu and 0.8 for Ni).

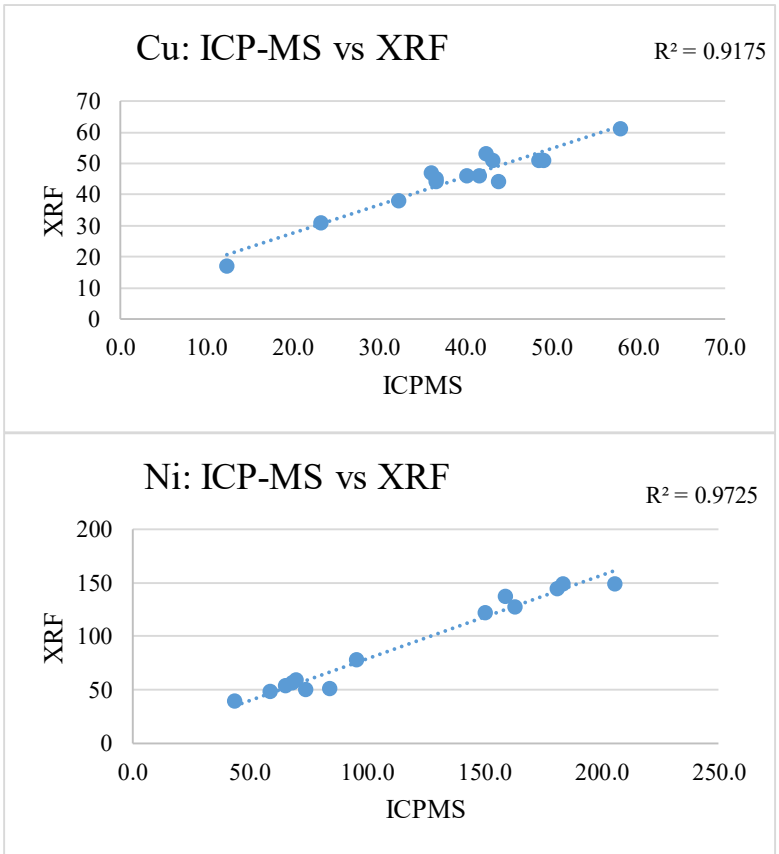

Figure 3.8: comparison between XRF and ICP-MS measured values (ppm) in sediment samples, for Ni (above) and Cu (below).

3. Method tests

From an analytical and methodologic point of view, the notable and worrying data is the correlation (R^2> 0.97) between the Hf and Pt concentrations (the latter can be considered as "apparent"). It is very clear, particularly in soil samples with high concentrations of Hf (Fig. 3.9), that this correlation is due to the isobaric interference of the HfO^+ ions on the 195 isotope of Pt. In this analytical configuration (oxygen as reaction gas and ON MASS mode) it is very unlikely that an accurate determination of Pt can be achieved, in the case of a high content of Hf.

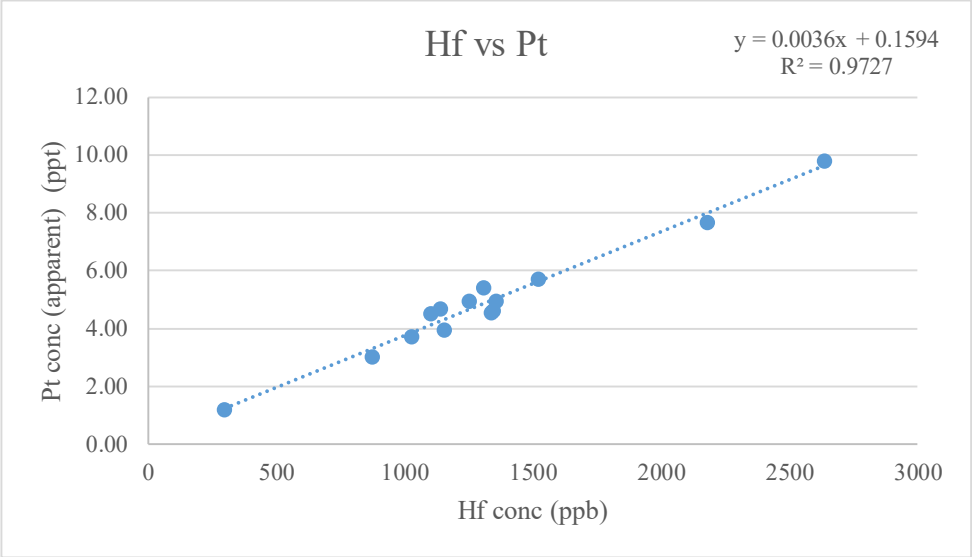

Figure 3.9: Strong correlation between Hf concentration and Pt (apparent) concentration.

3.3 Electron MicroProbe Analysis (EMPA)

The sample 6A (H-type chondrite) was prepared to proceed with an in situ investigation. The original blocks were thus cut and a thick (~100 microns) section was prepared. Natural oil and alcohol are used for the cutting grinding and polishing stages. SiC slurry was used for lapping, whereas the final polishing was made with diamond paste (3 and 1 µm particle sizes). Finally, it was washed in an ultrasonic cleaner for 3 minutes, using diluted acetone. During the same analytical investigation, another thin section was also prepared and analysed: a possible iron meteorite (sample 5E), which like the others, came from Morocco (Fig. 3.10).

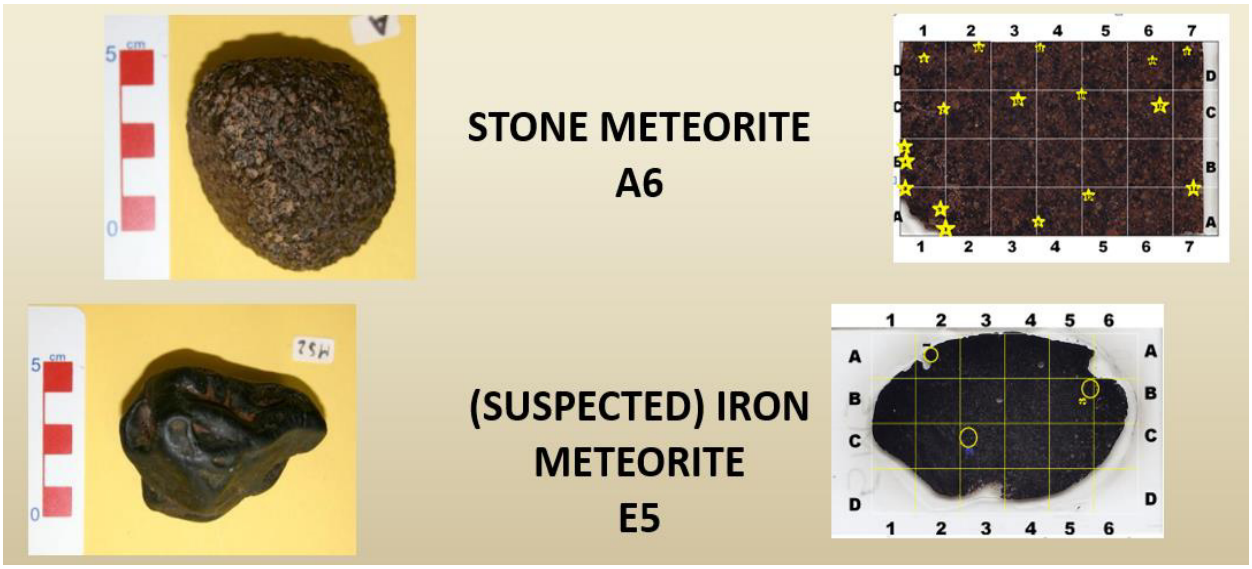

Figure 3.10: Investigated materials by EMPA

3. Method tests

The sections were analysed by electron microprobe using a Superprobe Jeol JXA 8200 (JEOL, Tokyo, Japan) at the Eugen F. Stumpfl Laboratory at the University of Leoben, Austria, using both ED (Energy Dispersive) and WD (Wavelenght Dispersive) systems.
In quantitative analyses of silicates, the electron microprobe was operated in the WDS mode, with an accelerating voltage of 15 kV and beam current of 10 nA. The diameter of the beam was about 1 μm. Counting times were 20 sec on the peak and 10 s on the left and right backgrounds with the exception of P (60 s on peak and 30 on background) and Ca (40 sec on peak and 20 on background).
In quantitative analyses of sulphides and alloys the accelerating voltage was 20 kV and counting times were 20 sec on the peak and 10 sec on the both backgrounds for all set of elements determined (As, Co, Ni, S, Fe, and Cu). Diffracting crystals, lines and standards used in determine each element are summarised in Table 3.13.

Element	line	Crystal	report as	Standard
		Silicate		
Na	Ka	TAP	Na2O	Sanidine
P	Ka	PETJ	P2O5	Apatite
Fe	Ka	LIF	FeO	Ilmenite
Mn	Ka	LIFH	MnO	Rhodonite
Cr	Ka	LIFH	Cr2O3	Chromite
Mg	Ka	TAP	MgO	SPIolivine
Si	Ka	PETJ	SiO2	Wollastonite
Ni	Ka	LIFH	NiO	Skutterudite
Ti	Ka	LIFH	TiO2	Rutile
Al	Ka	TAP	Al2O3	Sanidine
Ca	Ka	PETJ	CaO	Wollastonite
Co	Ka	LIFH	CoO	Skutterudite
K	Ka	PETH	K2O	Sanidine
		Sulphides and alloys		
Co	Ka	LIF	Co	Skutterudite
Ni	Ka	LIFH	Ni	NiS
S	Ka	PETJ	S	ZnS
Fe	Ka	LIFH	Fe	ZnS
Cu	Ka	LIFH	Cu	CuS

Table 3.13: Analytical condition for quantitative analysis with WDS in silicates, sulphides and alloys. Standards routinely used in the Lab Eugen F. Stumpfl Laboratory at the University of Leoben, (Austria) are also reported.

The sections were analysed to confirm or not the presence of possible PGE-bearing sulphide or metallic accessory phases. The search was carried out by a meticulous and systematic high enlargement scan of both thin sections, looking for highly reflective small crystals. The nature of each mineral was verified by the EDS (Energy Dispersive Spectrometry) fast scan. Unfortunately, this detailed exam did not allow me to identify any PGE-bearing phases. In fact, the identified accessory minerals mainly consisted of oxides (e.g., chromite) or barite together with major silicate phases (see Figs. 3.11-3.13).

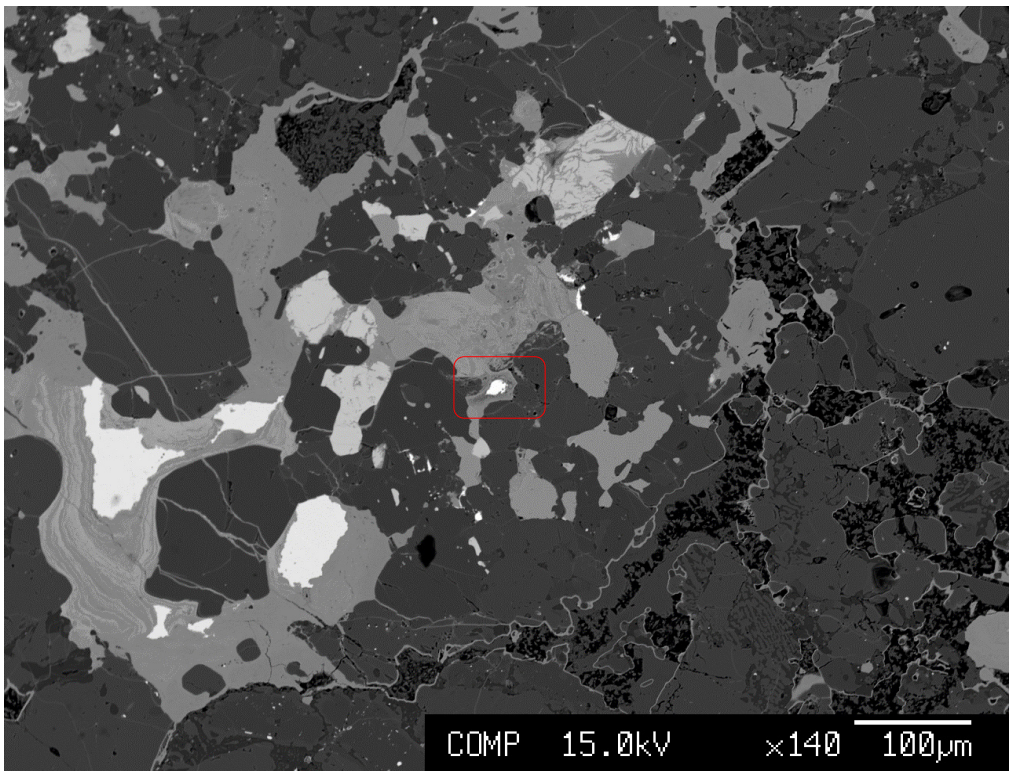

Figure 3.11: BSE Panoramic image for the summary identification of high reflectance points.

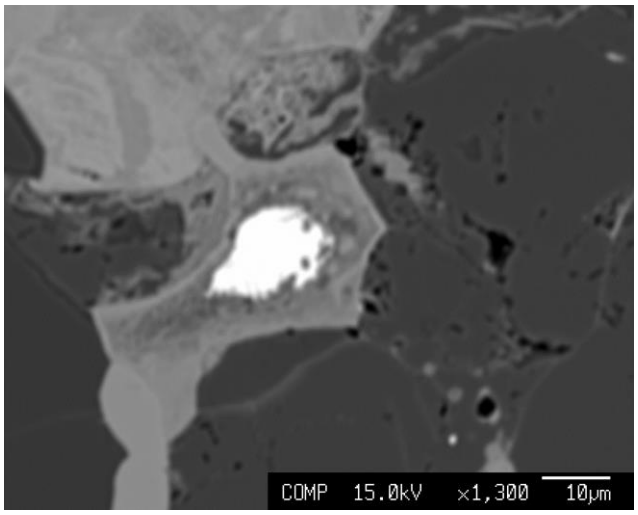

Figure 3.12: Enlargement of the area marked by a red box in Fig. 3.11, for fast EDS analysis (chromite).

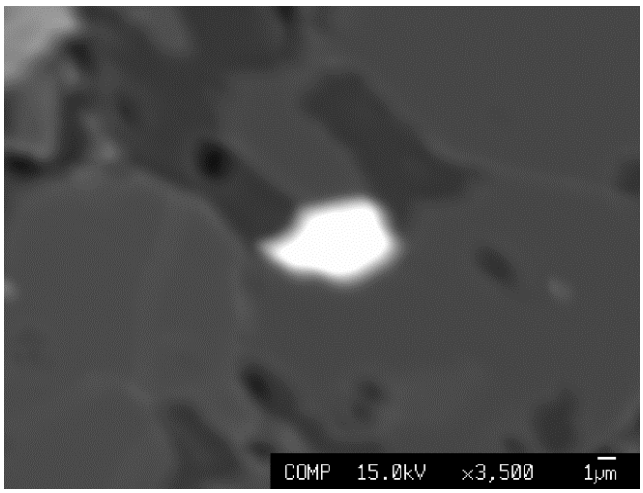

Figure 3.13: The smallest minerals were analysed at a higher magnification (barite).

Unfortunately, the detailed exam of the more reflective grains on both thin sections did not identify any PGE phases. The identified accessory minerals were oxide crystals (e.g., chromite) or barite. For sample 6A, however, the microprobe study allowed the determination of the quantitative composition of the main phases by WDS (Wavelength Dispersive Spectrometry). This permitted a preliminary classification of the meteorite, which has been the subject of scientific papers (*e.g.,* Lugari et al., 2018).
The determination of the major element concentration is also a preparatory step towards the LAM-ICP-MS (Laser Ablation Microprobe ICP-MS) determination of PGE traces in base metal sulphides and FeNi-metal: the elaboration of the signals obtained from trace element masses is based on the ratio of acquired signal/concentration on a major element used as an internal standard.
On the whole, quantitative WDS analyses were carried out on more than 320 points (silicate phases, apatites, oxides, sulphides and FeNi-metal). The average composition of the sulphide and FeNi-metal analysed in the 6A thin sections are reported and discussed in Chapter 4 and the complete data set is found in Appendix IV (Tables IV.1 and IV.2).

3.4 Laser Ablation Microprobe-ICP-MS analysis (LAM-ICP-MS)

The same two thin sections were subsequentely analysed at the IGG laboratory of the CNR in Pavia for the determination of the trace elements (including PGEs) in sulphides and in metal alloys. The rationale behind this additional analytical work, was to check if the concentration obtained by the dissolutions of the original bulk matrix were replicated (within the analytical errors) by mass balance calculation methods.
PerkinElmer SCIEX ELAN DCR-e quadrupole ICP-MS coupled with a Q-switched Nd: YAG laser source, model Brilliant (Quantel), whose fundamental emission (1064 nm) is converted to 266 nm by two harmonic generators, was used for LA-ICP-MS analysis of kamacite and taenite metal grains and sulphides of 6A chondrite (H-Type) and the supposed iron-meteorite 5E.
PGE isotopes targeted during analysis were ^{101}Ru, ^{103}Rh, ^{106}Pd, ^{192}Os, ^{193}Ir, and ^{195}Pt; however, results for other trace metal isotopes were also acquired (^{45}Sc, ^{49}Ti, ^{51}V, ^{53}Cr, ^{55}Mn, ^{59}Co, ^{60}Ni, ^{63}Cu, ^{66}Zn, ^{71}Ga, ^{72}Ge, ^{75}As, ^{90}Zr, ^{93}Nb, ^{107}Ag, ^{115}In, ^{121}Sb, ^{177}Hf, ^{181}Ta, ^{187}Re, ^{197}Au and ^{208}Pb). The isotopes selected for analysis were chosen based on their abundances (i.e., most abundant isotope) and limited interference with other elemental isotopes. Analytical parameters consisted of a frequency of 5 Hz, a spot size of ≈ 50 μm (Fig. 3.14), and a fluency of 10-12 J/cm^2. Utilizing a spot size smaller than 50 μm would have affected the number of counts collected during analysis (i.e., less material being ablated). The analysis was completed using He as a gas carrier. Each spot analysis was a total of 120 seconds: 50 seconds background time followed by a 10 second delay and 60 seconds of ablation (Fig. 3.15). Data reduction was done with the GLITTER software, using the reference synthetic glass NISTSRM 610 as external standard and ^{57}Fe as internal standard. According to Sylvester and Eggins, (1997), this glass certified reference material has allowed the quantification of Re, Au, and PGEs except for Ir, Os and Ru: for these elements compiled reference values are not available (GEOREM, Jochum 2005). Unfortunately, due to a software bug, data related to the Pt count acquisition were lost and it was not possible to obtain updated software in time to repeat the analyses.
Precision and accuracy were assessed via repeated analysis of in-house spinel reference material, and resulted better than ±15% at the ppm concentration level.
BSE images were compiled into maps to help identify metal grains in each specimen suitable for analysis based on general metal texture and size, as well as to assist with navigation and locating metal grains during other analyses. Reflected light microscopy was also used for identifying suitable metal targets for LA-ICP-MS and distinguishing between kamacite and taenite and sulphides grains.

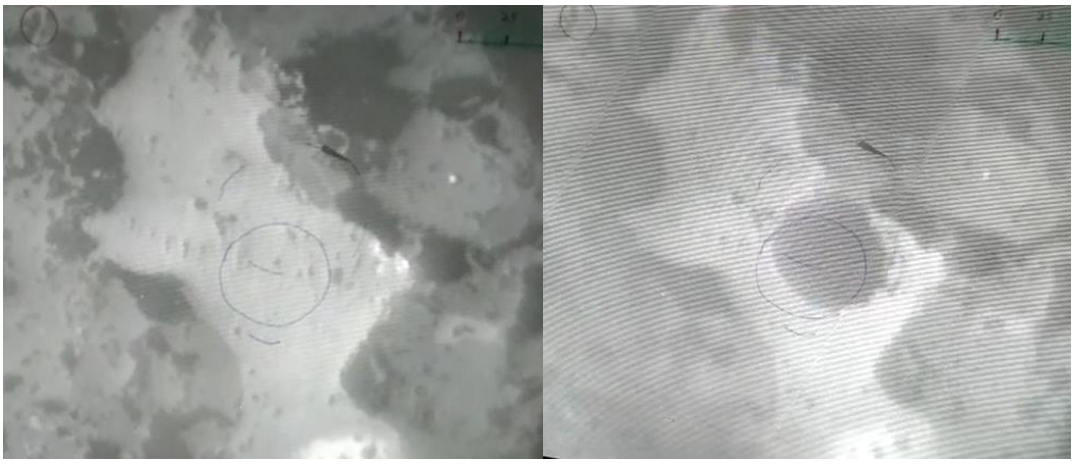

Figure 3.14: Spot analysis: before (on the left) and after (on the right) the ablation.

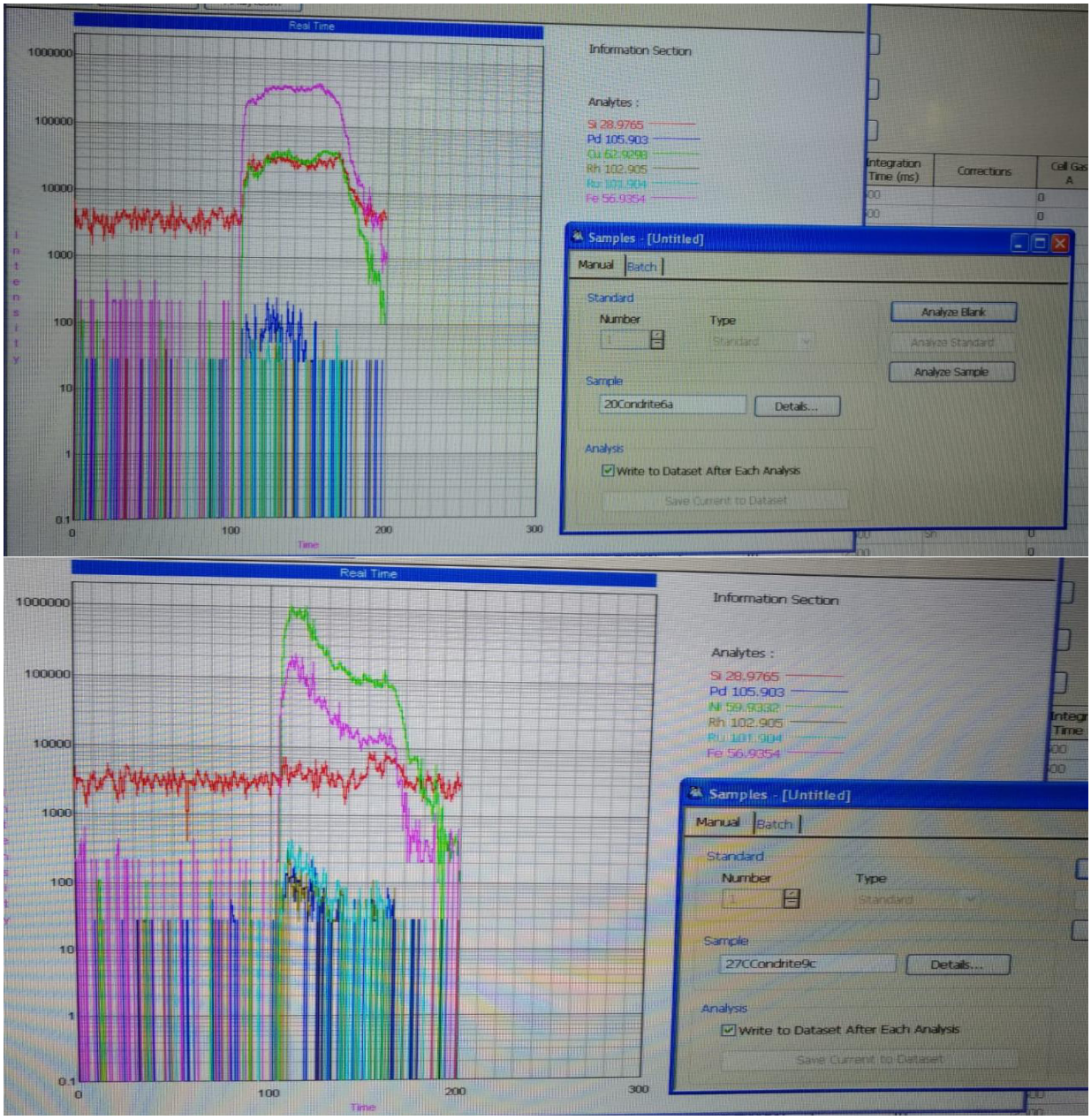

Figure 3.15: RTD (Real Time Display) showing the transient signal during the ablation of an alloy metal (above) and a sulphide phase (below).

3.5 Environmental sampling

3.5.1 Introduction

In order to abate the ever increasing emissions from automobiles, legislation in many countries has set limit values for the main exhaust pollutants HC, CO and NO*x*. These values are revised continually and reflect the state of the art in emission abatement technology. The only way to meet the limit values in cars equipped with petrol engines is through the installation of catalytic converters (Fritsche and Meisel, 2004).
The first installation of a catalytic converter on a general-purpose automobile in the USA occurred in October 1974. This was followed by the introduction of autocatalysts in Japan in 1976, Germany in 1984, Austria in 1987 and Brazil in 1996. Car catalysts were made mandatory in Sweden in 1989 and on all new cars produced in the European Union in 1993. An estimated 500 million vehicles worldwide in 2007 were equipped with an exhaust catalyst that uses PGEs (Sutherland et al. 2007).
In Italy, the catalytic converter became mandatory in 1993. In more than 39 million vehicles, more than 90% are now properly equipped (Source: ACI (Automobile Club of Italy) 2019).
Automobile catalysts are generally believed to be the main source of PGEs emitted into the environment. As already mentioned, these catalysts use Pd, Pt, and Rh to promote the removal of gaseous pollutants in vehicle exhausts, and a fraction of the PGEs in catalysts is emitted into the environment during vehicle operation (Moldovan et al., 2002). It is important to carry out systematic studies in order to build up a picture of how the PGEs are deposited and distributed in the roadside environment.

3.5.2 Site choice

To identify a suitable location to investigate the environmental distribution of PGEs, it was necessary to find the right road, with well defined characteristics: high traffic, accessibility on both sides, absence of vertical barriers (both natural and anthropic) which could hinder the lateral dispersion of the road particulate.
A stretch of the Bacchelli Road in Ferrara was chosen. (Fig. 3.16) This street is characterised by high intensity city traffic and it is surrounded on both sides by green areas: the Sottomura Park to the south and the Giorgio Bassani Park to the north. The presence of green areas is expected to show a steady gradual increase of the natural background values of the PGEs towards the road, where the anthropic contribution is higher.
Critical traffic conditions (frequent slowdowns, queues and repeated "stop and go") which would increase the PGE release in the environment (Lyubomirova and Dijingova, 2015), occur due to the presence of a traffic light system in the vicinity.
Ferrara Council implement 4 fixed stations (not always in use) and 6 mobile units for traffic surveys. In November 2018, a survey was carried out by the Council in Bacchelli Road for a company who was studying acoustic pollution. The data, integrated with data from a fixed station in Copparo Road, allowed the estimate of 8973000 automobiles equivalent/year that transited on Bacchelli Road (Cilio, personal communication).

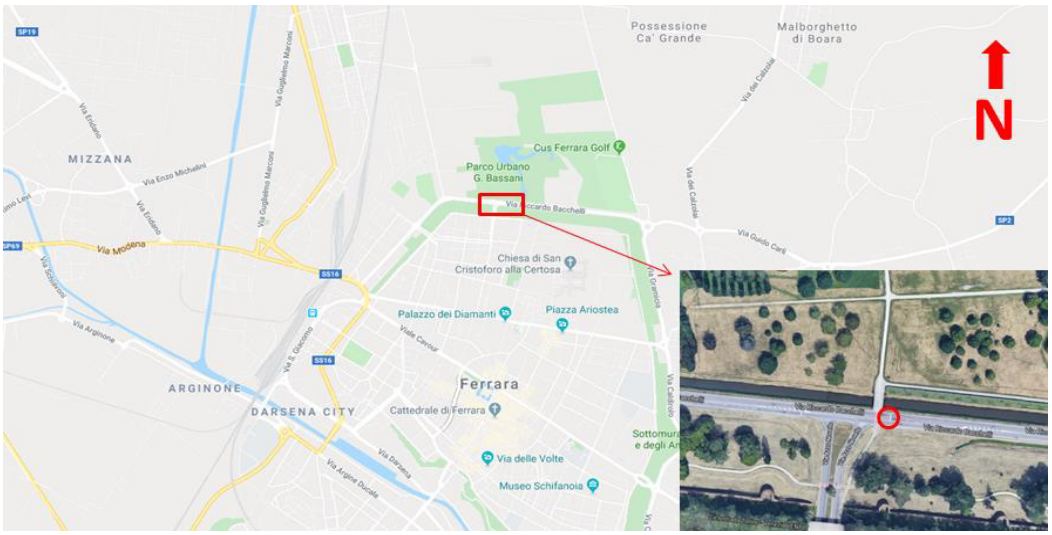

Figure 3.16: map of the study area.

3.5.3 Sampling

Sampling was carried out on the 8th of August, after 5 consecutive dry days and in a dry period: data collected by the closest meteorological stations ("Pontelagoscuro" and "Urban Ferrara") of the hydrometeorological network ARPA (Agenzia Regionale Protezione Ambientale), reported total precipitations of only 25-30 mm in the previous three weeks. (Table 3.14).

daily accumulated precipitation (Kg/m^2)					
	PONTELAGOSCURO	URBAN FERRARA		PONTELAGOSCURO	URBAN FERRARA
09-lug	0.6	1.2	25-lug	0.2	0
10-lug	1	0.8	26-lug	1.8	4.2
11-lug	0.2	7.6	27-lug	8.6	9.2
12-lug	0	0	28-lug	5.2	8.4
13-lug	11.6	10.2	29-lug	0	0
14-lug	0	0	30-lug	0	0
15-lug	5.2	1.6	31-lug	0	0
16-lug	0	0	01-ago	0	0
17-lug	0	0	02-ago	15.4	6.4
18-lug	0	0	03-ago	0	0
19-lug	0	0	04-ago	0	0
20-lug	0	0	05-ago	0	0
21-lug	0	0	06-ago	0	0
22-lug	0	0	07-ago	0	0
23-lug	0	0	08-ago	0	0
24-lug	0	0	09-ago	0	0

Table 3.14: Rainfall in the period prior of sampling. Data from ARPA Emilia Romagna. (Highlighted in yellow the sampling day).

The investigated road stretch is located at the crossing between Bacchelli Road and Azzo Novello Road. Samples of dust and fine gravel were collected on the road surface near the two roadsides. To the south of Bacchelli Road, in Sottomura Park, samples were collected at distances of 3 m, 5 m, and 10 m from the roadside. Further samples were also collected 50 m away from the roadside, within the city walls. Due to the presence of a canal that runs along the road, only one place was sampled to the north of Bacchelli Road, located in Parco Urbano, approximately 50 m away from the roadside (Fig. 3.17).

BSC	South of roadside	44°.850098	11°.620833
BN1	Northern farthest point	44°.850781	11°.620886
BS4	Southern farthest point	44°.849508	11°.620689

Figure 3.17: Location and geographic coordinates of some samples.

3. Method tests

At each sampling station, samples of common grass were collected, together with soil sampled at different depths: between 0 and 5 cm and between 5 and 10 cm.

3.5.4 Scheme of sample identification

The sample labelling system is as follows: B stands for via Bacchelli; N and S stand for north and south of the road, respectively; numbers from 1 to 4 (only for samples collected to the south of the road) increase with the distance from the road. The letters "a" and "b" identify the soil sub-samples as superficial (0-5 cm) and deep (5-10 cm), respectively.
BNC and BSC identify road dust and fine gravel samples collected at the north and south roadsides, respectively.
Finally, E at the beginning, is related to grass samples.

3.5.5 Sample processing

Grass samples

Each grass sample weighed a few tens of grams (wet weight) and was divided into two aliquots, one of which was washed with demineralised water to eliminate dust. In the label, the washed sub-sample is identified by a "w". The two sub-samples were then dried in an oven at 50 °C for 48 hours. Subsequently, they were finely chopped and mineralised on a hot plate:

1) In a teflon beaker, approximately one gram of grass was accurately weighted. 4 ml of H_2O_2 35% and 4 ml of HNO_3 65% were added. The beaker was then covered with parafilm and, after 15 minutes in an ultrasonic bath, was left to digest for the weekend at room temperature.
2) The parafilm was removed and the sample was evaporated on a hot plate at 130 °C until incipient dryness (about 6 hours).
3) Four ml of H_2O_2 35% and 4 ml of HNO_3 65% were added and it was again evaporated on a hot plate at 150 °C (about 2 hours).
4) Three ml of HNO_3 65% were added and it was covered with parafilm and, after 15 minutes in an ultrasonic bath, it was left to digest overnight at room temperature.
5) The parafilm was removed and the sample was evaporated on a hot plate at 130° until incipient dryness (about 2 hours).
6) Finally, 4 ml of AR (3 ml of HCL 37% + 1 ml of HNO_3 65%) were added and brought to final volume in a flask with deionised water.

Soil samples

Each soil sample (approx. 200-300 g) was cleaned by removing the largest lithic and vegetable fragments by hand (Fig 3.18). Samples were then dried in an oven at 105 °C for 24 hours.

Figure 3.18: Manual cleaning of the samples.

Subsequently, a ca. 50 g aliquot was finely grounded and homogenised by agate mortar mill. The powder was attacked by acid with a procedure similar to the one already mentioned above.
The only difference with respect to the previous test, was the use of a higher quantity of oxygen peroxide, due to the presence of a larger quantity of organic matter. In detail, after each evaporation cycle and the addition of 10 and 8 ml of Aqua Regia (AR), respectively, 2 ml of H_2O_2 were added to the residue. On two (one collected near the roadside and the other at the farthest point) of the twelve samples a recovery test was carried out following the same procedure previously described.

3.6 Test on Bottaccione section samples

These samples were prepared for a comparison with literature data of the concentration of Ir in a universally known stratigraphic sequence: the Bottaccione (Gubbio, Italy; e.g., Alvarez et al., 1980; Montanari and Coccioni, 2019) From 8 samples of the Bottaccione series (from BTT 382.10 to BTT 383. 10) small chips were taken by cutting the rocks with a petrographic cutting machine equipped with a diamond blade. Subsequently, the areas that showed traces of alteration were cleaned (using the same diamond blade) (Fig. 3.19). Finally, grinding (using agate tools) was carried out until it was reduced to a very fine dust powder.

Figure 3.19: Samples of the Bottaccione sequence, (Gubbio Italy). On the right, the witnesses preserved after the cut; on the left, the chips, cleaned from the superficial alteration, which were then powdered.

The dissolution, by acid attack, of a carbonate rock is certainly less problematic than silicate material. With this matrix, in fact, a total dissolution is easily reached: at the end of the procedure, there is therefore no solid residue to be separated from the solution by filtration or centrifugation. As in the case of the material already seen, the dissolution took place on a hot plate in an open system (low pressure), with a sequence of steps consisting of the addition of acids and evaporation at incipient dryness. For these carbonate samples, 6 ml of HF and 3ml of HNO_3 were added to about 0.25 g of powder. After hot reaction and evaporation, 8 ml of AR (6 ml of HCl 37% + 2 ml of HNO_3 65%) were added and the sample was again placed on a plate for evaporation. Finally, 3 ml of HCl and 1ml of HNO_3 were added to the residue and it was brought to volume in a 100 ml flask with milliQ water. In two samples a recovery test was also performed, by preparing the same sample in duplicate and adding, to one of the two aliquots, a spike of a standard solution of PGEs.

3.7 Test on BCR 723 reference material

To better evaluate the analytical results on urban soil samples, a new RM was acquired: the already mentioned certified reference material for the quality control of palladium, platinum and rhodium in road dust: BCR-723 (Zischka et al., 2002). This road-dust test material was collected from the ceiling of the Tanzenberg Tunnel (Styria/Austria), located 50 km north of the city of Graz (Austria). The collected material had a composition adequately representative of road dust, containing measurable quantities of Pt, Pd, and Rh. This RM certifies the concentrations of the three PGEs used in automobile catalysts and specifies the minimum quantity of powder to be processed. For other 19 elements, indicative reference values are provided (Fig. 3.20).

EUROPEAN COMMISSION
JOINT RESEARCH CENTRE
Institute for Reference Materials and Measurements

CERTIFIED REFERENCE MATERIAL
BCR® – 723

CERTIFICATE OF ANALYSIS

ROAD DUST			
Element	Mass fraction based on dry mass		Number of accepted sets of results p
	Certified value [1] [µg/kg]	Uncertainty [2] [µg/kg]	
Palladium	6.1	1.9	8
Platinum	81.3	2.5	16
Rhodium	12.8	1.3	9

[1] Mean of accepted data set means each calculated from six replicates on dry basis and also corrected for recovery. The certified values are traceable to the Internal System of Units (SI).
[2] The uncertainty is taken as the half-width of the 95 % confidence interval of the mean given in 1).

This certificate is valid for one year after purchase.

Sales date:

The minimum amount of sample to be used is 100 mg.

Indicative Values					
Element	Mass fraction based on dry mass				Number of accepted sets of data p
	Indicative value [1]		Uncertainty [2]		
Al	3.75	%	0.22	%	3
Ba	0.46	g/kg	0.04	g/kg	5
Cd	2.5	mg/kg	0.4	mg/kg	5
Co	29.8	mg/kg	1.6	mg/kg	5
Cr	440	mg/kg	18	mg/kg	6
Fe	3.29	%	0.20	%	6
Hf	2.2	mg/kg	0.7	mg/kg	6
Mn	1.28	g/kg	0.04	g/kg	5
Mo	40.0	mg/kg	0.6	mg/kg	4
Ni	171	mg/kg	3	mg/kg	4
Pb	866	mg/kg	16	mg/kg	5
Rb	75	mg/kg	5	mg/kg	6
Sb	28.2	mg/kg	2.3	mg/kg	5
Sr	254	mg/kg	19	mg/kg	6
Ti	2.58	g/kg	0.13	g/kg	4
Th	4.8	mg/kg	0.5	mg/kg	3
V	74.9	mg/kg	1.9	mg/kg	3
Y	12.5	mg/kg	1.8	mg/kg	4
Zn	1.66	g/kg	0.10	g/kg	6

[1] Mean value of p accepted data sets. The values are traceable to the Internal System of Units (SI).
[2] The uncertainty is taken as the standard deviation of the values used to calculate the indicative value.

Figure 3.20: BCR 723 Certificate of analysis; in the table above: elements with certified values; in the table below: elements with indicative values.

3. Method tests

The dissolution of the new RM was carried out three times, in order to verify the replicability.
The UBN standard was also added to the same dissolution batch and materials used in the preliminary tests of 2018 and 2019 were also prepared: the JP1, on which two recovery tests were carried out this time, and the chondritic meteorites 6A and 1B. Finally, a third meteoritic sample (an iron meteorite) from the same desert of Draa Valley (central Morocco) was also dissolved, with a slight modification of the procedure: decreased Hf quantity and increased AR quantity.

3.8 Installation / configuration TQ-ICP-MS

The prepared solutions were analysed with the new triple quadrupole spectrometer acquired by the Department of Physics and Earth Sciences of the University of Ferrara in 2020 (Fig. 3.21).

Figure 3.21: The new iCAP-TQ spectrometer installed at the Dep. of Physics and Earth Sc. of the University of Ferrara.

The Covid-19 pandemic delayed to late spring (2020) the setting up of the laboratory, which included the installation of new gas lines necessary for the collision/reaction cell. The new instrument was installed at the end of June and the first calibration tests on previously prepared solution could only start in August 2020.

3.8.1 Description of the instrument

The instrument is an iCAP-TQ spectrometer of Thermo Fisher Scientific.

Sample loading system. The spectrometer is equipped with a nebulisation chamber cooled by peltier effect and with integrated temperature control: this control system of the chamber and the produced aerosol, is able to provide excellent stability and minimise the formation of polyatomic ions (e.g., ArO^+, MO^+ etc.).
The nebuliser used for these measures is a Glass Expansion MicroMist 400 $\mu L/min^{-1}$ Quartz Concentric.
The four-way peristaltic pump allows the suction of the sample, the drainage of the spray chamber and the online introduction of the internal standard. This 4-channel and 12-roller pump is software-controlled, to guarantee more flexibility in the selection of the rotational velocity (set from 0.1 to 100 rpm), hence to allow the control of the sample's suction speed during the acquisition and in the passage from a sample to the next. The twelve rollers reduce pulsations and, compared to a standard peristaltic pump, they increase the precision and accuracy of the flow.

Ionisation source. The ions source consists of an inductively coupled plasma torch, which is powered by an RF generator, with a variable power of up to 1600 watts.
The high stability and efficiency solid state digital RF radio frequency generator is able to automatically and instantly adapt the oscillation frequency to the variation of the value of the impedance produced by changes in the matrix. The generator operates at a 27.12 MHz frequency, with a continuously variable power between 500 and 1600 W, in increments of 10 W capacity.
The quartz torch is quick-mount, with an XYZ alignment and adjustment system being entirely software-managed, automatic with a <0.01 mm alignment accuracy on the three XYZ axes and with graphical position display.
An integrated "PLASMA TV" video-camera allows remote monitoring of the plasma from a PC station, with display of the torch position and status of cones.

Interface. The delicate role of the interface is to deliver the ions produced in the ICP source at atmospheric pressure into the ionic focalisation region. The liquid cooling of the interface extends the lifetime of the cones and ensures that the contribution to the background noise produced by the orifice is negligible.
This revolutionary patented system of access to the interface eliminates the necessity to physically operate inside the instrument: in a single step, using a convenient handle at the front of the spectrometer, the interface moves towards the operator and this facilitates the routine maintenance and, above all, the direct inspection.
The interface consists of a solid block derived from pressed-fused steel on which the cones and the extraction lens (extraction cone) are installed.
The sampler and skimmer cones in the Nickel alloy patented Nicone™, have an orifice diameter of 1.1 mm and 0.5 mm, respectively. The skimmer cone can be equipped with a 3.5 mm insert (High Matrix tolerance), whose function is to minimise the deposit on the tip and the memory effects, or with a 2.8 mm insert (High sensitivity) to improve the analytical sensitivity.

Ionic focalisation system. The iCAP TQ ionic Optic, with three 90° deviations, is located at the head of the vacuum zone, immediately after the interface and before Q1; the 3D RAPID lens is the first SIMULTANEOUS 3D focusing system which deflects at 90° the ionic beam, with the aim to eliminate neutral particles and photons (Fig. 3.22).

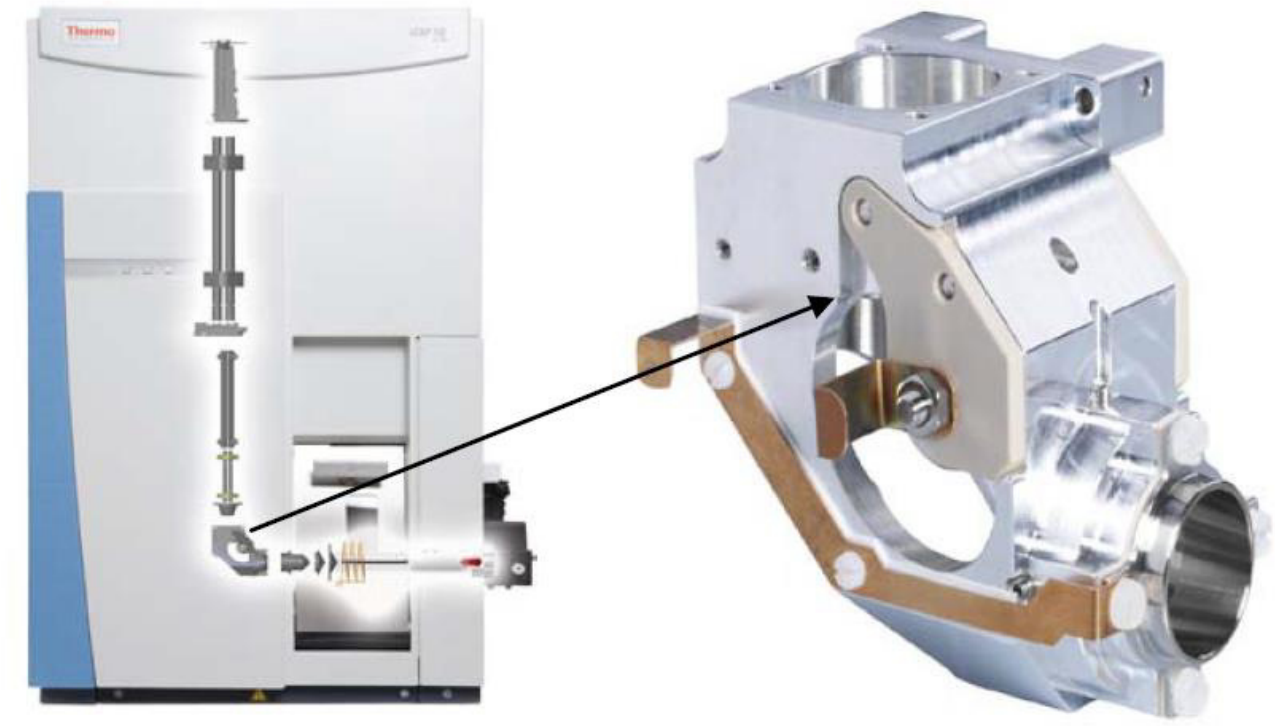

Thermo Fisher Scientific©

Figure 3.22: The 3D RAPID® lens.

The main function of the RapidLens is the 90° deflection of the ionic beam; the lens acts on the ionic beam immediately after the ionisation in the torch, before the Q1 – the Q2 (interference abatement cell) – the double 90° deflection (placed between Q2 and Q3) – the analyser quadrupole Q3 and the detector.
The 90° geometry allows an efficient elimination of all neutral particles and photons before they can travel along the following areas of the instrument and be deposited, which would compromise the analytical sensitivity and require periodic maintenance.
The neutral particles and photons are dispersed in the vacuum through an appropriate slit on the device positioned in correspondence to their straight trajectory. In this way the neutral particles cannot settle on any of the instrument's components, as in the case with a double 90° curvature system located in this area of the vacuum. Besides eliminating neutral particles and photons, the system focusses the ionic beam on the three spatial components (3D XYZ). Thanks to the introduction of a rotational electrical field, the system ensures both the simultaneous deflection of the entire ionic beam available at the first quadrupole Q1 and the maximum signal stability.
The RAPID 3D system, in fact, is able to apply the ideal focusing potential in function of the M\z (Mass\charge) and to completely cancel the need of maintenance.
The simultaneous ion transmission efficiency of the system on the whole mass range, is ensured by a rotational focussing device, located both at the inlet and outlet of the 90° deflection; it acts in such a way to simultaneously constrain all masses (low – mid – high) to traverse the 90° curvature with the same angular velocity (kinetic energy).
Thermo Fisher Scientific introduced a device with a 90° double curvature geometry (chicane) between Q2 and Q3, to direct the ions coming out from Q2 towards the analyser quadrupole Q3 with ideal trajectory and adequate kinetic energy.
This chicane device located in this area of the analyser, has the function to mainly eliminate possible neutral ions, generated by spurious collisions and/or reactions that may occur in the cell (Q2) between ions and used reaction gases; they can produce background noise and deposition on the Q3 rods.

Mass filtration system. The quadrupolar mass filter Q1, with a frequency of 4 MHz (twice as high as a traditional quadrupole) is able to select the passing analytes with an automatically variable resolution of at

least 1 amu, so as to accurately select the masses directed to the reaction/collision cell avoiding that potential interferents on the target mass may enter.
The second quadrupole (Q2) consists of the QCELL system (Fig. 3.23) which operates both in collision and reaction mode, in order to reduce the interference generated by the Plasma Ar and by the matrix, typical of the ICPMS technique. It consists of a square-section FLATPOLE quadrupole, placed after the first quadrupole Q1 at 90° from the plasma/interface zone. It is an excellent system which works both in reaction mode with reactive gases such as O_2, H_2, NH_3, CH_4, CH_3F, CO_2, N_2O, N_2, Xe or SF_6 and in collision mode with He and KED (the latter being a single quad mode).
The field lines of a square-rod quadrupole are equivalent, in terms of frequency, to the field lines generated by a hexapolar or octopolar device.

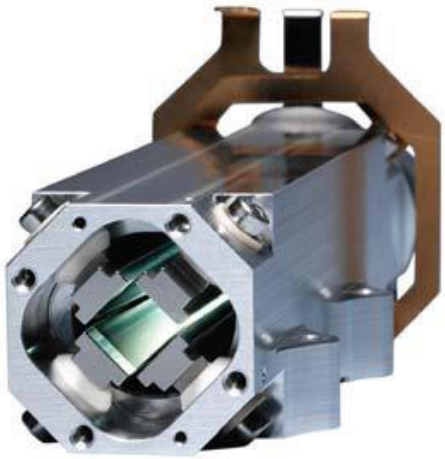

Thermo Fisher Scientific©

Figure 3.23: The square-section FLATPOLE quadrupole.

Finally, the analyser quadrupole (Q3) consists of a solid molybdenum bar quadrupole (size 230 mm * 12 mm), controlled by the solid-state system that generates a hyperbolic field.
The explorable mass range is between 2 and 290 amu and the scanning rate understood as Li-U-Li is greater than 90000 amu/sec. It is able to provide a minimum resolution of 0.2 amu, so as to expand the dynamic range of the analysis. The working frequency is 2 MHz.

Detector. The iCAP-TQ is provided with the ETP detector (a dynode electro-multiplier that operates simultaneously in analogue and digital mode), which allows to determine elementary concentrations in a range >11 orders of magnitude, with concentrations from < 5ppq to > 100ppm in a single analytical run within the same scan by monoisotopic species.
The instrument is entirely managed by the Q-TEGRA ISDN software, which operates in the last generation Windows system and allows the control of the instrument, analysis, data and report.

3.8.2 Site Preparation and Instrumental Configuration

The adopted instrumental configuration at the laboratory of the Department of Physics and Earth Sciences, required four new gas supply lines for the QCELL system (Fig. 3.24): three lines for reactive gases like O_2, H_2 and NH_3 to work in the reaction mode, and one line for He, to operate in collision and KED mode (in the single quadrupole mode). Unfortunately, only He and O_2 can be used at the moment, due to the bureaucracy linked to the authorisation for the use of inflammable gasses (ATEX Rules) which has not been resolved yet. (*ATEX (the name comes from the French words ATmosphères and EXplosibles) is an umbrella term which includes two directives of the European Union: - the 94/9/CE, which regulates equipment used in areas with explosion risk. This directive is addressed to manufacturers of equipment for use in areas with potentially explosive atmospheres and it requires the certification of these products; - the 99/92/CE for the health and safety of people working in explosive atmospheres and it applies to environments with explosion risk, where certified facilities and equipment are put into operation and it is therefore intended for the users.*

Figure 3.24: New gas supply lines for the QCELL system: on the left, the indoor second stage gas pressure regulators; on th right, the outdoor gas cabinet. Labels are in italian because the lab sites belong to an Italian institution.

3.8.3 Daily tuning of the instrument

The daily operating routine, before each measure series, follows a precise pattern: the plasma is turned on, followed by a brief warming up period, then the performance test, memorised in the software and which assesses the instrumental conditions, is carried out; sensitivity and stability are verified to be within the factory specification tollerance for a series of elements (Li, Co, In and U), which represent the entire spectrum of masses. Mass calibration and resolution are also tested. In addition to this, the background signal is verified to be below 1 and 2 cps for low (4.5 u.m.a.) and high (220.7 u.m.a.) masses, respectively. Finally, the ratios between Ce double and single charges ($^{140}Ce^{++}/^{140}Ce^{+}$) and between oxide and corresponding element (CeO^{+}/Ce^{+}) are checked to be below 0.04 and 0.02, respectively.

When the instrument does not meet the performance test and after each ordinary maintenance operation (cleaning or replacement of the cones, cleaning of the extraction lens, cleaning or replacement of the glassware and of the nebuliser, replacement of peristaltic pump tubings etc.), the instrumental tuning is carried out. It consists in the optimisation of the torch position (in the three dimensions of space) relative to the sampling cone orifice, in the regulation of the various flows of Ar (cooling, auxiliary and nebulisation) and other gases in the cell and in the setting of the voltage applied to the various lenses of the ion focusing system.

This operation is carried out automatically through various operating sequences preset in the software and with the use of a specific multielement solution. Auto-tuning sequence reports (setting of “interface” parameters without the use of gas in the cell and subsequent "advanced" optimisation of parameters for the use of the instrument in SQ-KED mode) are reported in the Appendices I and II. A performance test report is also described: in addition to the final result (passing or not passing the test), the used setting is also summarised (Fig. 3.25).

Tune Settings

Parameter	Gas check	Interface check
Interface	High Sensitivity	High Sensitivity
SQ/TQ	SQ	SQ
Reaction Gas	Kinetic Energy Discrimination	No reaction gas
Additional Gas Flow 1	0	0
Additional Gas Flow 2	0	0
Angular Deflection	-250	-250
Auxilliary Flow	0.8000	0.8000
Cool Flow	14	14
CR Bias	-21	-2
CR Entry Lens	-162	-162
CR Exit Lens	-40	-160
CR1 Flow	5.300	0.000
CR2 Flow	0.0000	0.0000
CR3 Flow	0.000	0.000
CR4 Flow	0.0000	0.0000
D1 Lens	-350	-200
D2 Lens	-159	-84.6
Deflection Entry Lens	-30	-30
Extraction Lens 1 Negative	0	0
Extraction Lens 1 Polarity	0	0
Extraction Lens 1 Positive	0	0
Extraction Lens 2	-127	-127
Focus Lens	-8	19.5
Nebulizer Flow	1.07	1.07
Peristaltic Pump Speed	40.0	40.0
Plasma Power	1,550	1,550
Pole Bias	-18	-1
Pole Bias Q1	1.44	1.44
Q1 Entry Lens	-75	-75
Q1 Focus Lens	-0.44	-0.44
Quad Entry Lens	-54	-28
Sampling Depth	5.00	5.00
Spray Chamber Temperature	2.7	2.7
Torch Horizontal Position	-.43	-.43
Torch Vertical Position	-0.27	-0.27

Figure 3.25: Extract of a QTEGRA performance report with the tune setting (complete report is in Appendix III).

3.8.4 Calibrations

Five multielement standards at variable concentrations between 1 and 500 ppt were prepared for analyses by external calibration, starting from the monoelement solutions reported in Table 3.15.

A solution for Re was prepared at 10 ppm by diluting 1ml of the original solution in a 100 ml flask. Afterwards, for the preparation of the calibration solution, a first multielement stock solution at 10 ppb concentration was prepared by diluting 1000 times (0.1 ml in a 100 ml flask) the original solutions (with the exception of the Re for which the above-mentioned solution was used). Finally, the calibration set was prepared with successive dilutions in a range from 1 to 500 ppt, as reported in Table 3.16.

Mono Element Aqueos RM	Supplier	Conc. ppm (µg/mL)	Matrix
Au	**LabKings**	**10**	**2% HCl**
Ir	**LabKings**	**10**	**10% HCl**
Os	**LabKings**	**10**	**10% HCl**
Re	**Merck**	**1000**	**5% HNO_3**
Rh	**LabKings**	**10**	**2% HCl**
Ru	**LabKings**	**10**	**2% HCl**
Pd	**LabKings**	**10**	**5% HCl**
Pt	**LabKings**	**10**	**5% HCl**

Table 3.15: Monoelement ICPMS standard solution used to prepare calibration solutions.

STD label	Dilution	Stock solution (mix at 10 ppb)	Flask Volume
1 ppt	**1 / 10000**	**0.05 ml**	**500 ml**
4 ppt	**1 / 2500**	**0.1 ml**	**250 ml**
10 ppt	**1 / 1000**	**0.1 ml**	**100 ml**
100 ppt	**1 / 100**	**1 ml**	**100 ml**
500 ppt	**1 / 20**	**5 ml**	**100 ml**

Table 3.16: Multielement standard solutions prepared for external calibration.

An In and Bi solution at 10 ppb was used as internal standardisation and mixed "online" with samples, blanks and calibration solutions. The ratio between the volume of the sample solution and the volume of the internal standard solution that reaches the nebuliser at a determined rotational velocity of the pump, is a function of the internal diameter of the tubing used for the relative suctions. For these measures, were used tubes with internal diameter (i.d.) of 0.51 mm for the sample solution (flow of about 9.5 µL/min for RPM) and 0.27 mm for the internal standard solution (flow of about 2.7 µL/min for RPM); in this way the ratio between the volume of the sample solution and the volume of the standard solution that are sucked is about 4:1. To select the isotope and the acquisition mode for each element, the instructions of the database of the parent company were followed (Thermo Fisher Scientific, 2020).

Gold is of primary importance for the identification of contamination in ores, metals and alloys; the interference of $^{181}Ta^{16}O+$ can, in fact, affect the ^{197}Au isotope. Hydride formation and peak tailing of the 196 and 198 isotopes of platinum, for example, may affect the determination of gold in platinum-bearing materials; this problem could be limited by using O_2 as a reaction gas in the collision cell, together with the application of the high mass resolution mode in the quadrupole. When NH_3 is used as a reaction gas, identical composition cluster ions can form, like for platinum (Table 3.17).

Element	Gold	
Available isotopes	^{197}Au (100%)	
Ionization Potential	9.23 eV	
Q1 resolution	Intelligent Mass Selection (iMS)	
Preferred analysis modes	Reaction Finder Default	Alternatives
	SQ-KED	TQ-O_2 (^{197}Au) or TQ-NH_3 (^{231}[^{197}Au(NH_3)$_2$])

Table 3.17: Analysis possible modes for Au determination. From "A comprehensive guide to method development using triple quadrupole ICP-MS" © 2020 Thermo Fisher Scientific.

The most abundant isotope of iridium is ^{193}Ir and it can create different problems during analyses: it can be affected by the interference of oxide or hydroxide ions of lutetium and hafnium or it can cause an oxide interference itself on the isotope 209 of Bi. In this case, the interference can be controlled by using O_2 in the reaction cell, as Ir has a limited reactivity (Table 3.18).

Element	Iridium	
Available isotopes	^{191}Ir (37.30%), ^{193}**Ir (62.30%)**	
Ionization Potential	9.12 eV	
Q1 resolution	Intelligent Mass Selection (iMS)	
Preferred analysis modes	Reaction Finder Default	Alternatives
	SQ-KED	TQ-O_2 (^{193}Ir)

Table 3.18: Analysis possible modes for Ir determination. From "A comprehensive guide to method development using triple quadrupole ICP-MS" © 2020 Thermo Fisher Scientific.

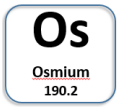

Among the various stable isotopes of osmium, ^{189}Os is the one mostly used for analysis. Os presents many problems during sample preparation and analysis: it is highly volatile in the oxidised form, therefore can be lost during microwave digestion; it can also be lost when opening the digestion vessel or even in the spray chamber, in which case it can lead to an overestimation. Moreover, Os is affected by interferences (Table 3.19).

Element	Osmium	
Available isotopes	^{184}Os (0.02%), ^{186}Os (1.58%), ^{187}Os (1.60%), ^{188}Os (13.30%), ^{189}**Os (16.10%),** ^{190}Os (26.40%), ^{192}Os (41.00%)	
Ionization Potential	8.71 eV	
Q1 resolution	Intelligent Mass Selection (iMS)	
Preferred analysis modes	Reaction Finder Default	Alternatives
	SQ-KED	TQ-O_2 (^{190}Os), TQ-NH_3 (^{204}[^{189}Os(^{14}N^{1}H)])

Table 3.19: Analysis possible modes for Os determination. From "A comprehensive guide to method development using triple quadrupole ICP-MS" © 2020 Thermo Fisher Scientific.

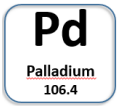

Palladium is unreactive towards O_2 therefore it can be analysed interference free on mass. ^{105}Pd is used because of the absence of isobaric overlap; High concentrations of ^{89}Y, sometimes used as internal

standard, may cause false positive results or elevated backgrounds through the formation of $^{89}Y^{16}O^{+}$ (Table 3.20).

Element	Palladium	
Available isotopes	^{102}Pd (1.02%), ^{104}Pd (11.14%), **^{105}Pd (22.33%),** ^{106}Pd (27.33%), ^{108}Pd (26.46%), ^{110}Pd (11.72%)	
Ionization Potential	8.34 eV	
Q1 resolution	Intelligent Mass Selection (iMS)	
Preferred analysis modes	Reaction Finder Default	Alternatives
	SQ-KED	TQ-O_2 (^{105}Pd)

Table 3.20: Analysis possible modes for Pd determination. From "A comprehensive guide to method development using triple quadrupole ICP-MS" © 2020 Thermo Fisher Scientific.

Both most abundant isotopes of platinum, (^{194}Pt 32.90% relative abundance and ^{195}Pt 33.80%) may be interfered from hafnium oxides and hydroxides. Pt can be analysed on mass using O_2 cell gas or, more efficiently, in shift mass mode using NH_3 as a reaction gas: in this case Pt undergoes different reactions forming ions like $^{229}[^{195}Pt(NH_3)^2]^+$ (Table 3.21).

Element	Platinum	
Available isotopes	^{190}Pt (0.01%), ^{192}Pt (0.79%), ^{194}Pt (32.90%), **^{195}Pt (33.80%),** ^{196}Pt (25.30%), ^{198}Pt (7.20%)	
Ionization Potential	9.02 eV	
Q1 resolution	Intelligent Mass Selection (iMS)	
Preferred analysis modes	Reaction Finder Default	Alternatives
	SQ-KED	TQ-O_2 (^{195}Pt) or TQ-NH_3 ($^{229}[^{195}Pt(NH_3)_2]$)

Table 3.21: Analysis possible modes for Pt determination. From "A comprehensive guide to method development using triple quadrupole ICP-MS" © 2020 Thermo Fisher Scientific.

Re is a very rare element and the 185 isotope can be used as an internal standard, because it is not affected by isobaric overlaps (Table 3.22).

Element	Rhenium	
Available isotopes	**^{185}Re (37.40%),** ^{187}Re (62.60%)	
Ionization Potential	7.88 eV	
Q1 resolution	Intelligent Mass Selection (iMS)	
Preferred analysis modes	Reaction Finder Default	Alternatives
	SQ-KED	TQ-O_2 (^{185}Re), TQ-NH_3 (^{185}Re)

Table 3.22: Analysis possible modes for Re determination. From "A comprehensive guide to method development using triple quadrupole ICP-MS" © 2020 Thermo Fisher Scientific Inc.

Rhodium can be affected by different interferences such as the copper-based, which can be avoided by using KED, or the lead-induced interference, which, in turn, can be controlled by using O_2 as a

reactive gas and by the on-mass mode. Rhodium is used as internal standard and higher concentrations of lead could be erroneously interpreted as a matrix effect (Table 3.23).

Element	Rhodium	
Available isotopes	^{103}**Rh (100%)**	
Ionization Potential	7.46 eV	
Q1 resolution	Intelligent Mass Selection (iMS)	
Preferred analysis modes	Reaction Finder Default	Alternatives
	SQ-KED	TQ-O_2 (^{103}Rh)

Table 3.23: Analysis possible modes for Rh determination. From "A comprehensive guide to method development using triple quadrupole ICP-MS" © 2020 Thermo Fisher Scientific Inc.

The isotope ^{101}Ru is frequently used for the determination of this element, because is very rarely affected by interferences. Ruthenium does not react to O_2, but only slightly to NH_3, in which case it can form a cluster ion by the addition of one molecule of NH_3 (Table 3.24).

Element	Ruthenium	
Available isotopes	^{96}Ru (5.52%), ^{98}Ru (1.88%), ^{99}Ru (12.70%), ^{100}Ru (12.60%), ^{101}**Ru (17.00%),** ^{102}Ru (31.60%), ^{104}Ru (18.70%)	
Ionization Potential	7.36 eV	
Q1 resolution	Intelligent Mass Selection (iMS)	
Preferred analysis modes	Reaction Finder Default	Alternatives
	SQ-KED	SQ-N/A

Table 3.24: Analysis possible modes for Ru determination. From "A comprehensive guide to method development using triple quadrupole ICP-MS" © 2020 Thermo Fisher Scientific.

As it was not possible to use ammonia, all the elements were tested in the SQ-KED and TQ-O2 "on mass" double mode. In the calibration curves report, the software (Fig. 3.28) provides the IDL (Instrumental Detection Limit), the BEC (Background Equivalent Concentration) and the R^2 (Determination Coefficient) values. The Limit of Detection (LOD) or Instrumental Detection Limit (IDL) of an isotope is defined as a multiple of the standard deviation of blank analysis (SD_{Blank}) associated to a calibration that is converted into a concentration value using the slope of the calibration function (a1). For Q-TEGRA the following formula specifies the LOD:

$$LOD = \left(\frac{3 \times SD_{Blank}}{a_1}\right)$$

The Background Equivalent Concentration (BEC) for the given isotope is defined based on its current calibration curve f(x) with

$$BEC = -f^{-1}(0)$$

The determination coefficient R^2 was greater than 0.995 for all the lines.
The IDL resulted to be ≤ 1 ppt for almost all the elements, apart from Pd (6 and 20 ppt in both modes) and Pt (2 ppt in the SQ-KED mode).
The BEC is < 1 ppt for Au, Os, Re and Ru, between 1 and 2 ppt for Rh and about 3 ppt for Pt. Only Pd showed high BEC in both the acquisition modes (6 and 45 ppt) (Fig. 3.26).

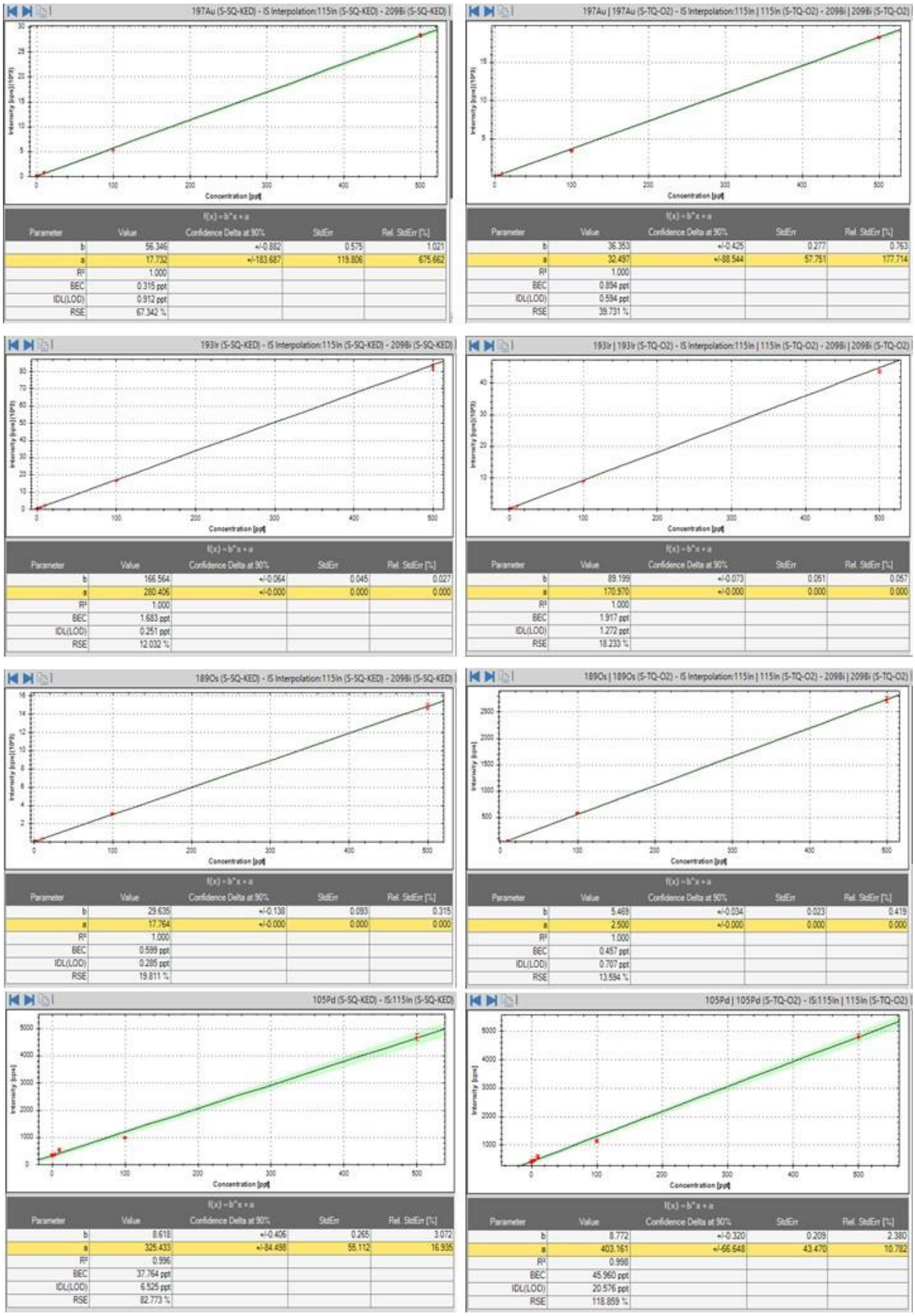

Figure 3.26: Calibration Curve report.

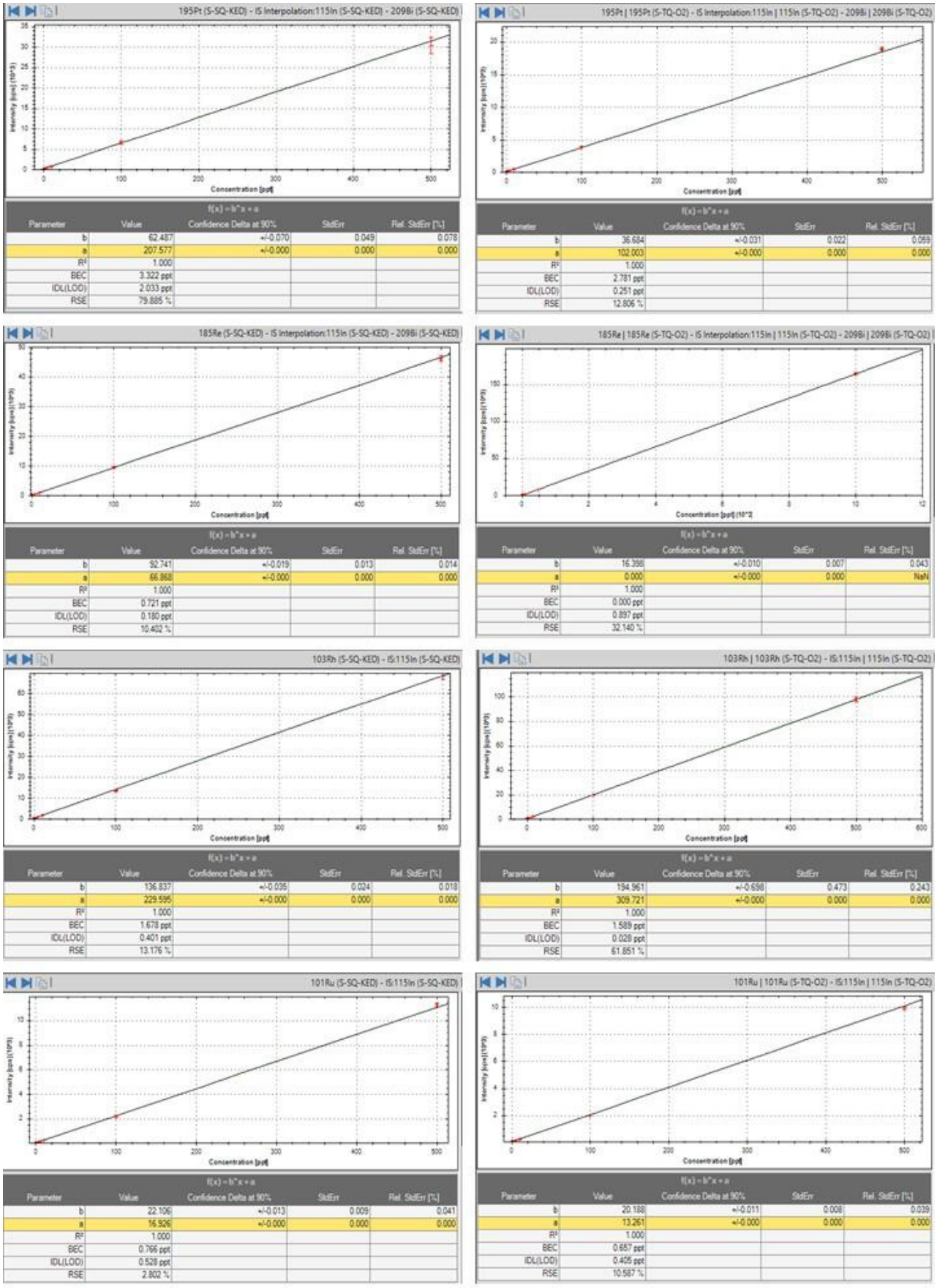

Fig 3.26 continued.

3. Method tests

Obviously, the good linearity of the response and the relatively low IDL obtained for almost all the elements in the calibrations with simple pure solutions, is a necessary condition, but not enough, to ensure good analyses in real complex matrix solutions as in this study. For this reason, for the analysis of the samples collected in via Bacchelli in August 2019, a more laborious calibration was carried out using the standard addition method (standard addition calibration).
Four aliquots of the same volume (5 ml) were taken from each sample solution: a spike of 0.1 ml of a multielement solution at increasing concentration of the analytes was added to each aliquot. As a first attempt, having no preliminary information on the expected concentrations, multielement solutions were prepared at the same concentration for all the elements to be determined (Table 3.25).

Spike name	PGEs + Re + Au Conc. (ppb)
Std 0	0
Std 1	0.5
Std 2	5
Std 3	10

Table 3.25: Multielement standard solution used for spike standard addition calibration.

This calibration technique provides accurate results also for difficult matrices (with high TDS). Being made of 98% of sample and varying (in the spike concentration) only for the 2%, the matrix is the same for all the calibration solutions.
In standard addition, the analyte concentration in the sample solution is obtained by reading the intercept of the calibration line with the negative half-axis of the abscissa (Fig. 3.27).

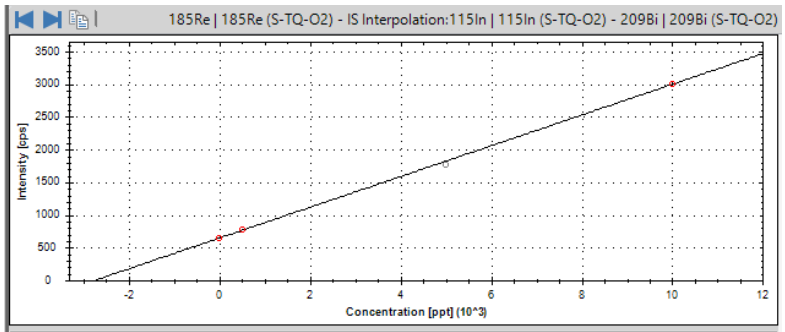

Figure 3.27: Curve Calibration in Standard Addition: example of Re.

f(x) = b*x + a

for f(x) = 0

is obtained **x = -a/b**

In the above example (Re determination in sample BS4b)

Re conc. = - x = - 651.8 / 0.235 = 2770 ppt

For a good accuracy of the results, it is necessary that the concentration in the additions is of the same order of magnitude as the concentration in the sample; cases like those in Fig. 3.28 are not acceptable because small variations in the intensity's reading in the standard, lead to large errors in the calculation of the analyte concentration.

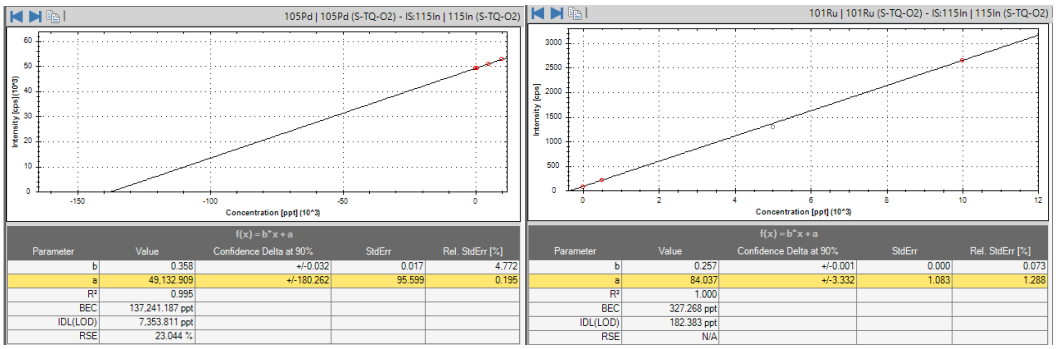

Figure 3.28: Examples of calibration with too concentrated (on the right) or too diluted spikes (on the left).

For this reason, a second calibration attempt was carried out with multielement spike solutions at different concentrations (Table 3.26).

Spike name	PGEs + Re + Au Conc. (ppb)
Std 0	0
Std A	Os, Re, Rh and Ru 0.5 ppb; Ir and Pd 1.0 ppb; Au and Pt 5 ppb
Std B	Os, Re, Rh and Ru 1.0 ppb; Ir and Pd 5.0 ppb; Au and Pt 10 ppb
Std C	Os, Re, Rh and Ru 5.0 ppb; Ir and Pd 10.0 ppb; Au and Pt 50 ppb

Table 3.26: New stock of spikes with elements in different concentration.

3.9 Experimental verification of the contribution of isobaric interferences

The standard addition calibration compensates for any signal suppression effect due to the difference between calibration and sample solutions, but it does not eliminate the problem of isobaric interference (substantial in the determination of PGEs).
Ammonia, which is considered the most effective cell reaction gas (Sugiyama and Shikamori, 2015; Desprez et al., 2016; Kutscher et al., 2019), could not be used; therefore, it was decided to verify the actual magnitude of the potential isobaric interferences on the isotopes of the analytes used, in the triple quadrupole configuration with oxygen as a cell reaction gas.
Due to the low reactivity of these noble metals, the on mass mode was chosen: the third quadrupole Q3 was set to filter the isotope's mass, with the expectation that any interfering ion would react quantitatively with oxygen in the Q2 and would then be eliminated by Q3. Several standard solutions containing the interfering elements at different concentrations but without the elements under study (PGEs, Re and Au) were prepared for this test. The resulting signals at the masses of the elements potentially affected by the interference were compared with the concentration of the interfering ones.
Based on literature data (Desprez et al., 2016) and on previous test results, the elements in the studied matrices affected by isobaric interferences were identified to be Pd, Pt and Au. The focus was therefore on verifying the actual impact of Sr, Y, Cu and Zn compounds at the mass 105 of Pd and of the Hf, Ta and Gd compounds at the masses 195 of Pt and 197 of Au (Table 3.27).

isotope	**relative abundance**	**potential interferences**			
		MO	**MOH**	**MAr**	**MCl**
^{105}Pd	**22.33**	$^{89}Y^{16}O^+$ $^{88}Sr^{17}O^+$ $^{87}Sr^{18}O$	$^{88}Sr^{16}O^1H^+$	$^{65}Cu^{40}Ar^+$	$^{68}Zn^{37}Cl^+$ $^{70}Zn^{35}Cl^+$
^{195}Pt	**33.83**	$^{179}Hf^{16}O^+$ $^{178}Hf^{17}O^+$ $^{177}Hf^{18}O^+$			
^{197}Au	**100**	$^{179}Hf^{16}O^+$ $^{178}Hf^{17}O^+$ $^{177}Hf^{18}O^+$	$^{180}Hf^{16}O^1H^+$ $^{179}Hf^{17}O^1H^+$ $^{178}Hf^{18}O^1H^+$	$^{157}Gd^{40}Ar^+$	

Table 3.27: isobaric polyatomic interferences on Pd, Pt and Au.

3. Method tests

The concentrations of the tested interfering solutions (for Hf and Ta, a multielement solution, already available at the laboratory and called HFSE, was initially used; it contained Nb, Zr, Hf and Ta. Successively, monoelement standards were also used for these elements) are summarised in Table 3.28. The concentration of the tested solutions was chosen in view of the mean concentration ranges in the matrices under study, taking into account the dilutions (100 to 1000) normally applied in the preparation of the samples. For Hf and Ta, in the second test, a higher range of concentrations was investigated using monoelement standard solutions.

Standard	**Sol 1**	**Sol 2**	**Sol 3**
	conc. (ppb)	**conc. (ppb)**	**conc. (ppb)**
I test			
HFSE (Nb, Zr, Hf and Ta)	**0.1**	**1**	**10**
Gd	**0.25**	**2.5**	**25**
Cu	**100**	**1000**	**10000**
Sr	**200**	**2000**	**20000**
Y	**10**	**100**	**1000**
Zn	**100**	**1000**	**10000**
II test			
Hf	**4**	**20**	**100**
Ta	**4**	**20**	**100**

Table 3.28 multielement (HFSE) and monoelement standard solutions used in experimental verification of isobaric interferences.

3.9.1 Interferences on palladium

It was clear from the first tests that the interference of the YO^+ and $SrOH^+$ ions on the 105 isotope of Pd is strong. The correlation between the apparent concentration of Pd in ppt (determined in external calibration both in single and triple quadrupole using In as internal standard for checking and correcting instrumental drift) and the concentration in ppb of Sr and Y is evident for both interfering elements: $R^2 = 1$ in TQ and > di 0.999 in SQ (Fig. 3.29).

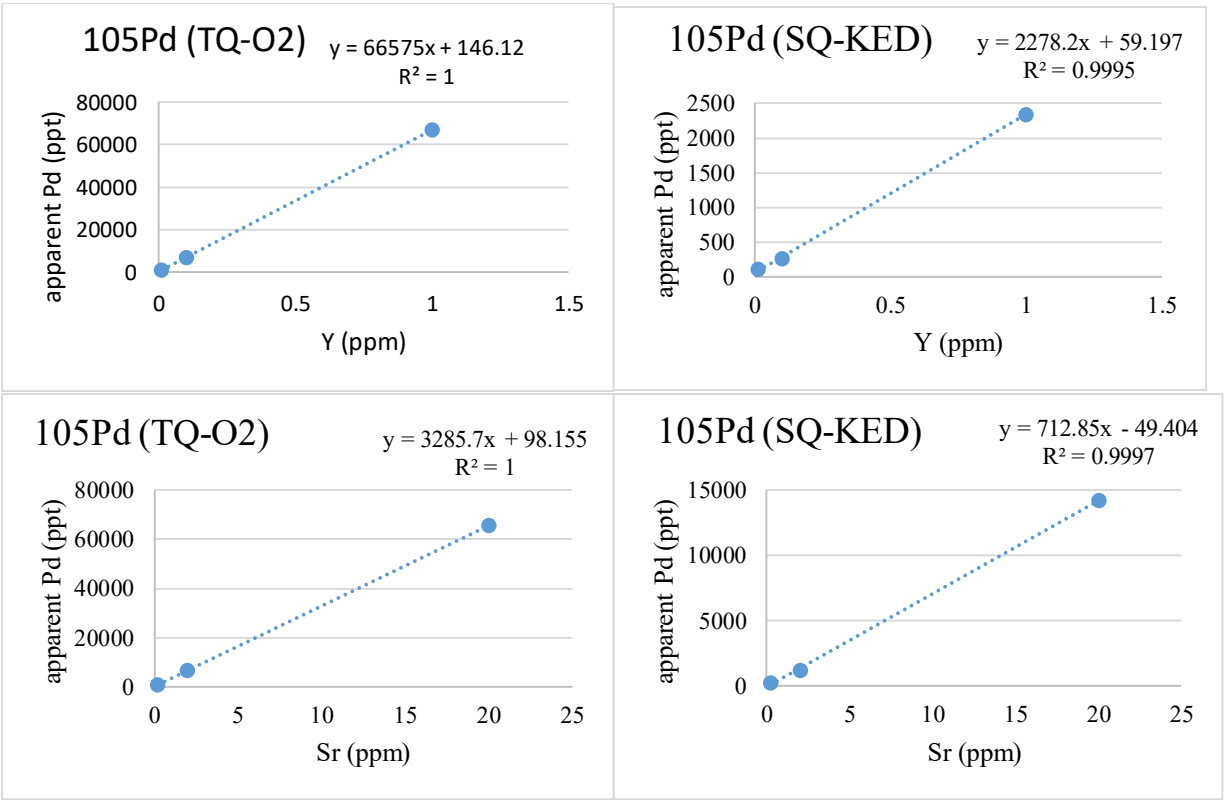

Figure 3.29: Contribution of Y (above) and Sr (below) at the ^{105}Pd mass. On the left: graph obtained with oxygen in TQ mode; on the right: graph obtained using helium in SQ-KED mode.

Of quite different impact is the interference of Cu (CuAr) and Zn (ZnCl): the apparent ppt of Pd due to the presence of these two metals, are of at least an order of magnitude lower than for Y and Sr, and, above all, they do not show any correlation to their concentration.
From the comparison of the results obtained in the two modes (SQ-KED and TQ-O_2), it appears evident that the triple quadrupole, with the use of oxygen in the cell, does not improve the control of the interferences on Pd; it will be necessary to test other gases (ammonia?) as a reaction gas.

3.9.2 Interferences on platinum

As in the case of Y and Sr on Pd, the correlation between the concentration of the HFSE (High Field Strength Element) standard and the apparent concentration of Pt is evident. Unlike Pd, however, in this case between the SQ- KED and the TQ measurements (left and right diagrams, fig. 3.30), the apparent Pt concentrations has been lowered by a factor 2 showing the efficiency of the TQ system to separate Pt from its interferences.

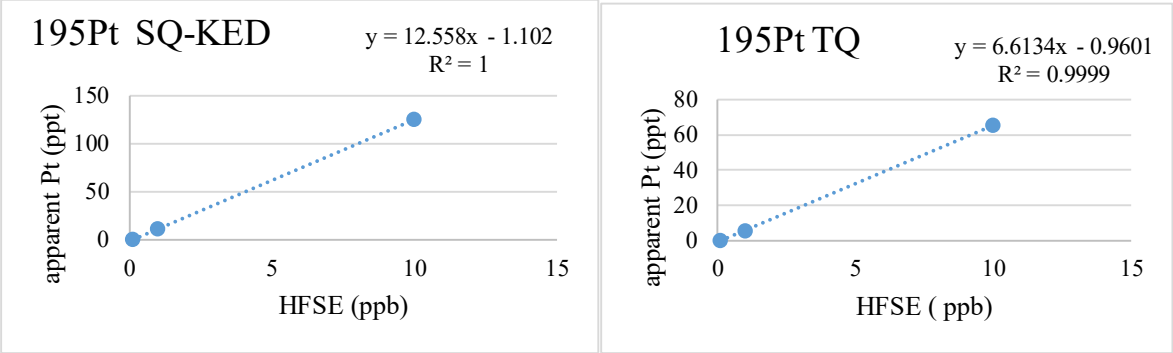

Figure 3.30: Contribution of the HFSE solution, at the 195Pt mass. On the left: graph obtained with helium in SQ-KED mode; on the right: graph obtained using oxygen in TQ mode.

For this reason, the second test with Hf monoelement solutions was carried out in TQ mode only (Fig. 3.31).

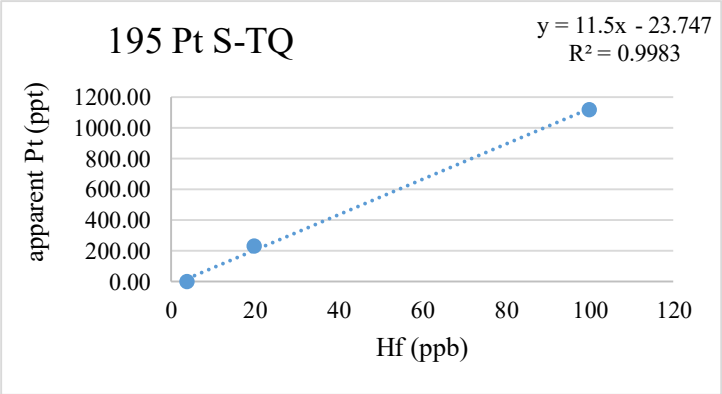

Figure 3.31: Contribution of hafnium at the ^{195}Pt mass in TQ-O_2 mode.

As for Cu and Zn on Pd, the Gd (GdAr) interference at the 195 mass of Pt, does not appear to be correlated to its concentration and the signal intensity produced at the 195 mass is negligible compared to the Hf one.

3.9.3 Interferences on gold

In the case of Au, the correlation between the concentration of the HFSE standard and the apparent ppt of Au is net, as already evidenced in the first test performed in the double mode (SQ and TQ) (Fig. 3.32).

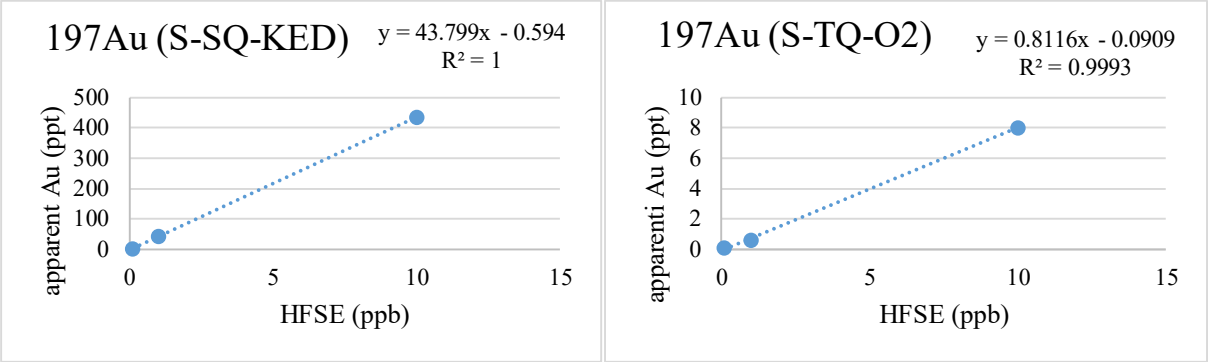

Figure 3.32: Contribution of the HFSE solution, at the 197Au mass. On the left: graph obtained with helium in SQ-KED mode; on the right: graph obtained using oxygen in TQ mode.

In this case it is clear that, with the acquisition in Triple Quadrupole mode, it is possible to reduce the interfering signal by about 50 times.
The second test was carried out with Hf and Ta monoelement solutions and in the TQ mode only; it quantified the contribution of the single ions (TaO^+ and $HfOH^+$) at the 197 mass of Au. The main contribution is clearly from the Ta oxide, which makes negligible the signal due to Hf (two orders of magnitude lower) (Fig. 3.33).

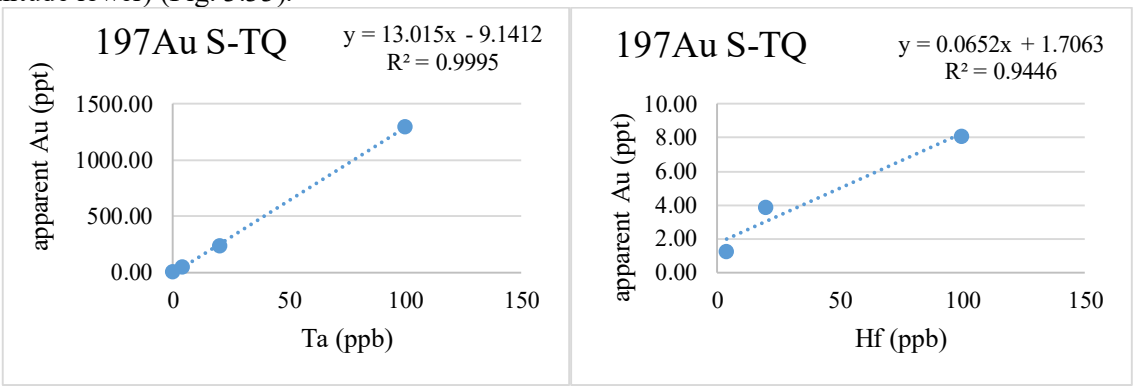

Figure 3.33: Contribution of the Ta (on the left) and Hf (on the right), at the 197Au mass.

As for Pt, there was no correlation between the concentration of Gd and the apparent concentration of Au; the signal recorded by the solution at 100 ppb (difficult to find in nature) would be equivalent to a concentration of just a couple of ppt of Au.

3.9.4 Mathematical correction

Once it was experimentally verified that in the present configuration (oxygen as the only cell reaction gas option) some spectral interferences cannot becompletely eliminated, a mathematical approach to the problem was considered. Several authors have recently proved that the use of ammonia in the cell combined to the shift mass mode is the only set up that allows an effective control on the interferences. (Sugiyama and Shikamori, 2015; Desprez et al., 2016; Kutscher et al., 2019). The installation of gas lines for the use of such a toxic and flammable gas, however, would create health and safety issues in the laboratory, which are not always manageable. For this reason, a "traditional" mathematical correction of the interferences was considered, which was used in the past before the advent of the new triple quadrupole spectrometers. This approach was used in several laboratories because it is quicker and simpler, when compared to the chemical separation/pre-concentration processes (Simitchiev et al., 2008 and reference therein).
In the case when an analyte isotope is interfered from several sources, the effect of each interferent must be accounted for in an additive scheme.
Such an approach, however, raises issues that have to be taken into account:
- from a purely practical point of view: additional time and reagents are needed to establish the relation between each interferent and its spectral effect over the analyte signal(s);
- from the point of view of result accuracy, it must be considered that the uncertainty of the corrected analyte signal is increased because the number of variables in the model equation is enhanced. It follows that the

part of the measured signal generated from the analyte could be very small in comparison to the fraction produced from the interferents, which makes the correction unreliable.
In this respect, Simitchiev et al, 2008 set a top value of a 20% contribution of the interfering signal to the mass of the element/compound affected by the interference, which means that the corrected signal is at least 5 times higher than its combined uncertainty.
In the present study, limited to the elements (Pd, Pt and Au), whose interferences were experimentally verified, the so called 'standard addition of the interfering element' was tested. This would allow the correction of the matrix dependant interference, by spiking an interferent to the sample solution. The signal which would result from the amount of the interfering element/compound added, can be calculated and used in order to correct the Intensity measured on the mass of the analyte:

$I_{AC} = I_{AU} - C_i * (I_{AS} - I_{AU}) / C_{iA}$
where:
I_{AC} = Intensity (Corrected) of the signal measured on the mass of the Analyte.
I_{AS} = Intensity on the mass of the Analyte measured in the Spiked solution.
I_{AU} = Intensity on the mass of the Analyte measured in the Unspiked solution.
C_i = Initial interferent concentration in the sample solution.
C_{iA} = Interferent concentration corresponding to the amount of interferent Added to the sample solution.

The measure of the enhancement of the analyte signal due to the concentration of the interfering element/compound corresponding to any single increment, can be defined as the factor of interference F_i

$F_i = (I_{AS} - I_{AU}) / C_{iA}$

By spiking sample aliquots with gradient interfering element/compound concentrations, F_i could be more precisely measured.
In such a way, the function between the generated interfering signal and the interferent concentration can be fitted to a linear mathematical model:

$I_{total} = F_i\text{-slope} * C_i + I_{AC}$
where: (F_i-slope) represents the factor of interference
I_{total} is the total signal measured on the mass of the analyte.

Unfortunately, the software does not include this type of correction, therefore it was needed to export the intensities (already corrected for the instrumental drift by the In and Bi internal standardisation) and elaborate in an excel spreadsheet to calculate the "F_i" correction factors.
The test was carried out on a subset of samples recently prepared: one solution of the three replicates of the BCR 723 standard (road dust); two solutions of the peridotitic standard JP1 (one original and one with the addition of a PGE, Au and Re spike) and the solutions of the three meteorites (two chondrites and one metallic).
For the correction of Pd, the solutions were prepared in this way: 1 ml of monoelement standard solution with progressively increasing concentration was added to four 2 ml aliquots of solution of each of the six samples mentioned above (Table 3.29).

Label	Sample Solution	Water (Blk)	Sr 20 ppb	Sr 100 ppb	Sr 500 ppb	Y 4 ppb	Y 20 ppb	Y 100 ppb
JP1	2 ml	1 ml						
JP1+Sr1	2 ml		1 ml					
JP1+Sr2	2 ml			1 ml				
JP1+Sr3	2 ml				1 ml			
JP1+Y1	2 ml					1 ml		
JP1+Y2	2 ml						1 ml	
JP1+Y3	2 ml							1 ml

Table 3.29: stock solution prepared for "standard addition of the interfering element" (determination of Pd in JP1).

For the correction of Pt and Au for each of the 6 tested materials, Ta and Hf monoelement solutions were added to the various aliquots of each sample (Table 3.30).

3. Method tests

Label	Sample Solution	Water (Blk)	Hf 4 ppb	Hf 20 ppb	Hf 100 ppb	Ta 4 ppb	Ta 20 ppb	Ta 100 ppb
723c	4 ml	1 ml						
723c+4Hf	4 ml		1 ml					
723c+20Hf	4 ml			1 ml				
723c+100Hf	4 ml				1 ml			
723c+4Ta	4 ml					1 ml		
723c+20Ta	4 ml						1 ml	
723c+100Ta	4 ml							1 ml

Table 3.30: stock solutions prepared for "standard addition of the interfering element" (determination of Pt and Au in BCR 723c).

Example: application of the correction algorithm using the standard addition method of the interferent, in the analysis of the JP1 standard for Au and Pt determination.
The sample was prepared in duplicate: in the replicate, a spike (0.05 ml of multi-elemental standard of PGEs, Re and Au (Table 3.31) was added before the acid attack, to verify the recovery and validate the method. The sample with the added spike was labelled with an asterisk (JP1*).

Element	Spike conc.	Spike Vol	Flask Vol	Added concentration in solution
	ppb	ml	ml	ppt
Au	50	0.05	100	25
Ir	10			5
Os	5			2.5
Pd	10			5
Pt	50			25
Re	5			2.5
Rh	5			2.5
Ru	5			2.5

*Table 3.31: Concentration of analytes added in the replicate JP1 *.*

Both the solutions (JP1 and JP1*) were suitably prepared as shown in Table 3.31 for the acquisition by the interferents' addition method. The acquisition sequence included:
- measurement of the six calibration PGE solutions (calibration range: 1ppt – 10 ppb) at increasing concentrations for the (external) calibration of PGEs;
- measurement of three pure Hf solutions at concentrations of 4, 20 and 100 ppb (for the determination of the Hf concentration in external calibration);
- measurement of three pure Ta solutions at concentrations of 4, 20 and 100 ppb (for the determination of the Ta concentration in external calibration);
- measurement of the solution set with interferent spikes added (JP1+0, JP1+4Hf, JP1+20Hf, JP1+100Hf, JP1 +4Ta, JP1 +20Ta, JP1 + 100 Ta and similarly for the JP1*);
- between each solution, the auto-sampling probe was washed with a 2% solution of HNO_3.
- after every homogeneous group of solutions, the measurement was repeated on a test tube filled with milliQ water: in this way it was possible to verify if, during the analysis, the background signal significantly increased due to a memory effect of highly concentration solutions.
After the acquisition, the measured intensities (cps) were corrected for the instrumental drift according to the signal recorded by the mass of the (Bi) internal standard, which was exported to an excel spreadsheet.
The calculation algorithm includes the following steps:

a) Elaboration of Hf and Ta calibration curve using the graph concentration vs intensity and the determination of their concentration in each solution (Fig. 3.34).

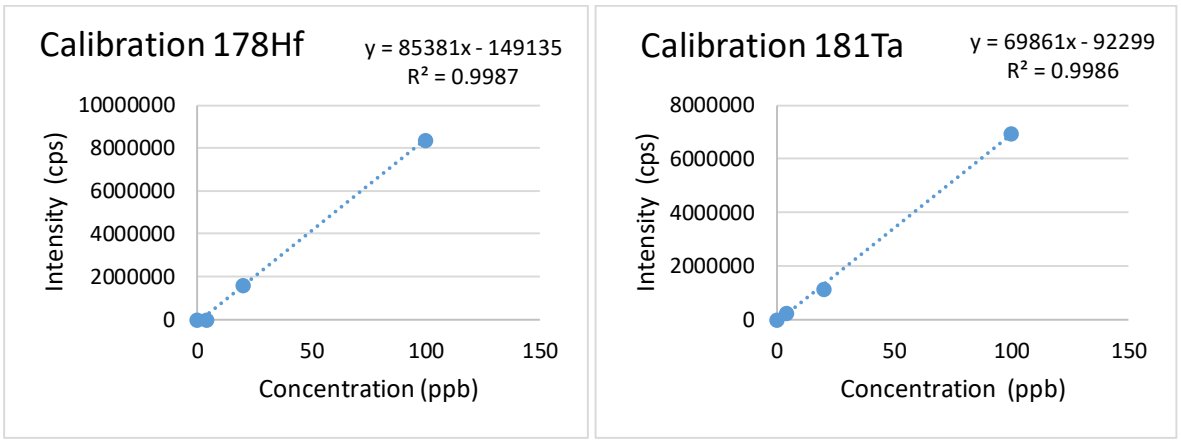

Fig. 3.34: external calibration curve of Hf (on the left) and Ta (on the right).

b) Background signal subtraction (concentration corresponding to the intercept of the calibration line with the Y axis). The size of this background signal is given by the ratio between intercept and slope of the calibration line, which corresponds to 1.75 ppb for Hf and 1.32 ppb for Ta.

c) Elaboration (for each set of the same matrix) of the added interferent concentration function vs cps measured at the mass of the element affected by the interference (e.g., Hf concentration vs cps on ^{195}Pt) (Fig. 3.35).

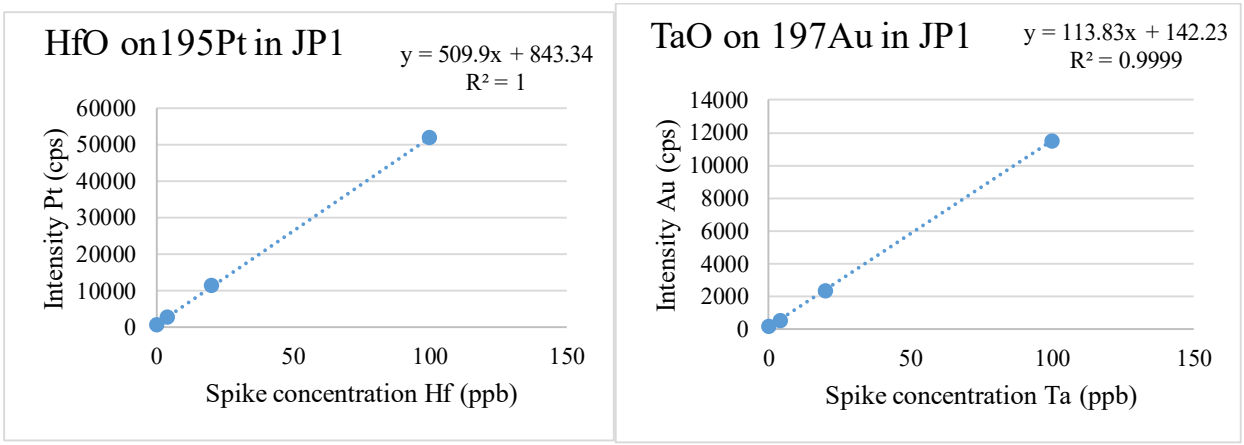

Figure 3.35: Correlation between Hf and Pt (on the left) and between Ta and Au (on the right): regression line slopes give factor of interferences.

d) From this line, the factor of interference F_i is obtained (for the JP1 example: 510 and 114 for Hf and Ta, respectively).

e) Elaboration of the Pt and Au calibration line, from the correlations between standard measures and acquired intensities (Fig. 3.36).

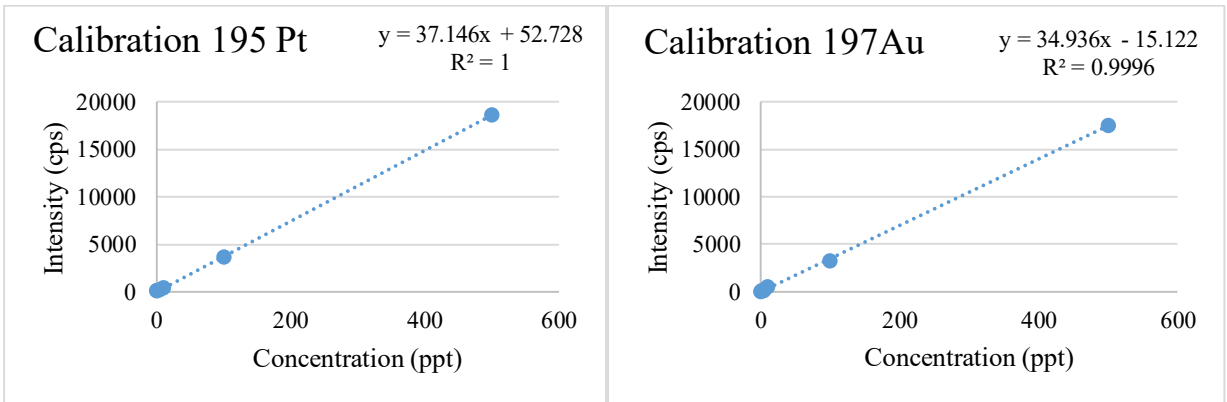

Figure 3.36: Calibration curves (by external calibration) of ^{195}Pt (on the left) and ^{197}Au (on the right).

f) Calculation of the Pt and Au concentrations by using the intensities acquired at the analyte's mass and corrected by subtracting the interferent's contribution (the latter is calculated by multiplying the factor of interference F_i by the determined interferent's concentration).

The calculation steps for Pt are reported in Table 3.32.

Isotope	Internal Standard Corrected Intensity (cps)	
	JP1	JP1*
^{178}Hf	19753	17932
^{195}Pt	894	1726
	Hf concentration (ppb)	
	1.98	1.96
Hf corrected (by Background) concentration (ppb)		
	0.23	0.21
	Pt intensity corrected for Hf interference	
	777	1622
	Pt concentration (ppt)	
	19.5	42.3

Table 3.32: Calculation steps in the determination of Pt in JP1 and JP1.*

Taking into account a dilution coefficient of the solute of about 200 (0.5 g of dissolved powder in 100 ml of solution), the Pt concentration in JP1 was 3.95 ppb, not too far off the compiled value of 4.9 ppb (published values' range: 3.99 to 5.1) (GEOREM Database, Jochum et al., 2005).
The same algorithm applied to the couple tantalum-gold, gave a result of 0.59 ppb, in the same order of magnitude of the reference value (0.35 ppb; published values' range: 0.23-0.35).
The percentage recovery obtained in JP1*, calculated as the ratio between the difference of the measured concentration in the sample with the addition (JP1* and in the sample "as it is" JP1) and the concentration of the added spike, is good for both Pt and Au, 88% and 82%, respectively.

4 Data description and discussion

4.1 Bulk rock HSEs in meteorites 6A, 1B and 5E

The same solutions of the two chondritic samples 6A and 1B, were analysed in three different laboratories over a period of two years (2018-2020), which unfortunately included the shutdown of laboratory activities in Italy and worldwide for the COVID-19 pandemic. The solutions were first analysed in the laboratories of the two companies that produce triple-quadrupole (TQ) ICP-MS spectrometers (Agilent©: and Thermo Fisher Scientific©, hereafter labelled Lab) and subsequently in the laboratories of the department of Physics and Earth Sciences of the University of Ferrara (named "UNIFE"). New prepared solutions were analysed twice over six months and the data reported in Table 4.1 are the average value. For these analytical runs the row data related to Pd, Pt and Au were corrected with the mathematical correction algorithm previously illustrated in Chapter 3. Ni and Cu, having similar geochemical behaviour, are also reported and discussed, when available.
The results are presented in Table 4.1 and Fig 4.1.

		1 B			1B/new sol							
		Lab1 2018	Lab2 2018	UNIFE 2020	UNIFE 2021 *	average	Std. Dev.	%RSD	average (without outlier)	Std. Dev. (without outlier)	%RSD (without outlier)	
Ni	ppm	6550	8940		9500	8330	1567	19	8330	1567	19	
Cu	ppm	60	71		70	67	6	9	67	6	9	
Os	ppb	465	435	795	440	534	175	33	447	16	4	
Ir	ppb	655	600	560	635	613	42	7	613	42	7	
Ru	ppb	820	820	920	930	873	61	7	873	61	7	
Rh	ppb	165	160	195	180	175	16	9	175	16	9	
Pt	ppb	920	840	770	980	878	92	10	878	92	10	
Pd	ppb	500	565	2500	660	1056	965	91	575	80	14	
Au	ppb	105	95	100	180	120	40	34	120	40	34	
Re	ppb	33	34	35	36	35	1	4	35	1	4	
		6 A			**6A/new sol**							
		Lab1 2018	Lab2 2018	UNIFE 2020	UNIFE 2021 *	average	Std. Dev.	%RSD	average (without outlier)	Std. Dev. (without outlier)	%RSD (without outlier)	
Ni	ppm	7270	11120		9000	9130	1928	21	9130	1928	21	
Cu	ppm	60	77		73	70	9	13	70	9	13	
Os	ppb	470	500	910	340	555	247	44	437	85	19	
Ir	ppb	605	625	695	705	658	50	8	658	50	8	
Ru	ppb	790	900	1070	1000	940	122	13	940	122	13	
Rh	ppb	160	195	200	190	186	18	10	186	18	10	
Pt	ppb	780	780	1030	1200	948	205	22	948	205	22	
Pd	ppb	450	1320	1130	780	920	385	42	920	385	42	
Au	ppb	100	110	120	155	121	24	20	121	24	20	
Re	ppb	30	35	45	45	39	8	20	39	8	20	

Table 4.1: Analysis of meteoritic samples. (Average of analyses run twice; highlighted in yellow, outlier values).*

4. Data description and discussion

On the whole, the reproducibility is good:

- **Ni:** the solution sent to the Lab1 and Lab2 run out after the determination of PGEs; the comparison with the UNIFE data was, therefore, only possible by using a different solution. Replicate analyses of 1B (UNIFE 2021) are well aligned with those from Lab2 (same reaction's gas), but about 30% higher with respect to the results from Lab1. In turn, the new solutions of 6A (UNIFE 2021) gives (on average) the same values obtained at Lab1 and Lab2 (Table 4.1).
- **Cu:** the results are in line with those of Ni. On the whole, there is good coherence between the data obtained with two different solutions, analysed in various laboratories within a two years time period.

PGEs

- Os: at first glance the comparability of the data is good, in particular between the recent data from the new solution and the previous ones from the external laboratories. The exception is the result from Ferrara on the first solution, which is almost double in both samples. However, there are known problems linked to the sample preparation, which make this an outlier. As already mentioned, in fact, Osmium is well known to be affected by physical interferences and losses occurring during sample preparation and analysis, especially because of its high volatility in its oxidised form (e.g., after a microwave digestion). As well as potentially being lost to the atmosphere on opening the digestion vessel, Os can also be volatilised preferentially in the spray chamber, which may lead to an overestimation when not calibrated using standards containing the same chemical form of Os. The analytical problem is too complex to be addressed together with the other PGEs and it would need a separate study.
- Ir, Ru and Rh: the comparability is excellent for the data from sample 1B (with %RSD below 10%). It is also good for sample 6A, where only for Ru the %RSD was just above 10%.
- Pt: the results are different in the two samples: for sample 1B the coherence between the results from the different laboratories on different solutions (%RSD < 10) is comparable to the one of Ir, Ru and Rh; for sample 6A, instead, the results from UNIFE both on the first and second solution, show values 30% higher than those from the external laboratories. With only the available data, I was not in the position to adequately discuss the difference in the Pt values, therefore I merely reported the results without interpreting them. At the moment, as it is addressed in the conclusions' chapter, it can only be observed that the determination of Pt in meteoritic samples with this simplified procedure seems to not be able to provide as reliable data as other well-established methods do.
- Pd: the results are not easy to interpret: in sample 1B, the data from Ferrara on the same solution already analysed by the external laboratories are overestimated by as much as 500%; the data from UNIFE on the new solution, instead, with the application of the correction algorithm for the Sr and Y interferences, reduce this difference down to 20-25% higher than the other laboratories. The data of sample 6A obtained in UNIFE and in LAB 2 are similar, but clearly higher (nearly 300%) than those from Lab 1. The last analysis carried out in UNIFE on the second solution and applying the correction algorithm already mentioned, produced an intermediate value (70% higher than Lab 2 and 60% lower than Lab 1). The difference between the two chondritic samples, could be explained by the different content of Y and, most of all, Sr, which is five times higher in sample 1B. It has to be taken into account that Lab 1 was the only one to use ammonia as a cell reaction gas.

- **Au**: the data obtained from the three laboratories on the first solution are coherent (%RSD 5 in 1B e 10 in 6A), while the most recent ones obtained from UNIFE on the new solution and despite the application of the mathematical correction, are 80% higher in sample 1B and 50% higher in sample 6A. This could be a possible consequence of the imperfect homogeneity of the powder (nugget effect), but further tests will be necessary to verify this.
- **Re**: the data reproducibility is excellent for sample 1B (RSD 1%) and fairly good for sample 6A (RSD 20%).

In the chondrite normalised (Palme et al., 2014) diagrams, both meteorites (H-type) show, as expected, HSE values in the same order of magnitude as the chondritic values (Fig. 4.1; Palme et al., 2014). The Pd positive anomaly is evident: it is certainly due to an analytical problem which did not occur in the laboratory that used ammonia and was mitigated, in the case of oxygen acquisition, by the mathematical correction algorithm.

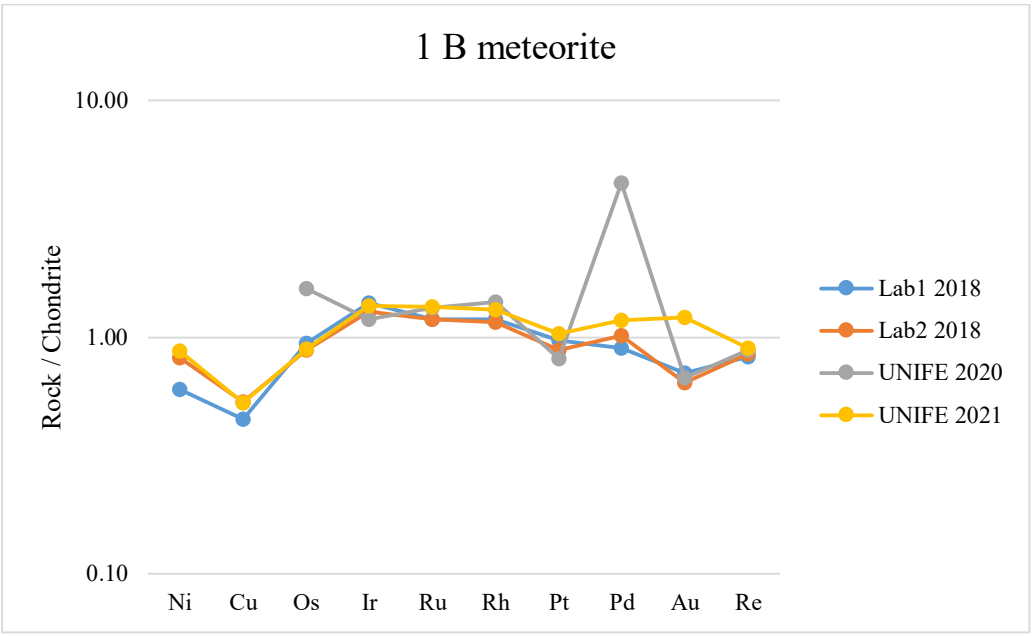

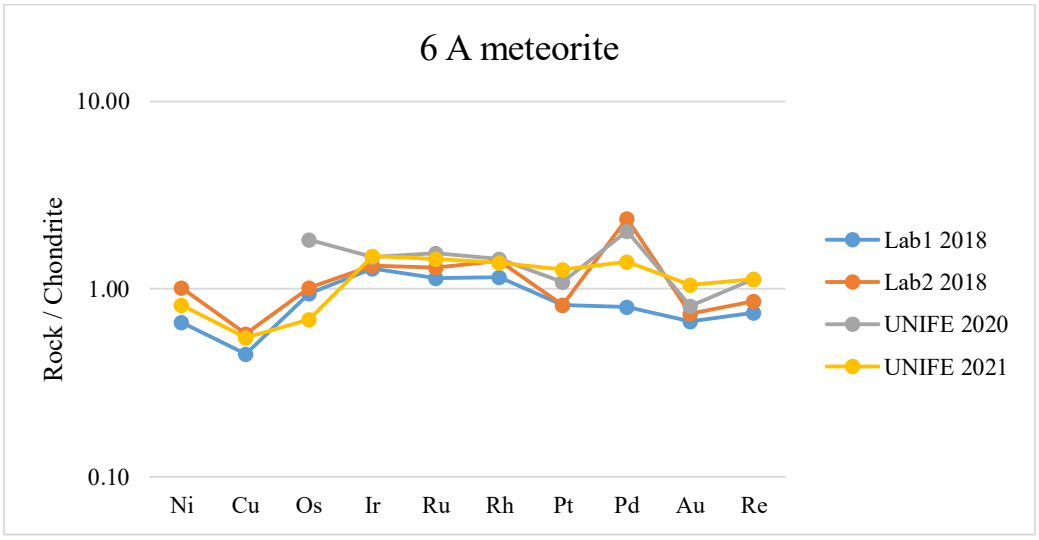

Figure 4.1: Siderophile elements of 1B and 6A meteorites, measured in two TQ-ICP-MS selling companies labs (Lab1 and Lab2) and at the labs of UNIFE. UNIFE 2021 replicate analyses at UNIFE using a new solution. C1 chondrite normalisation values from (Palme et al., 2014).

4.2 Major and trace (HSEs) analyses of FeNi-metal and sulphides in H-Chondrite 6A and suspected iron meteorite 5E.

The sample 6A (H-type chondrite) and the supposed iron meteorite (5E), were prepared for HSE (including PGEs) in-situ analyses using LA-ICP-MS. The rationale behind this additional analytical work, was to check if the concentrations obtained by the dissolution of the original bulk matrix were confirmed (within the analytical errors) by mass balance calculation methods.

Image JMicrovision© v1.2.7 software was used to evaluate the modal percentages of "silicates" and metal/sulphides matrix in 6A meteorite (Fig. 4.2). The intersection node of the prefigured grid corresponds to silicates (single grains or chondrules) or metal-alloy / sulphide. The relative percentages are estimated by counting the nodes.

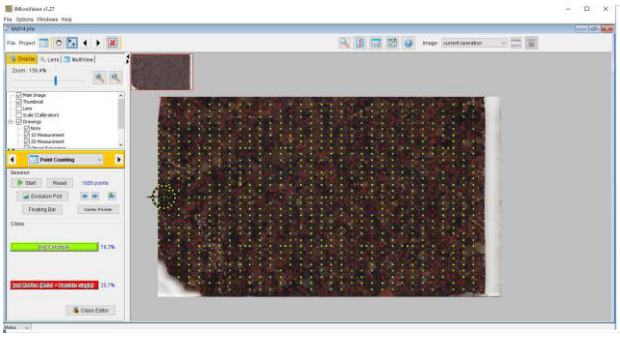

Figure 4.2: 6A meteorite section (4 x 2.5 cm); JMicrovision© v1.2.7 software. The grid intersects nodes of metal alloy/sulphur grains (red points) and silicate single grains and chondrules (yellow grains).

The percentages so obtained, were refined by comparing the nodes position with BSE elemental maps (Ni, S, Fe and Si; Fig. 4.3).

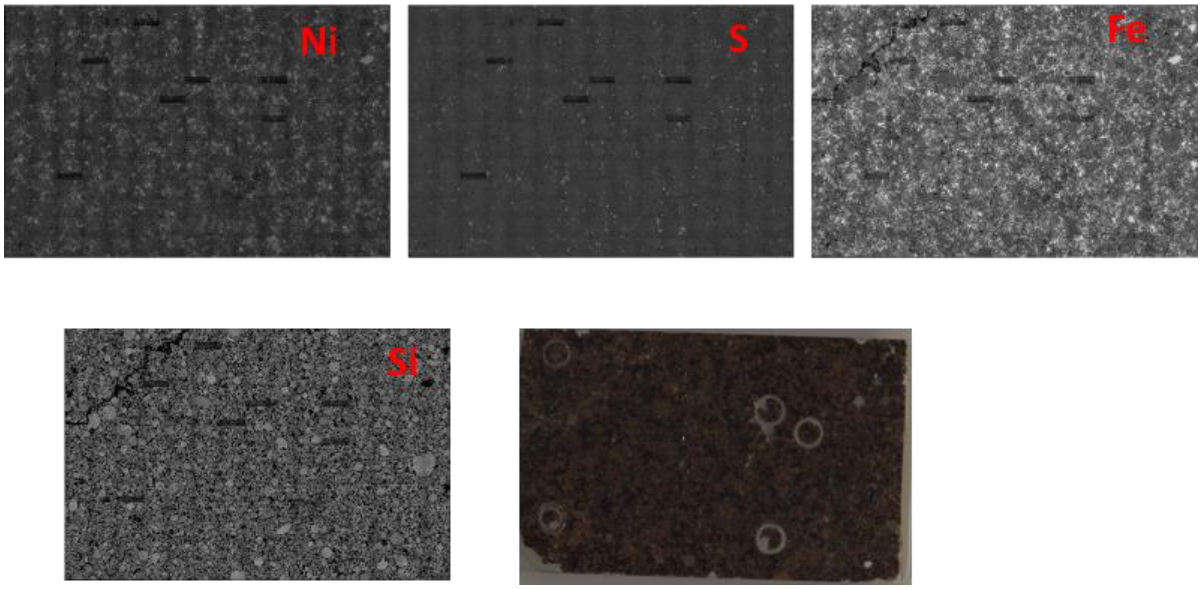

Figure 4.3: BSE elemental maps of 6A meteorite section (4 x 2.5 cm). Grey scale: the brighter the zone, the more concentrated the element. Right bottom: A thin section scan image is also reported.

The conclusive results were:

silicate grains and chondrules = 79.3% (FeNi-metal + sulphides + Fe-oxides) = 20.7%

Electron microprobe analyses were focused on metal phases and sulphides. The metal phases are composed of kamacite (Ni < 7wt %), which is the most abundant, followed by rarer taenite (Ni: 29.36 – 30.98 wt%). The Fe/Ni elemental proportions are in the range 12.7-14.8 in kamacites and 2.2-2.4 in taenite. The majority of the analysed sulphides are troilite. Only in one case, the higher nickel content (2.61 wt%), led to the mineral being classified as pentlandite. In Table 4.2, the average compositions of the mentioned FeNi-metal are reported (the complete data set is in Appendix IV, Tables IV.1 and IV.2).

FeNi-Metal						
	KAMACITE (84 analysis)			**TAENITE (4 analysis)**		
	Average	Std. Dev.	%RSD	Average	Std. Dev.	%RSD
As	0.09	0.036	38	0.08	0.06	69
Co	0.17	0.04	22	0.00	0.00	
Ni	7.19	2.51	35	30.1	0.7	2
S	0.0	0.0	131	0.00	0.00	119
Fe	92.0	2.4	3	70.6	0.6	1
Cu	0.01	0.02	350	0.09	0.04	44
Sulphides						
	TROILITE (32 analysis)			**PENTLANDITE (1 analysis)**		
	Average	Std. Dev.	%RSD			
As	0.04	0.022	49	0.04		
Co	0.00	0.00		0.12		
Ni	0.11	0.14	129	2.61		
S	36.2	0.7	2	32.4		
Fe	61.9	0.9	1	56.9		
Cu	0.04	0.09	257	0.07		

Table 4.2: average compositions of metallic alloys and sulphides identified in 6A meteorite section.

Due to the homogeneity of the sample, only a limited number of analyses were performed in 5E "meteorite".

Apart from a few silicates, whose composition is inconsistent with a natural genesis (i.e., olivine Fa 95.21 -95.51), 99% of the mineral assemblage of this rock is composed of Fe-oxide (FeO = 97.3-99.5 wt%). Ni is always below the detection limits.

Table 4.3 shows minimum, average and maximum LA-ICP-MS analyses of trace HSEs in metal-alloys and sulphides of 6A meteorite. An attempt to measure HSEs in 5E rock was made, but, as expected, no HSE content (except Ni at ppm level) was detected in the phases. The complete data set is in Appendix V (Tables V.1-V.3).
Kamacites of 6A meteorite contain Re from 0.03 to 1.1 ppm and Au in the range 0.08-3.67 ppm. Among PGEs, Rh varies from 0.04 to 2.64 ppm and Pd from 0.19 to 1.41 ppm. Ir and Os are always lower than L.O.D. (Limit Of Detection). Unfortunately, platinum data were not available.
In sulphides (all troilites), inter and intra-grain Rh, Pd, Re and Au contents are more homogeneous with respect to those of kamacites (Rh: 0.67 -1.8 ppm; Pd: 0.28 -1.13 ppm; Re: 0.11 - 0.74 ppm and Au; 0.52 - 2.26 ppm; Table 4.3).

The HSE trace profiles of both kamacite and troilites indicate a relatively constant enrichment of the PGEs (and Ni) in both minerals, with respect to the bulk composition (Fig. 4.4). The kamacite/bulk rock concentration ratios vary from 7 to 14 for Ni, Au, Rh and Re. In sulphides, the same element group is enriched, on average, 5-8 times the bulk rock composition.
On the whole, the relatively constant ratio between the concentration in the phases (sulphides and FeNi-metal) and the concentration in the meteorite (which is visible comparing the patterns in the graph), indicates that the meteorite's composition is the effect of the dilution of the phases (sulphides/alloys) in the silicate matrix. Only Pd and Cu show inconsistent ratios. In the case of Pd the problem is clearly analytical (overestimates in the bulk composition for an imperfect interference control). The case of Cu is more difficult to explain (probably the presence of non-analysed in LAM-ICP-MS phases such as penthlandite).

	FeNi metal			Sulphides		
	min	**average**	max	min	**average**	max
Sc	0.41	**0.89**	1.55	0.85	**1.43**	1.86
Ti	2.72	**10.5**	18.1	2.72	**220**	1360
V	0.42	**6.08**	15.8	0.79	**2.93**	7.72
Cr	40.2	**70.2**	125	19.7	**109**	677
Mn	100	**426**	980	43.7	**69.0**	120
Co	660	**3620**	5380	3230	**4350**	4830
Ni	8050	**64990**	90850	49200	**62700**	69500
Cu	99.9	**238**	499	75.8	**99.7**	158
Zn	1.24	**9.07**	17.7	1.05	**4.39**	11.8
Ga	0.39	**24.3**	34.8	8.64	**11.55**	24.28
Ge	43.0	**200**	310	73.3	**96.3**	193
As	4.10	**46.1**	71.7	10.0	**19.2**	41.9
Zr	0.06	**0.18**	0.39	0.16	**0.70**	1.35
Nb	0.03	**0.05**	0.08	0.02	**0.25**	0.65
Rh	0.04	**1.71**	2.64	0.67	**0.98**	1.80
Pd	0.19	**1.05**	1.41	0.28	**0.53**	1.13
Ag	0.04	**0.07**	0.15	n.d	**n.d**	n.d
In	0.02	**0.03**	0.04	0.03	**0.04**	0.06
Sb	0.17	**0.68**	0.92	0.24	**0.37**	0.57
Hf	0.05	**0.08**	0.11	0.13	**0.14**	0.15
Ta	0.01	**0.01**	0.01	0.04	**0.04**	0.04
Re	0.03	**0.63**	1.11	0.111	**0.374**	0.740
Au	0.08	**1.75**	3.67	0.52	**1.12**	2.26
Pb	0.60	**1.35**	2.28	0.15	**0.88**	1.61

Table 4.3: Minimum, average and maximum concentration of the elements determined in LAM-ICP-MS (n.d. is for not detected).

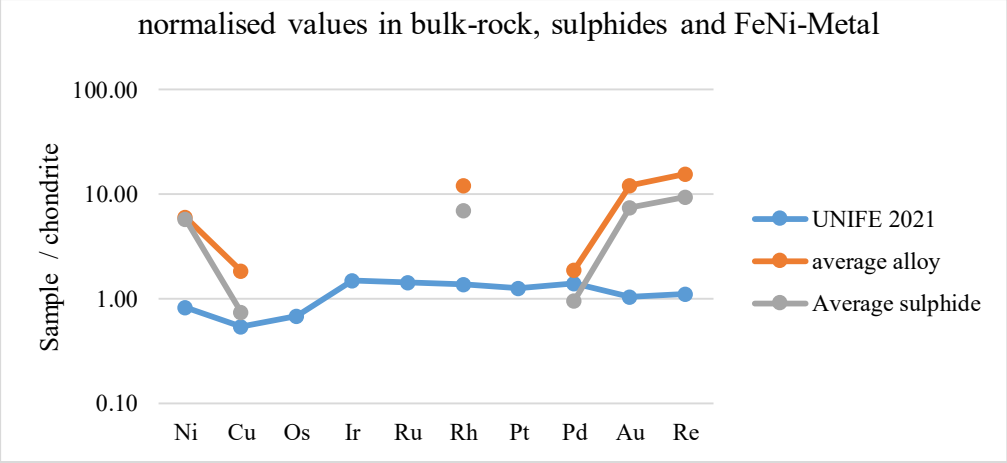

Figure 4.4: Comparison between bulk and in mineral compositions for 6A sample (chondrite normalization values by Palme et al., 2014).

4.3 Soil samples: PGEs in bulk contents

Data of analyses carried out by the standard addition calibration on soil samples collected in 2019 near via Bacchelli in Ferrara, are summarised in Table 4.4.

	BSC	**BS1a**	**BS1b**	**BS2a**	**BS2b**	**BS3a**	**BS3b**	**BS4a**	**BS4b**	**BNC**	**BN1a**	**BN1b**
Au	140	520	540	8570	1180	650	590	570	290	430	480	1520
Ir	51	30	67	36	49	40	33	96	91	39	98	110
Os	40	58	97	76	100	110	82	220	160	59	190	170
Pd	~~19300~~	~~7500~~	~~0~~	~~9600~~	~~10400~~	~~6600~~	~~7700~~	~~17300~~	~~13700~~	~~18000~~	~~17700~~	~~15700~~
Pt	3370	560	630	340	270	290	210	200	190	4620	210	200
Re	100	120	160	160	190	130	150	320	280	180	310	260
Rh	1320	190	230	110	110	120	110	110	96	1340	92	80
Ru	31	22	26	18	31	33	23	24	30	24	22	31

Table 4.4: Analyses of soil samples collected in 2019 in Ferrara (Italy). Concentrations are in ng/g (ppb) Pd values are in strikethrough because they are considered to be unlikely; see text for further explanation.

Pd values are not realistic and are not taken into account in the data interpretation: the mathematical correction for the HfO spectral interference was not applied because the interferent's contribution at the signal recorded at the interferent's mass is well above the acceptable limit of 20% (Simitchiev et al., 2008).

Table 4.5 shows the comparison between the measured concentration ranges of Pt and Rh, which are the main indicators, with Pd, of the anthropic contribution due to their use in autocatalysts, and literature data (Rauch and Morrison, 2008; Reith et al., 2014).

Platinum (ppb)	Rauch and Morrison 2008		Reith et al. 2018				This Thesis	
			Soils (unpolluted)		Soils (polluted, roadside)			
Provenience	min	MAX	min	MAX	min	MAX	min	MAX
Roadside Soil	25	250						
Lateritic, Australia			<5	70				
Southern British Columbia, Canada			2	155				
Background, Germany			0.4	0.8				
Perth, Australia					31	152		
Germany					50	261		
Seoul, Korea					3.8	444		
Roadside Soil in Ferrara							190	630

Rhodium (ppb)	Rauch and Morrison 2008		This thesis	
	min	MAX	min	MAX
Provenience				
Roadside Soil	4	40		
Roadside Soil in Ferrara			96	230

Table 4.5: Comparison between the concentration ranges measured in Ferrara soil samples and Literature data. (In the table above: Pt ranges and in the table below: Rh ranges).

The comparison with the ranges reported in the table, clearly shows that the results of this study are, on average, slightly higher for Pt and significantly higher for Rh.
The most interesting data, though, is the good correlation between the concentrations of Rh and Pt (Fig. 4.5), which seems to confirm the common origin (road traffic pollution) of the two elements.

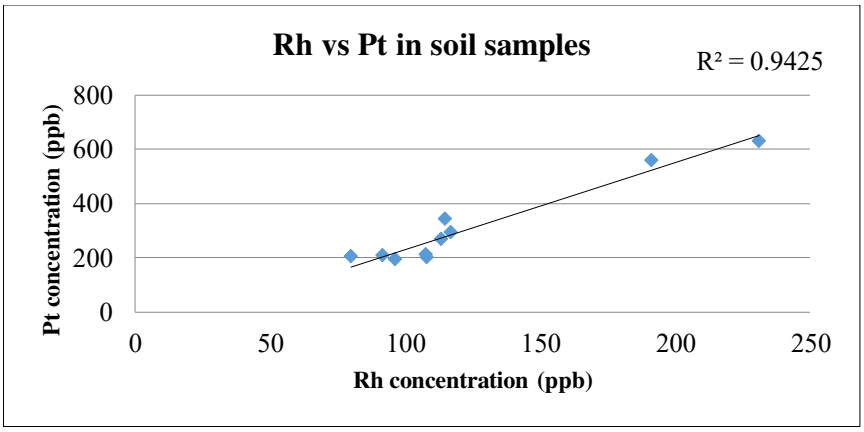

Figure 4.5: Rh concentration plotted against Pt concentration in soil samples.

Evidence of the anthropic origin of Rh and Pd, is also clearly shown in the graphs where, for the area south of the road, the distance from the roadside is plotted against the Rh and Pt measured concentrations (Fig. 4.6).

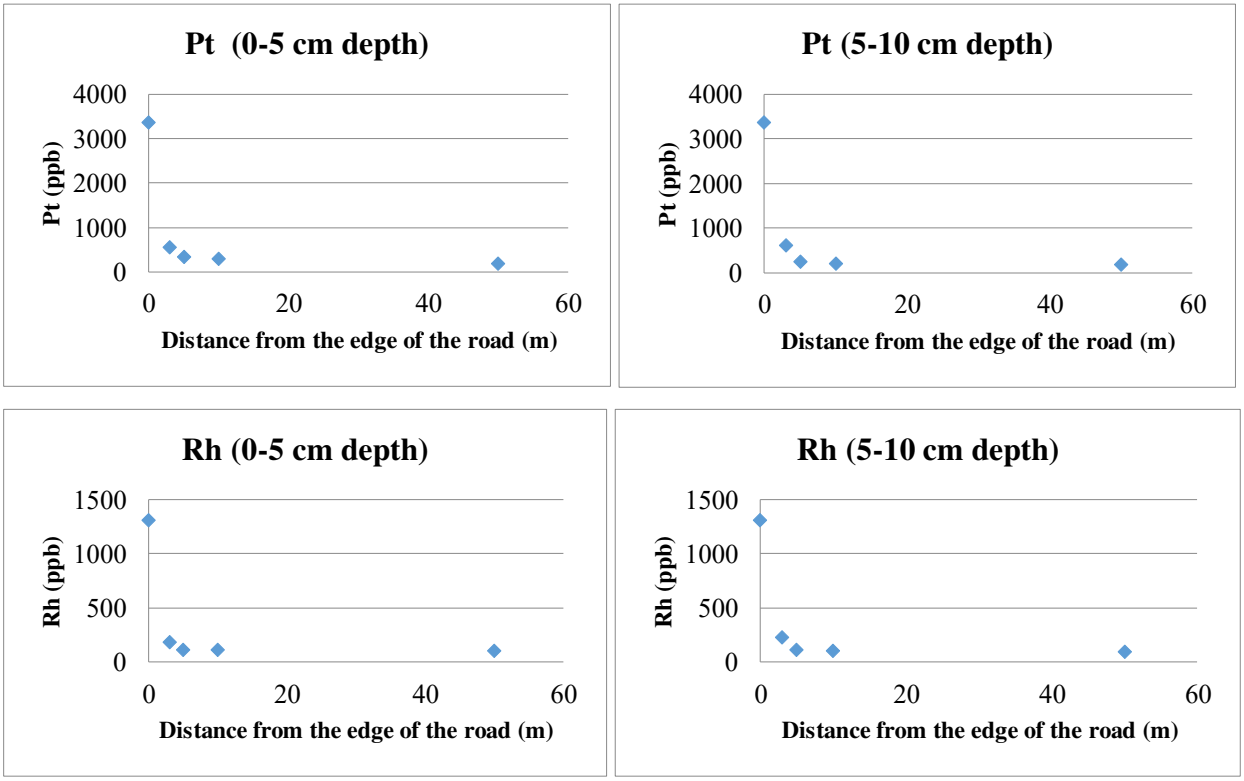

Figure 4.6: Concentration of Pt (above) and Rh (below) plotted against the distance from the edge of the road for soil samples collected south of Bacchelli road (Ferrara). On the left: superficial samples and on the right: deeper samples.

Regarding the northern area of the road, there was no clear evidence of a detailed pattern with the increased distance from the roadside (due to the presence of a water channel north of via Bacchelli (Fig. 4.7), but the Rh and Pt values measured at the roadside and in the spot sampled 50 m north (within the Giorgio Bassani

Park) are coherent with those at the roadside and at the point BS4 in the southern area of the road, where the BS4 point can be considered the representative of the natural uncontaminated background.
No significant differences were observed between superficial (0-5 cm deep; indicated with the lower-case "a") and deeper (5-10 cm; indicated with the lower-case "b") samples.

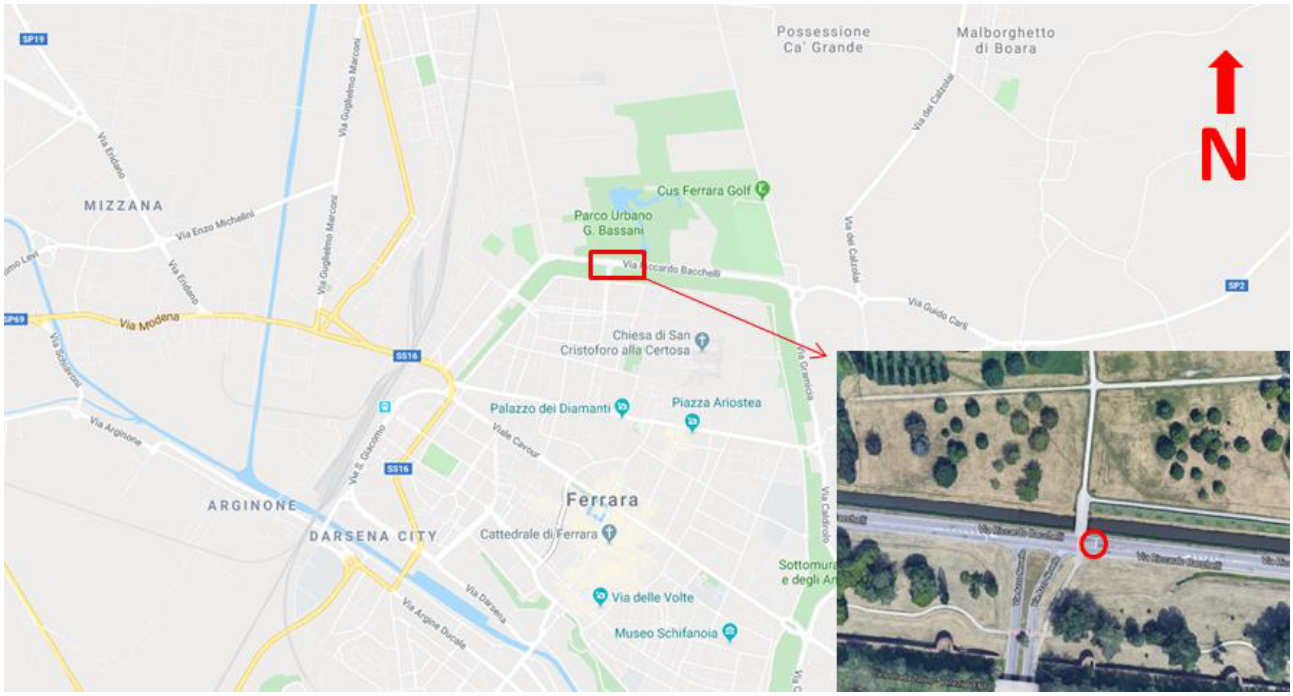

Figure 4.7: Map of the studied area.

A more complex interpretation is required for the positive correlation observed between Ir, Os and Re concentrations. It is not as clear and easily readable as the one between Pt and Rh, but it is, nonetheless, significant: R^2 0.77 between Re and Ir, 0.78 between Os and Ir and 0.88 between Os and Re (Figs. 4.8-4.10).

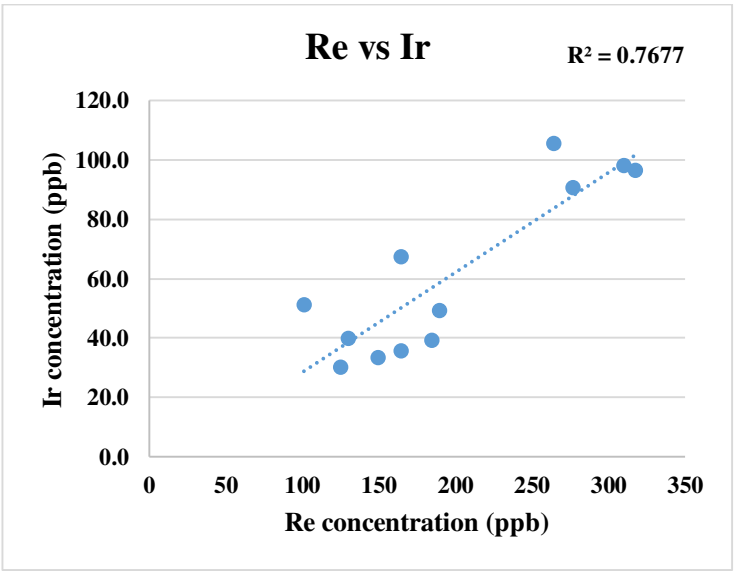

Figure 4.8: Re concentration plotted against Ir concentration in soil samples.

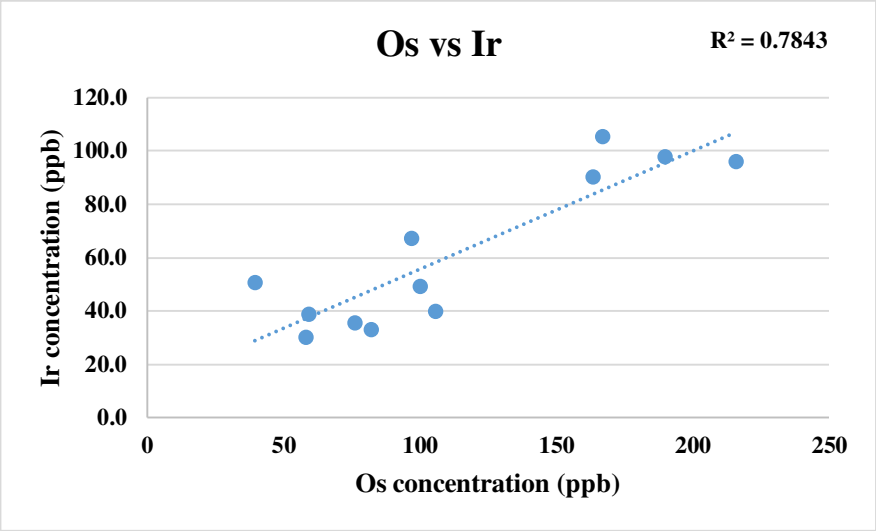

Figure 4.9: Os concentration plotted against Ir concentration in soil samples.

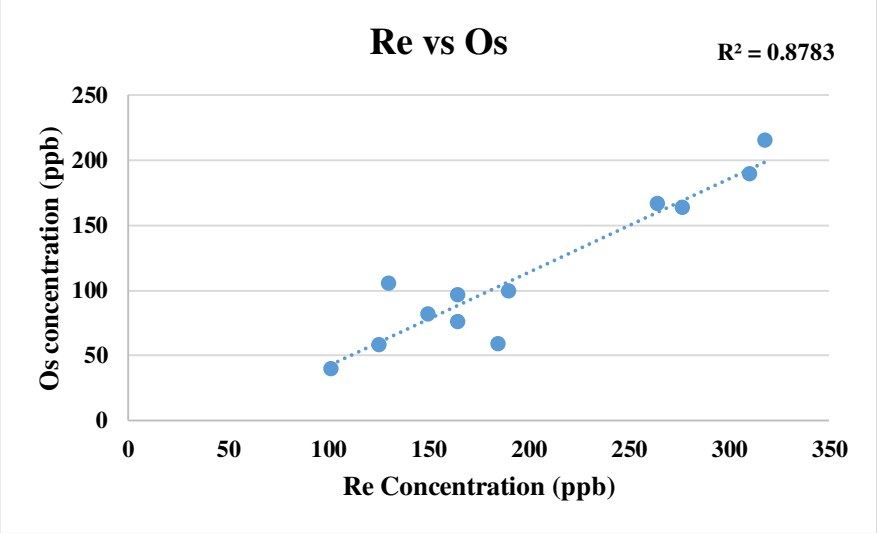

Figure 4.10: Re concentration plotted against Os concentration in soil samples.

Such correlations cannot be simply explained by the presence of a single interfering element, whose variation in concentration could justify the correlation with the three studied elements, because there is not such an element that could cause polyatomic ion interferences on all three investigated masses (185 for Re, 189 for Os and 193 for Ir). It is true, however, that all these elements can be affected by the interference of elements of the REE group (although for Re, the effect is expected to be minimal, Thermo Fisher Scientific 2020).

The correlation observed between the concentrations of Ir, Os and Re and the distance from the roadside in the samples from the southern side of the road, is odd and difficult to explain. Different from Pt and Rh, the concentration of these elements seems to increase with the distance from the roadside. Moreover, a difference between superficial and deep samples was observed and the correlation with the distance from the roadside is more evident in the superficial samples (0-5 cm) (Fig. 4.11).

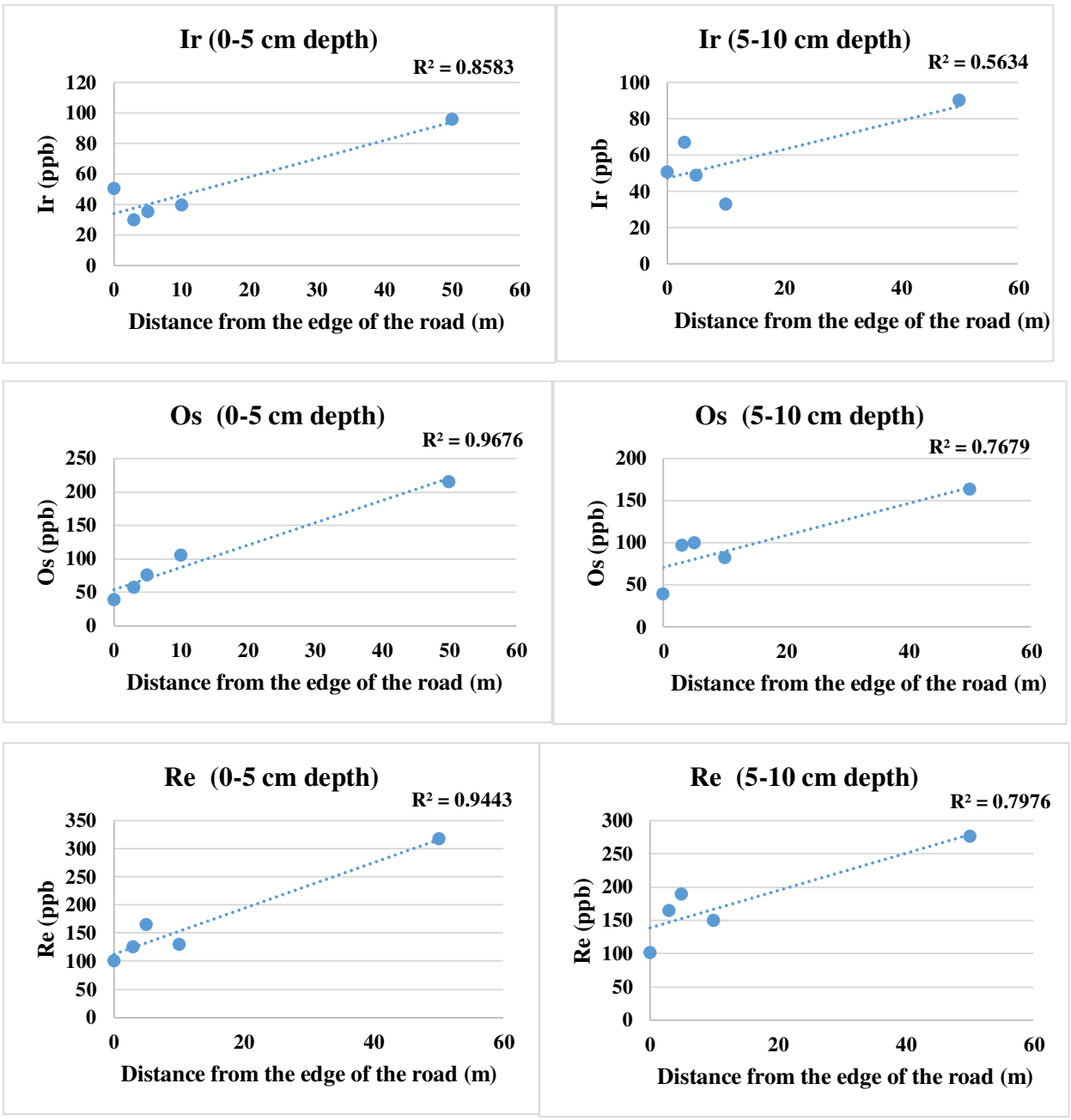

Figure 4.11: Ir, Os, and Re concentration plotted against the distance from the edge of the road for soil samples collected south of Bacchelli road (Ferrara). On the left: superficial samples and on the right: deeper samples.

The results from the vegetation collected in the same points as the soils are not significant. For this matrix, the standard addition calibration was also applied.
It has to be noted that the collection and analysis of vegetal samples, were not among the primary goals of this work. Plants were analysed merely to verify that the TQ-ICP-MS method of PGE determination could also be applied to this matrix.
For this reason, only the average recovery test data (between 89 and 104% for Ir, Pt, Rh, Re, e Ru; 60 % for Au and Pd, while it seems to be completely lost for Os) carried out on two of the six grass samples are reported.
The range of measured values is compared with literature data in Table 4.6.

Literature	Type of plant	Place	Pt (ppb)	Rh (ppb)
Ravindra et al., 2004	Grass	Germany	3.61 – 10.6	0.65 – 1.54
Lesniewska et al., 2004	Grass	Germany	3.13 – 11.8	
	Grass	Germany (High traffic density zone)	17.0 – 95.6	
Dubiella-Jackowska et al., 2009	Grass	Poland	7.44 - 9,37	0.56 – 0.86
	Grass	Germany	0.14 – 0.29	
	Grass	Belgium	1.4 – 1.7	
Lyubomirova and Djingova, 2015	Leaves of Taraxacum officinale	Bulgaria	2 - 15	
This thesis	Grass	Italy (Ferrara)	1.5 - 26	13.5 - 31

Table 4.6: Comparison between measured Pt and Rh concentration ranges and literature data.

Finally, the correlation observed between the Pt and Rh concentrations ($R^2 = 0.95$) of samples collected to the south of the road is reported in (Fig. 4.12). However, it should be noted that unlike the case of soils, no correlation with the distance from the roadside was observed.

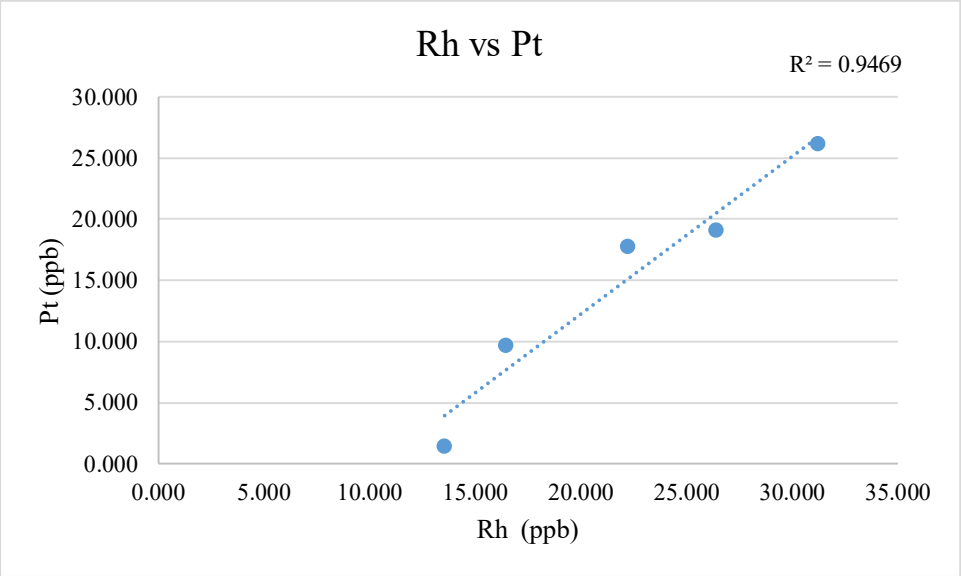

Fig. 4.12: Pt concentration plotted against Rh concentration in grass samples.

4.4 CRM PGEs (plus Co, Ni, Cu, Mo, Sn, Sb, Re, and Au)

The CRMs results are summarised below. It has to be noted that most of them were originally planned and developed for method validation and quality control in routine analyses for the determination of major elements and several trace elements, but not of PGEs. Only subsequently were they also characterised, more or less accurately, for these elements.

4.4.1 CRMs of soils (GXR5 and GXR6)

Compiled reference values for these two standards are not available for any of the PGEs; published data, however, are available for Au, Ir, Pd and Pt. It has also to be noted that these standards were previously affected by problems with different bottle heterogeneity (GEOREM database: Jochum et al. 2005).

The results of the analyses on solutions prepared in 2018 differ from PGE concentrations reported in literature, particularly for Ir and Pd. The excellent comparison with certified values of other elements with similar geochemical behaviour (siderophile/chalcophile), however, gives a high level of confidence in the sample preparation process. Table 4.7.

GXR5											
	Literature		2018 solutions								
ppb	min	MAX	Lab 1	Lab 2	UNIFE	average	std dev	%RSD	average (without outlier)	Std. Dev. (without outlier)	%RSD (without outlier)
Os			0.70	1.8	4.8	2.44	2.13	87	2.44	2.13	87
Ir	0.051		0.95	6.5	4.4	3.93	2.79	71	5.43	1.48	27
Ru			0.50	0.15	0.33	0.33	0.18	54	0.33	0.18	54
Rh			0.96	0.82	0.92	0.90	0.07	8	0.90	0.07	8
Pt	50		16.3	21.73	15.1	17.7	3.6	20	17.68	3.56	20
Pd	0.4		11.9	49.0	103	54.8	46.0	84	54.77	46.02	84
Au	90	160	23.8	9.16	9.36	14.1	8.4	60	9.26	0.14	2
Re			0.62	1.77	1.65	1.35	0.63	47	1.71	0.09	5
ppm	**compiled**										
Co	29.9				30						
Ni	75				72						
Cu	354				353						
Mo	31				27.2						
Sn	2				2.7						
Sb	1.63				1.6						

GXR6											
	Literature		2018 solutions								
ppb	min	MAX	Lab 1	Lab 2	UNIFE	average	std dev	%RSD	average (without outlier)	Std. Dev. (without outlier)	%RSD (without outlier)
Os			0.35	<LOD	3.48	1.92	2.21	116	1.92	2.21	116
Ir	0.032		1.28	7.50	7.34	5.37	3.55	66	7.42	0.11	2
Ru			0.70	0.44	0.44	0.52	0.15	29	0.52	0.15	29
Rh			2.40	0.16	0.42	0.99	1.22	123	0.29	0.18	62
Pt	*150*		24.1	20.6	24.4	23.0	2.1	9	23.0	2.1	9
Pd	2.2		4.2	61.5	164	76.4	80.7	106	112.5	72.2	64
Au	95	120	81	94.0	91	88.8	6.6	7	92.5	2.1	2
Re			0.27	1.57	2.47	1.44	1.11	77	1.44	1.11	77
ppm	**compiled**										
Co	13.8				15.2						
Ni	27				27.9						
Cu	66				70.8						
Mo	2.4				2.65						
Sn	1.7				1.3						
Sb	3.6				3.77						

Table 4.7: Measured and reference values in CRMs of soils (highlighted in yellow outlier values).

4. Data description and discussion

Regarding Pt, the results obtained from the same solution by the three laboratories are coherent, but they are significantly lower than the literature values, which are, anyway, compiled as simple "information value" (35-40% in GXR5 and 15-20% in GXR6).

Au shows different results from the three laboratories: Lab 1 (the only one that used ammonia as a cell reactive gas) produced a measured value for GXR5 double that of the other two laboratories and significantly lower than the two literature data values (one of which is compiled as "information value"). On the contrary, sample GXR6 showed good reproducibility of the data from the three laboratories (%RSD 7.5%) and the closest value (95 ppt) is compiled as a "proposed value" (GEOREM database: Jochum et al. 2005).

4.4.2 CRMs of ultramafic matrix (JP1 and UBN)

Table 4.8 reports the JP1 standard results. Compiled values (only as "proposed value") for nearly all the determined elements are available in literature. With the exception of Os, due to possible loss during acid attack, the obtained results are in the same range as that from literature (or at least in the same order of magnitude).
The comparability with the compiled values of the other siderophile/chalcophile elements is excellent.

	JP1											
	Literature			2018 solutions								
ppb	**proposed**	min	MAX	Lab 1	Lab 2	UNIFE	average	std dev	%RSD	average (without outlier)	Std. Dev. (without outlier)	%RSD (without outlier)
Os	7.9	2.98	12.8	0.56	<LOD	1.69	1.13	0.80	71	1.13	0.80	71
Ir	2		6.1	0.08	0.61	1.48	0.72	0.71	98	1.05	0.62	59
Ru	6.5	0.32	6.27	2.4	1.90	3.19	2.49	0.65	26	2.49	0.65	26
Rh		0.875	1.09	0.42	0.21	0.52	0.38	0.16	41	0.38	0.16	41
Pt	4.9	3.99	5.1	3.2	8.04	3.95	5.08	2.59	51	3.60	0.50	14
Pd	1.3	1.2	1.63	<LOD	1.76	<LOD	1.76			1.76		
Au	0.3	0.23	0.35	6.4	0.62	0.59	2.54	3.34	132	0.61	0.02	4
Re	0.015		0.29	0.09	0.06	0.14	0.10	0.04	41	0.10	0.04	41
ppm	**compiled**	min	MAX									
Co	116	93	132			104						
Ni	2460	2201	2752			2200						
Cu	6.72	3.46	9.3			3.78						
Mo	0.087	0.122	0.16			0.19						
Sn	0.05	0.026	0.036			0.02						
Sb	0.034	0.03	0.044			0.05						

Table 4.8: Measured and reference values in JP1 (highlighted in yellow outlier values).

Two recovery tests, were also carried out on this standard; a spike with different concentrations of PGEs was added at the second and third aliquots of the powder. The results show recovery between 78 and 110% for seven of the nine tested elements: beside Os, which can easily volatise during the acid attack, only Pd showed a worse recovery. The test failure was probably due more to the poor accuracy of the determination (inefficient control of the spectral interferences) than to a real loss of the element in the various phases of the solution's preparation.
The published values for UBN (for which compiled values are not available, not even as simple "proposed" or "information" values) are reported in Table 4.9 and compared to those measured by external calibration and without the mathematical correction at the TQ-ICP-MS laboratory of UNIFE.

	UBN		
ppb	range published value		UNIFE
	min	MAX	
Os	1.83	6.33	1.93
Ir	1.83	3.61	1.06
Ru	3.14	7.24	3.24
Rh	0.86	1.2	3.09
Pt	5	15.67	40.2
Pd	4.4	7.83	88
Au	0.47	1.7	4.91
Re	0.04	0.26	2.27

Table 4.9: Measured and reference values in UBN.

Os, Ir and Ru values are comparable with the value range reported in (GEOREM database: Jochum et al., 2005), while Rh and Au are higher, but in the same order of magnitude.
The Re value was 10 times higher than the maximum limit of the range and there is no evident explanation for this behaviour. Pt and, most of all, Pd excessively high values, instead, can be ascribed to the interference control: the use of ammonia as cell reaction gas, would improve the results. It was not possible to measure the concentrations of the other set of siderophile/chalcophile elements, because of a lack of solution. The good results for other elements of petrological interest (i.e., HFSE and REE), however, proved the efficacy of the dissolution procedure.

4.4.3 CMR of Road dust (BCR 723)

This standard was prepared in triplicate and the solid residue after the separation by centrifugation of the solution, was dried in an oven and subjected to diffractometric analysis for the identification of any phases present. The triplicates are identified with the letters a, b, c in Table 4.10 e Figs 4.13 and 4.14.
The results show excellent reproducibility of the dissolution procedure, with an RSD lower than 10% for all the examined elements. According to the ratio between the certified or indicative (depending on the element) concentration and the measured (as average of the triplicates) concentration, however, the recovery of PGEs and other metallic elements seems to be insufficient (between 60 and 85% for the vast majority), with minimums of 50-55% for Pt, Cr and Fe.
Although reproducible, the sample dissolution process appears to be faulty; this is also proved by the X-Ray diffractometric (XRD) analyses carried out at the laboratories of the Department of Physics and Earth Sciences of the University of Ferrara.
Powder diffraction patterns were obtained with a Bruker D8 DaVinci Diffractometer equipped with a LYNXEYE_XE (1D mode) detector, using a Cu Kα1, Kα2 radiation in the 4–80° 2θ range and a counting time of 1.5 s/step, step size 0.02°. Phase identification was achieved by search-match using the EVA v.14.0 program by Bruker and the Powder Diffraction File database (PDF) v. 9.0.133. The XRD pattern collected on the synthesised powders, showed that the peaks are attributable to sulphurs, in particular to pentlandite. The presence of these sulphurs in the residue can explain the failure in the recovery of the elements with a strong chalcophile/siderophile tendency. A significant bituminous component clearly played a key role in preventing the total dissolution of the powder.

	BCR 723					Measured value					
ppb	**certified value (ppb)**	**indicative value (ppm)**	**Published value**								
			min	MAX		BCR723a	BCR723b	BCR723c	***average***	*std dev*	*%RSD*
Os			0.46	1.206		1.09	1.32	1.24	***1.22***	*0.11*	*9.4*
Ir			0.53	0.956		1.23	1.23	1.36	***1.28***	*0.07*	*5.8*
Ru			0.85			0.721	0.690	0.645	***0.685***	*0.038*	*5.6*
Rh	**12.8**		10.3	21.8		8.25	8.74	9.71	***8.90***	*0.74*	*8.4*
Pt	**81.3**		64	101		41.4	43.7	45.5	***43.5***	*2.1*	*4.8*
Pd	**6.1**		4.2	7.28		~~619~~	~~590~~	~~646~~	***~~618~~***	*28*	*4.5*
Au			10	20.6		N.D.	N.D.	N.D.			
Re			6.65	10.7		6.82	6.70	7.90	***7.14***	*0.66*	*9.2*
Al		37500							**26700**		
Ba		460							**345**		
Cd		2.5							**1.55**		
Co		29.8							**22.8**		
Cr		440							**211**		
Fe		32900							**16700**		
Hf		2.2									
Mn		1280							**1070**		
Mo		40							**34.3**		
Ni		171							**128**		
Pb		866							**520**		
Rb		75							**48**		
Sb		28.2							**24**		
Sr		254							**210**		
Ti		2580							**1860**		
V		**74.9**							**59**		
Zn		**1660**							**1270**		

Table 4.10: Comparison between reference and measured values on BCR723 reference material.

The XRD patterns of the three residues are very similar; those of samples 723b and 723c, in particular, are almost totally superimposable Fig. 4.13.

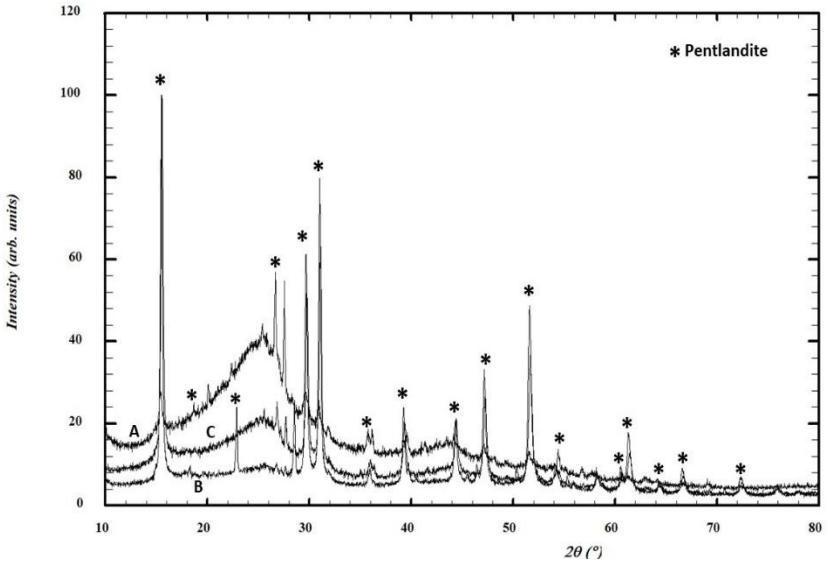

Figure 4.13: XRPD patterns collected for solid residues (samples A, B and C, respectively) after acid attack of three replicates BCR 723 reference material. The reference peaks of pentlandite are well detected in the amorphous matrix.

The only observed difference is the variable degree of crystallinity, which ranges from 35% in sample A (Fig 4.14a) to 66% in sample B (Fig. 4.14b). Sample C shows an intermediate percentage of crystallinity of 52% (Fig. 4.14c).

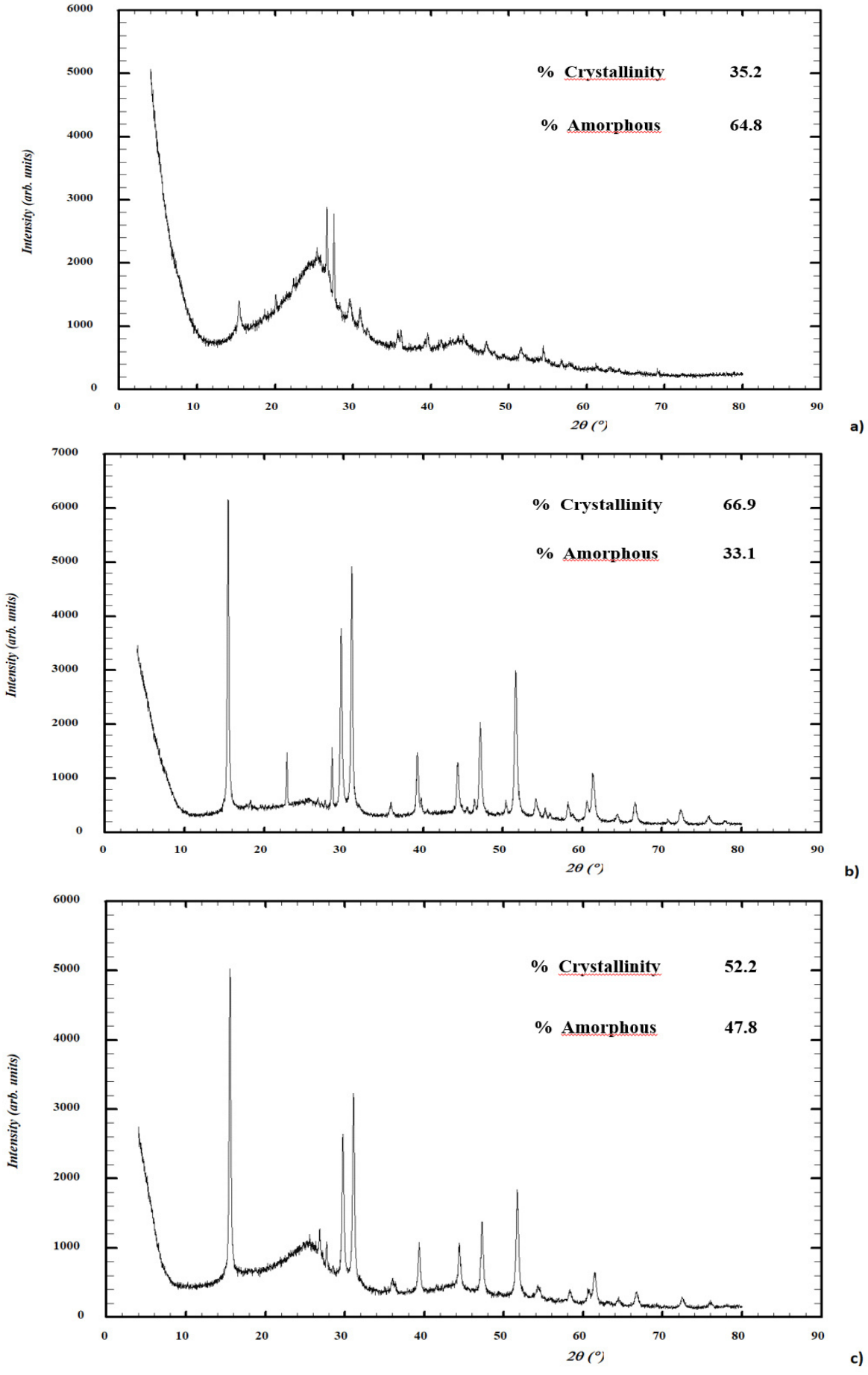

Figure 4.14: Single XRPD patterns of the three (a, b, c) replicates of solid residues of BCR 723, highlighting the different amorphous contents.

4.5 Pelagic limestones (Bottaccione section, Gubbio, Italy)

The order of magnitude of the iridium concentration detected in the eight samples analysed is consistent with the natural background recorded in the stratigraphic sequence above and below the K / Pg limit: overall the Ir content ranges from 0.32 to 0.72 ppb, with an average value of 0.50 ppb. Fig 4.15.
These values should be well discriminated (over an order of magnitude lower) from those predicted in the thin enriched layer, which, unfortunately, was not possible to analyse for this work.
The success of the recovery tests (between 110 and 115%) confirm the validity of the analytical protocol and the reliability of the data.

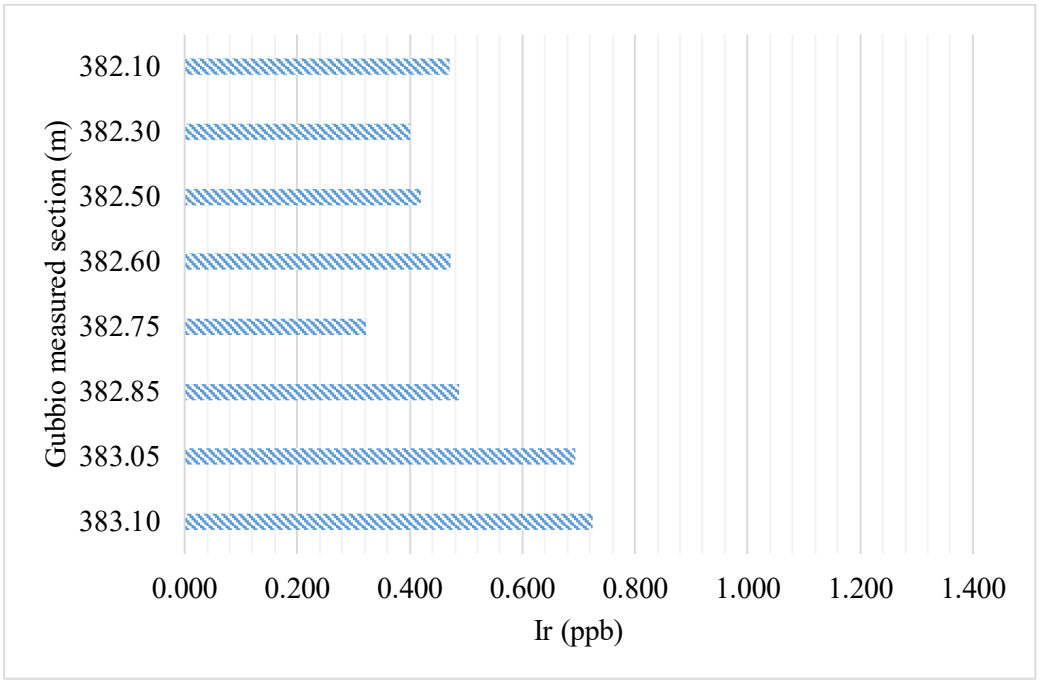

Fig 4.15: Iridium concentration in the analysed samples of the Bottaccione sequence (Gubbio, Italy).

5 Conclusive remarks and future prospects

The determination of PGE abundances in geological and environmental bulk samples, is challenging, due to the low concentration of these elements and their heterogeneous distribution in rocks of silicate and carbonate matrices (nugget effect).
The focus of this doctoral thesis was to test if a simplified sample preparation technique can be used for analyses with the latest generation of triple quadrupole spectrometers TQ-ICP-MS. The measurement of PGE abundances provides important information about the geological/cosmological and environmental processes that modelled our planet and human life.
The sample preparation, the evaluation of an analytical strategy and the instrument set-up, together with the research activity, were planned to be carried out at the laboratories of the University of Ferrara and at both the TQ-ICP-MS selling companies, who made available their facilities for this project.
It is worth noticing that the laboratory activities were carried out over a period of three years (2018-2021), which included the shutdown of laboratories in Italy and worldwide due to the COVID-19 pandemic, therefore, the initial program suffered an inevitable partial reduction in experimental analyses.
The indirect effects of the pandemic on an experimental thesis of this type were, unfortunately, decisive.
For this reason, the number of tests on a set of natural samples (of geological/cosmological interest) as well as on Certified Reference Materials (CRMs), are less than the number necessary for the official validation of the proposed analytical protocol.

An important critical issue worth mentioning, is that the sample preparation at low pressure does not assure the complete recovery of the all HSEs in the solution: as is well known by the scientific community, Os suffers a quantitative loss during dissolution and it cannot therefore be determined accurately. The limited access to the laboratory facilities, prevented the possibility to further address the Os issue; consequently, no results are reported in this thesis.

Notwithstanding this, interesting analytical results were obtained:

- The simplified method of a low-pressure acid digestion (on a hot plate in open system) can be reliably used for most of the tested elements (PGEs, Au and Re) and at least for some of the studied matrices.
- Among the different materials analysed in this thesis and the possible applications of the developed procedure, meteorites and mantle rock samples are not suitable candidates for high quality results, which can be instead obtained by other consolidated and tested digestion methods (high-pressure) and related extraction/pre-concentration protocols (Chu, 2021). For these kinds of material, the procedure followed in this work does not provide the required precision and accuracy.
- Measurements are possible only with TQ-ICP-MS that uses NH_3 (ammonia) and O_2 as cell reaction gases. Tests were made with and without ammonia (in the latter, O_2 was used).
  In matrices containing a high concentration of potential interfering elements (i.e., Y, Sr, Hf, Ta, etc.), the most accurate PGE values were obtained only with ammonia as a cell reaction gas. Interesting to note, however, is that if the expected abundances are in the range of 10- 100 ppb, O_2 gives precise and accurate results when elemental interferences have been previously evaluated.
- An interesting, result regards the measurements of the bulk PGE content in the pelagic limestone of the Gubbio (Italy) sequence, worldwide known as the Cretaceous/Paleogene (KT or $KP_{g)}$ boundary. The anomalous Ir content (3-4 order of magnitude higher than the background average of continental crust values) provides evidence for a meteoritic impact event, which is considered to be the trigger for one of the five largest biological extinction events that occurred on our planet.

5. Conclusive remarks and future prospects

Eight sample solutions from sediments close to the Ir enriched level were prepared using a low-pressure dissolution procedure. The results proved that this approach is efficient in determining the Ir content even at very low concentrations (< ppb level) in a carbonate matrix. TQ-ICP-MS measurements of solutions (low-pressure dissolution) are sensitive enough to discriminate the minim values of Ir enrichments attributable to the effect of a meteoritic impact.

To my knowledge, this procedure has never been applied to the (KT or KP_g) boundary tracing rocks in any geochemical study worldwide, which instead present data obtained by the INAA analytical method, which requires complex sample handling.

Interesting future prospects, related to the analytical work, would be to analyse geologically well characterised samples of the KT (or KP_g) level in Italy and worldwide, to determine the "minimum Ir enrichment value", (i.e., standard value). This would facilitate the identification of similar geological contexts which would have not been detected otherwise.

This aspect is addressed in a manuscript currently in preparation.

From the perspective of a scientific study for understanding the extent of even minimal PGE pollution in the environment this work can be considered as an original study about the PGE content in urban soils.

To my knowledge, it was the first time that measurements of the PGE content in urban soil of Emilia Romagna region (Italy) were obtained. As a preliminary result, the PGE content is strictly related to the characteristics of the local traffic (e.g., frequency, vehicle typology) and less to the nature of the soil. These data have to be validated by a large future analytical work, which would take into account many other variables related to the chemical/physical aspects and possibly contribute to the creation of a database of PGE risk in urban zones.

Finally, a further possible prospect could be to apply this analytical procedure to other fields, for example industrial applications, such as the recovery of secondary raw materials, which is becoming an unavoidable worldwide necessity. The simplified protocol tested in this thesis, would allow indicative and fast analyses of large quantity of samples in those cases when the high precision and accuracy of the data are not required.

References

Afiattalab, F. and Wasson, J.T. (1980) Composition of the metal phases in ordinary chondrites: implications regarding classification and metamorphism. Geochimica et Cosmochimica Acta, 44, 431-446.

Alard, O., Griffin, W.L., Lorand, J.P., Jackson S., and O'Reilly S.R. (2000) Non-chondritic distribution of highly siderophile elements in mantle sulfide. Nature, 407, 891–894.

Alard, O., Griffin, W.L., Pearson, N.J., Lorand, J.P. and O'Reilly, S.Y. (2002) New insights into the Re–Os systematics of sub-continental lithospheric mantle from in situ analysis of sulfides. Earth and Planetary Science Letters, 203, 651–663.

Alvarez, L.W., Alvarez, W., Asaro F. and Michel, H.V. (1980) Extraterrestrial cause for the Cretaceous-Tertiary extinction. Science, 208, 1095–1108.

Ando, A. (1984) New silicate rock reference materials issued from the Geological Survey of Japan, 1984. Geochemical Journal, 18, 215-216.

Arblaster, J.W. (1995) The thermodynamic properties of ruthenium on ITS-90. Calphad, 19, 339-347.

Arndt, N.T., Lesher, C.M. and Czamanske, G.K. (2005) Mantle-derived magmas and magmatic Ni–Cu–(PGE) deposits. Economic Geology 100th Anniversary Volume, 5–23.

Aulbach, S., Creaser, R.A., Pearson, N.J., Simonetti, S.S., Heaman, L.M., Griffin, W.L. and Stachel, T. (2009) Sulfide and whole rock Re–Os systematics of eclogite and pyroxenite xenoliths from the Slave Craton, Canada. Earth and Planetary Science Letters, 283, 48–58.

Balaram, V., Ramavati, M., Banakar, V.K., Hein, J.R., Rao, C.R.M., Gnaneswara Rao, T. and Dasaram, B. (2006) Determination of the platinum-group elements (PGE) and gold (Au) in manganese nodule reference samples by nickel sulphide fire-assay and Te coprecipitation with ICP-MS. Indian Journal of Marine Sciences, 35(1), 7-16.

Barefoot, R.R. and Van Loon, J.C. (1999) Recent advances in the determination of the platinum group elements and gold. Talanta, 49, 1-14.

Barnes S-J. and Ripley E.M. (2016) Highly siderophile and strongly chalcophile elements in magmatic ore deposits. Reviews in Mineralogy & Geochemisty, 81, 725–774.

Beccaluva, L., Bianchini, G., Bonadiman, C., Siena, F. and Vaccaro, C. (2004) Coexisting anorogenic and subduction-related metasomatism in mantle xenoliths from the Betic Cordillera (southern Spain). Lithos, 75, 67-87.

Becker, H., and Walker, R. J. (2003) In search of extant Tc in the early solar system: ^{98}Ru and ^{99}Ru abundances in iron meteorites and chondrites. Chemical Geology 196, 43–56. DOI 10.1016/S0009-2541(02)00406-0.

Becker, H. and Dale, C.W. (2016) Re–Pt–Os isotopic and highly siderophile element behavior in oceanic and continental mantle tectonite. Reviews in Mineralogy & Geochemisty, 81, 369–440.

Becker, H., Dalpe, C., and Walker, R. J. (2002) High-precision Ru isotopic measurements by multi-collector ICP-MS. Analyst 127, 775–780. DOI 10.1039/b200596d.

Becker, H., Horan, M.F., Walker, R.J., Gao, S., Lorand, J.P. and Rudnick, R.L. (2006) Highly siderophile element compositions of the earth's primitive mantle. Geochimica et Cosmochimica Acta, 70, 4528–4550. DOI 10.1016/j.gca.2006.06.004.

Bertrand, G., Cassard, D., Arvanitidis, N., Stanleyc, G. and the EuroGeoSurvey Mineral Resources Expert Groupd (2016) Map of critical raw material deposits in Europe. Energy Procedia. 97, 44 – 50.

Bianchini, G., Beccaluva, L., Nowell, G.M., Pearson, D.G. and Siena, F. (2011) Mantle xenoliths fromTallante (Betic Cordillera): insights into the multi-stage evolution of the south Iberian lithosphere. Lithos, 124, 308-318.

Bianchini, G., Natali, C., Di Giuseppe, D. and Beccaluva, L. (2012) Heavy metals in soils and sedimentary deposits of the Padanian Plain (Ferrara, Northern Italy): Characterisation and biomonitoring. Journal of Soils and Sediments,12 (7),1145-1153.

Birck, J.-L., Roy-Barman, M., and Capmas, F. (1997) Re–Os isotopic measurements at the femtomole level in natural samples. Geostandards Newsletter, 20, 19–27. DOI 10.1111/j.1751908X.1997.tb00528.x.

Bischoff, A., Palme, H., Ash, R.D., Clayton, R.N., Schultz, L., Herpers, U., Stoffler, D., Grady, M.M., Pillinger, C.T., Spettel, B., Weber, H., Grund, T., Endress, M., and Weber, D. (1993) Paired Renazzo-type (CR) carbonaceous chondrites from the Sahara. Geochimica et Cosmochimica Acta, 57, 1587–1603.

Bockrath, C., Ballhaus, C., and Holzheid, A. (2004) Fractionation of the Platinum-group elements during mantle melting. Science, 305, 1951–1953.

Bokhari, S.N.H., Meisel, T. and Walkner, C. (2015) Interference removals on Pd, Ru and Au with ICP-QQQ-MS in PGE RM. Geophysical Research Abstracts, 17, EGU2015-13473-2.

Bonadiman, C., Coltorti, M., Duggen, S., Paludetti, L., Siena, F., Thirlwal, M., and Upton, B.G.J (2008) Paleozoic subduction-related and kimberlite or carbonatite metasomatism in the Scottish lithosperic mantle. Journal of the Geological Society, 293, special volume, 303-333.

Bonadiman, C., Brombin, V., Andreozzi, G.B., Benna, P., Coltorti, M., Curetti, N., Faccini, B., Merli, M., Pelorosso, B., Stagno, V., Tesauro, M. and Pavese, A. (2021) Phlogopite-pargasite coexistence in an oxygen reduced spinel-peridotite ambient. Scientific Reports, 11, 11829.

Bond, G.C., (1991) General introduction to catalysis by platinum-group metals. *In*: F.R. Hartley (Ed.). Chemistry of the Platinum Group Metals: Recent Developments. Elsevier, New York, 106–123.

Boss, A.P. (2003) The solar nebula. *In*: A.M, Davis (Ed.). Meteorites, Comets, and Planets, Treatise on Geochemistry (First Edition), Elsevier-Pergamon, Oxford, 1, 63–82.

Brearley, A. J. and Jones R. H. (1998) Chondritic meteorites. *In*: J.J. Papike, (Ed.). Planetary Materials, Reviews in Mineralogy, Mineralogical Society of America, 36, 3-1 - 3-398.

Brenan, J.M. (2008a) The Platinum-Group Elements: "Admirably Adapted" for Science and Industry. Elements, 4, 227-232.

Brenan, J.M. (2008b) Re–Os fractionation by sulfide melt-silicate melt partitioning: A new spin. Chemical Geology, 248, 140–165.

Brenan, J.M. and McDonough, W.F. (2009) Core formation and metal–silicate fractionation of osmium and iridium from gold. Nature Geosciences 2, 798–801.

Brenan, J.M., Bennett, N.R. and Zajacz, Z. (2016) Experimental Results on Fractionation of the Highly Siderophile Elements (HSE) at variable pressures and temperatures during Planetary and Magmatic Differentiation. Reviews in Mineralogy and Geochemistry, 81, 1-87.

Bromfield, C.S. and Shride, A.F. (1956) Mineral resources of the San Carlos Indian Reservation Arizona. U.S. Geological Survey Bulletin, 1027-N, 613-91.

Bunch, T. E., Keil, K. and Olsen, E. (1970) Mineralogy and petrology of silicate inclusions in iron meteorites. Contribution in Mineralogy and Petrology, 25, 297-340.

Carlson, R.W., Shirey, S.B. and Schönbächler, M. (2008) Applications of PGE radioisotope systems in geo- and cosmochemistry. Elements, 4, 239–245.

Cassard, D., Bertrand, G., Billa, M., Serrano, J.J., Tourlière, B., Angel, J.M. and Gaál, G. (2015) ProMine Mineral Databases: New Tools to Asses Primary and Secondary Mineral Resources in Europe. *In:* P. Weihed (Ed.). 3D, 4D and Predictive Modelling of Major Mineral Belts in Europe, Mineral Resource Reviews, Springer International Publishing Switzerland, 9-58. DOI 10.1007/978-3-319-17428-0_2.

Cerceau, C.I., Carvalho, C.dF., Silveira Rabelo, A.C., Gouvea dos Santos, C., Dias Gonçalves, S.M. and Varej E.V. (2016) Recovering lead from cupel waste generated in gold analysis by Pb-Fire assay. Journal of Environmental Management, 183, 771-776.

Chen, K, Walker, R. J., Rudnick, R. L., Gao, S., Gaschnig, R. M., Puchtel, I. S., Tang, M. and Hu, Z.-C. (2016) Platinum-group element abundances and Re-Os isotopic systematics of the upper continental crust through time: Evidence from glacial diamictites. Geochimica et Cosmochimica Acta, 191, 1–16.

Chicchella, D., Fedele, L., De Vivo, B., Albanese, S. and Lima, A. (2008) Platinum group element distribution in the soils from urban areas of the Campania region (Italy). Geochemistry: Exploration, Environment, Analysis, 8, 31–40.

Chou, C.L. (1978) Fractionation of siderophile elements in the Earth's upper mantle. Proceedings of the Ninth Lunar and Planetary Science Conference, 1, 219–230.

Chu, Z. (2021) Analytical Methods for Os Isotope Ratios and Re-PGE Mass Fractions in Geological Samples. Frontiers in Chemistry. 8:615839. DOI 10.3389/fchem.2020.615839.

Chu, Z. Y., Yan, Y., Chen, Z., Guo, J., Yang, Y. Y., Li, C. F., et al. (2015a) A comprehensive method for precise determination of Re, Os, Ir, Ru, Pt, Pd concentrations and Os isotopic compositions in geological samples. Geostandard and Geoanalytical Research, 39, 151–169. DOI 10.1111/j.1751-908X.2014.00283.x.

Cinti, D., Angelone, M., Masi, U. and Cremisini C. (2002) Platinum levels in natural and urban soils from Rome and Latium (Italy): significance for pollution by automobile catalytic converter. Science of the Total Environment 293, 47–57.

Cohen, A.S. and Waters, F.G. (1996) Separation of osmium from geological materials by solvent extraction for analysis by thermal ionisation mass spectrometry. Analytica Chimica Acta, 332, 269–275.

Collins, G.S., Patel, N., Davison, T.M., Rae, A.S.P., Morgan, J.V. and Gulick, S.P.S. (2020) IODP-ICDP Expedition 364 Science Party and Third-Party Scientists. A steeply-inclined trajectory for the Chicxulub impact. Nature Communications 11, 1480.

Coltorti, M., Bonadiman, C., Hinton, R.W., Siena, F. and Upton B.G.J. (1999) Carbonatite metasomatism of the oceanic upper mantle: Evidence from clinopyroxenes and glasses in ultramafic xenoliths of Grande Comore, Indian Ocean. Journal of Petrology, 40, 133-165.

Dai, X., Koeberl, C. and Fröschl, H. (2001) Determination of platinum group elements in impact breccias using neutron activation analysis and ultrasonic nebulization inductively coupled plasma mass spectrometry after anion exchange preconcentration. Analytica Chimica Acta, 436, 79–85.

Dale, C.W., Macpherson, C.G., Pearson, D.G., Hammond, S.J. and Arculus, R.J. (2012) Inter-element fractionation of highly siderophile elements in the Tonga Arc due to flux melting of a depleted source. Geochimica et Cosmochimica Acta, 89, 202-225.

Day, J.M.D. and Walker, R.J. (2015) Highly siderophile element depletion in the Moon. Earth and Planetary Science Letters, 423, 114–12.

Day, J. M. D., Walker, R. J., and Warren, J. M. (2017) 186Os–187Os and highly siderophile element abundance systematics of the mantle revealed by abyssal peridotites and Os-rich alloys. Geochimica et Cosmochimica Acta, 200, 232–254. DOI 10.1016/j.gca.2016.12.013.

Day, J. M. D., Pearson, D. G., and Nowell, G. M. (2003) High precision rhenium and platinum isotope dilution analyses by plasma ionisation multi-collector mass spectrometry," In Plasma source mass spectrometry: applications and emerging technologies. Editors J. G. Holland and S. D. Tanner (Cambridge: The Royal Society of Chemistry), 374–390. DOI 10.1039/9781847551689- 00374.

Day, J.M.D., Brandon, A.D. and Walker, R.J. (2016) Highly Siderophile Elements in Earth, Mars, the Moon, and Asteroids. Reviews in Mineralogy & Geochemistry, 81, 161-238.

Day, J. M. D., Waters, C. L., Schaefer, B. F., Walker, R. J., and Turner, S. (2016b) Use of hydrofluoric acid desilicification in the determination of highly siderophile element abundances and Re–Pt–Os isotope systematics in mafic–ultramafic rocks. Geostandard and Geoanalytical Research, 40, 49–65. DOI 10.1111/j. 1751-908X.2015.00367.x.

Desprez, A., Demar, D., Jean-Soro, L., Pèru, D. and Bouet, S. (2016) Analysis of platinum group elements (PGE) in road dust CRM using the Agilent 8800 triple quadrupole ICP-MS in MS/MS mode. Technical Report © Agilent Technologies, Inc. 2016 Printed in EU, 2016-03-14 5991-6768EN.

Dubbiella-Jackowska, A., Kudłak, B. and Polkowska, Z. (2009) Environmental fate of traffic-derived Platinum Group Metals. Analytical Chemistry, 39, 251–271.

Dunn, T.L., Cressey, G., McSween Jr., H.Y., McCoy, T.J. and Bland, P.A. (2010) Analysis of ordinary chondrites using powder X-ray diffraction: 1. Modal mineral abundances. Meteoritics & Planetary Science 45, 123–134.

Engel, K. and McDonough, W.F. (2016) Geochemical models of the Earth and the crustal geoneutrino flux. *In*: L. Ludhova (Ed.). Geo-neutrino. Open Academic Press.

European Commission (2010) Anonymous authors. Critical raw materials for the EU- Report of the ad-hoc working group on defining critical raw materials. European Commission, Critical Raw Materials for the EU. Report of the Ad-Hoc Working Group on Defining Critical Raw Materials. Brussels, Belgium pp.85.

European Commission, (2014) Anonymous authors. Report on critical raw materials for the EU. Report of the ad-hoc Working Group in defining critical raw materials: Brussels, Belgium, pp.41.

Fischer-Gödde, M., Becker, H. and Wombacher, F. (2010) Rhodium, gold and other highly siderophile element abundances in chondritic meteorites. Geochimica et Cosmochimica Acta, 74, 356–379.

Fischer-Gödde, M., Becker, H., and Wombacher, F. (2011) Rhodium, gold and other highly siderophile elements in orogenic peridotites and peridotite xenoliths. Chemical Geology, 280, 365–383. DOI 10.1016/j.chemgeo.2010.11.024.

Folens, K., Van Labeke, M.C. and Laing, G.D. (2017) Impact of an Urban Environment on Trace Element Concentrations in Domestically Produced Lettuce (Lactuca sativa L.) Water Air Soil Pollution, 228 (12), 457. DOI 10.1007/s11270-017-3635-7.

Folens, K., Van Acker, T., Bolea-Fernandez, E., Cornelis, G., Vanhaecke, F., Laing, G.D. and Rauch, S. (2018) Identification of platinum nanoparticles in road dust leachate by single particle inductively coupled plasma-mass spectrometry. Science of the Total Environment, 615, 849-856.

References

Fortin, M.-A., Riddle, J., Desjardins-Langlais, Y., and Baker, D.R. (2015) The effect of water on the sulfur concentration at sulfide saturation (SCSS) in natural melts. Geochimica et Cosmochimica Acta, 160, 100–116.

Frank, E.A., Maier, W.D., S.J. and Mojzsis, S. (2016) Highly siderophile element abundances in Eoarchean komatiite and basalt protoliths. Contribution in Mineralogy and Petrology, 171, 29.

Frenzel, M., Kullik, J., Reuter, M.A. and Gutzmer, J., (2017) Raw material "criticality" - sense or nonsense? Journal of Physics D Applied Physics 50(12):123002. DOI 10.1088/1361-6463/aa5b64.

Frey, F.A. and Green, D.H. (1974) The mineralogy, geochemistry, and origin of lherzolite inclusions in Victorian basanites. Geochimica et Cosmochimca Acta, 38, 1023–1059.

Frey, F.A. and Prinz, M. (1978) Ultramafic inclusions from San Carlos, Arizona: petrological and geochemical data bearing on their petrogenesis. Earth and Planetary Science Letters, 38, 129–176.

Fritsche, J. and Meisel, T. (2004) Determination of anthropogenic input of Ru, Rh, Pd, Re, Os, Ir and Pt in soils along Austrian motorways by isotope dilution ICP-MS. Science of the Total Environment, 325, 145–154.

Galer, S.J.G. and O'Nions, R.K. (1989) Chemical and isotopic studies of ultramafic inclusions from the San Carlos volcanic field, Arizona: A bearing on their petrogenesis. Journal of Petrology, 30, 1033-1064.

Gannoun, A., Burton, K. W., Parkinson, I. J., Alard, O., Schiano, P., and Thomas, L. E. (2007) The scale and origin of the osmium isotope variations in mid-ocean ridge basalts. Earth and Planetary Science Letters, 259, 541–556. DOI 10.1016/j.epsl.2007.05.014.

Gannoun, A., Burton, K.W., Day, J.M.D., Harvey J., Schiano, P. and Parkinson, I. (2016) Highly siderophile element and Os isotope systematics of volcanic rocks at divergent and convergent plate boundaries and in intraplate settings. Reviews in Mineralogy and Geochemistry, 81, 651–724.

Girolami, G.S. (2012) Osmium weighs in. Nature Chemistry, 4, 954.

Gladney, E.S., Burns, C.E. and Roelandts, I. (1984) 1982 compilation of elemental concentration data for the United States Geological Survey's geochemical exploration reference samples GXR-1 to GXR-6. Geostandards Newsletter, 8, 119-154.

Goddin, J.R.J. (2019) Identifying supply Chain risks for critical and strategic materials. *In*: S.E. Offerman (Ed.). Critical Materials - Underlying Causes and Sustainable Mitigation Strategies. World Scientific Publishing Co. Pte. Ltd., Singapore, 117–150.

Goderis, S., Sato, H., Ferrière L., Birger Schmit B., Burney D., Kaskes, P., Vellekoop,J., Wittmann, A., Chernonozhkin ,S.M., Claeys, P., De Graaff, S.J., Déhais, T., De Winter, N.J., Elfman, M., Feignon, J-G., Ishikawa, A., Koeberl, C., Kristiansson, P., Neal, C.R., Owens, J.O., Schmieder, M., Sinnesael, M., Vanhaecke, F., Van Malderen,S.J.M., BralowerT.J., Gulick, S.P.S., Kring, D.A., Lowery, C.M., Morgan, J.V., Smit, J., Whalen, M.T. and Iodp-Icdp Expedition 364 Scientists (2021) Globally distributed iridium layer preserved within the Chicxulub impact structure. Science Advances, 7, 9, eabe3647.

Goldberg, E., Uchiyama, A. and Harrison, B. (1951) The distribution of nickel, cobalt, gallium, palladium and gold in iron meteorites. Geochimica et Cosmochimca Acta, 2, 1-25.

Goldstein, J.I., Scott, E.R.D. and Chabot, N.L. (2009) Iron meteorites: Crystallization, thermal history, parent bodies, and origin. Geochemistry, 69, 293-325.

Gordon, C. L. (1943) Modification of the Carius combustion tube to minimize losses by explosion: pressures attained on heating nitric acid to 300°C. Journal of Research of the National Bureau of Standards, 30, 107–111. DOI 10.6028/jres.030.009.

Gordon, C. L., Schlecht, W. G., and Wichers, E. (1944) Use of sealed tubes for the preparation of acid solutions of samples for analysis, or for small-scale refining: pressures of acids heated above 100°C. Journal of Research of the National Bureau of Standards, 33, 457–470. DOI 10.6028/jres.033.027.

Gradstein, F.M., Ogg, J.G., Schmitz, M. and Ogg G. (Eds.) (2012) The Geologic Time Scale, Elsevier.

Graedel, T.E., Barr, R., Chandler, C., Chase, T., Choi, J., Christoffersen, L., Friedlander, E., Henly, C., Jun, C., Nassar, N.T., Schechner, D., Warren, S., Yang, M.-Y. and Zhu, C. (2012) Methodology of metal criticality determination. Environmental Science & Technology, 46, 1063–1070. doi.org/10.1021/es203534z.

Griffin, W.L., Graham, S., O'Reilly, S.Y. and Pearson, N.J. (2004) Lithosphere evolution beneath the Kaapvaal Craton: Re–Os systematics of sulfides in mantle-derived peridotites. Chemical Geology, 208, 89–118.

Gros, M., Lorand, J.P. and Luguet, A. (2002) Analysis of platinum group elements and gold in geological materials using NiS fire assay and Te coprecipitation; the NiS dissolution step revisited. Chemical Geology, 185, 179-190.

Grossman, L. (1972) Condensation in the primitive solar nebula. Geochimica et Cosmochimica Acta, 36, 597, 619.

Grossman, L. and Larimer J. W. (1974) Early chemical history of the solar system. Reviews of Geophysics and Space Physics, 12, 71–101.

Grossman, J.N. and Brearley, A.J. (2005) The onset of metasomatism in ordinary and carbonaceous chondrites. Meteoritics & Planetary Science, 40, 87–122.

Guo, F.F., Svetov, S., Maier, W.D., Hanski, E., Yang, S.H. and Rybnikova, Z. (2020) Geochemistry of komatiites and basalts in Archean greenstone belts of Russian Karelia with emphasis on platinum-group elements. Mineralium Deposita, 55, 971–990. DOI org/10.1007/s00126-019-00909-0.

Harvey, J., Gannoun, A., Burton, K.W., Schiano, P., Rogers, N.W. and Alard, O. (2010) Unravelling the effects of melt depletion and secondary infiltration on mantle Re–Os isotopes beneath the French Massif Central. Geochimica et Cosmochimca Acta, 74, 293–320. DOI 10.1016/j.gca.2009.09.031.

Hassler, D.R., Peucker-Ehrenbrink, B. and Ravizza, G.E. (2000) Rapid determination of Os isotopic composition by sparging OsO4 into a magnetic-sector ICP-MS. Chemical Geology, 166, 1–14.

Helmers, E. (1997) Platinum emission rate of automobiles with catalytic converters – Comparison and assessment of results from various approaches. Environmental Science and Pollution Research, 4, 100-103.

Hoatson, D.M., (1998) Platinum-group element mineralisation in Australian Precambrian layered mafic–ultramafic intrusions. Journal of Australian Geology and Geophysics., 17, 139–151.

Hooda, P.S., Miller, A. and Edwards, A.C. (2007) The distribution of automobile catalysts-cast platinum, palladium and rhodium in soils adjacent to roads and their uptake by grass. Science of the Total Environment, 384, 384–392.

Huss, G. R., Deloule, E., Hutcheon, I. D. and Wasserburg, G. J. (1993) Compositional heterogeneity in Orgueil Sic: More comparisons with Murchison. Meteoritics, 28, 368-369.

Huss, G. R., Rubin, A. E. and Grossman, J. N. (2006) Thermal Metamorphism in Chondrites. *In*: D.S. Lauretta and H.Y. McSween Jr. (Eds.). Meteorites and the Early Solar System II, University of Arizona Press, Tucson, 567-586.

Hwang, H.-M., Fiala, M.J., Park, D. and Wade, T.L. (2016) Review of pollutants in urban road dust and stormwater runoff: part 1. Heavy metals released from vehicles. International Journal of Urban Sciences, 20, 334-360. DOI 10.1080/12265934.2016.1193041.

Iavicoli, I. and Leso, V. (2015) Iridium. *In*: G.F Nordberg, B.A. Fowler and M. Nordberg (Eds.). Handbook on the Toxicology of Metals, vol 2. 4E. Elsevier, 855-878.

Ishikawa, A., Senda, R., Suzuki, K., Dale, C.W. and Meisel, T. (2014) Re-evaluation digestion methods for highly siderophile element and 187 Os Isotope analysis: evidence from geological reference materials. Chemical Geology, 384, 27–46. DOI 10.1016/j.chemgeo.2014.06.013.

Jacobson, S.A., Morbidelli, A., Raymond, S.N., O'Brien, D.P., Walsh, K.J. and Rubie, D.C. (2014) Highly siderophile elements in Earth's mantle as clock for the Moon-forming impact. Nature, 508, 84–87.

Jagoutz, E., Palme, H., Blum, H., Cendales, M., Dreibus, G., Spettel, B., Lorenz, V. and Wänke, H. (1979) The abundances of major, minor and trace elements in the Earth's mantle as derived from primitive ultramafic nodules. Proceedings of the Tenth Lunar and Planetary Science Conference 2 (A80–23617 08–91), 2031–2050.

Jarosewich, E.J, Nelen, J.A. and Norberg, J.A. (1980) Reference samples for electron microprobe analysis Geostandards Newsletter., 4, 43-47.

Jochum, K.P., Nohl, U., Herwing, K., Lammel, E. Stoll, B. and Hofmann, A.W (2005) GeoRem: A New Geochemical Database for Reference Materials and Isotopic Standards. Geostandards and Geoanalytical Research, 29 (3), 333-338. DOI 10.1111/j.1751-908X.2005.tb00904.x.

Johnson, T., Benedix, G., Bland, P. (2016) Metamorphism and partial melting of ordinary chondrites: Calculated phase equilibria. Earth and Planetary Science Letters, 433, 21-30.

Juvonen, R., Lakomaa, T. and Soikkeli, L. (2002) Determination of gold and the platinum group elements in geological samples by ICP-MS after nickel sulphide fire assay: difficulties encountered with different types of geological samples. Talanta, 58, 595-603.

Karandashev, V.K., Khvostikov, V.A., Nosenko, S.V. and Burmii, Zh.P. (2017) Stable Highly Enriched Isotopes in Routine Analysis of Rocks, Soils, Grounds, and Sediments by ICP-MS. Inorganic Materials, 53, 1432–1441.

Kimura, K., Lewis, R.S. and Anders, E. (1974) Distribution of gold and rhenium between nickel–iron and silicate melts: implications for abundance of siderophile elements on the Earth and Moon. Geochimica et Cosmochimica Acta. 38, 683–701.

Kiseeva, K. and Wood, B.J. (2015) The effects of composition and temperature on chalcophile and lithophile element partitioning into magmatic sulphides. Earth and Planetary Science Letters, 26, DOI 10.1016/j.epsl.2015.05.012.

Kleine, T., Münker, C., Mezger, K. and Palme, H. (2002) Rapid accretion and early core formation on asteroids and the terrestrial planets from Hf-W chronometry. Nature, 418(6901), 952-955.

Koeberl, Ch. (2006) Impact Processes on the Early Earth. Elements, 2, 211-216.

Koek, M., Kreuzer, O.P., Maier, W.D., Porwal, A.K., Thompson M. and Guj P. (2010) A review of the PGM industry, deposit models and exploration practices: implications for Australia's PGM potential. Resources Policy, 35, 20–35.

Krot, A.N., Keil, K, Scott, E.R.D., Goodrich, C.A. and Weisberg M.K. (2014) Classification of Meteorites and their genetic relationships. *In:* H.D. Holland and K.T. Turekian (Eds.). Treatise on Geochemistry (Second Edition), Elsevier, 1, 1-68.

Kutscher, D., Leykin, A., Nelms, S. and McSheehy Ducos, S. (2018) ICP-MS Analysis of Noble Metals at Low Levels in Geological Reference Materials and Ores. Spectroscopy, 33, 16-25.

Kutscher, D., Leykin, A., Nelms, S. and McSheehy Ducos, S. (2019) Analysis of noble metals at low levels in geological reference materials and ores. Application note 44410 ©Thermo Fisher Scientific.

Latunussa, C.E.L., Georgitzikis, K., Torres de Matos, C., Grohol, M., Eynard, U., Wittmer D., Mancini, L., Unguru M., Pavel C., Carrara, S., Mathieux, F., Pennington, D. and Blengini, G.A. (2020) Study on the EU's list of Critical Raw Materials (2020) Critical Raw Materials Factsheets (Final): Brussels, Belgium. EC, Brussels. (Belgium), 1-819.

Le Maitre, R., Streckeisen, A., Zanettin, B., Le Bas, M., Bonin, B., and Bateman, P. (Eds.) (2002) Igneous Rocks: A Classification and Glossary of Terms: Recommendations of the International Union of Geological Sciences Subcommission on the Systematics of Igneous Rocks (Second Edition). Cambridge University Press.

Lesniewska, B.A., Godlewska-Zylkiewicz, B., Bocca, B., Caimi, S., Caroli, S. and Hulanicki A. (2004) Platinum, Palladium and Rhodium content in road dust, tunnel dust and common grass in Bialistok area (Poland): a pilot study. Science of the Total Environment, 321, 93–104. DOI 10.1016/j.scitotenv.2003.07.004.

Li, J., Jiang, X.-Y., Xu, J.-F., Zhong, L.-F., Wang, X.-C., Wang, G.-Q., et al. (2014) Determination of platinum-group elements and Re–Os isotopes using ID-ICP MS and N-TIMS from a single digestion after two-stage column separation. Geostandard and Geoanalytical Research, 383, 37–50. DOI 10.1111/j.1751-908X.2013.00242.x.

Li, J., Zhao, P. P., Liu, J., Wang, X. C., Yang, A. Y., Wang, G. Q., et al. (2015). Reassessment of hydrofluoric acid desilicification in the Carius tube digestion technique for Re–Os isotopic determination in geological samples. Geostandard and Geoanalytical Research, 39, 17–30. DOI 10.1111/j.1751 908X.2014.00299.x.

Liu, J., and Selby, D. (2018) A matrix-matched reference material for validating petroleum Re-Os measurements. Geostandard and Geoanalytical Research, 42 (1), 1–17. DOI 10.1111/ggr.12193.

Lodders, K. (2003) Solar System abundances and condensation temperatures of the elements. The Astrophysical Journal, 591, 220-1247.

Lodders, K., Palme, H. and Gail, H.P. (2009) Abundances of the Elements in the Solar System. *In*: J.E, Trumper (Ed.). Astronomy and Astrophysics, Landolt-Bornstein, New Series, VI/4B, 4.4, Berlin, Springer-Verlag, 560-630.

Lorand J.-P., Luguet A. and Alard O. (2008) Platinum-Group Elements: A New Set of Key Tracers for the Earth's Interior Elements, 4, 247-252. doi: 10.2113/gselements.4.4.247.

Lorand, J.-P., Alard, O. and Godard, M. (2009) Platinum-group element signature of the primitive mantle rejuvenated by melt-rock reactions: evidence from Sumail peridotites (Oman Ophiolite). Terra Nova, 21, 35-40. DOI 10.1111/j.1365-3121.2008.00850.x.

Lorand, J.-P., Luguet, A. and Alard, O. (2013) Platinum-group element systematics and petrogenetic processing of the continental upper mantle: A review. Lithos, 164-167, 2-21.

Lugari, C., Boadiman, C., Martucci, A., Rodeghero, E., Tassinari, R. and Vaccaro, C. (2018). Preliminary chemical and mineralogical analyses of two ordinary chondrites from Draa Valley, Zagora (Morocco). Plinius, 44, 286. doi:10.19276/plinius.2018.03016.

Luguet, A. and Reisberg, L. (2016) Highly siderophile element and ^{187}Os signatures in non–cratonic basalt–hosted peridotite xenoliths: Unravelling the origin and evolution of the post-Archean lithospheric mantle. Reviews in Mineralogy & Geochemistry, 81, 305–367.

Luguet, A., Shirey, S. B., Lorand, J.-P., Horan, M. F., and Carlson, R. W. (2007) Residual platinum-group minerals from highly depleted harzburgites of the Lherz (France) and their role in HSE fractionation of the mantle. Geochimica et Cosmochimica Acta, 71, 3082–3097. DOI 10.1016/j.gca.2007.04.011.

Luguet, A., Nowell, G. M., and Pearson, D. G. (2008) 184Os/188Os and 186Os/188Os measurements by negative thermal ionisation mass spectrometry (N-TIMS): effects of interfering element and mass fractionation corrections on data accuracy and precision. Chemical Geology, 248, 342–362. DOI 10.1016/j.chemgeo. 2007.10.013.

Lyubomirova, V. and Djingova, R. (2015) Accumulation and distribution of Pt and Pd in roadside dust, soil and vegetation in Bulgaria. *In:* F. Zereini and C.L.S. Wiseman (Eds.). Platinum Metals in the Environment 243-255. doi: 10.1007/978-3-662-44559-4_15.

Marchesi, C., Griffin, W.L., Garrido, C.J., Bodinier, J.L. and Pearson, N.J. (2010) Persistence of mantle lithospheric Re-Os signature during asthenospherization of the subcontinental lithospheric mantle: insights from in situ isotopic analysis of sulfides from the Ronda peridotite (Southern Spain). Contribution in Mineralogy and Petrology, 159, 315–330.

Markey, R., Stein, H. J., Hannah, J. L., Zimmerman, A., Selby, D., and Creaser, R. A. (2007) Standardizing Re–Os geochronology: a new molybdenite reference material (Henderson, USA) and the stoichiometry of Os salts. Chemical Geology, 244, 74–87. DOI 10.1016/j.chemgeo.2007.06.002.

Mavrogenes, J.A. and O'Neill, H.St.C. (1999) The relative effects of pressure, tem-perature and oxygen fugacity on the solubility of sulfide in mafic magmas. Geochimica et Cosmochimica Acta, 63, 1173–1180.

McBride, N. and Gilmor, I. (Eds.) (2005) An introduction to the Solar System, Cambridge: The Open University and Cambridge University Press.

McDonough, W. F. (2014) Compositional model for the Earth's core. *In*: H.D. Holland, K.K. Turekian (eds). Treatise on Geochemistry (Second Edition), Vol. 3, 559–577 Elsevier.

McDonough, W.F. (2017). Earth's Core. *In:* W.M. White (Ed.). Encyclopedia of Geochemistry. Springer International Publishing AG. DOI 10.1007/978-3-319-39193-9_258-1.

McDonough, W.F. and Sun, S.S. (1995) The Composition of the Earth. Chemical Geology, 120, 223-253.

Meisel, T. and Moser J. (2004a) Reference materials for geochemical PGE analysis: new analytical data for Ru, Rh, Pd, Os, Ir, Pt and Re by isotope dilution ICP-MS in 11 geological reference materials. Chemical Geology, 208, 319–338.

Meisel, T., and Moser, J. (2004b) Platinum-group element and rhenium concentrations in low abundance reference materials. Geostandard and Geoanalytical Research, 28, 233–250. DOI 10.1111/j.1751-908X.2004.tb00740.x.

Meisel, T. and Horan, M.F. (2016) Analytical Methods for the Highly Siderophile Elements. Reviews in Mineralogy & Geochemisty, 81, 89-106.

Meisel, T., Moser, J. and Wegscheider, W. (2001a) Recognizing heterogeneous distribution of platinum group elements (PGE) in geological materials by means of the Re–Os isotope system. Fresenius' Journal of Analytical Chemistry, 370, 566–572.

Meisel, T., Moser, J., Fellner, N., Wegscheider, W. and Schoenberg, R. (2001b) Simplified method for the determination of Ru, Pd, Re, Os, Ir and Pt in chromitites and other geological materials by isotope dilution ICP-MS and acid digestion. Analyst, 126, 322–328.

Meisel, T., Reisberg, L., Moser, J., Carignan, J., Melcher, F. and Brügmann, G. (2003a) Re–Os systematics of UBN, a serpentinised peridotite reference material. Chemical Geology, 201, 161–179.

Meisel, T., Fellner, N., and Moser, J. (2003b) A simple procedure for the determination of platinum group elements and rhenium (Ru, Rh, Pd, Re, Os, Ir and Pt) using ID-ICP-MS with an inexpensive on-line matrix separation in geological and environmental materials. Journal of Analytical Atomic Spectrometry, 18, 720–726. DOI 10.1039/b301754k.

Melchiorre, M., Coltorti, M., Bonadiman, C., Faccini, B., O'Reilly, S.Y. and Pearson, N.J. (2011) The role of eclogite in the rift-related metasomatism and Cenozoic magmatism of Northern Victoria Land, Antarctica, Lithos, 124, 319-330.

Moldovan, M., Palacios, M.A., Gomez, M.M., Morrison, G., Rauch, S., McLeod, C., Ma, R., Caroli, S., Alimonti, A., Petrucci, F., Bocca, B., Schramel, P., Zischka, M., Pettersson, C., Wass, U., Luna, M., Saenz J.C. and Santamaria, J. (2002) Environmental risk of particulate and soluble platinum group

elements released from gasoline and diesel engine catalytic converters. Science of the Total Environment, 296, 199-208.

Moldovan, M., Rauch, S., Morrison, G. M., Gomez, M. and Palacios, M.A. (2003) Impact of ageing on the distribution of platinum group elements and catalyst poisoning elements in automobile catalysts. Surface and Interface Analysis, 35 (4), 354–359.

Montanari, A. and Coccioni R. (2019) The serendipitous discovery of an extraterrestrial iridium anomaly at the Cretaceous-Palaeogene boundary in Gubbio and the rise of a far-reaching theory. Bollettino della Società Paleontologica Italiana, 58 (1), 77-83.

Morcelli, C.P.R., Figueiredo, A.M.G, Enzweiler, J., Sarkis J.E.S., Jorge, A.P.S. and Kakazu, M. (2004) Determination of Platinum-Group Elements in Geological Reference Materials by High Resolution-ICP-MS after Nickel Sulfide Fire-Assay Collection and Te Co-Precipitation. Geostandards and Geoanalytical Research, 28-2, 305-310.

Morgan, J. W., and Walker, J. M. (1989) Isotopic determinations of rhenium and osmium in meteorites by using fusion, distillation and ion-exchange separations. Anal. Chim. Acta. 222, 291–300. DOI 10.1016/S0003-2670(00)81904-2.

Mudd, G.M. (2012) Key trends in the resource sustainability of platinum group elements. Ore Geology Reviews, 46, 106–117.

Mudd, G.M., Jowitt, S.M. and Werner T.T. (2018) Global platinum group element resources, reserves and mining - A critical assessment. Science of the Total Environment, 622-623, 614-625.

Mungall, J.E. and Naldrett, A.J. (2008) Ore deposits of the platinum-group elements. Elements, 4, 253–258.

Mungall, J.E. and Brenan, J.M. (2014) Partitioning of Platinum Group Elements and Au between liquid and basalt and the origin of the crust–mantle fractionation of the chalcophile elements. Geochimica et Cosmochimica Acta, 125, 265–289.

Naldrett, A.J. (2010) Secular Variation of Magmatic Sulfide Deposits and Their Source Magmas. Economic Geology, 105, 669-688.

Naldrett, A.J. (2011) Fundamentals of magmatic sulfide deposits. Reviews in Economic Geology, 17, 1–50.

Naldrett, A.J. and Duke, J.M. (1980) Platinum metals in magmatic sulphide ores. Science, 208, 1417-1424.

O'Driscoll, B. and González-Jiménez, J. (2016) Petrogenesis of the platinum-group minerals. Reviews in Mineralogy & Geochemisty, 81, 489–578.

O'Neill, H.St.C., and Mavrogenes, J.A. (2002) The sulfide capacity and the sulfur content at sulfide saturation of silicate melts at 1400°C and 1 bar. Journal of Petrology, 43, 1049–1087.

O'Neill, HStC., Dingwell, D.B., Borisov, A., Spettel, B. and Palme, H. (1995) Experimental petrochemistry of some highly siderophile elements at high temperatures, and some implications for core formation and the mantle's early history. Chemical Geology, 120, 255–273.

Palacios, M.A., Gomez, M.M., Moldovan, M., Morrison, G., Rauch, S., McLeod, C., Ma, R., Laserna, J., Lucena, P., Caroli, S., Alimonti, A., Petrucci, F., Bocca, B., Schramel, P., Lustig, S., Zischka, M., Wass, U., Stenbom, B., Luna, M., Saenz, J.C., Santamaria, J. and Torrens, J.M. (2000) Platinum-group elements: quantification exhaust fumes and studies of catalyst surfaces. Science of the Total Environment, 257, 1-15.

Palme, H. (2008) Platinum-Group Elements in Cosmochemistry. Elements, 4, 233-238.

Palme, H. and O'Neill, HStC. (2014) Cosmochemical estimates of mantle composition. *In*: R.W. Carlson, R. W. (Ed.). Treatise on Geochemistry (Second Edition), Elsevier, 3, 1–39.

Palme, H., Lodders, K. and Jones A. (2014) Solar System Abundances of the Elements. *In*: H.D., Holland, K.T., Turekian, (Eds.). Treatise on Geochemistry (Second Edition), Elsevier, 2, 15-36.

Papike J.J, Ryder, G. and Shearer, C.H. (1998) Lunar Samples. Reviews in Mineralogy and Geochemistry, 36, 5.1-5.234.

Pearson, D.G. and Woodland, S.J. (2000) Solvent extraction / anion exchange separation and determination of PGEs (Os, Ir, Pt, Pd, Ru) and Re-Os isotopes in geological samples by isotope dilution ICP-MS. Chemical Geology, 165, 87–107.

Pearson, N. J., Alard, O., Griffin, W. L., Jackson, S. E., and O'Reilly, S. Y. (2002) In situ measurement of Re–Os isotopes in mantle sulfides by laser ablation multicollector-inductively coupled plasma mass spectrometry: analytical methods and preliminary results. Geochimica et Cosmochimica Acta, 66, 1037–1050. DOI 10.1016/S0016-7037(01)00823-7.

Pearson, D.G., Canil, D. and Shirey S.B. (2003) Mantle samples included in volcanic rocks: xenoliths and diamonds. *In*: R.W. Carlson (Ed.). Treatise on Geochemistry (First edition), 2, 171–276.

Pearson, D.G., Irvine, G.J., Ionov, D.A., Boyd, F.R. and Dreibus, G.E. (2004) Re–Os isotope systematics and platinum group element fractionation during mantle melt extraction: a study of massif and xenolith peridotite suites. Chemical Geology, 208, 29–59.

Perry, B.J., Van Loon, J.C. and Speller, D.V. (1992) Dry-chlorination Inductively coupled plasma mass spectrometric method for the determination of platinum group elements in rocks. Journal of Analytical Atomic Spectrometry, 7, 883-888.

Pilchin, A. and Eppelbaum L. (2017) Concentration of Platinum Group Elements during the Early Earth Evolution: A Review. Natural Resources, 8, 172-233. DOI 10.4236/nr.2017.83012.

Puchtel, I. S., Walker, R. J., Touboul, M., Nisbet, E. G. and Byerly, G. R. (2014) Insights into early Earth from the Pt–Re–Os isotope and highly siderophile element abundance systematics of Barberton komatiites. Geochimica et Cosmochimica Acta, 125, 394–413.

Qi, L. and Zhou M.F. (2008) Determination of Platinum-Group Elements in OPY-1: Comparison of Results using Different Digestion Techniques. Geostandards and Geoanalytical Research, 32-3, 377-387.

Qi, L., Zhou, M. F., and Wang, C. Y. (2004) Determination of low concentrations of platinum group elements in geological samples by ID-ICP-MS. Journal of Analytical Atomic Spectrometry, 19, 1335–1339. DOI 10.1039/b400742e.

Qi, L., Zhou, M.F., Wang, C.Y. and Sun, M. (2007) Evaluation of a technique for determining Re and PGEs in geological samples by ICP-MS coupled with a modified Carius tube digestion. Geochemical Journal 41, 407-414.

Qi, L., Zhou, M. F., Gao, J. F., and Zhao, Z. (2010) An improved Carius tube technique for determination of low concentrations of Re and Os in pyrites. Journal of Analytical Atomic Spectrometry, 25, 585–589. DOI 10.1039/b919016c.

Qi, L., Gao, J. F., Huang, X. W., Hu, J., Zhou, M. F., and Zhong, H. (2011) An improved digestion technique for determination of platinum-group elements in geological samples. Journal of Analytical Atomic Spectrometry, 26, 1900–1904. DOI 10.1039/c1ja10114e.

Rauch S. and Morrison G.M. (2008) Environmental Relevance of the Platinum-Group Elements. Element, 4, 259-263.

Rauch, S., Hemond, H.F. and Peucker-Ehrenbrink, B. (2004) Recent changes in platinum group element concentrations and osmium isotopic composition in sediments from an urban lake. Environmental Science & Technology, 38, 396-402.

Rauch, S., Hemond, H.F., Barbante, C., Owari, M., Morrison, G.M., Peucker-Ehrenbrink, B. and Wass, U. (2005) Importance of Automobile Exhaust Catalyst Emission for the Deposition of Platinum, Palladium and Rhodium in the Northern Hemisphere. Environmental Science & Technology, 29, 8156-9162.

Ravindra, K., Bencs, L. and Van Grieken, R. (2004) Platinum group elements in the environment and their health risk. Science of the Total Environment, 318, 1-43.

Reisberg, L., and Meisel, T. (2002) The Re-Os isotopic system: a review of the analytical techniques. Geostandards Newsletter, 26, 249–267. DOI 10.1111/j.1751-908X.2002.tb00633.x.

Reith, F., Campbell, S.G., Ball, A.S., Pring, A. and Southam, G. (2014) Platinum in earth surface environments. Earth Science Reviews, 131, 1–21. DOI 10.1016/J.EARSCIREV.2014.01.003.

Righter, K. (2003) Metal–silicate partitioning of siderophile elements and core formation in the early Earth. Annual Review of Earth and Planetary Sciences, 31, 135–174.

Righter, K. and Drake, M. J. (1996). Core formation in Earth's Moon, Mars, and Vesta. Icarus, 124, 512–528.

Righter, K., Danielson, L.R., Pando, K.M., Williams, J., Humayun, M., Hervig, R.L. and Sharp T.G. (2015) Highly siderophile element (HSE) abundances in the mantle of Mars are due to core formation at high pressure and temperature. Meteoritics & Planetary Science, 50, 1–28.

Rubie, D.C., Frost, D.J., Mann, U., Asahara, Y., Nimmo, F., Tsuno, K., Kegler, P., Holzheid, A., and Palme, H. (2011) Heterogeneous accretion, composition and core-mantle differentiation of the Earth, Earth Planet. Sci. Lett., 301, 31–42. DOI 10.1016/j.epsl.2010.11.030.

Rubie, D.C., Laurenz, V., Jacobson, S.A., Morbidelli, A., Palme, H., Vogel, A.K. and Frost, D.J. (2016) Highly siderophile elements were stripped from Earth's mantle by iron sulfide segregation. Science, 353(6304), 1141-1144.

Rushmer, T., Minarik, W.G., Taylor G.J. (2000) Physical processes of core formation. *In:* R.M. Canup and K. Righter (Eds.). Origin of the Earth and Moon, University of Arizona Press, Tucson, 227-243.

Schrijvers, D., Hool, A., Blengini, G.A., Chen, W.Q., Dewulf, J., Eggert, R., van Ellen, L., Gauss, R., Goddin, J., Habib, K., Hagelüken, C., Hirohata, A., Hofmann-Amtenbrink, M., Kosmol, J., Le Gleuher, M., Grohol, M., Ku, A., Lee, M.H., Liu, G., Nansai, K., Nuss, P., Peck, D., Reller, A., Sonnemann, G., Tercero, L., Thorenz, A. and Wäger, P.A. (2020) A review of methods and data to determine raw material criticality. Resources, Conservation & Recycling, 155, 1-17.

Schulte, P., Alegret, L., Arenillas ,I., Arz, J.A., Barton, P.J., Bown, P.R., Bralower, T.J., Christeson, G.L., Claeys, P., Cockell, C.S., Collins, G.S, Deutsch, A. , Goldin ,T.J., Goto, K., Grajales-Nishimura, J.M., Grieve, R.A.F. , Gulick, S.P.S., Johnson, K.R. , Kiessling, W., Koeberl, C., Kring, D.A., MacLeod, K.G., Matsu,i T., Melosh, J., Montanari, A., Morgan ,J.V., Neal, C.R., Reimold, D.J., Nichols, R.D., Norris, E., Pierazzo, G., Ravizza, M., Rebolledo-Vieyra, W.U., Robin, E., Salge, T., Speijer R.P., Sweet, A.R., Urrutia-Fucugauchi, J., Vajda, V., Whalen, M.T. and Willumsen P.S. (2010) The Chicxulub asteroid impact and mass extinction at the Cretaceous-Paleogene boundary. Science 327, 1214–1218.

Scott, E.R.D. (1972) Chemical fractionation in iron meteorites and its interpretation. Geochimica et Cosmochimica Acta 36, 1205- 1236.

Scott E.R.D. and Krot A.N. (2014) Chondrites and their components. *In*: A.M. Davis (Ed.) Meteorites and Cosmochemical Processes. Treatise on Geochemistry (Second Edition), Elsevier, 1, 65-137.

Sharpless, K.B. (2002) Searching for new reactivity (Nobel lecture). Angewandte Chemie International Edition. 241(12):2024-2032. PMID: 19746596.

Shirai, N., Nishino, T., Li, X., Amakawa, H. and Ebihara, M. (2003) Precise determination of PGE in a GSJ reference sample JP-1 by ID-ICPMS after nickel sulphide fire assay preconcentration. Geochemical Journal, 37, 531-536.

Shirey, S. B., and Walker, R. J. (1995) Carius tube digestion for low blank rhenium osmium analysis. Analytical Chemistry, 34, 2136–2141. DOI 10.1021/ac00109a036.

Sylvester, P.J, and Stephen M. Eggins, S.M. (1997) Analysis of Re, Au, Pd, Pt and Rh in NIST Glass Certified Reference Materials and Natural Basalt Glasses by Laser Ablation ICP-MS. Geostandards Newsletters, 21, 215-229.

Simitchiev, K., Stefanova, V., Kmetov, V., Andreev, G., Sanchez, A. and Canals A. (2008) Investigation of ICP-MS spectral interferences in the determination of Rh, Pd and Pt in road dust: Assessment of correction algorithms via uncertainty budget analysis and interference alleviation by preliminary acid leaching. Talanta, 77, 889–896.

Smith, D.G.W., Miúra, Y. and Launspach, S. (1993) Fe, Ni and Co variations in the metals of some antarctic chondrites. Earth and Planetary Science Letters 120, 487-498.

Smythe, D.J., Bernard, J., Wood B.J. and Kiseeva E.S. (2017) The S content of silicate melts at sulfide saturation: New experiments and a model incorporating the effects of sulfide composition. American Mineralogist, 102-4. DOI 10.2138/am-2017-5800CCBY.

Sugiyama, N. (2017) Removal of Complex Spectral Interferences on Noble Metal Isotopes. *In:* Handbook of ICP-QQQ Applications using the Agilent 8800 and 8900 ©Agilent Technologies,5991-2802EN, 87-91.

Sugiyama, N. and Shikamori, Y. (2015) Removal of spectral interferences on noble metal element using MS/MS reaction cell mode of a triple quadrupole ICP-MS. Journal of Analytical Atomic Spectrometry, 30, 2481-2487.

Sun, S.S. (1982) Chemical composition and origin of the earth's primitive mantle. Geochimica et Cosmochimica Acta, 46, 179-192.

Sun, Y. L., Zhou, M. F., and Sun, M. (2001) Routine Os analysis by isotope dilution inductively coupled plasma mass spectrometry: OsO_4 in water solution gives high sensitivity. J. Anal. At. Spectrom. 16, 345–349. DOI 10.1039/b008533m.

Sutherland, R.A., Pearson, D.G. and Ottley C.J. (2007) Platinum-group elements (Ir, Pd, Pt nd Rh) in road-deposited sediments in two urban watersheds, Hawaii. Applied Geochemistry, 22, 1485-1501.

Tagle, R. and Hecht L. (2006) Geochemical identification of projectiles in impact rocks. Meteoritics & Planetary Science 41: 1721-1735.

Tagle, R. and Berlin, J. (2008) A database of chondrite analyses including platinum group elements, Ni, Co, Au, and Cr: Implications for the identification of chondritic projectile. Meteoritics & Planetary Science 43, 541–559.

Thermo Fisher Scientific (2020) Anonymous authors. A comprehensive guide to method development using triple quadrupole ICP-MS. © 2020 Thermo Fisher Scientific, 1-42.

Togashi, S. and Terashima, S. (1997) The behaviour of gold in unaltered island arc tholeiitic rocks from Izu-Oshima, Fuji and Osoreyama volcanic areas, Japan. Geochimica et Cosmochimica Acta, 61, 543-554.

Torres de Matos, C., Wittmer, D., Mathieux, F. and Pennington, D. (2020) Revision of the material system analyses specifications. Join Research Centre (JRC) Technical Reports 118827 EUR 30091 EN (ISBN 978-92-76-10734-7 ISSN 1831-9424 DOI 10.2760/374178)

Touboul, M., Puchtel, I.S. and Walker, R.J. (2012) ^{182}W evidence for long term preservation of early mantle differentiation products. Science. 335, 1065–1069.

Touboul, M., Liu, J., O'Neil, J., Puchtel, I.S. and Walker, R.J. (2014) New insights into the Hadean mantle revealed by ^{182}W and highly siderophile element abundances of supracrustal rocks from the Nuvvuagittuq Greenstone Belt, Quebec, Canada. Chemical Geology, 383, 63–75.

Vaillancourt, C., Sproule, R.A., MacDonald, C.A. and Lesher, C.M. (2003) Investigation of mafic-ultramafic intrusions in Ontario and implications for Platinum Group Element mineralization: operation Treasure hunt. Ontario Geological Survey, Open File Report 6102, pp 335.

Walker, R. J. (1988) Low-blank chemical separation of rhenium and osmium from gram quantities of silicate rock for measurement by resonance ionization mass spectrometry. Analytical Chemistry, 60, 1231–1234. DOI 10.1021/ac00162a026.

Wang, Z. and Becker, H. (2014) Abundances of Sulfur, Selenium, Tellurium, Rhenium and Platinum-Group Elements in Eighteen Reference Materials by Isotope Dilution Sector-Field ICP-MS and Negative TIMS Geostandards and Geoanalytical Research, 38, 189–209.

Wang, K.L., O'Reilly, S.Y., Griffin, W.F., Pearson, N.J. and Zhang M. (2009) Sulphides in peridotite xenoliths from Penghu Islands, Taiwan: melt percolation, PGE fractionation and the lithospheric evolution of the South China block. Geochimica et Cosmochimica Acta. 73, 4531–4557.

Wasson, J. T. (1999) Trapped melt in IIIAB irons; solid/liquid elemental partitioning during the fractionation of the IIIAB magma. Geochimica et Cosmochimica Acta 63, 2875-2889.

Wasson, J. T. and Kimberlin, J. (1967) The chemical classificationof iron meteorites-II. Irons and pallasites with germanium concentrations between 8 and 100 ppm. Geochimica et Cosmochimica Acta, 31, 2065–2093.

Wasson, J. T. and Kallemeyn, G. W. (2002) The IAB iron-meteorite complex: A group, five subgroups, numerous grouplets, closely related, mainly formed by crystal segregation in rapidly cooling melts. Geochimica et Cosmochimica Acta 66, 2445–2473.

Wasson, J.T. and Choi, B-G. (2003) Main-group pallasites: chemical composition, relationship to IIIAB irons, and origin. Geochimica et Cosmochimica Acta, 67, 3079–3096.

Wasson, J.T., Heinz, J., Huber, H. J., and Malvin, D.J. (2007) Formation of IIAB iron meteorites. Geochimica et Cosmochimica Acta 71, 760-781.

Wee, B.S., Ebihara, M. and Wood, A.K.H. (2011) Determination of platinum group elements in terrestrial rocks using nickel sulphide fire assay isotope dilution ICP-MS. The Malaysian Journal of Analytical Sciences, 5, 265 – 272.

Weisberg, M.K., Prinz M., Clayton R.N., Mayeda T.K., Grady M.M., Franchi I., Pillinger C.T., Kallemeyn, G.W. (1996) The K (Kakangari) chondrite grouplet. Geochimica et Cosmochimica Acta, 60, 4253-4263.

Weisberg, M.K., McCoy, T.J. and Krot, A.E. (2006) Systematics and evaluation of meteorite classification. *In*: D. Lauretta and H.Y. McSween Jr. (Eds.). Meteorites and the early solar system II. University of Arizona Press, Tucson, 19–52.

Whiteley, J.D. and Murray, F., (2005) Determination of platinum group elements (PGE) in environmental samples by ICP-MS: a critical assessment of matrix separation for the mitigation of interferences. Geochemistry: Exploration, Environment, Analysis, 5, 3–10.

Wichers, E., Schlecht, W. G., and Gordon, C. L. (1944) Attack of refractory platiniferous materials by acid mixtures at elevated temperatures. Journal of Research of the National Bureau of Standards, 33, 363–381.

Willbold, M., Elliot, T. and Moorbath, S. (2011) The tungsten isotopic composition of Earth's mantle before the terminal bombardment. Nature. 477, 195-198.

Willbold, M., Mojzsis, S.J., Chen, H-W. and Elliott, T. (2015) Tungsten isotope composition of the Acasta Gneiss Complex. Earth and Planetary Science Letters, 419, 168–177.

Wilshire, H.G. and Shervais, J.W. (1975) Al-augite and Cr-diopside ultramafic xenoliths in basaltic rocks from western United States. Physics and Chemistry of the Earth, 9, 257-272.

References

Wittig, N, Pearson, D.G., Baker, J.A. Duggen S. and Hoernle, K. (2010) A major element, PGE and Re–Os isotope study of Middle Atlas (Morocco) peridotite xenoliths: Evidence for coupled introduction of metasomatic sulphides and clinopyroxene. Lithos. 115, 15–26.

Wood, J.A. (1967) Chondrites: Their metallic minerals, thermal histories, and parent planets, Icarus, 6, 1-49.

Wood, B. J., Halliday, A. N. and M. Rehkamper (2010) Volatile accretion history of the Earth, Nature, 457, E6–E7.

Wood, B.J., Smythe, D.J. and Harrison, T. (2019) The condensation temperatures of the elements: a reappraisal. American Mineralogist, 104, 844–856.

Yokoyama, T. and Walker, R. J. (2016) Nucleosynthetic Isotopic Variations of Siderophile and Chalcophile Elements in the Solar System. Reviews in Mineralogy & Geochemistry, 81,107-160.

Yokoyama, T., Rai, V. K., Alexander, M. O., Lewis, R. S., Carlson, R. W., Shirey, S. B., et al. (2007) Osmium isotope evidence for uniform distribution of s- and r process components in the early solar system. Earth and Planetary Science Letters, 259, 567–580. DOI 10.1016/j.epsl.2007.05.017.

Yokoyama, T., Alexander, C. M. O., and Walker, R. J. (2010) Osmium isotope anomalies in chondrites: results for acid residues and related leachates. Earth and Planetary Science Letters, 291, 48–59. DOI 10.1016/j.epsl.2009.12.048.

Zientek, M.L. and Loferski, P.J. (2010) Platinum-Group Elements-So Many Excellent Properties. Assessment report on Southern Africa PGE: ISSN 2327–6932. DOI 10.3133/fs20143064.

Zindler, A. and Jagoutz, E. (1980) Isotope and trace element systematics in mantle-derived peridotite nodules from San Carlos. EOS, 61(197), 374.

Zindler, A. and Jagoutz, E. (1988) Mantle cryptology. Geochimica et Cosmochimica Acta, 52, 319-333.

Zischka, M., Schramel, P., Muntau, H., Rehnert, A., Gomez Gomez, M., Stojanik, B., Wannemaker, G., Dams, R. Quevauviller, P. and Maier, E.A. (2002) A new certified reference material for the quality control of palladium, platinum and rhodium in road dust, BCR-723. Trends in Analytical Chemistry, 21, n.12, 851-868.

On line sources:

Precious Metal Management - Johnson Mattey PIc, 2020 http://www.platinum.matthey.com/

Bloomberg https://www.bloomberg.com/quote/XPT:CUR

ACI (Automobile Club of Italy) 2019 http://www.opv.aci.it/WEBDMCircolante/

ARPA Emilia Romagna https://www.arpae.it/it/temi-ambientali/meteo/report-meteo

Meteortical Bullettin database- https://www.lpi.usra.edu/meteor/metbull.php

Appendix I: Autotune interface report

Autotune Report

QTEGRA

System

Start time:	1/11/2021 1:42:38 PM
Instrument:	iCAP TQ
User:	DESKTOP-NOVQMON\Utente
Template:	InterfaceTune HighSensitivity
Instrument Serial Number:	TQ00217
Solution:	iCAP TQ TUNE solution
End time:	1/11/2021 1:56:07 PM
Result:	The autotuning was successful.

Intensity Changes

Analyte	Original result	Tuned result
115In	292877	478947
140Ce	291189	476404
140Ce.16O	4125	9518
7Li	87201	112449
59Co	152064	230065
238U	278745	510126
140Ce.16O/140Ce	0.0142	0.02

Control Changes

Control	Unit	Original value	Tuned value
Nebulizer Flow	[l/min]	1.0682	1.0939
Torch Horizontal Position	[mm]	-0.4	-0.7
Torch Vertical Position	[mm]	0.12	-0.27
Extraction Lens 2	[V]	-172	-154
CR Entry Lens	[V]	-108	-67.5
Pole Bias Q1 Set	[V]	1.56	1.56
Q1 Focus Lens Set	[V]	1.6	1.3
Q1 SQ-mode RF Dac Offset		-840	-860
Q1 Entry Lens Set	[V]	-96	-82.25

Autotune Report

QTEGRA

Graphical Results

Stage name: Torch position
Control: Torch Horizontal Position
Analyte: 115In

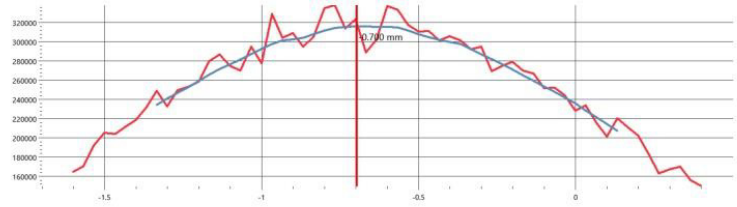

Stage name: Torch position
Control: Torch Vertical Position
Analyte: 115In

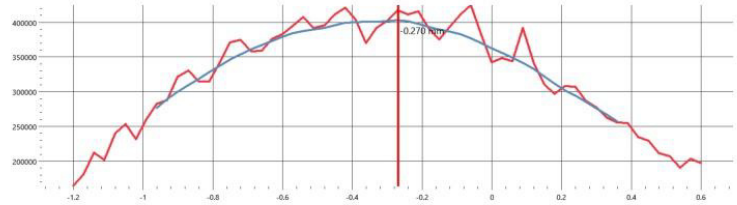

Stage name: Nebulizer, CeO/Ce < 4 %
Control: Nebulizer Flow
Analyte: 115In

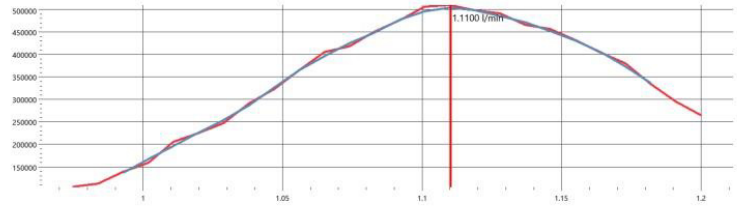

Stage name: Nebulizer, CeO/Ce < 4 %
Control: Nebulizer Flow
Analyte: 140Ce.16O

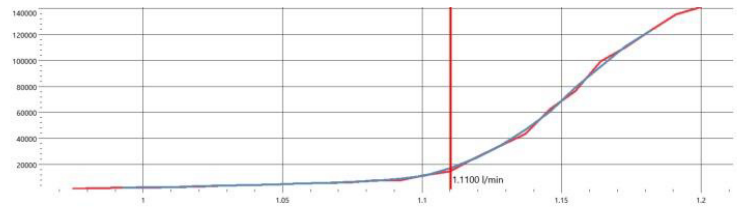

Stage name: Nebulizer, CeO/Ce < 4 %
Control: Nebulizer Flow
Analyte: 140Ce

Autotune Report

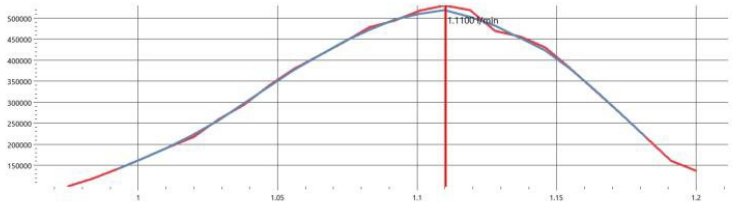

Stage name: Nebulizer, CeO/Ce < 4 %
Control: Nebulizer Flow
Analyte: 140Ce.16O/140Ce

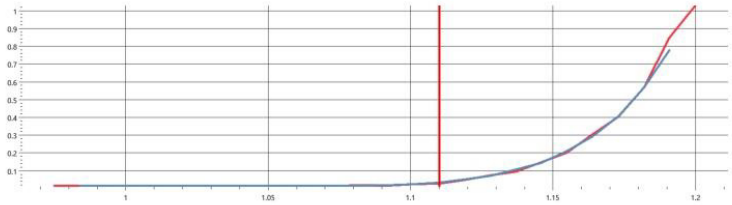

Stage name: Extraction Lens 2
Control: Extraction Lens 2
Analyte: 115In

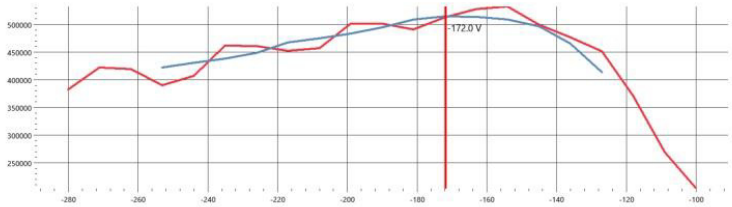

Stage name: Q1 Bias max%Tune (max U but Li>90%; RC 20%)
Control: Pole Bias Q1 Set
Analyte: 7Li

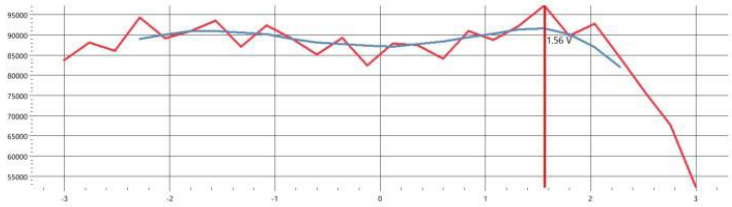

Stage name: Q1 Bias max%Tune (max U but Li>90%; RC 20%)
Control: Pole Bias Q1 Set
Analyte: 238U

Autotune Report

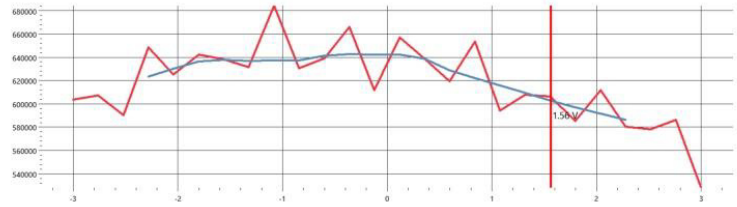

Stage name: CR Entry Lens max%Tune (max Li but Co>90%)
Control: CR Entry Lens
Analyte: 7Li

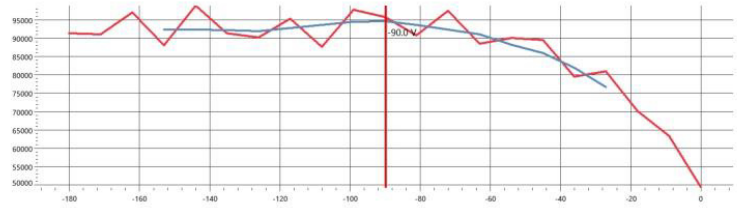

Stage name: CR Entry Lens max%Tune (max Li but Co>90%)
Control: CR Entry Lens
Analyte: 59Co

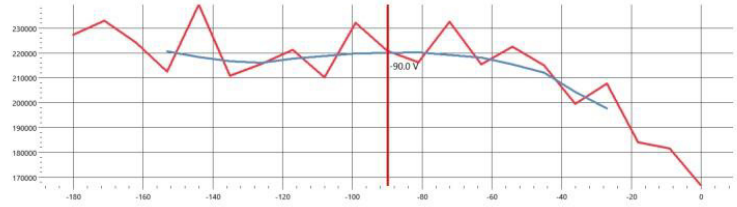

Stage name: Q1 Focus max%Tune (max U but Li>90%; RC 20%)
Control: Q1 Focus Lens Set
Analyte: 7Li

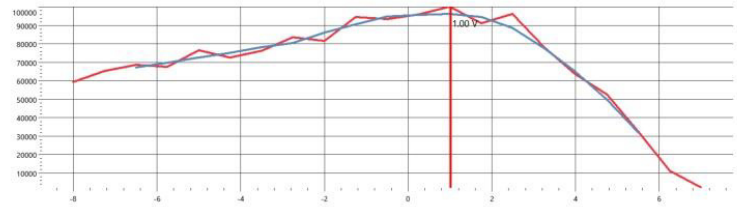

Stage name: Q1 Focus max%Tune (max U but Li>90%; RC 20%)
Control: Q1 Focus Lens Set
Analyte: 238U

Autotune Report

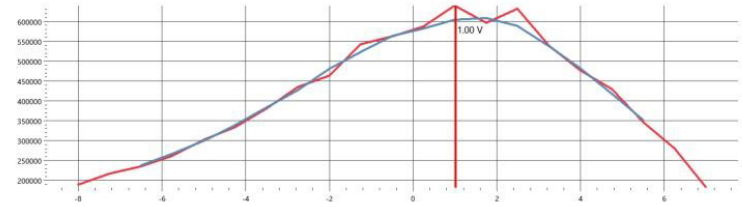

Stage name: Q1 Entry max%Tune (max U but Li>90%; RC 20%)
Control: Q1 Entry Lens Set
Analyte: 7Li

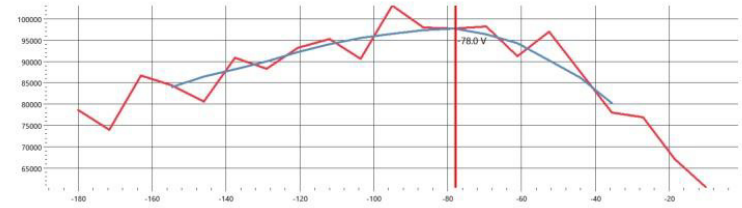

Stage name: Q1 Entry max%Tune (max U but Li>90%; RC 20%)
Control: Q1 Entry Lens Set
Analyte: 238U

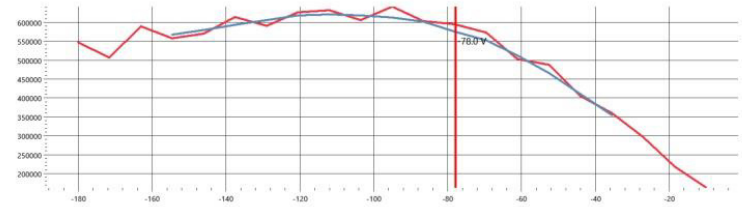

Stage name: Nebulizer again, CeO/Ce < 2 %
Control: Nebulizer Flow
Analyte: 115In

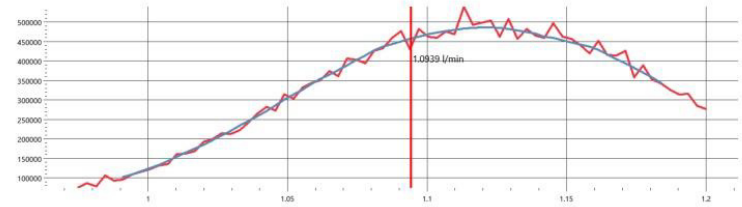

Stage name: Nebulizer again, CeO/Ce < 2 %
Control: Nebulizer Flow
Analyte: 140Ce.16O

Autotune Report

QTEGRA

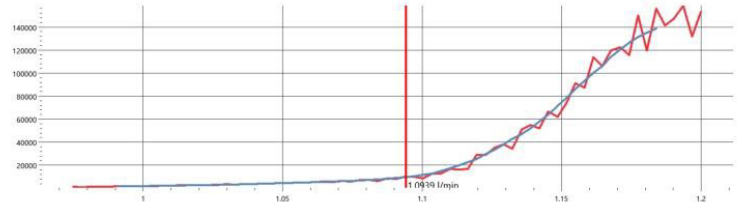

Stage name: Nebulizer again, CeO/Ce < 2 %
Control: Nebulizer Flow
Analyte: 140Ce

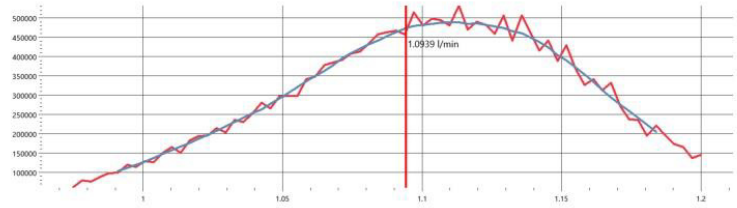

Stage name: Nebulizer again, CeO/Ce < 2 %
Control: Nebulizer Flow
Analyte: 140Ce.16O/140Ce

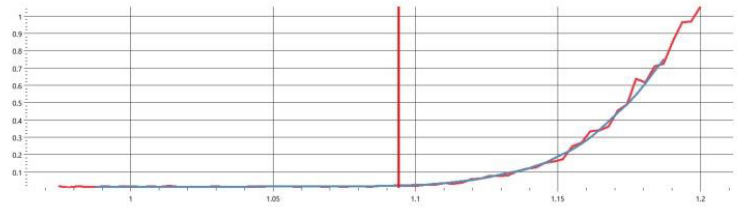

Stage name: Extraction Lens 2 again
Control: Extraction Lens 2
Analyte: 59Co

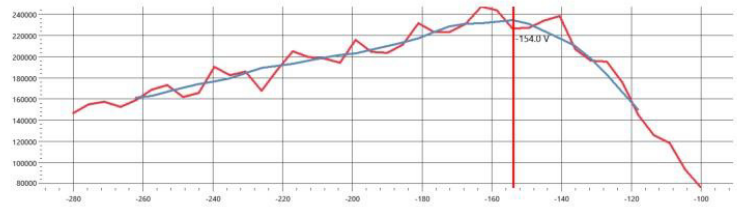

Stage name: Q1 Bias again
Control: Pole Bias Q1 Set
Analyte: 7Li

Autotune Report

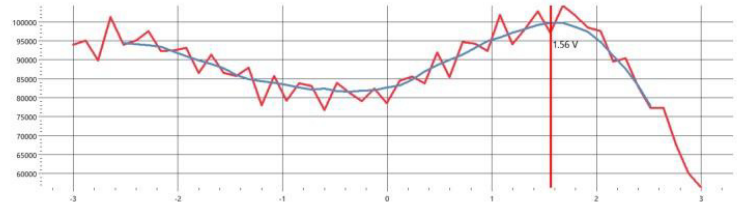

Stage name: Q1 Bias again
Control: Pole Bias Q1 Set
Analyte: 238U

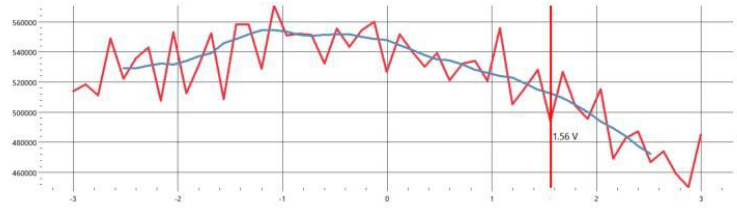

Stage name: CR Entry Lens again
Control: CR Entry Lens
Analyte: 7Li

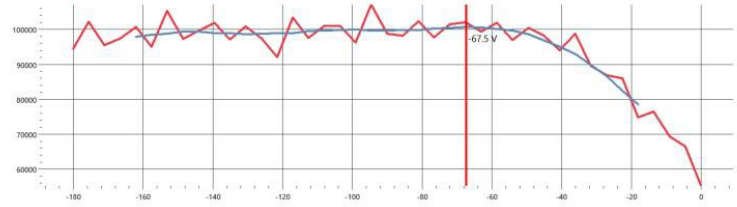

Stage name: CR Entry Lens again
Control: CR Entry Lens
Analyte: 59Co

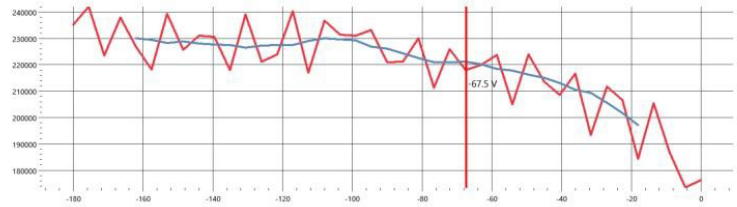

Stage name: Q1 Focus again
Control: Q1 Focus Lens Set
Analyte: 7Li

Autotune Report

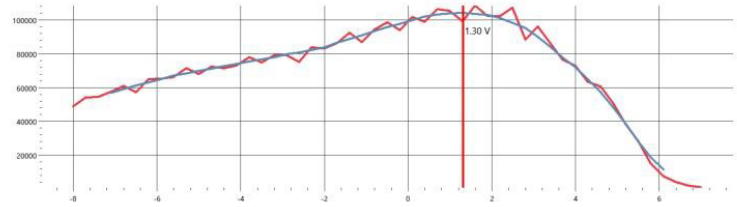

Stage name: Q1 Focus again
Control: Q1 Focus Lens Set
Analyte: 238U

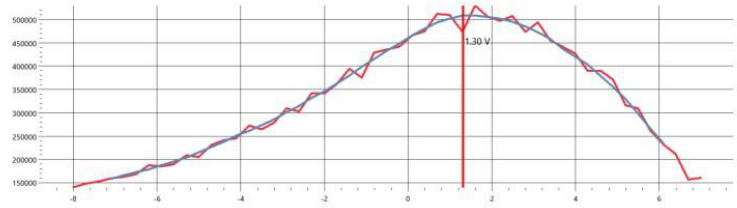

Stage name: Q1 Entry again
Control: Q1 Entry Lens Set
Analyte: 7Li

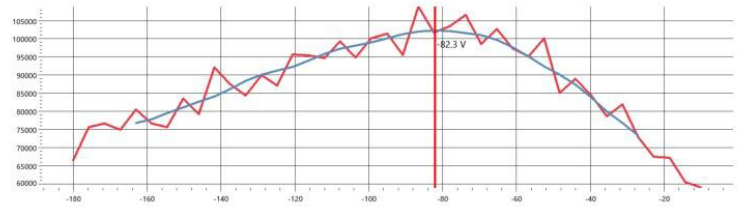

Stage name: Q1 Entry again
Control: Q1 Entry Lens Set
Analyte: 238U

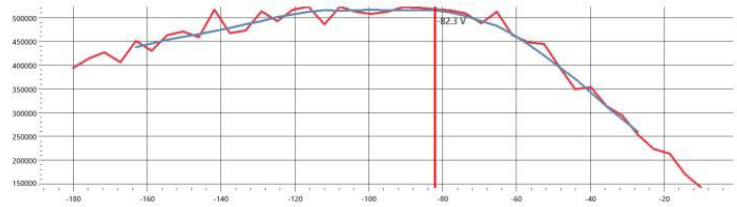

Stage name: Q1 low mass transmission
Control: Q1 SQ-mode RF Dac Offset
Analyte: 7Li

Autotune Report

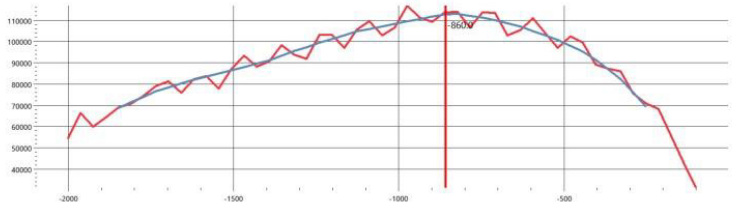

Autotune Report

QTEGRA

Tune Settings

Parameter	Value
CR Bias	-2
CR Exit Lens	-160
Focus Lens	19.5
D1 Lens	-200
D2 Lens	-84.6000000000001
Quad Entry Lens	-28
Pole Bias	-1
CR RF Low Mass Amplitude Offset	-280
CR1 Flow	0
CR2 Flow	0
CR3 Flow	0
CR4 Flow	0
Additional Gas Flow 1	0
Additional Gas Flow 2	0
Q1 Entry Lens	-82.25
Angular Deflection	-250
Deflection Entry Lens	-30
Extraction Lens 1 Polarity	0
Extraction Lens 1 Negative	0
Extraction Lens 1 Positive	0
Spray Chamber Temperature	2.7
CR Entry Lens	-67.5
Peristaltic Pump Speed	40
Cool Flow	14
Sampling Depth	5
Plasma Power	1550
Auxilliary Flow	0.8
Nebulizer Flow	1.09392857142857
Torch Horizontal Position	-0.7
Torch Vertical Position	-0.27
Extraction Lens 2	-154
Q1 Focus Lens	1.3
Pole Bias Q1	1.56
Q1 SQ-mode RF Dac Factor	600
Q1 SQ-mode parameter b	0.65
Q1 SQ-mode RF Dac Offset	-860
Dry Pump Speed	77
CR RF High Mass Amplitude Factor	130
CR RF High Mass Amplitude Offset	0
CR RF High Mass Amplitude Exponent	0.65
CR RF Low Mass Amplitude Factor	130
CR RF Low Mass Amplitude Exponent	0.65
CR Parameter Mass Switch Point	300

Appendix II: Autotune Advanced Report

Autotune Report

QTEGRA

System

Start time:	2/8/2021 2:28:18 PM
Instrument:	iCAP TQ
User:	DESKTOP-NOVQMON\Utente
Template:	AdvancedTune KED
Instrument Serial Number:	TQ00217
Solution:	iCAP TQ TUNE solution
End time:	2/8/2021 2:33:43 PM
Result:	The autotuning was successful.

Intensity Changes

Analyte	Original result	Tuned result
51V	1397	1598
59Co	33126	35638
115In	41571	48161
7Li	104	128
59Co/51V	23.7052	22.2973

Control Changes

Control	Unit	Original value	Tuned value
Focus Lens	[V]	-8.5	-8
D2 Lens	[V]	-159.76	-162
Quad Entry Lens	[V]	-58	-56
CR1 Flow	[ml/min]	4.733	4.675
CR RF Low Mass Amplitude Offset		-510	-510

Autotune Report

QTEGRA

Graphical Results

Stage name: Coarse interference reduction
Control: CR1 Flow
Analyte: 59Co

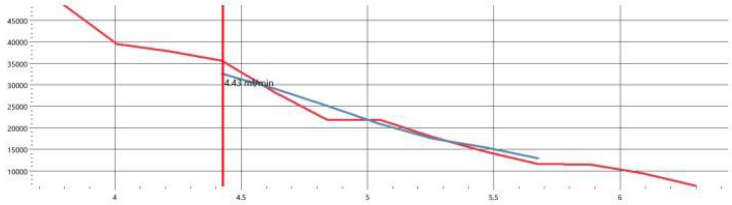

Stage name: Coarse interference reduction
Control: CR1 Flow
Analyte: 59Co/51V

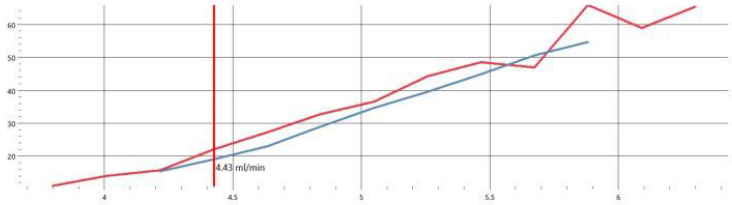

Stage name: Plasma independent Lenses, 1. Iteration
Control: D2 Lens
Analyte: 59Co

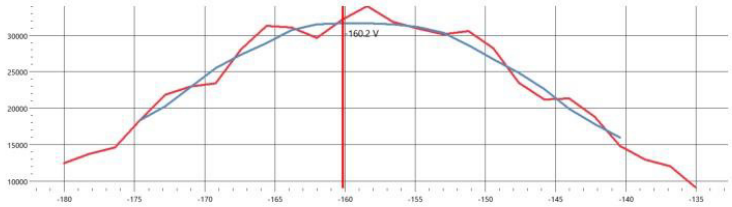

Stage name: Plasma independent Lenses, 1. Iteration
Control: Focus Lens
Analyte: 59Co

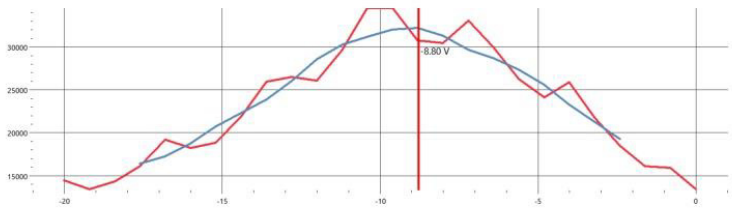

Stage name: Plasma independent Lenses, 1. Iteration
Control: Quad Entry Lens
Analyte: 59Co

Autotune Report

QTEGRA

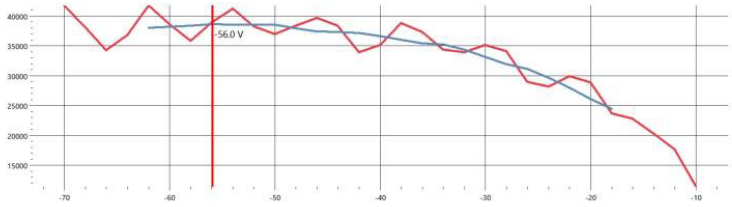

Stage name: Plasma independent Lenses, 2. Iteration
Control: D2 Lens
Analyte: 59Co

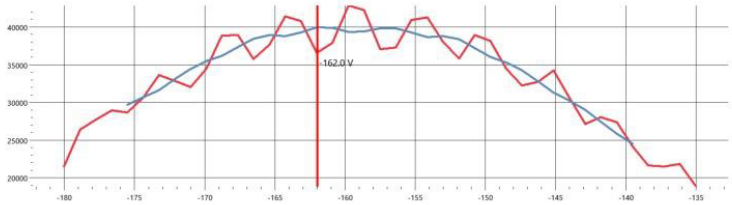

Stage name: Plasma independent Lenses, 2. Iteration
Control: Focus Lens
Analyte: 59Co

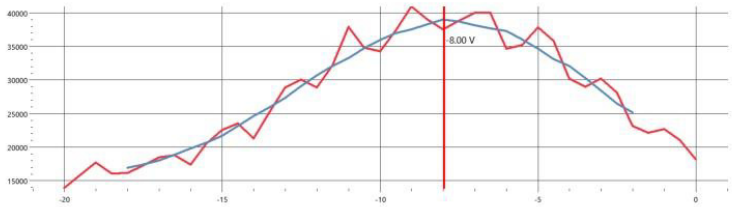

Stage name: Plasma independent Lenses, 2. Iteration
Control: Quad Entry Lens
Analyte: 59Co

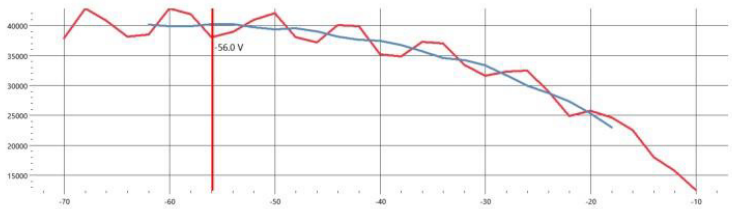

Stage name: Optimizing low mass transmission CR
Control: CR RF Low Mass Amplitude Offset
Analyte: 7Li

Autotune Report

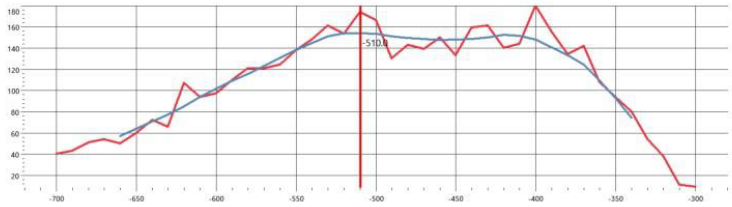

Stage name: Fine Interference reduction
Control: CR1 Flow
Analyte: 59Co

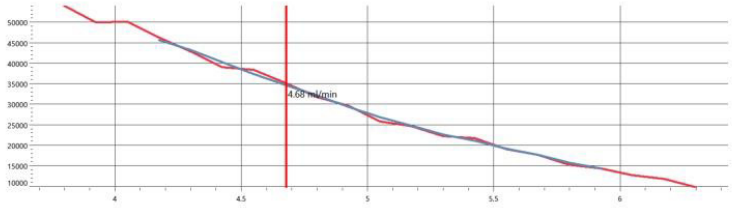

Stage name: Fine Interference reduction
Control: CR1 Flow
Analyte: 59Co/51V

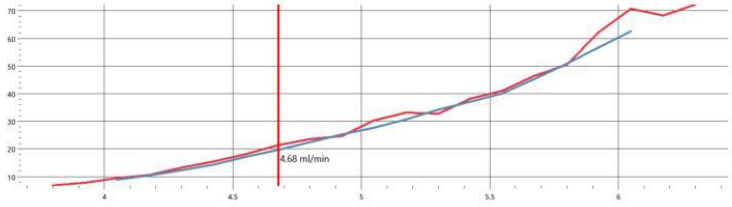

Autotune Report

QTEGRA

Tune Settings

Parameter	Value
CR Bias	-21
CR Exit Lens	-40
Focus Lens	-8
D1 Lens	-350
D2 Lens	-162
Quad Entry Lens	-56
CR RF Low Mass Amplitude Offset	-510
Pole Bias	-18
CR1 Flow	4.675
CR2 Flow	0
CR3 Flow	0
CR4 Flow	0
Additional Gas Flow 1	0
Additional Gas Flow 2	0
Q1 Entry Lens	-129
Angular Deflection	-250
Deflection Entry Lens	-30
Extraction Lens 1 Polarity	0
Extraction Lens 1 Negative	0
Extraction Lens 1 Positive	0
Spray Chamber Temperature	2.7
Peristaltic Pump Speed	40
Cool Flow	14
Sampling Depth	5
Plasma Power	1550
Auxilliary Flow	0.8
Nebulizer Flow	1.065
Torch Horizontal Position	-0.47
Torch Vertical Position	-0.3
Extraction Lens 2	-164
Q1 Focus Lens	-3.08
CR Entry Lens	-144
Pole Bias Q1	-1.2
Q1 SQ-mode RF Dac Factor	600
Q1 SQ-mode parameter b	0.65
Q1 SQ-mode RF Dac Offset	-1088
Dry Pump Speed	76.996336996337
CR RF High Mass Amplitude Factor	130.000047683761
CR RF High Mass Amplitude Offset	0.00953675225901819
CR RF High Mass Amplitude Exponent	0.650000238418806
CR RF Low Mass Amplitude Factor	130.000047683761
CR RF Low Mass Amplitude Exponent	1
CR Parameter Mass Switch Point	299.999904632477

Appendix III: Performance check report

Performance check

QTEGRA

System

Time:	9/2/2020 8:19:37 AM
Instrument:	iCAP TQ
Operator:	OPTIPLE-UD1UU18\Administrator
Template:	S-SQ-KED
Instrument Serial Number:	TQ00217
Last updated by:	Autotune-InterfaceTune HighSensitivity-20200825-130310412.imatdat
Solution:	iCAP TQ Tune Solution

List of performed Checks

Check type: Gas check
Performance Report name: CR Gas KED

Performed steps	Start time	End time	Result
Sensitivity	9/2/2020 8:19:40 AM	9/2/2020 8:21:41 AM	Passed

Check type: Interface check
Performance Report name: High Sensitivity

Performed steps	Start time	End time	Result
Q3 mass calibration	9/2/2020 8:21:47 AM	9/2/2020 8:22:48 AM	Passed
Sensitivity	9/2/2020 8:22:49 AM	9/2/2020 8:32:15 AM	Passed
Vacuum	9/2/2020 8:32:15 AM	9/2/2020 8:32:15 AM	Passed

Performance check

QTEGRA

Gas check

Sensitivity & Stability Test

Result	Runs	Sweeps
Passed	50	5

Sensitivity

Analyte	Result	Value	Condition	Limit
Bkg4.5	Passed	0.064 CPS	Less than	0.5 CPS
59Co/35Cl.16O	Passed	69.5	Greater than	18.0
59Co	Passed	48,054.0 CPS	Greater than	40,000.0 CPS

Stability

Analyte	Value	Limit
59Co	1.7%	2

Performance check

QTEGRA

Interface check

Q3 Mass Calibration Test

Result	Channels	Dwell	MeasureWidth	PointSpacing	Sweeps
Passed	75	0.04	1.5	0.02	5

Analyte	Result	Centroid Mass [u]	Offset	Peak width [u]	Peak width min [u]	Peak width max [u]
7Li	Passed	6.9954	0.0206	0.771	0.650	0.850
59Co	Passed	58.9168	0.0164	0.747	0.650	0.850
115In	Passed	114.8901	0.0138	0.742	0.650	0.850
209Bi	Passed	208.9680	0.0124	0.735	0.650	0.850

Sensitivity & Stability Test

Result	Runs	Sweeps
Passed	60	10

Sensitivity

Analyte	Result	Value	Condition	Limit
Bkg4.5	Passed	0.08 CPS	Less than	1.0 CPS
Bkg220.7	Passed	0.03 CPS	Less than	2.0 CPS
7Li	Passed	77,681.0 CPS	Greater than	65,000.0 CPS
59Co	Passed	195,126.0 CPS	Greater than	150,000.0 CPS
238U	Passed	380,136.0 CPS	Greater than	330,000.0 CPS
140Ce.16O/140Ce	Passed	0.0189	Less than	0.02
140Ce++/140Ce	Passed	0.0319	Less than	0.04
115In	Passed	413,192.0 CPS	Greater than	300,000.0 CPS

Stability

Analyte	Value	Limit
7Li	0.6%	2
59Co	0.8%	2
238U	1.6%	2
115In	0.8%	2

Vacuum Check

Parameter	Result	Value
Analyzer Pressure	Vacuum ok	2.750e-7
Interface Pressure		1.769e+0

Performance check

QTEGRA

Tune Settings

Parameter	Gas check	Interface check
Interface	High Sensitivity	High Sensitivity
SQ/TQ	SQ	SQ
Reaction Gas	Kinetic Energy Discrimination	No reaction gas
Additional Gas Flow 1	0	0
Additional Gas Flow 2	0	0
Angular Deflection	-250	-250
Auxilliary Flow	0.8000	0.8000
Cool Flow	14	14
CR Bias	-21	-2
CR Entry Lens	-117	-117
CR Exit Lens	-40	-160
CR1 Flow	4.953	0.000
CR2 Flow	0.0000	0.0000
CR3 Flow	0.000	0.000
CR4 Flow	0.0000	0.0000
D1 Lens	-350	-200
D2 Lens	-160.875	-84.6
Deflection Entry Lens	-30	-30
Extraction Lens 1 Negative	0	0
Extraction Lens 1 Polarity	0	0
Extraction Lens 1 Positive	0	0
Extraction Lens 2	-176.5	-176.5
Focus Lens	-8	19.5
Nebulizer Flow	1.0514	1.0514
Peristaltic Pump Speed	40.0	40.0
Plasma Power	1,550	1,550
Pole Bias	-18	-1
Pole Bias Q1	0.72	0.72
Q1 Entry Lens	-127.5	-127.5
Q1 Focus Lens	1.6	1.6
Quad Entry Lens	-54	-28
Sampling Depth	5.00	5.00
Spray Chamber Temperature	2.7	2.7
Torch Horizontal Position	.19	.19
Torch Vertical Position	0.47	0.47

Performance check

QTEGRA

Q3 Mass Calibration Peaks

Group name: Interface check

Analyte: 115In

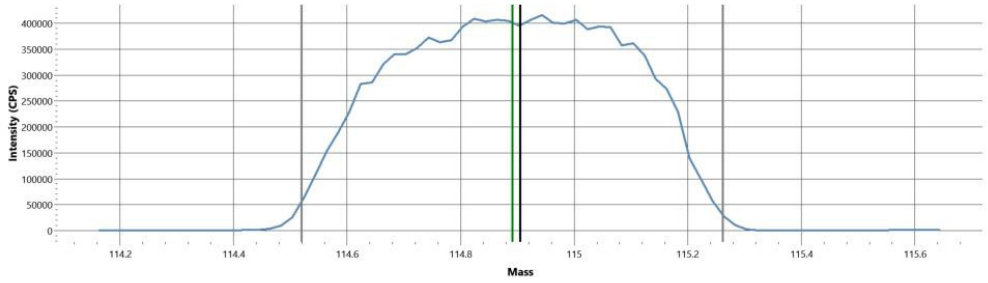

Analyte: 209Bi

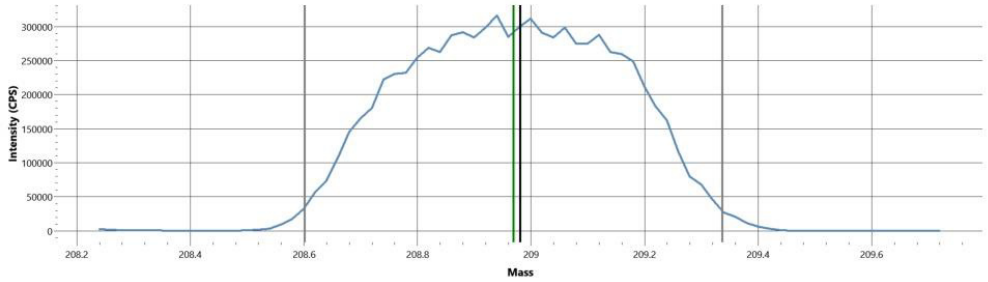

Analyte: 59Co

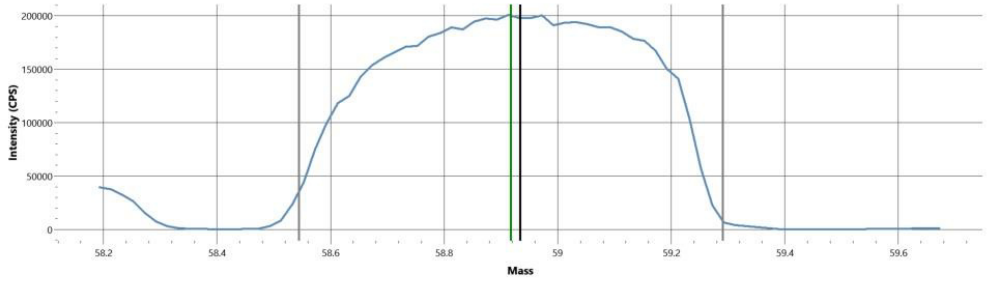

Analyte: 7Li

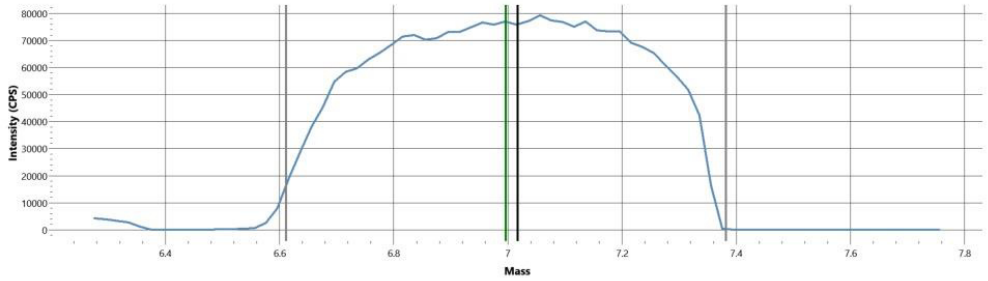

Appendix IV: EMPA results

spot	A6-C5-6 an1	A6-C5-6 an2	A6-C5-6 an3	A6-C5-6 an4	A6-C5-6 an5	A6-C5-6 an6	A6-C5-6 an7
As	0.08	0.12	0.06	0.12	0.07	0.14	0.05
Co	0.17	0.12	0.18	0.18	0.21	0.15	0.11
Ni	6.98	7.06	7.03	7.08	7.01	6.96	7.05
S	0.01	0.00	0.00	0.01	0.00	0.00	0.02
Fe	92.44	91.98	92.27	92.58	92.67	91.94	92.89
Cu	0.00	0.00	0.00	0.15	0.00	0.01	0.00
Total	99.67	99.29	99.54	100.11	99.95	99.19	100.12

spot	A6-C5-6 an8	A6-C5-6 an9	A6-C5-6 an10	A6-C5-6 an11	A6-C5-6 an12	A6-C5-6 an13	A6-C5-6 an14
As	0.09	0.05	0.08	0.06	0.12	0.04	0.13
Co	0.13	0.16	0.20	0.18	0.19	0.15	0.16
Ni	7.00	6.98	7.06	7.00	7.18	7.19	6.97
S	0.01	0.01	0.01	0.00	0.02	0.01	0.00
Fe	91.99	92.82	92.64	92.80	92.92	92.82	93.08
Cu	0.00	0.00	0.00	0.00	0.00	0.00	0.00
Total	99.23	100.01	99.99	100.04	100.43	100.21	100.34

spot	A6-C5-6 an15	A6-C5-6 an16	A6-C5-6 an17	A6-C5-6 an18	A6-C5-6 an19	A6-C5-6 an20	A6-C5-6 an26
As	0.12	0.07	0.08	0.09	0.12	0.02	0.06
Co	0.13	0.21	0.17	0.13	0.13	0.17	0.19
Ni	7.00	6.82	7.07	6.98	7.06	6.97	6.70
S	0.01	0.01	0.00	0.01	0.00	0.02	0.00
Fe	93.60	92.86	92.93	93.00	92.13	93.22	92.30
Cu	0.00	0.00	0.04	0.00	0.00	0.00	0.00
Total	100.86	99.96	100.30	100.21	99.44	100.39	99.25

spot	A6-C5-6 an27	A6-D7- an28	A6-D7- an29	A6-D7- an30	A6-D7- an31	A6-D7- an32	A6-D7- an33
As	0.10	0.07	0.06	0.13	0.11	0.12	0.10
Co	0.22	0.21	0.16	0.20	0.16	0.19	0.16
Ni	6.71	6.98	6.91	6.95	6.61	6.90	6.84
S	0.01	0.01	0.00	0.00	0.01	0.01	0.00
Fe	92.41	92.09	93.17	92.54	91.51	91.61	91.92
Cu	0.00	0.00	0.00	0.00	0.00	0.00	0.00
Total	99.45	99.37	100.30	99.83	98.40	98.82	99.03

spot	A6-D7- an34	A6-D7- an35	A6-D7- an36	A6-D7- an37	A6-D7- an38	A6-C3-15 an51	A6-C3-15 an52
As	0.12	0.12	0.14	0.16	0.12	0.18	0.09
Co	0.21	0.14	0.20	0.19	0.15	0.18	0.17
Ni	6.75	6.52	6.72	6.61	6.79	6.74	6.80
S	0.00	0.00	0.01	0.02	0.02	0.00	0.00
Fe	91.08	91.17	91.00	91.62	91.69	92.24	92.17
Cu	0.00	0.00	0.00	0.03	0.00	0.00	0.00
Total	98.15	97.95	98.07	98.62	98.77	99.34	99.22

Table IV.1: EMPA major component of FeNi-metal analysed in 6A sample (wt%)

spot	A6-C3-15 an54	A6-C3-15 an55	A6-C3-15 an56	A6-C3-15 an57	A6-C3-15 an58	A6-C3-15 an59	A6-C3-15 an62
As	0.14	0.06	0.09	0.08	0.13	0.16	0.08
Co	0.21	0.18	0.15	0.20	0.16	0.17	0.20
Ni	6.96	7.00	6.98	6.95	6.86	6.85	6.97
S	0.03	0.00	0.00	0.01	0.00	0.00	0.00
Fe	91.26	91.79	91.90	91.64	91.75	91.79	92.82
Cu	0.00	0.00	0.00	0.00	0.00	0.00	0.02
Total	98.59	99.03	99.12	98.87	98.90	98.97	100.10

spot	A6-C3-15 an63	A6-C3-15 an64	A6-C3-15 an65	A6-D2-13 an66	A6-D2-13 an67	A6-D2-13 an68	A6-D2-13 an69
As	0.13	0.14	0.06	0.06	0.09	0.13	0.09
Co	0.21	0.23	0.16	0.17	0.17	0.13	0.14
Ni	7.00	7.10	7.05	6.77	6.81	6.88	6.61
S	0.00	0.00	0.02	0.00	0.00	0.00	0.00
Fe	92.43	92.21	92.08	91.96	92.11	92.05	92.22
Cu	0.00	0.00	0.00	0.00	0.00	0.00	0.00
Total	99.76	99.68	99.36	98.96	99.18	99.19	99.06

spot	A6-D2-13 an70	A6-D2-13 an71	A6-D2-13 an74	A6-D2-13 an75	A6-D2-13 an76	A6-D2-13 an77	A6-D2-13 an78
As	0.09	0.06	0.04	0.09	0.13	0.06	0.12
Co	0.18	0.13	0.14	0.18	0.19	0.10	0.10
Ni	6.72	6.83	6.85	6.89	6.93	6.93	6.95
S	0.00	0.02	0.00	0.00	0.01	0.00	0.00
Fe	93.20	92.74	92.69	92.51	92.39	93.20	92.48
Cu	0.00	0.00	0.00	0.00	0.00	0.00	0.08
Total	100.19	99.79	99.72	99.66	99.65	100.29	99.74

spot	A6-D2-13 an79	A6-D2-13 an80	A6-D2-13 an82	A6-D2-13 an83	A6-D2-13 an84	A6-D6-10 an87	A6-D6-10 an88
As	0.05	0.04	0.13	0.10	0.10	0.09	0.06
Co	0.12	0.00	0.21	0.13	0.14	0.20	0.17
Ni	6.82	29.87	6.95	7.02	7.03	6.78	6.86
S	0.00	0.00	0.01	0.00	0.00	0.00	0.00
Fe	92.10	71.15	91.45	92.33	92.21	92.01	92.71
Cu	0.00	0.06	0.00	0.00	0.00	0.00	0.00
Total	99.08	101.12	98.75	99.59	99.48	99.09	99.80

spot	A6-D6-10 an89	A6-D6-10 an90	A6-D6-10 an94	A6-D6-10 an95	A6-D6-10 an96	A6-D6-10 an97	A6-D4-11 an103
As	0.06	0.11	0.08	0.01	0.15	0.13	0.10
Co	0.21	0.12	0.12	0.18	0.18	0.19	0.20
Ni	6.73	6.86	6.88	6.29	6.67	6.95	7.17
S	0.00	0.03	0.00	0.00	0.00	0.00	0.00
Fe	92.59	92.80	93.36	92.88	93.46	92.19	91.87
Cu	0.00	0.02	0.00	0.00	0.00	0.00	0.00
Total	99.60	99.92	100.44	99.37	100.46	99.45	99.34

Table IV.1: continued

spot	A6-D4-11 an104	A6-D4-11 an105	A6-D4-11 an106	A6-D4-11 an107	A6-D4-11 an109	A6-D4-11 an110	A6-D4-11 an111
As	0.10	0.02	0.12	0.08	0.12	0.16	0.10
Co	0.14	0.27	0.11	0.14	0.16	0.22	0.16
Ni	6.93	6.63	6.92	6.99	6.99	7.01	7.21
S	0.03	0.03	0.01	0.01	0.01	0.01	0.00
Fe	92.33	93.05	91.43	91.79	92.15	92.46	92.40
Cu	0.00	0.00	0.00	0.02	0.00	0.02	0.00
Total	99.53	99.99	98.59	99.03	99.43	99.88	99.87

spot	A6-D4-11 an112	A6-D4-11 an113	A6-D4-11 an114	A6-D4-11 an115	A6-D4-11 an116	A6-D4-11 an117	A6-D4-11 an118
As	0.07	0.07	0.10	0.03	0.06	0.13	0.12
Co	0.15	0.20	0.16	0.19	0.16	0.16	0.18
Ni	7.08	7.02	7.10	7.18	6.87	7.10	7.00
S	0.00	0.02	0.00	0.00	0.02	0.00	0.00
Fe	92.20	91.40	91.70	91.70	91.44	90.99	91.08
Cu	0.00	0.00	0.00	0.00	0.00	0.00	0.04
Total	99.51	98.72	99.05	99.10	98.55	98.39	98.41

spot	A6-D2-13 an73	A6-D2-13 an80	A6-D6-10 an101	A6-D6-10 an102
As	0.03	0.04	0.13	0.13
Co	0.00	0.00	0.00	0.00
Ni	30.98	29.87	29.36	30.37
S	0.01	0.00	0.01	0.00
Fe	70.21	71.15	71.03	69.96
Cu	0.07	0.06	0.15	0.07
Total	101.29	101.12	100.67	100.52

Table IV.1: continued

spot	A6-C5-6 an21	A6-C5-6 an22	A6-C5-6 an23	A6-C5-6 an24	A6-C5-6 an25	A6-D7- an39	A6-D7- an40
As	0.03	0.03	0.03	0.04	0.09	0.01	0.05
Co	0.00	0.00	0.00	0.00	0.00	0.00	0.00
Ni	0.01	0.06	0.03	0.00	0.00	0.36	0.01
S	36.18	36.55	36.56	36.21	36.66	35.30	36.47
Fe	62.52	62.42	62.31	62.54	63.00	60.59	62.41
Cu	0.00	0.08	0.00	0.00	0.00	0.00	0.00
Total	98.74	99.13	98.93	98.80	99.75	96.26	98.94

spot	A6-D7- an41	A6-D7- an42	A6-D7- an43	A6-D7- an44	A6-D7- an45	A6-D7- an46	A6-D7- an47
As	0.03	0.03	0.05	0.04	0.07	0.01	0.04
Co	0.00	0.00	0.00	0.00	0.00	0.00	0.00
Ni	0.01	0.05	0.14	0.23	0.06	0.02	0.01
S	36.55	36.43	35.23	36.04	36.41	35.20	36.24
Fe	62.52	62.27	61.58	62.04	61.78	61.54	62.52
Cu	0.00	0.06	0.00	0.00	0.02	0.00	0.00
Total	99.11	98.83	97.00	98.35	98.33	96.76	98.82

spot	A6-D7- an48	A6-D7- an49	A6-D7- an50	A6-C3-15 an53	A6-C3-15 an60	A6-C3-15 an61	A6-D2-13 an72
As	0.06	0.04	0.02	0.04	0.07	0.09	0.06
Co	0.00	0.00	0.00	0.00	0.00	0.00	0.00
Ni	0.13	0.04	0.36	0.03	0.02	0.00	0.19
S	36.45	36.47	36.45	34.76	36.47	37.07	33.53
Fe	61.66	62.29	58.72	60.97	62.25	62.05	61.03
Cu	0.10	0.00	0.27	0.02	0.00	0.00	0.46
Total	98.39	98.84	95.82	95.82	98.81	99.20	95.27

spot	A6-D2-13 an81	A6-D2-13 an86	A6-D6-10 an91	A6-D6-10 an92	A6-D6-10 an93	A6-D6-10 an98	A6-D6-10 an99
As	0.05	0.04	0.07	0.00	0.01	0.06	0.04
Co	0.00	0.00	0.00	0.00	0.00	0.00	0.00
Ni	0.63	0.16	0.21	0.13	0.00	0.20	0.16
S	36.69	36.50	36.49	37.07	36.67	36.04	35.45
Fe	61.98	61.90	62.08	60.52	62.74	62.46	60.05
Cu	0.00	0.00	0.00	0.00	0.00	0.00	0.00
Total	99.35	98.60	98.85	97.72	99.43	98.75	95.70

spot	A6-D6-10 an100	A6-D4-11 an108	A6-D4-11 an119	A6-D4-11 an120		A6-D2-13 an85
As	0.06	0.04	0.06	0.07		0.04
Co	0.00	0.00	0.00	0.00		0.12
Ni	0.19	0.00	0.02	0.01		2.61
S	36.54	36.67	36.44	36.93		32.42
Fe	62.22	62.30	62.55	62.21		56.91
Cu	0.05	0.05	0.00	0.05		0.07
Total	99.06	99.06	99.07	99.27		92.17

Table IV.2: EMPA Major component of sulphides (wt%).

Appendix V: LAM-ICP-MS results

Spot	08C1	09C1bis	10C1c	11C2a	12C2b	13C2c	18C5a	19C5b	20C6a
Sc	1.55	0.41	0.63	<0.39	<0.40	0.48	<0.35	0.70	<0.22
Ti	13.4	<1.05	7.84	2.72	8.60	18.1	<1.32	7.42	12.4
V	1.63	13.9	3.57	0.42	<0.22	2.33	<0.164	9.43	15.8
Cr	48.6	64.5	108	59.2	55.1	90.4	40.2	62.3	125
Mn	981	717	276	107	133	160	100	430	374
Co	3180	3720	3920	5380	5090	2960	4630	3460	660
Ni	59330	65730	64110	89540	90850	34720	88660	89560	8050
Cu	146	221	116	244	310	100	250	345	499
Zn	17.7	13.8	16.0	<0.82	2.04	2.15	1.24	5.35	5.77
Ga	27.4	13.8	34.8	29.0	30.2	26.6	23.7	30.1	0.39
Ge	203	107	310	230	277	192	199	233	43.0
As	45.4	39.8	56.0	56.8	71.7	43.9	42.0	55.9	4.10
Zr	0.06	0.27	<0.079	0.08	0.20	0.24	<0.080	0.15	0.39
Nb	0.03	<0.021	<0.029	<0.035	<0.035	0.06	<0.030	0.05	0.08
Rh	1.91	1.55	2.64	1.88	2.27	1.86	1.28	1.78	0.04
Pd	1.10	0.99	1.33	1.19	1.41	1.14	0.92	1.17	0.19
Ag	0.04	0.15	<0.053	<0.066	<0.095	0.04	0.10	<0.058	<0.053
In	<0.012	0.04	<0.026	<0.020	<0.036	<0.008	<0.020	<0.035	0.023
Sb	0.87	0.17	0.79	0.57	0.7	0.72	0.51	0.92	<0.063
Hf	<0.051	<0.090	<0.100	<0.103	<0.105	0.08	0.07	0.052	0.113
Ta	<0.013	<0.016	<0.00	<0.011	<0.015	0.01	<0.0151	<0.016	<0.011
Re	0.71	0.39	0.49	0.65	0.90	0.51	0.81	1.11	0.03
Au	1.20	1.04	0.67	2.78	3.67	2.51	1.82	2.53	0.08
Pb	1.89	2.05	2.28	0.60	1.09	0.63	0.88	<0.040	0.88

Table V.1: LAM-ICP-MS trace components of FeNi-metal analysed in 6A sample (ppm).

Appendix V

Spot	14C3a	15C3b	16C4a	17C4b	21C7a	22C7b	23C8a	24C8b	25C9a	26C9b	27C9c
Sc	<0.48	<0.47	<0.97	<0.65	<0.24	<0.24	1.86	<0.75	1.64	0.85	1.38
Ti	<2.53	2.72	<4.35	<2.77	1370	24.8	<6.05	19.5	35.8	61.3	6.48
V	<0.24	<0.27	<0.47	<0.32	0.79	0.82	<0.59	7.72	2.16	3.14	<0.42
Cr	19.7	26.8	45.4	25.1	31.5	179	34.6	677	53.9	73.1	33.3
Mn	44.8	43.7	54.2	56.2	86.4	82.3	57.5	59.0	77.1	120	78.8
Co	4220	4400	4640	4740	3230	3500	4720	4830	4540	4570	4480
Ni	59960	61750	61540	66810	69530	49200	68390	67490	57130	65330	62650
Cu	79.9	75.77	91.4	97.4	140	158	103	99.6	80.7	80.0	90.4
Zn	1.49	<1.45	<2.14	<1.43	1.05	6.13	<2.79	11.8	3.5	2.98	3.82
Ga	11.0	11.2	10.5	8.89	24.3	13.1	11.5	8.88	9.11	9.98	8.64
Ge	73.3	84.9	86.5	86.1	193	94.5	90.0	98.8	85.4	85.9	81.3
As	24.7	13.6	10.0	17.8	41.9	21.4	18.1	18.3	19.5	15.7	10.3
Zr	<0.113	<0.095	<0.16	<0.093	0.16	<0.049	<0.29	<0.19	0.6	1.35	<0.15
Nb	<0.046	<0.031	<0.083	<0.048	0.65	<0.029	<0.082	<0.047	0.023	0.088	<0.063
Rh	0.79	0.93	0.67	0.74	1.80	0.93	0.87	0.70	1.12	1.16	1.03
Pd	0.28	0.36	0.40	0.59	1.13	0.69	0.51	0.480	0.490	0.510	0.440
Ag	<0.065	<0.085	<0.21	<0.16	<0.062	<0.041	<0.23	<0.18	<0.071	<0.084	<0.21
In	<0.040	0.06	<0.057	<0.042	0.026	<0.017	<0.068	<0.051	<0.023	<0.018	<0.043
Sb	0.57	0.24	0.39	0.26	0.54	0.37	<0.28	0.34	0.32	0.29	0.35
Hf	0.15	<0.00	<0.144	<0.17	<0.048	<0.077	<0.35	<0.20	0.13	<0.16	<0.109
Ta	<0.026	0.04	<0.064	<0.035	0.04	<0.011	<0.081	<0.066	<0.009	<0.020	<0.040
Re	0.11	0.20	0.25	0.30	0.74	0.42	0.33	0.28	0.49	0.51	0.48
Au	1.08	1.34	0.90	1.28	2.26	0.83	0.52	0.85	1.29	0.91	1.03
Pb	0.15	0.18	0.62	1.61	1.29	1.50	1.01	1.12	0.3	0.79	1.11

Table V.2: LAM-ICP-MS trace elements of sulphides in 6A (ppm).

	E5-28A	E5-29b	E5-30c	E5-31c
Sc	9.37	12.7	13.1	11.8
Ti	870	1010	1280	1220
V	107	108	89	114
Cr	276	328	283	384
Mn	1270	1800	2110	1760
Co	3.86	3.12	4.18	2.74
Ni	4.02	34.1	27.8	18.6
Cu	5.65	9.52	37.2	19.6
Zn	14.7	7.59	49.9	44.6
Ga	12.4	11.3	14.2	12.7
Ge	49.1	47.4	44.9	45.6
As	<0.96	<0.95	2.15	2.19
Zr	36.9	45.1	86.7	64.0
Nb	1.66	3.07	7.08	4.65
Rh	<0.040	<0.038	0.034	<0.031
Pd	<0.021	0.028	0.021	<0.019
Ag	0.11	<0.077	0.47	0.44
In	0.29	0.97	2.3	1.07
Sb	<0.16	0.17	0.42	0.43
Hf	1.13	1.12	2.31	1.83
Ta	<0.032	0.16	0.6	0.29
Re	<0.048	<0.043	0.043	<0.046
Au	<0.070	<0.054	<0.087	<0.043
Pb	0.83	0.74	9.69	8.21

Table V.3: LAM-ICP-MS trace elements of spots in 5E sample (ppm)

Appendix VI: TQ-ICP-MS results (tests at the Thermo Fisher laboratory, Rodano, Italy)

		VM1P	VM1S	VM2P	VM2S	VM3P	VM5P	VM5S
Ni	(ppm)	69.5	73.8	84.2	65.3	67.9	58.7	43.4
Cu	(ppm)	36.6	58.0	43.8	36.1	36.6	32.2	23.2
Ru	(ppb)	0.872	1.004	0.968	0.988	0.876	1.151	1.329
Rh	(ppb)	1.03	1.10	1.22	1.44	1.13	1.06	1.35
Pd	(ppb)	8.37	8.61	9.27	9.10	8.23	8.44	8.90
Hf	(ppb)	2640	2180	1310	1100	296	1520	1030
Re	(ppb)	1.57	0.83	1.76	2.33	1.10	1.04	0.73
Os	(ppb)	<LOD	<LOD	<LOD	<LOD	<LOD	<LOD	<LOD
Ir	(ppb)	7.58	6.27	3.25	2.19	0.00	3.54	1.83
Pt	(ppb)	9.81	3.96	4.54	4.61	4.94	4.95	3.02
Au	(ppb)	<LOD	<LOD	<LOD	<LOD	<LOD	<LOD	<LOD

		VP3P	VP3S	VP4P	VP5P	VP5Pr	VP5S	VP6S
Ni	(ppm)	159	163	95.5	183	205	151	181
Cu	(ppm)	40.2	41.6	12.3	43.1	49.0	42.4	48.5
Ru	(ppb)	1.509	1.190	0.952	0.822	0.782	1.182	0.879
Rh	(ppb)	1.72	1.09	0.89	0.66	0.08	1.32	0.53
Pd	(ppb)	13.9	9.40	8.81	10.8	4.65	8.37	5.26
Hf	(ppb)	1140	1150	1350	1340	1360	1250	874
Re	(ppb)	0.69	0.89	0.73	1.36	0.52	0.58	0.23
Os	(ppb)	<LOD	<LOD	<LOD	<LOD	<LOD	<LOD	<LOD
Ir	(ppb)	2.11	1.95	2.68	3.00	2.46	2.73	1.83
Pt	(ppb)	5.41	4.51	1.20	7.68	5.70	3.73	4.70
Au	(ppb)	<LOD	<LOD	<LOD	<LOD	<LOD	<LOD	<LOD

Table VI-1: Results of TQ-ICP-MS analyses on agricultural soil samples carried out at the Thermo Fisher laboratory, Rodano, Italy.

		CN2	GC/11/2	GC11/2r	GC11/6	A4
Ru	(ppb)	5.97	1.93	1.78	0.74	<LOD
Rh	(ppb)	2.21	0.61	0.73	1.23	0.41
Pd	(ppb)	11.33	3.30	2.09	2.58	0.57
Re	(ppb)	0.71	22.1	23.6	28.9	0.17
Os	(ppb)	5.14	1.00	1.27	0.64	0.05
Ir	(ppb)	2.69	0.63	0.57	1.06	<LOD
Pt	(ppb)	8.26	5.70	5.37	5.66	1.76
Au	(ppb)	<LOD	4.69	6.00	5.64	<LOD

		A5	LE5	LE7	TL1	TL45
Ru	(ppb)	4.83	0.34	1.87	2.40	3.17
Rh	(ppb)	0.77	0.61	0.74	0.49	0.83
Pd	(ppb)	1.88	1.42	0.44	0.86	1.66
Re	(ppb)	0.17	0.20	0.42	0.13	0.52
Os	(ppb)	3.02	0.61	0.48	0.90	0.90
Ir	(ppb)	2.32	0.36	0.59	1.35	1.76
Pt	(ppb)	4.30	3.03	2.14	3.20	5.07
Au	(ppb)	<LOD	<LOD	<LOD	<LOD	<LOD

Table VI-2: Results of TQ-ICP-MS analyses on xenolith samples carried out at the Thermo Fisher laboratory, Rodano, Italy.

Appendix VII: List of acronymis used in the text

ACI	Automobile Club Italia
AR	Aqua Regia
ARPA	Agenzia Regionale per la Protezione Ambientale
BEC	Background Equivalent Concentration
BSE	Back Scattered Electron
CC	Carbonaceous Chondrites
cps	count per second
CRMs	Certified Reference Materials
DTG	Differential ThermoGravimetric Analysis
EC	European Commission
EMPA	Electron MicroProbe Analyse
EUDC	Extra Urban Driving Cycles
GSJ	Geological Survey of Japan
HFSE	High Field Strenght Element
HPA	High Pressure Asher
HR-ICP-MS	High Resolution ICP-MS
HSE	High Siderophile Element
ICP-MS	Inductively Coupled Plasma-Mass Spectrometry
ICP-QMS	Inductively Coupled Plasma- Quadrupole Mass Spectrometry
ICP-SFMS	Inductively Coupled Plasma- Sector Field Mass Spectrometry
ID	Isotopic Dilution
IDL	Instrument Detection Limit
INNA	Instrumentla Neutronic Activation Analysis
IPGE	Iridium PGE
IUGS	International Union of Geological Sciences
IUPAC	International Union of Pure and Applied Chemistry
JRC	Joint Research Centre
K/T or K/Pg	Cretaceous-Tertiary or Cretaceous-Paleogene boundary
LAM-ICP-MS	Laser Ablation Microprobe ICPMS
LOD	Limit Of Detection
MC-ICP-MS	Multi Collector-Inductively Coupled Plasma-Mass Spectrometry
NTIMS	Negative-Thermal Ionisation Mass Spectrometry
OC	Ordinary Chondrites
PFA	PerFluoroalkoxy Alkanes
PGE	Platinum Group Element
PM	Primordial Mantle
ppb	part per million (µg of analyte per Kg of sample)
PPGE	Palladium PGE
ppm	part per million (mg of analyte per Kg of sample)
ppt	part per million (ng of analyte per Kg of sample)
TQ-ICP-MS or QQQ-ICP-MS	Triple Quadrupole ICP-MS

REE	Rare Earth Element
rpm	round per minute
RSD	Relative Standard Deviation
UDC	Urban Driving Cycles
USGS	United States Geological Survey
WPC	Winter Plasma Conference
wt%	weight percent
XRD	X-Ray Diffraction
XRPD	X-Ray Powder Diffraction
XRF	X-Ray Fluorescence